Synthesis, Characterization and Oxidative Reactivity of Bio-inspired Mn^{III}-Hydroxo and Mn^{III}-Alkylperoxo Complexes

By

Adedamola A. Opalade

Submitted to the graduate degree program in Chemistry and the Graduate Faculty of the University of Kansas in partial fulfillment of the requirements for the degree of Doctor of Philosophy.

_____

Chairperson: Dr. Timothy A. Jackson

_____

Dr. Mikhail V. Barybin

_____

Dr. James D. Blakemore

_____

Dr. Ward H. Thompson

_____

Dr. Juan Bravo-Suarez

Date Defended: July 30, 2021

The Dissertation Committee for Adedamola A. Opalade

certifies that this is the approved version of the following dissertation:

Synthesis, Characterization, and Oxidative Reactivity of Bio-inspired Mn^{III}-Hydroxo and Mn^{III}-Alkylperoxo Complexes

_____

Chairperson: Dr. Timothy A. Jackson

Date Approved: July 30, 2021

Abstract

Enzymes such as manganese lipoxygenase (MnLOX), manganese superoxide dismutase (MnSOD), and manganese-dependent homoprotocatechuate 2,3-dioxygenase (MnHPCD) employ the redox versatility of manganese to perform important biological reactions. The elementary steps in the catalytic cycles of some of these enzymes involve concerted-proton electron transfer (CPET) reactions featuring a mononuclear Mn^{III}-hydroxo motif present in the enzyme active site. These Mn^{III}-hydroxo motifs display hydrogen bonding with neighboring amino acid residues, but it is unclear how this hydrogen bonding interaction controls reactivity. This knowledge gap is addressed in this dissertation by the generation of synthetic Mn^{III}-hydroxo complexes with and without intramolecular hydrogen bonding. Kinetic studies of these model complexes reveal the influence of this hydrogen bonding interaction on CPET reactions and offer insights into the potential role of the hydrogen-bonding interactions observed in the active sites of MnLOX and MnSOD.

The driving force for CPET reactions depend fundamentally on the reduction potential and basicity of the Mn^{III}-hydroxo unit. Therefore, the $Mn^{III/II}$ reduction potential and the pK_a of the Mn^{III}-hydroxo complexes can be modulated to control reactivity with substrates. This dissertation reports how steric perturbation was used to increase the $Mn^{III/II}$ reduction potential in an amide-containing N_5^- ligated Mn^{III}-hydroxo complex. Using the 2-(bis((6-methylpyridin-2-yl)methyl)amino)-N-(quinolin-8-yl)acetamide (H^{6Me}dpaq) ligand, a sterically encumbered Mn^{III}-hydroxo complex – $[Mn^{III}(OH)(^{6Me}dpaq)]^+$ was synthesized. The steric perturbation led to an elongated Mn-$N_{pyridine}$ bond, which causes the Lewis acidity of the Mn center to increase. The increased Lewis acidity consequentially increases the $Mn^{III/II}$ reduction potential. The increased $Mn^{III/II}$ reduction potential enhanced the CPET reactivity of the $[Mn^{III}(OH)(^{6Me}dpaq)]^+$ complex

with O-H bond by three-fold relative to the complex without sterics – $[Mn^{III}(OH)(dpaq)]^{+}$ (dpaq = 2-[bis(pyridin-2ylmethyl)]amino-N-quinolin-8-yl-acetamidate). This show how structural perturbation can be employed to modulate thermodynamic parameters, which will eventually control reactivity.

Alkylperoxomanganese(III) (Mn^{III}-OOR) intermediates are proposed in the mechanisms of several manganese-dependent enzymes like MnLOX and MnHPCD. However, their characterization has been challenging due to their inherent thermal instability. Fundamental understanding of these important intermediates' structural and electronic properties is limited to a series of complexes with thiolate-containing N_4S^- ligands. These well-characterized complexes are metastable, yet unreactive in the direct oxidation of organic substrates. Because the stability and reactivity of Mn^{III}-OOR complexes are likely to be highly dependent on their local coordination environment, we have generated two new Mn^{III}-OOR complexes using an amide-containing N_5^- ligand. Using the H^{6Me}dpaq ligand, $[Mn^{III}(OO^tBu)(^{6Me}dpaq)](OTf)$ and $[Mn^{III}(OOCm)(^{6Me}dpaq)](OTf)$ complexes were generated through the reaction of their Mn^{II} or Mn^{III} precursors with stoichiometric amount of ^{t}BuOOH and CmOOH, respectively. Both new Mn^{III}-OOR complexes are stable at room-temperature stable ($t_{1/2}$ = 5 and 8 days, respectively, at 298 K in CH_3CN) and capable of direct reactivity with phosphine substrates. These complexes are the most stable Mn^{III}-alkylperoxo complexes reported thus far and the first Mn^{III}-alkylperoxo complexes capable of direct oxidation of substrates. The stability of these Mn^{III}-OOR adducts render them amenable for detailed characterization, including by X-ray crystallography for $[Mn^{III}(OOCm)(^{6Me}dpaq)](OTf)$, which allow obtaining metric information, like the Mn^{III}-OOR O-O bond length for correlations with other Mn^{III}-alkylperoxo complexes. Thermal decomposition studies support a decay pathway of the Mn^{III}-OOR complexes by O-O bond homolysis. In contrast,

direct reaction of $[Mn^{III}(OOCm)(^{6Me}dpaq)]^{+}$ with PPh_3 provided evidence of heterolytic cleavage of the O-O bond. The Mn^{III}-alkylperoxo adducts also undergo hydrolysis in the presence of water to generate the Mn^{III}-hydroxo species, a reaction that mimics a step in the mechanism of MnLOX. These studies reveal that the local coordination sphere can tune both the stability and chemical reactivity of Mn^{III}-OOR complexes.

Acknowledgment

I want to thank GOD and give HIM all the glory for taking me to this point in life. It is not by power, nor is it by might, but by HIS grace that I made it this far. It was a rough ride, but HE is faithful, and I would not have made it without drawing strength from HIM daily.

I want to thank my advisor, Professor Timothy A. Jackson; you are my *savior*, and you have a unique effect on my life trajectory. From the first day, I sat in your CHEM 830 class. I appreciated your teaching style. I learned a lot about inorganic spectroscopic techniques from that class and got introduced to computational calculations, a field that has always been of interest, but I did not know how to get started. I appreciate your kindness in taking me into your lab when I was troubled after leaving my previous lab at the beginning of my third year. I am delighted today that I made a move to join your lab. I appreciate your patience with me when I was learning, and I am still learning. You are one of the few advisors who have many students and commitments, but still make time to meet with their students to brainstorm and troubleshoot research challenges. This helped guide my research and get things done the right way. Aside from academics, I have learned a lot more from you. I appreciate your attention to detail, clarity, purposefulness, and approaches to solving problems. I have come to appreciate these traits more and developing more of these traits in my life too. Additionally, I appreciate your support during my job search; your words of encouragement were reassuring and kept me trying till I succeeded. Thank you so much!

I want to thank my research advisory, candidacy exam, and dissertation committee members. To Professor Mikhail V. Barybin, you recruited me to KU, and you are influential to my success at KU. Thank you for your support when I was challenged with switching research group, and I also thank you for helping me with my isotopic labeling experiments. You supported me with your advice and helped with the experimental setups. I also spent a great deal of time in your lab using

your FTIR and electrochemical instruments. Thank you very much for being a member of my dissertation committee! To Dr. James D. Blakemore, you made me appreciate the MO diagram and group theory more when I took your CHEM 730. I appreciate your encouragement, suggestions and insights into how to make things work with my research. Thank you for allowing me to do electrochemical experiments in your lab and use your safety gears during my isotopic labeling experiments. Thank you for your service as a member of my research advisory, candidacy, and final dissertation committee. To Professor Ward H. Thompson, my first encounter with you was at the ACS MWRM in 2015 at St. Joseph; when you led me to the poster session of the Barybin's group, I never knew that my exploration would lead me to your CHEM 750 class. I enjoyed the class as it provided helpful knowledge, which later became handy in my research in Jackson's group. Thank you for your support and service as a member of my research advisory, candidacy, and final dissertation committee. To Professor Paul R. Hanson, I enjoyed being a TA in your organic chemistry class. Your lab has also provided me with some of the tools and instruments that I used in my research; I believe that if any lab has got anything, then Hanson's lab has got it. Thank you for being a member of my candidacy exam. To Dr. Juan J. Bravo-Suarez, thank you for serving on my candidacy exam and dissertation committee. I have enjoyed having you be a part of my graduate career!

I want to thank Justin T. Douglas and Sarah A. Neuenswander for their help with EPR and NMR. I enjoyed the discussions with you, Sarah. I appreciate the support of Lawrence L. Seib. You were accommodating with GC/MS and ESI-MS experiments, especially during my product analysis experiments. I want to say a big thank you to Victor W. Day for the XRD analysis. It took some trials before we could get the crystal structure for the Mn^{III}-alkylperoxo complex. Therefore, I want to thank you for your patience during this time. I thank you for your prompt responses to

requests even after your retirement. Thank you so much! I also want to thank Dr. Travis Witte for always allowing me to use the FTIR instruments. I appreciate your kindness and support throughout my graduate career.

I am blessed to have worked with some of the past and current members of the Jackson's group. The universe has been very nice to have aligned me to meet and work with you all. I thank you all for your love and sacrifices. To Joshua D. Parham, thank you for showing me the rope when I first joined the group. I enjoyed discussing my crazy scientific business ideas with you, and thank you for being my friend. To Melissa C. Denler, you are so friendly to everyone! My first direct encounter with you was when we gave our DyMERS presentation at Malott, and you allowed me to use your fancy laser pointer. Thank you for also listening to my concerns when experiments were not working and for your word of knowledge and motivation on how I should keep trying and things will eventually work. You have been a wonderful friend, and I am glad that you introduced me to Bryce as well. I look forward to many years of friendship with you two. To Yuri "H." Lee (my dearest friend), we have been friends since the first day of the international students' orientation, even before we realized that we are in the same program. Somehow, destiny brought us together into the same research group again, and we shared the same office space for three years. Thank you for putting up with me and being a wonderful friend. It is so sad that you did not complete your classes at my Ping-Pong training academy, but I understand the demand from your academic work. Hopefully, you will re-enroll someday and graduate in flying colors. You have grown to become a good scientist, and I admire your in-depth knowledge of EPR. You are an incredible scientist, and you are going to do great things. I hope we will be able to work together again someday. To Elizabeth N. Grotemeyer, I am glad we ended up in the same research group because I enjoyed taking the CHEM 720 class with you, and it is interesting because Robert Adams

and I also weathered through the CHEM 750 together. It has been nice to be friends with you both. Moreover, it is so sad that the COVID-19 pandemic disrupted our plans to get 'Jackson's Group Gym' started. Thank you both for allowing me to come to your weekly gym. Well, I have to say that there is something that I am *absolutely* sure about, and it is that you will do great wherever you go after grad school because you are all-rounded with the training you received in Jackson's group. To Jaycee, it was lovely working with you. I appreciate your help in getting me started on submitting jobs to the HPC and navigating the cluster. I enjoyed our discussions on hacks to avoid unnecessary expenditures. To Priya Singh, we met at an event before we even realized that we would be in the same program, and interesting enough, we joined Jackson's group at almost the same time. You are doing great in research and managing the lab activities! I look forward to your works in moving forward with the hydrogen bonding project. It has been nice talking to you about life, and I will miss you. To Sam, it was nice working with you, and thank you for being a great friend. I missed your homemade pastries! To Helena, time went by so fast, and the pandemic lockdown with the restrictions did not allow us to spend much time together, but the little time in my last days will be memorable. It has been great to work with you, and I enjoyed our conversations. Thank you for being my friend. You will do great, and I am looking forward to you completing your degree soon. To Eleanor Stewart-Jones, I was very excited when I heard that you would be going to Yale for graduate school. I am very proud of you, and I am looking out to impactful work from you. To Logan Hessefort, it was great working with you during your REU program. I thought I was the most zealous and adventurous until I met you. I am pleased that you decided to pursue a Ph.D. program at ASU. I look forward to your graduation invitation soon.

To the KU chemistry department, thank you for your support. I enjoyed my time here, and everyone here cares about the success of the students. It is beautiful to see how everyone works

together for a common goal and contributes to the success of one another in our department. This created a positive environment for me, knowing there is always someone who can help me in the building.

To all my friend outside of the lab, Yun Peng (Yuni), Javier S. Gutierrez (Javi G), Amit Kumar, Wade Henke, David R. Maldonado, Jerusha McFarland, Riddhi R. Golwanker, Julie A. Leseberg, Shawn R. Kelsey, Braelyn M. Page, Emranul H. M. Haque, Sacchindra S. Gamage (Sacchi), Monisola K. Okeowo-Dairo, Oluwaseun O. Mesele, Chibuike I. Maximilian, Damilola O. Fateru, Gbemisola F. Ojo, Sodiq O. Waheed (a friend like a brother), Elvis O. Ebikade, Yetunde T. Sokefun, Mayowa Ojo, Maduka Maduka, Simeon Ogundiran, and anyone else I may have unintentionally forgotten. Thank you all for being a part of my life.

To Dr. Andrew B. Williams, I appreciate your encouragement and supports. I always looked forward to meeting you and your family every Friday. I wish you success on your new mission in South Carolina. To Dr. Nikolay N. Gerasimchuk, when I was choosing an advisor for my Master's degree, I never knew I was choosing a lifelong relationship. I appreciate the support and kindness from you and your family.

To my mom and dad, you always tell us that you will support us to any height. Thank you for keeping your words, encouraging me, and always being there for me. To my sisters and brother, thank you for being wonderful siblings. You guys make life more meaningful and add colors to my world. To the love of my life – Cynthia C. Esiaka, thank you for always being there for me. I appreciate your unwavering support through my Ph.D. program. There is no way that I would have made it without you. Thank you for always having my back. I pray for the successful completion of your Ph.D. degree, and I look forward to the beautiful future ahead of us.

Table of Contents

Abbreviations and Acronyms

BDE	bond dissociation enthalpy
BDFE	bond dissociation free energy
CPET	concerted proton electron transfer
CV	cyclic voltammetry
DFT	density functional theory
DHA	9,10-dihydroanthracene
EPR	electron paramagnetic resonance
ET	electron transfer
CPCM	conductor-like polarizable continuum model
CV	cyclic voltammetry
EPR	electron paramagnetic resonance
ESI-MS	electrospray ionization mass spectrometry
MeCN	acetonitrile
MnLOX	manganese lipoxygenase
MnSOD	manganese superoxide dismutase
MnHPCD	manganese-homoprotocatechuate 2,3-dioxygenase
MO	molecular orbital
NMR	nuclear magnetic resonance
OEC	oxygen evolving complex
PCET	proton-coupled electron transfer
PT	proton transfer
DFT	density functional theory
TD-DFT	time dependent density functional theory
TEMPOH	2,2’-6,6’-tetramethylpiperidine-1-ol
UV	ultraviolet
XRD	X-ray diffraction

Chapter 1

Bioinspired Mn^{III}-hydroxo and Mn^{III}-alkylperoxo Complexes

1.1 Introduction

Manganese is a very desirable metal because of its high relative abundance, low cost, environmental friendliness, and variety of catalytically accessible oxidation states.[1-4] Manganese complexes display a profoundly wide range of chemistry and have been very useful in catalyzing several reactions industrially and biologically.[5-10] Manganese catalysts have industrial applications in epoxidation of olefins[11], selective reduction of NO_x to dinitrogen[1], and dehydrogenation of alcohols to produce important chemicals.[3] Biologically, manganese is important in the oxygen evolving complex (OEC) of photosystem II, which generates dioxygen, protons and electrons from water.[12] Other Mn-dependent enzymes such as Mn-superoxide dismutase (MnSOD), Mn-lipoxygenase (MnLOX) and Mn-homoprotocatechuate 2,3-dioxygenase (MnHPCD) are vital biologically and environmentally. MnSOD is responsible for cellular detoxification by converting harmful superoxide radicals into dioxygen and less harmful hydrogen peroxide.[5, 13, 14] The MnLOX enzyme catalyzes the oxidation of polyunsaturated fatty acids into their hydroperoxides, which are further metabolized into biologically active compounds that act as inflammatory mediators and reproductive/growth regulators in plants.[5, 15] The MnHPCD is found in soil bacteria and is responsible for environmental detoxification by converting aromatic compounds into intermediates used in primary metabolism using dioxygen. This reaction is beneficial because it helps Nature reclaim the carbon sequestered in aromatic compounds.[5, 8, 16] Even though these enzymes are of vital biological importance, detailed mechanistic understanding of these processes is not fully attained. The involvement of Mn(III) intermediates has been postulated for these enzymes[5, 8], and synthetic small molecules that mimic the activity of these enzymes have been used to model elementary steps proposed for these enzymes.[17] In these enzymes, it is generally proposed that the Mn center is redox-active and spectroscopic measurements, as well as

computational studies, have revealed that Mn^{III}/Mn^{II} is the most common redox cycle for the electron and atom transfer reactions of MnSOD, MnLOX and MnHPCD.[5]

1.2 Mn^{III}-hydroxo species in biology (MnSOD and MnLOX)

Active site Mn^{III}-hydroxo units have been proposed to be central to the reactivity of the MnSOD and MnLOX enzymes.[18-22] In the resting state of the MnSOD, the Mn metal is in the +3 oxidation state, coordinated by three histidine residues, an aspartate residue and a solvent molecule that is most likely a hydroxo ligand. This solvent is an aqua ligand in the reduced (Mn^{II}) form of the enzyme (Figure 1.1).[18-22] These ligands enforce a trigonal bipyramidal geometry around the Mn center. It is proposed that the Mn in MnSOD is initially present as Mn^{II} when the holoenzyme is first produced in the cell and later oxidized to the Mn^{III} resting state.[5, 22] MnSOD catalyzes the disproportionation of the superoxide radical by a two-step reaction, in which the oxidation state of the Mn center cycles between the +2 and +3 oxidation states. The first step of the reaction involves the MnSOD in the resting state (Mn^{III}) with superoxide radical anion (Figure 1.2). In this reaction, the hydroxo-ligated Mn^{III}SOD is reduced by an electron from the superoxide radical anion and uptake a proton from water to form the aqua-ligated Mn^{II}SOD (Figure 1.2).[5, 19, 23-26] The active-site Mn^{II} center then reacts with a second superoxide radical anion, by a proton-coupled electron transfer mechanism, producing a hydroperoxyl anion and Mn^{III}. Neighboring water molecules can subsequently protonate this anion to produce hydrogen peroxide (Figure 1.2). Since MnSOD acts as both an oxidant and a reductant in this catalytic pathway, the midpoint potential of the enzyme must be midway between the standard reduction potentials for the respective potential couples of $O_2^{\cdot -}/O_2$ and $O_2^{\cdot -}/H_2O_2$.[5, 19, 23-25]

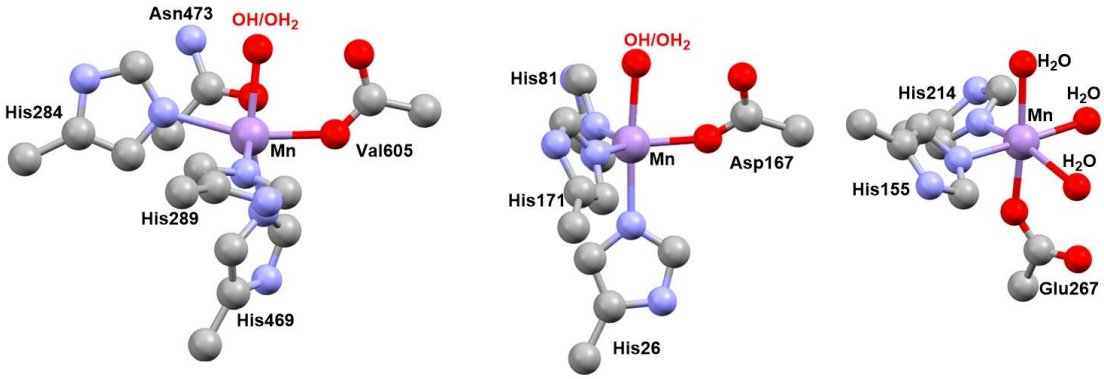

Figure 1.1. Active site structures of three Mn-dependent enzymes. Left: MnLOX (PDB file: 5FNO), middle: MnSOD (PDB file: 1VEW), and right: MnHPCD (PDB file: 1F1R).

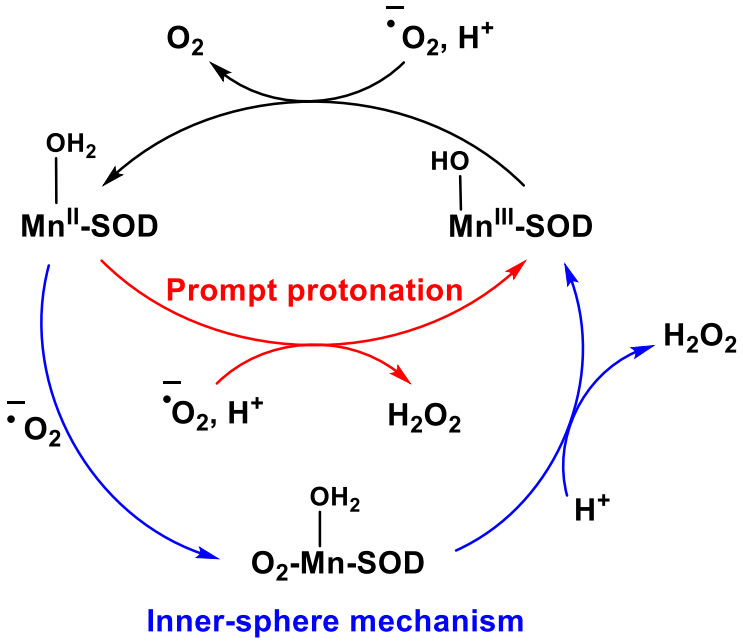

Figure 1.2. Proposed mechanism for MnSOD disproportionation of superoxide radical anion, showing the prompt-protonation pathway and inner-sphere mechanism.[5, 14, 26-31]

The active site of the MnLOX in its oxidized form features a mononuclear Mn^{III} center in a six-coordinate geometry. The Mn^{III} is bound by an hydroxo ligand, three histidine residues, an asparagine residue and a carboxylate group of the C-terminal valine (Figure 1.1).[18-21] The details of how MnLOX oxidizes fatty acids have been a topic of debate.[32] The MnLOX enzyme oxidizes

polyunsaturated fatty acids containing *cis,cis*-1,4-pentadiene to their corresponding 1-hydroperoxy-*trans,cis*-2,4-diene. The mechanism involves the Mn^{III}-OH unit of the MnLOX enzyme abstracting a hydrogen atom from the bis-allylic C-H bond of the fatty acid, forming a Mn^{II}-OH_2 unit and substrate radical (Figure 1.3). The radical undergoes rearrangement to produce a more stable radical intermediate. This intermediate reacts with dioxygen, producing a peroxyl radical. In one mechanism, the peroxyl radical abstracts a hydrogen atom from the Mn^{II}-OH_2 unit to regenerate Mn^{III}-OH unit and release the hydroperoxide product.[33] Kinetic studies of the MnLOX have shown the initial concerted proton-electron transfer (where electron and proton are transfer in the same kinetic step) step with a KIE of 28 between the Mn^{III}-OH unit and substrate to be rate-limiting.[20, 34] Therefore, little is known about the mechanism following this step. Due to the significant involvement of Mn^{III}–OH unit in the catalytic pathways of the MnLOX and MnSOD, there has been increasing interest in probing the properties and reactivity of synthetic Mn^{III}–OH complexes.[35-41]

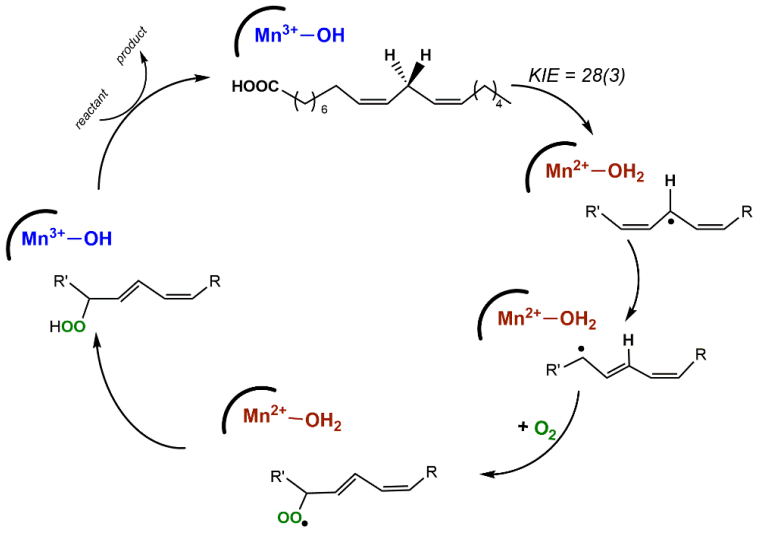

Figure 1.3. Proposed mechanism for fatty acid peroxidation by MnLOX enzyme.

1.3 Mn^{III}-alkylperoxo species in biology (MnHPCD, MnSOD and MnLOX)

The soil bacteria *Arthrobacter globiformis* detoxify the environment (the soil) by metabolizing aromatic compounds (for example catechols, 1,4-hydroquinones, *o*-aminophenols, and salicyclates) resulting from agricultural herbicides and pesticides through ring opening reactions. This process is mediated by the MnHPCD enzyme.[5, 42-44] The active site of the resting enzyme has a Mn^{II} ion in a distorted octahedral environment, coordinated by two histidine residues and a glutamate, with the rest of the coordination sites occupied by three water molecules (Figure 1.1).[5, 43] During the first step of the catalytic reaction, the water molecules are displaced, and two of these sites are occupied by the substrate, which binds in a bidentate fashion through two donor atoms (Figure 1.4). The third site allows binding of dioxygen (Figure 1.4). It was initially proposed that the Mn^{II} center did not change oxidation state during the catalytic cycle.[45] However, Hendrich *et al.* performed detailed EPR experiments and quantitative analysis of metal oxidation states of MnHPCD as it turns over the natural homoprotocatechuate (HPCA) substrate. These studies gave insight into the nature and oxidation state of the Mn-center intermediates in I-IV in Figure 1.4.[8] Most importantly, their experiment reported the appearance of a low concentration intermediate immediately after the addition of O_2 to samples of MnHPCD prepared with a significant excess of HPCA. This intermediate was quantified and identified by EPR spectroscopy to be a Mn^{III}-radical species. It is currently not established if the Mn^{III}-radical intermediate is a Mn^{III}-superoxide or Mn^{III}-peroxo species. However, the presence of a Mn^{III}-intermediate implicates a redox change of the Mn-center during the catalytic cycle.[8] This Mn^{III}-radical intermediate underwent a reaction with the substrate to form a Mn^{II}-alkylperoxo intermediate IV in Figure 1.4.[8, 46, 47] In light of this information, the consensus about the catalytic pathway is that the Mn^{II}-center binds O_2 to form the Mn^{III}-radical intermediate which reacts with the bound substrate to form a Mn^{II}-alkylperoxo

adduct. The Mn^{II}-alkylperoxo adduct undergoes rearrangement to insert an oxygen atom into the substrate ring, leading to ring cleavage upon protonation in aqueous environment (Figure 1.4).

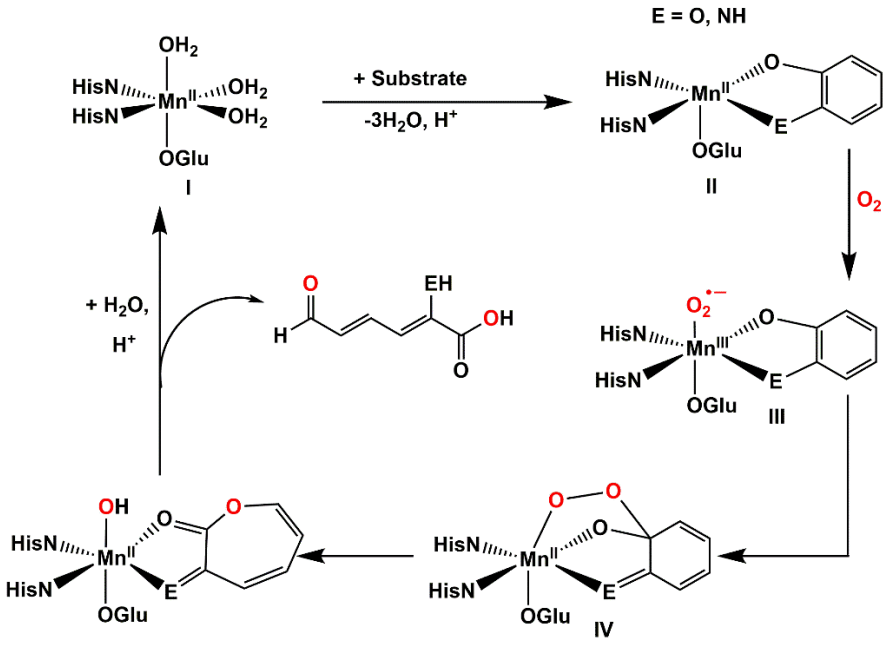

Figure 1.4. Proposed mechanism for ring-cleavage of aromatic compounds by MnHPCD.[8, 43]

Mn^{III}-peroxo intermediates are also reported in the mechanism of the MnSOD enzyme. MnSOD displayed the most complicated kinetics of any member of the SOD family. It was found by pulse-radiolysis studies that at low superoxide concentration, MnSOD exhibits ping-pong behavior, such that $O_2^{\bullet-}$ is oxidized to O_2 by the oxidized form of the enzyme in one step, and $O_2^{\bullet-}$ is reduced to H_2O_2 by the reduced form of the enzyme in another step (Figure 1.2).[26, 48] Each of these steps is first order with respect to the superoxide radical anion and utilizes a proton (Figure 1.2).[49-51] At a high concentration of the superoxide radical anion, the consumption of the superoxide is biphasic. The initial phase is fast and first-order with respect to the superoxide radical anion, while the second phase is a slow zero-order phase.[26, 49-51] This biphasic behavior has been interpreted using the gating mechanism,[14, 52] where superoxide radical anion is either reduced by

Mn^{II}SOD to give H_2O_2 (prompt protonation mechanism), or superoxide radical anion reacts with Mn^{II}SOD to form an inhibited complex, which slowly decays to give Mn^{III}SOD and H_2O_2 (inner sphere mechanism, see Figure 1.2).[26] The fast initial phase of the biphasic kinetics consist of the superoxide consumption by both paths, and the slow zero-order phase represents the slow decay of the inhibited complex.[26] The nature of the inhibited complex is yet to be established, but it is generally believed to be a Mn^{III}-peroxo specie. Computational studies have provided reports in support of both an end-on and side-on peroxo complexes.[53-56] Side-on peroxide coordination was observed in the crystals obtained when *E. coli* MnSOD was soaked in peroxide, but this species might not correspond to the Mn^{III}-peroxo intermediate observed in the kinetic studies.[57]

The involvement of a Mn^{III}-alkylperoxo intermediate in MnLOX comes from an alternative mechanism, presented in Figure 1.5. In this alternative mechanism, the substrate peroxyl radical displaces the aqua ligand of the Mn^{II} center to form a Mn^{III}–alkylperoxo adduct. This species is then hydrolyzed by water to yield the hydroperoxo product and the Mn^{III}–hydroxo resting state.[4, 58] A support for this mechanism comes from a crystal structure of a metastable fatty acid-lipoxygenase intermediate complex called purple lipoxygenase, formed from the reaction FeLOX with fatty acid substrate. X-ray crystallography and EPR studies show that the purple lipoxygenase is an end-on iron (III) peroxide complex.[59]

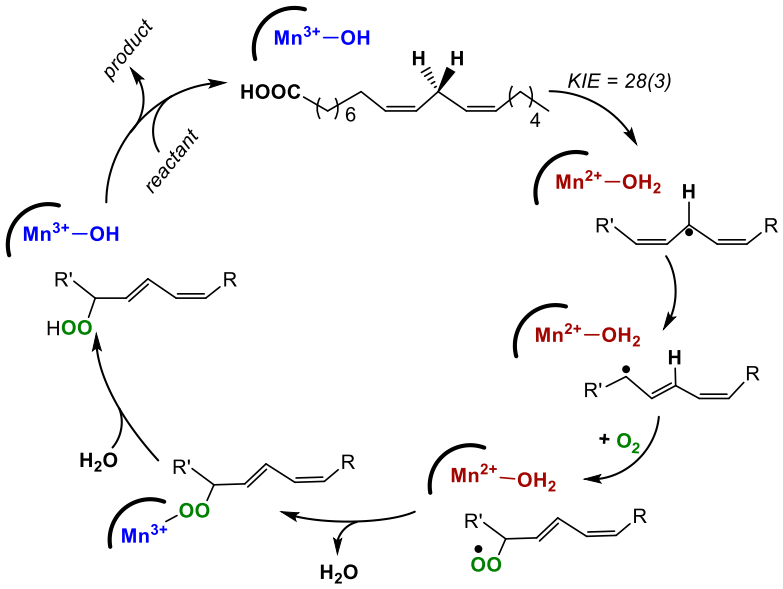

Figure 1.5. Proposed alternative mechanism for fatty acid peroxidation by MnLOX enzyme showing Mn^{III}-alkylperoxo intermediate.[58]

1.4 Mn^{III}-hydroxo Model Complexes

A proton-coupled electron transfer (PCET) reaction is any reaction that involve the transfer of a proton and an electron regardless of the kinetic mechanisms.[60-63] This reaction is important biologically and employed by enzymes like MnLOX and MnSOD to oxidize their substrates. Because the MnLOX and MnSOD have Mn^{III}-OH unit in their active-sites, synthetic mononuclear Mn^{III}-hydroxo complexes are targets for modeling the activity of the MnLOX and MnSOD enzymes in PCET reactions with substrates.[64-66] However, synthetic mononuclear Mn^{III}-hydroxo units are rare.[4] The first crystallographically characterized mononuclear Mn^{III}-OH unit was reported in 1992 by Armstrong *et al*. (supported by Schiff base ligand).[67] From 20 years after this first report (1992-2012), only seven structurally-characterized Mn^{III}-hydroxo units were reported.[36, 67-72] However, in the last 9 years, there has been increased interest in Mn^{III}-hydroxo adducts and new compounds have been reported.[4, 66] This section will focus on the established

synthetic routes used to generate Mn^{III}-hydroxo complexes, explore their oxidative reactivity with substrates, and discuss improvements to the reactivity of these complexes.

1.4.1 Preparation and characterization of Mn^{III}-hydroxo Adducts

Mn^{III}-hydroxo complexes are most commonly prepared from the reaction of a Mn^{II} precursor complex and dioxygen.[65, 66, 73, 74] This route is very desirable because, in principle, it could be developed to perform catalytic turnover, thus providing a relatively greener and less expensive aerobic oxidation catalyst as opposed to more expensive precious metals used industrially.[75] Meanwhile, some studies reported the formation of multinuclear μ-oxo-(or μ-hydroxo-) bridged species from dioxygen preparation.[36, 65, 74, 76] Further studies demonstrated how steric encumbrance and the presence of H_2O is critical to prevent the formation of these multinuclear species.[36, 73, 74, 76] In the proposed mechanism for the dioxygen oxidation of Mn^{II} to generate the mononuclear Mn^{III}-hydroxo complex, a Mn^{II} center first reacts with dioxygen to generate a Mn^{III}-superoxo species, which is trapped by a second Mn^{II} center to produce a μ-peroxo-dimanganese(III,III) species as proposed by Kovacs and Borovik (Scheme 1.1).[36, 77-80] This μ-peroxo-dimanganese(III,III) species is proposed to undergo O-O homolysis to produce either two Mn^{IV}-oxo units or a bis(μ-oxo)dimanganese(IV,IV) intermediate.[4, 36] In continuation of the pathway that leads to the formation of the Mn^{IV}-oxo units, the Mn^{IV}-oxo intermediate could abstract hydrogen atom from solvent to form the Mn^{III}-hydroxo complex, as proposed by Borovik *et al.* (Scheme 1.1, pathway A),[36] or the Mn^{IV}-oxo species can be attacked by remnant Mn^{II} starting complex to form (μ-oxo)dimanganese(III,III) species, which then hydrolyze in the presence of water to produce the mononuclear Mn^{III}-hydroxo product (Scheme 1.1, pathway B) as proposed by Kovacs *et al.*[65, 79, 81]

Pathway A will show a 2 : 1 Mn : O_2 stoichiometry, while pathway B will have a 4 : 1 Mn : O_2 stoichiometry (Scheme 1.1).[4] To distinguish between these mechanisms and understand the influence of steric on the mechanism, Parham *et al*. used two Mn^{II} complexes – $[Mn^{II}(dpaq)]^+$ and $[Mn^{II}(dpaq^{2Me})]^+$ as a probe (Figure 1.6).[73, 82] Dioxygen titrations were performed with the $[Mn^{II}(dpaq)]^+$ and $[Mn^{II}(dpaq^{2Me})]^+$ to form their Mn^{III}-hydroxo complexes. It was found that the $[Mn^{II}(dpaq)]^+$ requires 4 : 1 Mn : O_2 stoichiometry, while the $[Mn^{II}(dpaq^{2Me})]^+$ requires 2 : 1 Mn : O_2 stoichiometry to form the Mn^{III}-hydroxo complexes. This shows that pathway A is consistent with the dioxygen oxidation of $[Mn^{II}(dpaq^{2Me})]^+$ to form $[Mn^{II}(OH)(dpaq^{2Me})]^+$, while pathway B is consistent with the dioxygen oxidation of $[Mn^{II}(dpaq)]^+$ to form $[Mn^{II}(OH)(dpaq)]^+$.[82] Isotopic labeling experiments, in which the dioxygen oxidation of the Mn^{II} complexes was carried out in d_3-MeCN, also supported the observed pathways for these complexes. The oxidation of $[Mn^{II}(dpaq)]^+$ in d_3-MeCN did not result in any deuterium incorporation in the Mn^{III}-hydroxo product, while the oxygenation of $[Mn^{II}(dpaq^{2Me})]^+$ in d_3-MeCN showed the formation of $[Mn^{III}(OD)(dpaq^{2Me})]^+$.[82] The result from this work shows the effect of sterics in controlling the pathway for the dioxygen oxidation of Mn^{II} precursor to their Mn^{III}-hydroxo complexes.

Additionally, a study performed by Borovik *et al.* using a tripodal ligand based on tris(*N*-alkylcarbamoylmethyl)amine have shown that the source of the hydroxo ligand in Mn^{III}-hydroxo complexes, prepared by dioxygen oxidation of the Mn^{II} precursor complex originates from the dioxygen.[36]

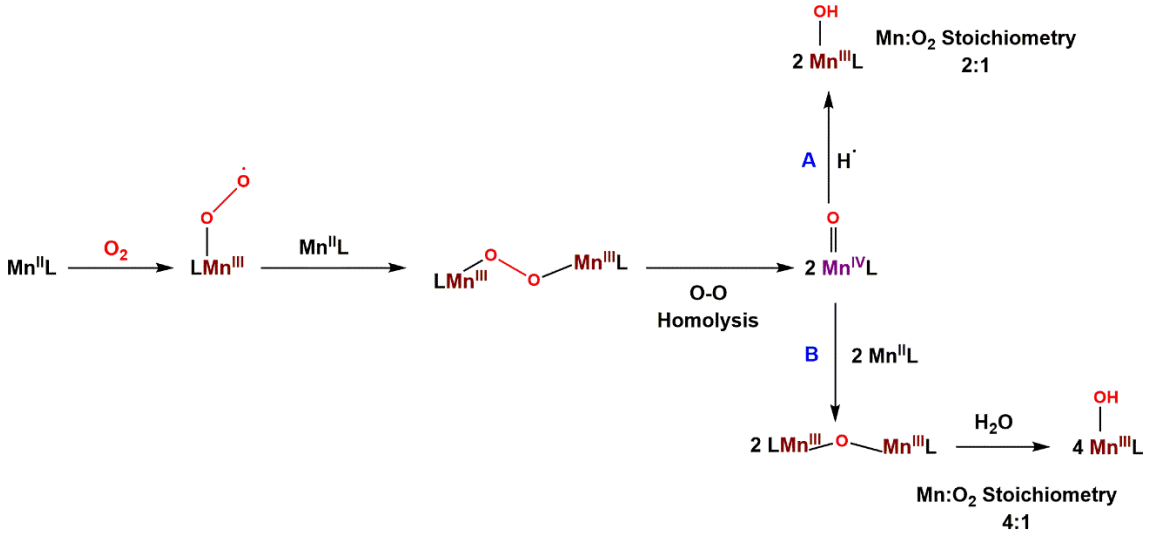

Scheme 1.1. Proposed mechanism for the dioxygen oxidation of Mn^{II}-complexes to generate Mn^{III}–hydroxo complexes. L = generic representation for ligand (Figure adapted from ref. 4).

Aside from the preparation of Mn^{III}-hydroxo complexes by the reaction of a Mn^{II} precursor with dioxygen, chemical oxidants like iodosobenzene (PhIO) have also been used to generate mononuclear Mn^{III}-hydroxo complexes.[70, 73, 74, 76] PhIO is a two-electron chemical oxidant, typically acting as an oxygen-atom transfer reagent. While there is no detailed mechanism explaining the formation of Mn^{III}-hydroxo species by PhIO, some valuable insights can be obtained from previous studies where PhIO was employed in the synthesis of the Mn^{IV}-oxo species.[83-87] The Mn^{IV}-oxo species can react with remnant Mn^{II}-specie to form (μ-oxo)dimanganese(III,III) species, which will hydrolyze in the presence of water to produce the mononuclear Mn^{III}-hydroxo product scheme 1.1.

Finally, Mascharak *et al.* have also demonstrated the direct synthesis of Mn^{III}-hydroxo complex from $PaPy_2QH$ ($PaPy_2QH$ = *N*,*N*-Bis(2-pyridylmethyl)amine-*N*-ethyl-2-quinolinecarboxamide) ligand and a Mn^{III}-salt. During preparation, an aliquot amount of H_2O was added to the reaction mixture.[69] Thus, it is reasonable to believe that the oxygen atom of the

hydroxo ligand in this case originates from the water molecule that was added. A subsequent chapter of this dissertation will introduce how Mn^{III}-hydroxo complex can be produced by hydrolysis of a Mn^{III}-alkylperoxo complex.

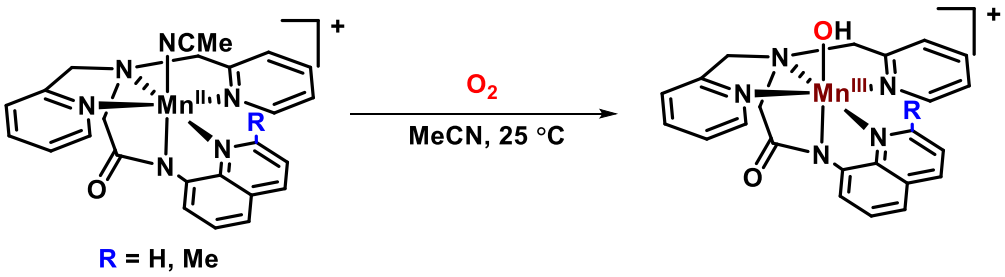

Figure 1.6. Reaction of solvento $[Mn^{II}(dpaq^{2R})]^{+}$ complexes with dioxygen to form $[Mn^{III}(OH)(dpaq^{2R})]^{+}$ complexes in MeCN solution at 25 °C. When R = H, it is referred to as $[Mn^{II}(dpaq)]^{+}$ and when R = Me, it is referred to as $[Mn^{II}(dpaq^{2Me})]^{+}$ in the text.[4, 82]

1.4.2 Oxidative Reactivity of Mn^{III}-hydroxo Complexes

Mn^{III}-hydroxo complexes have been shown to be capable of oxidizing C-H and O-H bonds of substrates by PCET.[65, 70, 73] PCET can be concerted (CPET), or it can occur in a stepwise manner, where the proton and electron are transfer sequentially by ET-PT (electron transfer followed by a proton transfer) or PT-ET (proton transfer followed by an electron transfer) mechanisms (Scheme 1.2).[60] In some cases, a concerted process can circumvent the high energy intermediates potentially formed from the stepwise ET or PT steps.[60]

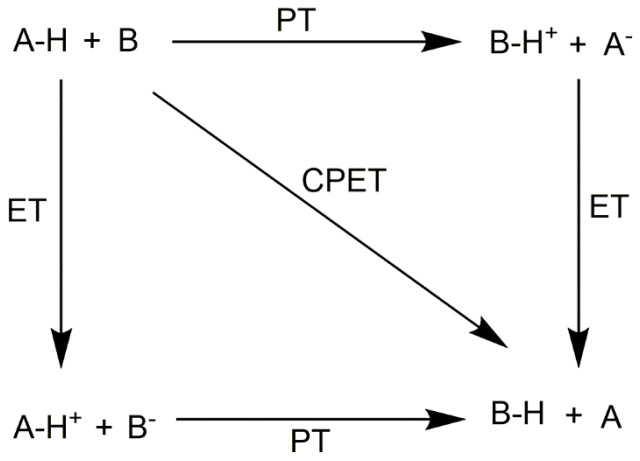

Scheme 1.2. Schematic representation showing concerted vs. stepwise transfer of proton and electron.

CPET reactions are common in enzymes.[60-63] For example in MnLOX, the Mn^{III}-hydroxo unit acts as the CPET agent to initiate substrate oxidation.[20, 34] A prominent report of a Mn^{III}-hydroxo complex that mimics MnLOX activity comes from Goldsmith *et al*., where they reported that a $[Mn^{III}(OH)(PY5)]^{2+}$ (PY5 = 2,6-bis(bis(2-pyridyl)- methoxymethane)pyridine) (Figure 1.7) is capable of oxidizing C-H bonds of hydrocarbons like toluene, fluorene, 9,10-DHA and xanthene (C-H BDFE = 75 – 88 kcal/mol), thereby mimicking the MnLOX activity.[70]

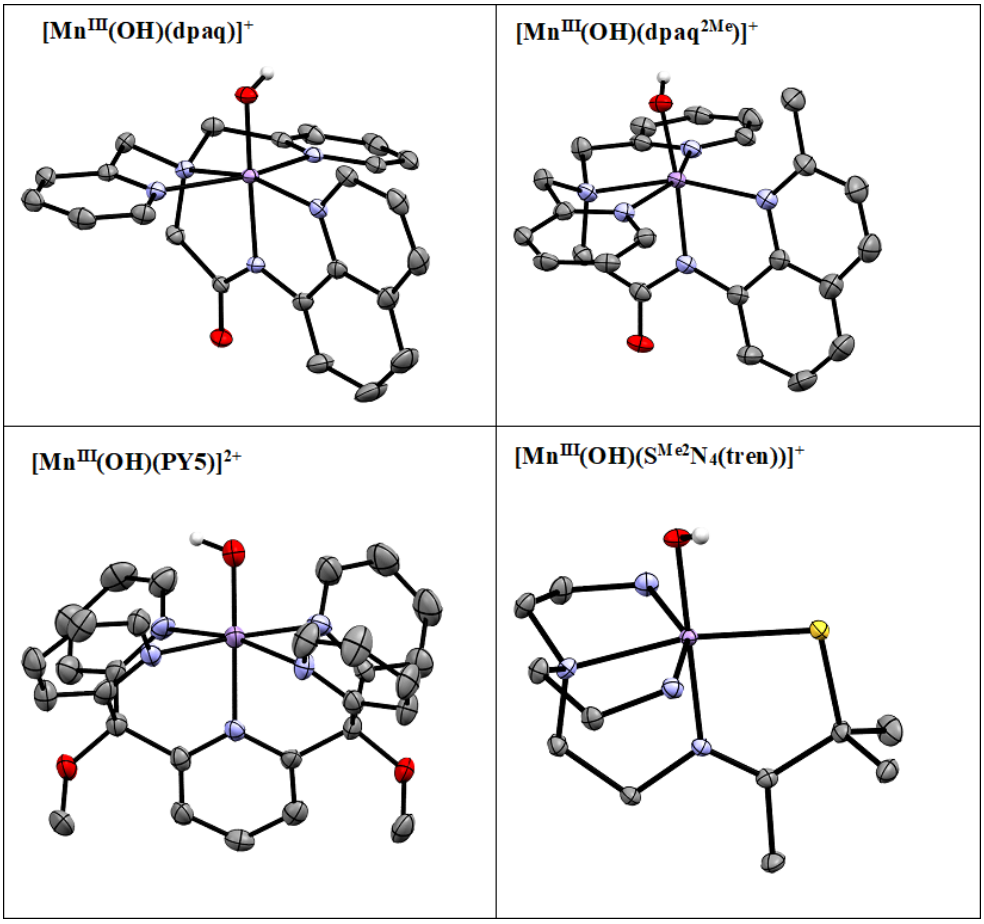

Figure 1.7. XRD structure of $[Mn^{III}(OH)(dpaq)]^{+}$[73, 88], $[Mn^{III}(OH(dpaq^{2Me})]^{+}$[73], $[Mn^{III}(OH)(PY5)]^{2+}$[70], and $[Mn^{III}(OH)(S^{Me2}N_4(tren))]^{+}$[65]. Solvents, counter-ions and non-hydroxo hydrogen atoms were removed for clarity.

Another class of Mn^{III}-hydroxo complexes that are capable of oxidizing C-H bonds comes from our group, where we reported two dpaq complexes – $[Mn^{III}(OH)(dpaq)]^{+}$ and $[Mn^{III}(OH)(dpaq^{2Me})]^{+}$ (Figure 1.6 and 1.7) that are capable of oxidizing C-H bond of xanthene.[73] The motivation for using the dpaq ligand originates from the monoanionic net charge of the ligand when it coordinates to the metal ion, which mimics the net charge of the amino-acid derived ligands of MnLOX (Figure 1.1). These complexes have k_{obs} values of 8 x 10^{-3} and 2.5 x 10^{-3} s^{-1}, respectively, for their reactivity with 250 equiv. of xanthene at 50 °C in MeCN.[73] DFT calculations showed that $[Mn^{III}(OH)(dpaq)]^{+}$ oxidizes xanthene at a faster rate than $[Mn^{III}(OH)(dpaq^{2Me})]^{+}$,

because of the steric encumbrance from the 2-methyl substituent on the quinoline ring in the $[Mn^{III}(OH)(dpaq^{2Me})]^{+}$. The transition state revealed that steric hinderance caused xanthene to be oriented differently with the $[Mn^{III}(OH)(dpaq^{2Me})]^{+}$, compared to the orientation in $[Mn^{III}(OH)(dpaq)]^{+}$.[73] The reorientation in $[Mn^{III}(OH)(dpaq^{2Me})]^{+}$ introduced a destabilizing effect that caused the transition state of $[Mn^{III}(OH)(dpaq^{2Me})]^{+}$ to be higher than that of $[Mn^{III}(OH)(dpaq)](OTf)$ by about 3 kcal/mol.[73]

The k_{obs} values for xanthene oxidation by $[Mn^{III}(OH)(dpaq)]^{+}$ and $[Mn^{III}(OH)(dpaq^{2Me})]^{+}$ can be compared to the k_{obs} value obtained by extrapolating the second-order rate constant for the reaction of $[Mn^{III}(OH)(PY5)]^{2+}$ with xanthene to 250 equiv. of xanthene. The k_{obs} values for $[Mn^{III}(OH)(dpaq)]^{+}$ and $[Mn^{III}(OH)(dpaq^{2Me})]^{+}$ are 10-30 fold slower than that of $[Mn^{III}(OH)(PY5)]^{2+}$ (8×10^{-2} s^{-1}).[66] This enhanced reactivity for $[Mn^{III}(OH)(PY5)]^{2+}$ could be caused by the higher $Mn^{III/II}$ reduction potential of $[Mn^{III}(PY5)(OH)]^{2+}$ (+0.14 V vs Fc/Fc^{+} in MeCN)[70] compared to those of the $[Mn^{III}(OH)(dpaq)]^{+}$ and $[Mn^{III}(OH)(dpaq^{2Me})]^{+}$ (-0.73 V and -0.62 V respectively, vs Fc/Fc^{+} in MeCN).[66, 70, 73]

Efforts have been taken to improve the capability of Mn^{III}-hydroxo adducts in activating C-H bonds. A significant method to modulate the oxidative reactivity of Mn^{III}-hydroxo units involve the introduction of a Lewis acid. Studies performed in our group, where we added $Sc(OTf)_3$ and $Al(OTf)_3$ to $[Mn^{III}(OH)(dpaq)]^{+}$ solution gave rise to a new intermediate that is spectroscopically distinct from $[Mn^{III}(OH)(dpaq)]^{+}$.[89] This new intermediate was characterized by ^{1}H NMR spectroscopy to be the Mn^{III}-aqua complex – $[Mn^{III}(OH_2)(dpaq)]^{2+}$. $[Mn^{III}(OH_2)(dpaq)]^{2+}$ reacts with 9,10-DHA (a substrate that $[Mn^{III}(OH)(dpaq)]^{+}$ displays no activity towards) and displayed a 30-fold enhancement in rate relative to the only Mn^{III}-hydroxo complex ($[Mn^{III}(OH)(PY5)]^{2+}$) known to react with 9,10-DHA.[70, 89] The treatment of $[Mn^{III}(OH)(dpaq)]^{+}$ with Brønsted acids lead

to the same effect.[89] Thus, it was concluded that the primary influence of the Lewis acids is to coordinate water and increase the Brønsted acidity of the solution, thereby promoting the protonation of the Mn^{III}-OH unit.[89] Nam *et al.* also reported that the reaction of $[Mn^{III}(OH)(dpaq)]^{+}$ with triflic acid leads to the formation of crystallographically characterized $[Mn^{III}(OH_2)(dpaq)]^{2+}$.[90] This $[Mn^{III}(OH_2)(dpaq)]^{2+}$ reaction with xanthene at 25 °C in MeCN shows substantial enhancement in rate relative to the reaction of $[Mn^{III}(OH)(dpaq)]^{+}$ with xanthene at 50°C in MeCN.[90] The relative enhancement in rate is credited towards the increase in the $Mn^{III/II}$ reduction potential of the $[Mn^{III}(OH_2)(dpaq)]^{2+}$ when compared to the $[Mn^{III}(OH)(dpaq)]^{+}$ (1.03 and -0.1 V respectively, vs. SCE).[90]

Mn^{III}-hydroxo units are also capable of oxidizing O-H bonds of TEMPOH. TEMPOH is a substrate commonly used for CPET reactions because of its relatively weaker O-H bond (BDFE = 66.5 kcal mol^{-1} in MeCN at 298 K), high pK_a value (pK_a = 41 in MeCN) and the difficulty in oxidation ($TEMPOH^{+/\bullet}$ $E_{p,a}$ = 0.71 V vs. $Fc^{+/0}$).[60] Kovacs *et al.* reported a thiolate-ligated $[Mn^{III}(OH)(S^{Me2}N_4(tren))]^{+}$ complex (Figure 1.7) that is capable of CPET reactivity with TEMPOH substrate with a second-order rate constant (k_2) of 2.1 x 10^3 $M^{-1}s^{-1}$ at 25 °C in MeCN. Our group also reported that $[Mn^{III}(OH)(dpaq)]^{+}$ and $[Mn^{III}(OH)(dpaq^{2Me})]^{+}$ are able to oxidize TEMPOH (k_2 = 1.1 and 3.9 $M^{-1}s^{-1}$ respectively at -35 °C in MeCN). The $[Mn^{III}(OH)(dpaq^{2Me})]^{+}$ complex is more reactive than $[Mn^{III}(OH)(dpaq)]^{+}$ because the steric perturbation by the 2-methyl group in the $[Mn^{III}(OH)(dpaq^{2Me})]^{+}$ caused an elongation of the Mn-$N_{quinoline}$ bond in $[Mn^{III}(OH)(dpaq^{2Me})]^{+}$ relative to $[Mn^{III}(OH)(dpaq)]^{+}$ by 0.11 Å. This elongation leads to a more Lewis acidic Mn^{III} center in $[Mn^{III}(OH)(dpaq^{2Me})]^{+}$ and thus a higher $Mn^{III/II}$ reduction potential by 0.11 V. The activation parameters for the reactions of these complexes with TEMPOH shows that the $\Delta S^{\ddagger}$ contribution to the $\Delta G^{\ddagger}$ is relatively higher for $[Mn^{III}(OH)(dpaq^{2Me})]^{+}$ by *ca.* 6

cal/mol/K due to the steric strain from the 2-methyl substituent, but the $\Delta H^{\ddagger}$ for $[Mn^{III}(OH)(dpaq^{2Me})]^{+}$ was decreased by nearly two-fold relative to $[Mn^{III}(OH)(dpaq)]^{+}$. Thus the $\Delta G^{\ddagger}$ for $[Mn^{III}(OH)(dpaq^{2Me})]^{+}$ is 1.4 kcal/mol lower than that of the $[Mn^{III}(OH)(dpaq)]^{+}$.[73] The reduced $\Delta G^{\ddagger}$ explains why the reactivity of $[Mn^{III}(OH)(dpaq^{2Me})]^{+}$ with TEMPOH is faster than that of $[Mn^{III}(OH)(dpaq)]^{+}$.[73] The reactivity of the $[Mn^{III}(OH)(dpaq)]^{+}$ and $[Mn^{III}(OH)(dpaq^{2Me})]^{+}$ can be compared to the thiolate-ligated $[Mn^{III}(OH)(S^{Me2}N_4(tren))]^{+}$ reported by Kovacs.[65] Comparison shows that $[Mn^{III}(OH)(S^{Me2}N_4(tren))]^{+}$ is faster than $[Mn^{III}(OH)(dpaq)]^{+}$ and $[Mn^{III}(OH)(dpaq^{2Me})]^{+}$ by *ca.* two order of magnitudes.[66, 74] Given the difference in the local environment of the dpaq-ligated complexes from the thiolate-ligated $[Mn^{III}(OH)(S^{Me2}N_4(tren))]^{+}$, it is difficult to gain insight into how to modulate reactivity.

It is already clear how structural perturbation influences the behavior of the Mn^{III}-hydroxo unit from the comparative studies of the $[Mn^{III}(OH)(dpaq)]^{+}$ and $[Mn^{III}(OH)(dpaq^{2Me})]^{+}$. To gain more insight into how electronic modulation through the ligand scaffold could impact the kinetic and thermodynamic properties of the Mn^{III}-hydroxo complexes and consequently control their reactivity, our group embarked on investigating a series of Mn^{III}-hydroxo complexes – $[Mn^{III}(OH)(dpaq^{5R})]^{+}$ (R = H, NO_2, OMe, and Cl), where the 5-position of the quinoline was substituted (Scheme 1.3).[74] This electronic modulation leads to an overall change in the $Mn^{III/II}$ reduction potential by *ca.* 250 mV for the extremes of $[Mn^{III}(OH)(dpaq^{5NO2})]^{+}$ and $[Mn^{III}(OH)(dpaq^{5OMe})]^{+}$. This variation in the $Mn^{III/II}$ reduction potential shows direct and linear correlation with the logarithm of the second-order rate constants ($\log(k_2)$) of the complexes with TEMPOH at -35 °C. The largest rate constant was obtained for the most electron-deficient complex – $[Mn^{III}(OH)(dpaq^{5NO2})]^{+}$ (k_2 = 7(1) M^{-1} s^{-1}) and the smallest rate constant obtained for the least electron deficient complex – $[Mn^{III}(OH)(dpaq^{5OMe})]^{+}$ (k_2 = 0.8(1) M^{-1} s^{-1}). The correlation

between the reduction potential vs. Hammett σ_{para} varies more strongly than the pK_a vs. Hammett σ_{para}, and therefore contributes more to the BDFE of the Mn^{II}-OH_2 complexes.[74] This shows that the $Mn^{III/II}$ reduction potential's contribution to the reaction driving force is more significant. The overall effect reflects as a small variation in the second-order rate constants for TEMPOH oxidation by the $[Mn^{III}(OH)(dpaq^{5R})]^+$ complexes (0.8(1) – 7(1) $M^{-1}s^{-1}$).[74]

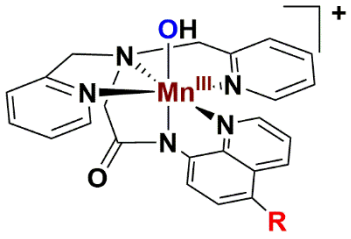

R = H, NO_2, Cl, OMe

$[Mn^{III}(OH)(dpaq^{5R})]^+$

Scheme 1.3. Molecular structure of $[Mn^{III}(OH)(dpaq^{5R})]^+$, where R = H, NO_2, Cl and OMe.

Structural and spectroscopic studies on various enzymes have shown that the enzymes can interact with their second-sphere to perform their functions.[91] This may also be important in the design of metal complexes to mimic the activity of these enzymes.[92] For example, the active sites of MnLOX and MnSOD feature hydrogen bonding interactions between the hydroxo ligand of the Mn^{III}-hydroxo unit and neighboring amino acids. While there were studies that discussed the importance of the hydrogen bond between coordinated solvent and the second-sphere glutamine ligand in MnSOD,[14] comparatively less attention has been paid to the consequences of the hydrogen bond between the hydroxo and carboxylate ligands in either MnSOD or MnLOX. Thus, in the subsequent chapters of this dissertation, we will discuss how we control the reactivity of Mn^{III}-hydroxo complexes by hydrogen bonding interaction. Since primary coordination sphere are also correlated to enzyme functions, we will also discuss how steric perturbation along the

equatorial Mn-$N_{pyridine}$ bonds for a derivative of $[Mn^{III}(OH)(dpaq)]^{+}$ modulates the reactivity of the Mn^{III}-hydroxo unit.

1.5 Mn^{III}-alkylperoxo Model Complexes

Mn-alkylperoxo adducts are common and important intermediates in various oxygenase enzymes, where they can be directly involved in substrate oxidation or precede the formation of high-valent Mn-oxo species.[93, 94] Given the importance of the Mn-alkylperoxo adducts, efforts have been directed towards their isolation, synthesis, and characterization.[95] However, this task has proven to be difficult, due in part to the thermal instability of Mn^{III}-alkylperoxo adducts.[95] Therefore, very few mononuclear Mn-alkyperoxo species (biological or synthetic) have been characterized. The first synthetically isolated and structurally characterized Mn-alkylperoxo complex was an end-on Mn^{II}-alkylperoxo complex – $Mn^{II}(OOCm)(Tp^{tBu,iPr})$ reported by Moro-oka *et al.*, which (Figure 1.8).[96] This complex was synthesized by the addition of cumyl hydroperoxide (CmOOH) to a solution of $[Mn^{II}(OH)(Tp^{tBu,iPr})]$ ($Tp^{tBu,iPr}$ = hydrotris(3-tert-butyl-5-iso-propyl-1-pyrazolyl)borate). This Mn^{II}-alkylperoxo complex is unstable at room temperature, and unreactive towards organic substrates.[96]

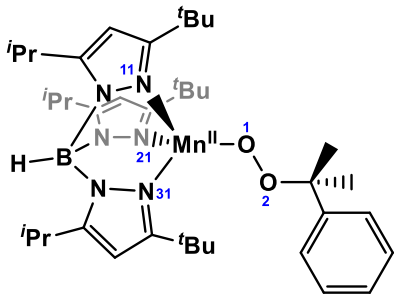

$Mn^{II}(OOCMe_2Ph)(Tp^{tBu,iPr})$

Figure 1.8. Molecular structures of $Mn^{II}(OOCm)(Tp^{tBu,iPr})$ complex. Selected bond lengths (Å) and angles (deg) are as follows: Mn-O1, 1.964(3); Mn-N11, 2.132(3); Mn-N21, 2.161(3); Mn-N31, 2.159(3); O1-O2, 1.411(4).[96]

The majority of the known Mn-peroxo complexes are the side-on complexes (Figure 1.9).[97-105] Pioneering work on the synthesis and structural characterization of end-on Mn^{III}-alkylperoxo adducts was done by Kovacs *et al.* They reported crystallographically characterized thiolate-ligated $[Mn^{III}(OOR)(N_4S)]^+$ alkylperoxo complexes, $[Mn^{III}(S^{Me2}N_4(QuinoEN))(OO^tBu)]^+$ and $[Mn^{III}(S^{Me2}N_4(QuinoEN))(OOCm)]^+$ complexes (Figure 1.10), generated by the reaction of $[Mn^{II}(S^{Me2}N_4(QuinoEN))]^+$ with ^{t}BuOOH and CmOOH respectively, in the presence of Et_3N in dichloromethane at -15 °C.[106] They went further by reporting four additional structures that are structurally related to previous complexes, all with the general formula $[Mn^{III}(OOR)(N_4S)]^+$.[95] The availability of these set of structures with a similar local coordination environment, yet still with systematic structural variations, allowed for the development of structure-reactivity correlations.[95] Interestingly, these long Mn–N distances are correlated with the alkylperoxo O-O bond lengths, which vary from 1.43 to 1.47 Å (Figure 1.11).[95] As shorter Mn–N distances gave longer O-O bonds, it was proposed that less Lewis acidic Mn^{III}-centers yielded more activated Mn^{III}-alkylperoxo adducts. By using variable-temperature kinetic studies, the O-O bond lengths for these Mn^{III}-alkylperoxo complexes were also correlated to their thermal decay rates. Mn^{III}-alkylperoxo adducts with longer O-O bonds decayed more rapidly, with lower $\Delta H^{\ddagger}$ values (Figure 1.11) and $\Delta S^{\ddagger}$ values that were more negative.[95] Because of the correlation between the Mn-N distances and the O-O bond lengths, these results suggest that activation of Mn^{III}-alkylperoxo complexes can be controlled by the donor strength of groups *cis* to the alkylperoxo unit.

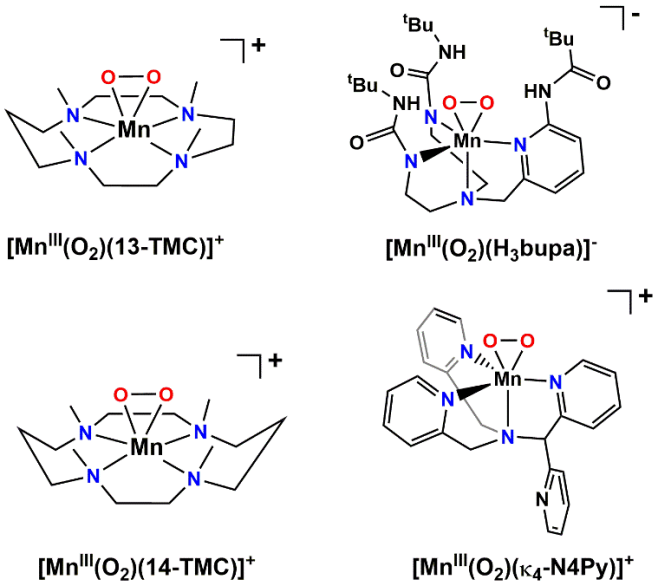

Figure 1.9. Some examples of side-on Mn^{III}-peroxo species.[97-105]

Thermal decomposition studies and analysis of the decay products of the Mn^{III}-cumylperoxo adduct supported a decay by homolytic cleavage of the alkylperoxo O-O bond.[95] These studies also show that the O-O bond of the end-on Mn^{III}-alklylperoxo complexes is more activated than the side-on peroxo complexes (1.431 – 1.468 Å vs. 1.403 – 1.428 Å).[95] This difference may explain why the side-on complexes are more common than the end-on complexes.

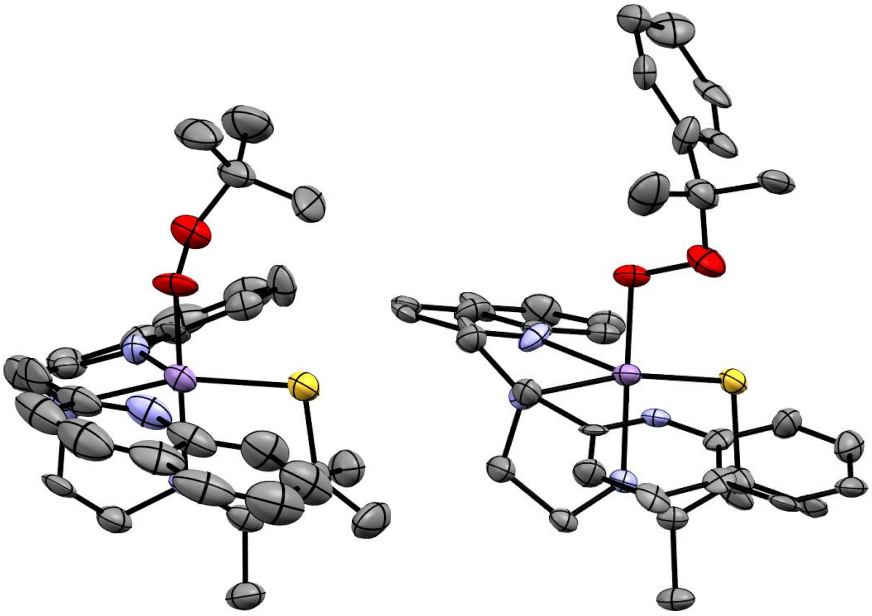

Figure 1.10. X-ray crystal structures of $[Mn^{III}(S^{Me2}N_4(QuinoEN))(OO^tBu)]^+$ (left) and $[Mn^{III}(S^{Me2}N_4(QuinoEN))(OOCm)]^+$ (right) complexes showing 50% probability thermal ellipsoids. Counter ions, solvent of crystallization, and hydrogen atoms are removed for clarity.[106]

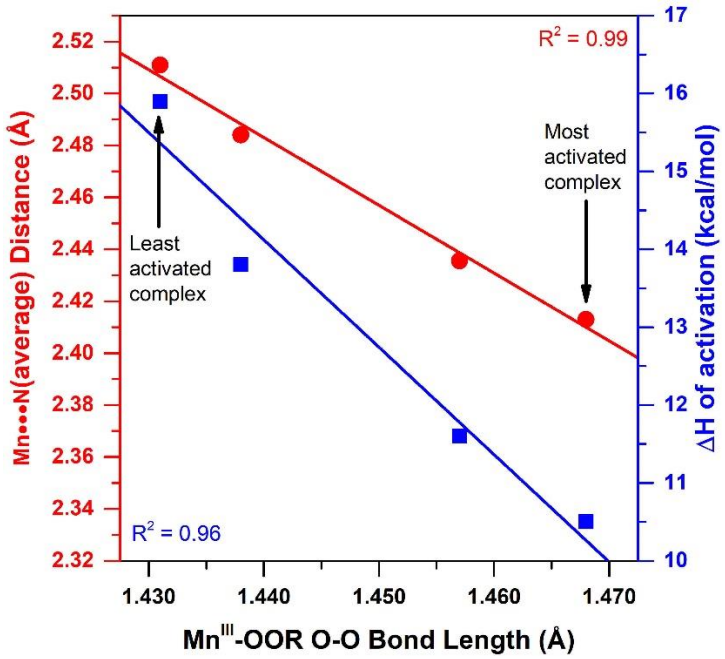

Figure 1.11. Correlation between the average Mn-N distance, $\Delta H^{\ddagger}$ and alkylperoxo O-O bond length for $[Mn^{III}(OOR)(N_4S)]^+$ complexes.[95]

It is important to note that these complexes are metastable at -15 °C and display no direct reactivity towards substrates. While this work provided a highly impactful contribution to the Mn^{III}-alkylperoxo chemistry in terms of structure-stability relationships, some questions still need to be addressed. Why do the $[Mn^{III}(OOR)(N_4S)]^+$ complexes display no activity towards substrate? Other metal alkylperoxo complexes, such as Fe-,[107, 108] Co-,[109-111] and Cu-alkylperoxo[112-114] adducts, are capable of oxidizing substrates, such as 1,4-cyclohexadiene, 2-phenylpropionaldehyde, and triphenylphosphine. Why is the reactivity of Mn^{III}-alkylperoxo adducts unlike their Mn^{III}-hydroperoxo analogues, which have been shown to be capable of reactions like CPET, oxygen atom transfer (OAT), aldehyde deformylation, and sulfoxidation?[115, 116] Is the inactivity of the $[Mn^{III}(OOR)(N_4S)]^+$ complexes because of the difference in the nature of the metal center or related to the local coordination sphere? Finally, what factors determine the decomposition pathway? For Fe-alkylperoxo adducts, experimental and computational methods indicate that the spin state of the Fe center determines if the Fe-alkylperoxo will decay by Fe-O or O-O bond cleavage, where the low-spin complexes are thermodynamically favored to decay by O-O bond homolysis and high spin complexes by Fe-O bond homolysis.[117-120]

To answer the first question, our group investigated the stability and reactivity of Mn^{III}-alkylperoxo by using the Hdpaq and $Hdpaq^{2Me}$ ligands, which have an all nitrogen coordination sphere. Two new Mn^{III}-alkylperoxo complexes – $[Mn^{III}(OO^tBu)(dpaq)]^+$ and $[Mn^{III}(OO^tBu)(dpaq^{2Me})]^+$ were reported.[121] However, these complexes were unstable ($t_{1/2}$ = 3200 and 3600 s, respectively, for 2 mM solutions in CH_3CN at -15 °C) but were characterized by electronic absorption, Mn K-edge X-ray absorption, and FT-IR spectroscopies.[121] The requirement of excess amounts of the ^{t}BuOOH for the formation of these complexes made studies of reactivity and investigations of the thermal decay pathway difficult. Just recently, Kovacs *et al.* reported a

metastable alkoxide derivative[122] of previously reported $[Mn^{III}(S^{Me2}N_4(6\text{- Me-DPEN}))(OO^tBu)]^+$, [95, 122] in which the ligand framework and molecular charge are maintained, but the inner coordination sphere was varied by replacing the monoanionic thiolate with a monoanionic alkoxide (Figure 1.12). This modification leads to an enhancement in stability of the complex compared to the thiolate-ligated version.[122] This result further shows the influence of the local coordination environment on the stability of Mn^{III}-alkylperoxo complexes. Nonetheless, the new complex did not show any reactivity with substrates. Thus, the preparation of Mn^{III}-alkylperoxo species that display chemical reactivity with substrates similar to other metal-alkylperoxo and the Mn^{III}-hydroperoxo analogues remains undiscovered. In addition, the factors that determine the decomposition pathways of Mn^{III}-alkylperoxo complexes are yet to be uncovered.

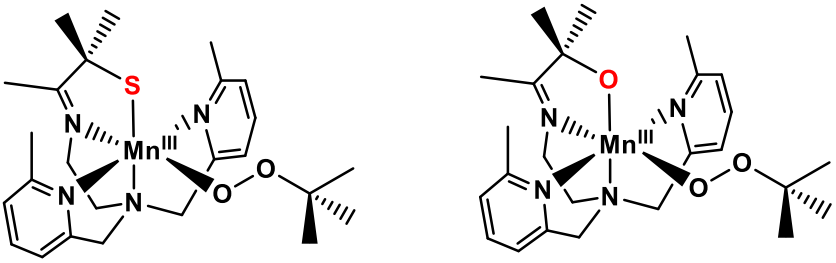

$[Mn^{III}(OO^tBu)(S^{Me2}N_4(6\text{-MeDPEN}))]^+$ **$[Mn^{III}(OO^tBu)(O^{Me2}N_4(6\text{-MeDPEN}))]^+$**

Figure 1.12. Molecular structures of $[Mn^{III}(S^{Me2}N_4(6\text{-Me-DPEN}))(OO^tBu)]^+$ (left) and $[Mn^{III}(O^{Me2}N_4(6\text{-Me-DPEN}))(OO^tBu)]^+$ (right) complexes.[106]

The work presented in the chapter 3 was carried out to add to the limited knowledge about the chemistry of Mn^{III}-alkylperoxo complexes. This chapter contain descriptions of the synthesis of two room-temperature stable Mn^{III}-alkyperoxo complexes using a new derivative of the dpaq ligand, their thermal decay pathways and presents the reactivity of these Mn^{III}-alkyperoxo complexes with phosphine and phenolic substrates.

1.6 References

1. S. Zhang, B. Zhang, B. Liu and S. Sun, *RSC Advances*, 2017, **7**, 26226-26242.
2. H. Xu, N. Yan, Z. Qu, W. Liu, J. Mei, W. Huang and S. Zhao, *Environmental Science & Technology*, 2017, **51**, 8879-8892.
3. K. R. Rohit, S. Radhika, S. Saranya and G. Anilkumar, *Advanced Synthesis & Catalysis*, 2020, **362**, 1602-1650.
4. J. R. Mayfield, E. N. Grotemeyer and T. A. Jackson, *Chemical Communications*, 2020, **56**, 9238-9255.
5. W. Zhu and N. G. J. Richards, *Essays in Biochemistry*, 2017, **61**, 259-270.
6. A.-F. Miller, *Current Opinion in Chemical Biology*, 2004, **8**, 162-168.
7. C. Su, M. Sahlin and E. H. Oliw, *Journal of Biological Chemistry*, 2000, **275**, 18830-18835.
8. W. A. Gunderson, A. I. Zatsman, J. P. Emerson, E. R. Farquhar, L. Que, Jr., J. D. Lipscomb and M. P. Hendrich, *Journal of the American Chemical Society*, 2008, **130**, 14465-14467.
9. R. Hage and A. Lienke, *Journal of Molecular Catalysis A: Chemical*, 2006, **251**, 150-158.
10. R. Hage and A. Lienke, *Angewandte Chemie International Edition*, 2006, **45**, 206-222.
11. B. S. Lane and K. Burgess, *Chem Rev*, 2003, **103**, 2457-2473.
12. D. J. Vinyard, G. M. Ananyev and G. C. Dismukes, *Annual Review of Biochemistry*, 2013, **82**, 577-606.
13. A. K. Holley, V. Bakthavatchalu, J. M. Velez-Roman and D. K. St Clair, *International journal of molecular sciences*, 2011, **12**, 7114-7162.
14. Y. Sheng, I. A. Abreu, D. E. Cabelli, M. J. Maroney, A.-F. Miller, M. Teixeira and J. S. Valentine, *Chemical Reviews*, 2014, **114**, 3854-3918.
15. Y. Chen, A. Wennman, S. Karkehabadi, Å. Engström and E. H. Oliw, *Journal of Lipid Research*, 2016, **57**, 1574-1588.
16. J. B. Broderick, *Essays in Biochemistry*, 1999, **34**, 173-189.
17. J. P. McEvoy and G. W. Brudvig, *Chemical Reviews*, 2006, **106**, 4455-4483.
18. A.-F. Miller, F. Padmakumar, D. Sorkin, A. Karapetian and C. K. Vance, *J. Inorg. Biochem.*, 2003, **93**, 71-83.
19. A.-F. Miller, *Curr. Opin. Chem. Biol.*, 2004, **8**, 162-168.
20. C. Su, M. Sahlin and E. H. Oliw, *Journal of Biological Chemistry*, 2000, **275**, 18830-18835.
21. A. Wennman, S. Karkehabadi and E. H. Oliw, *Archives of Biochemistry and Biophysics*, 2014, **555–556**, 9-15.
22. C. K. Vance and A.-F. Miller, *Biochemistry*, 2001, **40**, 13079-13087.
23. T. A. Jackson, C. T. Gutman, J. Maliekal, A.-F. Miller and T. C. Brunold, *Inorganic Chemistry*, 2013, **52**, 3356-3367.
24. C. K. Vance and A. F. Miller, *Biochemistry*, 2001, **40**, 13079-13087.
25. V. J. P. Lévêque, C. K. Vance, H. S. Nick and D. N. Silverman, *Biochemistry*, 2001, **40**, 10586-10591.
26. E. N. Grotemeyer and T. A. Jackson, in *Reference Module in Chemistry, Molecular Sciences and Chemical Engineering*, Elsevier, 2020, DOI: https://doi.org/10.1016/B978-0-12-409547-2.14851-6.

27. D. F. Leto and T. A. Jackson, *J. Biol. Inorg. Chem.*, 2014, **19**, 1-15.
28. C. Bull, E. C. Niederhoffer, T. Yoshida and J. A. Fee, *Journal of the American Chemical Society*, 1991, **113**, 4069-4076.
29. A. S. Hearn, M. E. Stroupe, D. E. Cabelli, J. R. Lepock, J. A. Tainer, H. S. Nick and D. N. Silverman, *Biochemistry*, 2001, **40**, 12051-12058.
30. Y. Sheng, E. Butler Gralla, M. Schumacher, D. Cascio, D. E. Cabelli and J. Selverstone Valentine, *Proceedings of the National Academy of Sciences*, 2012, **109**, 14314.
31. J. L. Hsu, Y. Hsieh, C. Tu, D. O'Connor, H. S. Nick and D. N. Silverman, *J Biol Chem*, 1996, **271**, 17687-17691.
32. L. Que and R. Y. N. Ho, *Chemical Reviews*, 1996, **96**, 2607-2624.
33. N. Lehnert and E. I. Solomon, *JBIC Journal of Biological Inorganic Chemistry*, 2003, **8**, 294-305.
34. A. Wennman, S. Karkehabadi and E. H. Oliw, *Archives of Biochemistry and Biophysics*, 2014, **555–556**, 9-15.
35. Z. Shirin, B. S. Hammes, V. G. Young and A. S. Borovik, *Journal of the American Chemical Society*, 2000, **122**, 1836-1837.
36. Z. Shirin, A. S. Borovik and V. G. Young Jr, *Chemical Communications*, 1997, DOI: 10.1039/A703395H, 1967-1968.
37. C. R. Goldsmith, A. P. Cole and T. D. Stack, *J Am Chem Soc*, 2005, **127**, 9904-9912.
38. R. Gupta and A. S. Borovik, *J. Am. Chem. Soc.*, 2003, **125**, 13234.
39. R. Gupta, T. Taguchi, A. S. Borovik and M. P. Hendrich, *Inorg. Chem.*, 2013, **52**, 12568.
40. M. K. Coggins, L. M. Brines and J. A. Kovacs, *Inorg Chem*, 2013, **52**, 12383-12393.
41. G. B. Wijeratne, B. Corzine, V. W. Day and T. A. Jackson, *Inorg Chem*, 2014, **53**, 7622-7634.
42. H. W. Doelle, in *Bacterial Metabolism (Second Edition)*, ed. H. W. Doelle, Academic Press, 1975, DOI: https://doi.org/10.1016/B978-0-12-219352-1.50012-8, pp. 490-558.
43. P. Kumar, S. V. Lindeman and A. T. Fiedler, *Journal of the American Chemical Society*, 2019, **141**, 10984-10987.
44. Y. Wang, J. Li and A. Liu, *J Biol Inorg Chem*, 2017, **22**, 395-405.
45. J. P. Emerson, E. G. Kovaleva, E. R. Farquhar, J. D. Lipscomb and L. Que, Jr., *Proc Natl Acad Sci U S A*, 2008, **105**, 7347-7352.
46. G. J. Christian, S. Ye and F. Neese, *Chemical Science*, 2012, **3**, 1600-1611.
47. V. Georgiev, T. Borowski and P. E. M. Siegbahn, *JBIC Journal of Biological Inorganic Chemistry*, 2006, **11**, 571-585.
48. F. Lavelle, M. E. McAdam, E. M. Fielden, P. B. Roberts, K. Puget and A. M. Michelson, *Biohem. J.*, 1977, **161**, 3-11.
49. M. Pick, J. Rabani, F. Yost and I. Fridovich, *J. Am. Chem. Soc.*, 1974, **96**, 7329-7333.
50. M. E. McAdam, F. Lavelle, R. A. Fox and E. M. Fielden, *Biochem. J.*, 1977, **165**, 81-87.
51. M. E. McAdam, R. A. Fox, F. Lavelle and E. M. Fielden, *Biochem. J.*, 1977, **165**, 71-79.
52. I. A. Abreu and D. E. Cabelli, *Biochimica et Biophysica Acta (BBA) - Proteins and Proteomics*, 2010, **1804**, 263-274.
53. T. A. Jackson, A. Karapetian, A.-F. Miller and T. C. Brunold, *Biochemistry*, 2005, **44**, 1504-1520.
54. I. A. Abreu, J. A. Rodriguez and D. E. Cabelli, *The Journal of Physical Chemistry B*, 2005, **109**, 24502-24509.

55. R. Carrasco, I. Morgenstern-Badarau and J. Cano, *Inorganica Chimica Acta*, 2007, **360**, 91-101.
56. L. Rulíšek, K. P. Jensen, K. Lundgren and U. Ryde, *Journal of Computational Chemistry*, 2006, **27**, 1398-1414.
57. J. Porta, A. Vahedi-Faridi and G. E. O. Borgstahl, *Journal of Molecular Biology*, 2010, **399**, 377-384.
58. A. Company, J. Lloret-Fillol and M. Costas, in *Comprehensive Inorganic Chemistry II (Second Edition)*, eds. J. Reedijk and K. Poeppelmeier, Elsevier, Amsterdam, 2013, DOI: https://doi.org/10.1016/B978-0-08-097774-4.00323-5, pp. 487-564.
59. O. Y. Borbulevych, J. Jankun, S. H. Selman and E. Skrzypczak-Jankun, *Proteins: Structure, Function, and Bioinformatics*, 2004, **54**, 13-19.
60. J. J. Warren, T. A. Tronic and J. M. Mayer, *Chemical Reviews*, 2010, **110**, 6961-7001.
61. J. M. Mayer, *Accounts of Chemical Research*, 2011, **44**, 36-46.
62. J. J. Warren and J. M. Mayer, *Biochemistry*, 2015, **54**, 1863-1878.
63. J. W. Darcy, B. Koronkiewicz, G. A. Parada and J. M. Mayer, *Accounts of Chemical Research*, 2018, **51**, 2391-2399.
64. C. R. Goldsmith, R. T. Jonas and T. D. P. Stack, *Journal of the American Chemical Society*, 2002, **124**, 83-96.
65. M. K. Coggins, L. M. Brines and J. A. Kovacs, *Inorganic Chemistry*, 2013, **52**, 12383-12393.
66. D. B. Rice, A. A. Massie and T. A. Jackson, *Accounts of Chemical Research*, 2017, **50**, 2706-2717.
67. D. M. Eichhorn and W. H. Armstrong, *Journal of the Chemical Society, Chemical Communications*, 1992, DOI: 10.1039/C39920000085, 85-87.
68. S. El Ghachtouli, B. Lassalle-Kaiser, P. Dorlet, R. Guillot, E. Anxolabéhère-Mallart, C. Costentin and A. Aukauloo, *Energy & Environmental Science*, 2011, **4**, 2041-2044.
69. A. A. Eroy-Reveles, Y. Leung, C. M. Beavers, M. M. Olmstead and P. K. Mascharak, *Journal of the American Chemical Society*, 2008, **130**, 4447-4458.
70. C. R. Goldsmith, A. P. Cole and T. D. P. Stack, *Journal of the American Chemical Society*, 2005, **127**, 9904-9912.
71. T. J. Hubin, J. M. McCormick, N. W. Alcock and D. H. Busch, *Inorg Chem*, 2001, **40**, 435-444.
72. Z. Shirin, B. S. Hammes, V. G. Young and A. S. Borovik, *Journal of the American Chemical Society*, 2000, **122**, 1836-1837.
73. D. B. Rice, G. B. Wijeratne, A. D. Burr, J. D. Parham, V. W. Day and T. A. Jackson, *Inorganic Chemistry*, 2016, **55**, 8110-8120.
74. D. B. Rice, A. Munasinghe, E. N. Grotemeyer, A. D. Burr, V. W. Day and T. A. Jackson, *Inorganic Chemistry*, 2019, **58**, 622-636.
75. P. Saisaha, J. W. de Boer and W. R. Browne, *Chemical Society Reviews*, 2013, **42**, 2059-2074.
76. D. B. Rice, S. D. Jones, J. T. Douglas and T. A. Jackson, *Inorganic Chemistry*, 2018, **57**, 7825-7837.
77. M. K. Coggins, X. Sun, Y. Kwak, E. I. Solomon, E. Rybak-Akimova and J. A. Kovacs, *Journal of the American Chemical Society*, 2013, **135**, 5631-5640.

78. D. C. R. Brazzolotto, Fabian G.; Smith-Jones, Julian; Retegan, Marius; Amidani, Lucia; Faponle, Abayomi S.; Ray, Kallol; Philouze, Christian; de Visser, Sam P.; Gennari, Marcello; Duboc, Carole, *Angewandte Chemie*, 2017, **56**, 8211-8215.
79. M. K. Coggins, X. Sun, Y. Kwak, E. I. Solomon, E. Rybak-Akimova and J. A. Kovacs, *Journal of the American Chemical Society*, 2013, **135**, 5631-5640.
80. J. A. Rees, V. Martin-Diaconescu, J. A. Kovacs and S. DeBeer, *Inorganic Chemistry*, 2015, **54**, 6410-6422.
81. M. K. Coggins, S. Toledo, E. Shaffer, W. Kaminsky, J. Shearer and J. A. Kovacs, *Inorganic Chemistry*, 2012, **51**, 6633-6644.
82. J. D. Parham, G. B. Wijeratne, J. R. Mayfield and T. A. Jackson, *Dalton Transactions*, 2019, **48**, 13034-13045.
83. X. Wu, M. S. Seo, K. M. Davis, Y.-M. Lee, J. Chen, K.-B. Cho, Y. N. Pushkar and W. Nam, *Journal of the American Chemical Society*, 2011, **133**, 20088-20091.
84. D. F. Leto, R. Ingram, V. W. Day and T. A. Jackson, *Chemical Communications*, 2013, **49**, 5378-5380.
85. P. Singh, E. Stewart-Jones, M. C. Denler and T. A. Jackson, *Dalton Transactions*, 2021, **50**, 3577-3585.
86. M. C. Denler, A. A. Massie, R. Singh, E. Stewart-Jones, A. Sinha, V. W. Day, E. Nordlander and T. A. Jackson, *Dalton Transactions*, 2019, **48**, 5007-5021.
87. A. A. Massie, M. C. Denler, L. T. Cardoso, A. N. Walker, M. K. Hossain, V. W. Day, E. Nordlander and T. A. Jackson, *Angewandte Chemie International Edition*, 2017, **56**, 4178-4182.
88. G. B. Wijeratne, B. Corzine, V. W. Day and T. A. Jackson, *Inorganic Chemistry*, 2014, **53**, 7622-7634.
89. D. B. Rice, E. N. Grotemeyer, A. M. Donovan and T. A. Jackson, *Inorganic Chemistry*, 2020, **59**, 2689-2700.
90. M. Sankaralingam, Y.-M. Lee, D. G. Karmalkar, W. Nam and S. Fukuzumi, *Journal of the American Chemical Society*, 2018, **140**, 12695-12699.
91. A. S. Borovik, *Accounts of Chemical Research*, 2005, **38**, 54-61.
92. H. M. Colquhoun, J. F. Stoddart and D. J. Williams, *Angewandte Chemie International Edition in English*, 1986, **25**, 487-507.
93. P. F. Fitzpatrick, *Biochemistry*, 2003, **42**, 14083-14091.
94. S. C. Peck and W. A. van der Donk, *JBIC Journal of Biological Inorganic Chemistry*, 2017, **22**, 381-394.
95. M. K. Coggins, V. Martin-Diaconescu, S. DeBeer and J. A. Kovacs, *Journal of the American Chemical Society*, 2013, **135**, 4260-4272.
96. H. Komatsuzaki, N. Sakamoto, M. Satoh, S. Hikichi, M. Akita and Y. Moro-oka, *Inorganic Chemistry*, 1998, **37**, 6554-6555.
97. M. S. Seo, J. Y. Kim, J. Annaraj, Y. Kim, Y.-M. Lee, S.-J. Kim, J. Kim and W. Nam, *Angewandte Chemie International Edition*, 2007, **46**, 377-380.
98. J. Annaraj, J. Cho, Y.-M. Lee, S. Y. Kim, R. Latifi, S. P. de Visser and W. Nam, *Angew. Chem. Int. Ed.*, 2009, **48**, 4150-4153.
99. R. A. Geiger, S. Chattopadhyay, V. W. Day and T. A. Jackson, *Journal of the American Chemical Society*, 2010, **132**, 2821-2831.
100. R. L. Shook, W. A. Gunderson, J. Greaves, J. W. Ziller, M. P. Hendrich and A. S. Borovik, *Journal of the American Chemical Society*, 2008, **130**, 8888-8889.

101. R. A. Geiger, D. F. Leto, S. Chattopadhyay, P. Dorlet, E. Anxolabéhère-Mallart and T. A. Jackson, *Inorganic Chemistry*, 2011, **50**, 10190-10203.
102. D. F. Leto, S. Chattopadhyay, V. W. Day and T. A. Jackson, *Dalton Trans.*, 2013, **42**, 13014.
103. H. E. Colmer, A. W. Howcroft and T. A. Jackson, *Inorganic Chemistry*, 2016, **55**, 2055-2069.
104. M. C. Denler, G. B. Wijeratne, D. B. Rice, H. E. Colmer, V. W. Day and T. A. Jackson, *Dalton Transactions*, 2018, **47**, 13442-13458.
105. U. P. Singh, A. K. Sharma, S. Hikichi, H. Komatsuzaki, Y. Moro-oka and M. Akita, *Inorganica Chimica Acta*, 2006, **359**, 4407-4411.
106. M. K. Coggins and J. A. Kovacs, *Journal of the American Chemical Society*, 2011, **133**, 12470-12473.
107. I. Ghosh, S. Banerjee, S. Paul, T. Corona and T. K. Paine, *Angewandte Chemie International Edition*, 2019, **58**, 12534-12539.
108. S. Hong, Y.-M. Lee, K.-B. Cho, M. S. Seo, D. Song, J. Yoon, R. Garcia-Serres, M. Clémancey, T. Ogura, W. Shin, J.-M. Latour and W. Nam, *Chemical Science*, 2014, **5**, 156-162.
109. F. A. Chavez, C. V. Nguyen, M. M. Olmstead and P. K. Mascharak, *Inorganic Chemistry*, 1996, **35**, 6282-6291.
110. F. A. Chavez, J. M. Rowland, M. M. Olmstead and P. K. Mascharak, *Journal of the American Chemical Society*, 1998, **120**, 9015-9027.
111. F. A. Chavez and P. K. Mascharak, *Accounts of Chemical Research*, 2000, **33**, 539-545.
112. S. Itoh, *Accounts of Chemical Research*, 2015, **48**, 2066-2074.
113. B. Kim, D. Jeong and J. Cho, *Chemical Communications*, 2017, **53**, 9328-9331.
114. H. Oh, W.-M. Ching, J. Kim, W.-Z. Lee and S. Hong, *Inorganic Chemistry*, 2019, **58**, 12964-12974.
115. H. So, Y. J. Park, K.-B. Cho, Y.-M. Lee, M. S. Seo, J. Cho, R. Sarangi and W. Nam, *Journal of the American Chemical Society*, 2014, **136**, 12229-12232.
116. M. Sankaralingam, Y.-M. Lee, S. H. Jeon, M. S. Seo, K.-B. Cho and W. Nam, *Chemical Communications*, 2018, **54**, 1209-1212.
117. M. Costas, M. P. Mehn, M. P. Jensen and L. Que, *Chemical Reviews*, 2004, **104**, 939-986.
118. J. Stasser, F. Namuswe, G. D. Kasper, Y. Jiang, C. M. Krest, M. T. Green, J. Penner-Hahn and D. P. Goldberg, *Inorganic Chemistry*, 2010, **49**, 9178-9190.
119. X. Shan, J.-U. Rohde, K. D. Koehntop, Y. Zhou, M. R. Bukowski, M. Costas, K. Fujisawa and L. Que, *Inorganic Chemistry*, 2007, **46**, 8410-8417.
120. N. Lehnert, R. Y. N. Ho, L. Que and E. I. Solomon, *Journal of the American Chemical Society*, 2001, **123**, 8271-8290.
121. J. D. Parham, G. B. Wijeratne, D. B. Rice and T. A. Jackson, *Inorganic Chemistry*, 2018, **57**, 2489-2502.
122. A. N. Downing, M. K. Coggins, P. C. Y. Poon and J. A. Kovacs, *Journal of the American Chemical Society*, 2021, **143**, 6104-6113.

Chapter 2

Controlling the Reactivity of a Metal-Hydroxo Adduct by a Hydrogen Bond

The contents of this chapter have been submitted to *J. Am. Chem. Soc.* and are undergoing revisions.

2.1 Introduction

Metal-oxygen adducts (*i.e.*, metal-oxo, -peroxo, and -hydroxo species) feature prominently in the proposed mechanisms of a variety of metalloenzymes and small-molecule, synthetic catalysts.[1-7] In many cases, these metal-oxygen species are involved in critical substrate oxidation steps in the catalytic cycle. While it is now well established that high-valent metal-oxo species can be involved in such reactions, there are increasing examples of mid- and high-valent metal-hydroxo species that can effect substrate oxidation reactions.[8-17] Two metalloenzymes that rely on mid-valent metal(III)-hydroxo adducts to perform their function are manganese superoxide dismutase (MnSOD) and manganese lipoxygenase (MnLOX). MnSOD regulates the levels of reactive oxygen species in the cell by catalyzing the disproportionation of superoxide to hydrogen peroxide and dioxygen.[18-20] The MnLOX enzyme catalyzes the oxidation of polyunsaturated fatty acids into their hydroperoxides, which are further metabolized into biologically active oxylipins such as a leukotrienes and jasmonates. These oxylipins act as inflammatory mediators and reproductive/growth regulators in plants.[19, 21]

The MnSOD and MnLOX enzymes both feature active sites containing mononuclear Mn centers with coordinated solvent ligands (Figure 2.1).[19, 20, 22, 23] When these enzymes are in their Mn^{III} oxidation states, the solvent ligand is presumed to be in the hydroxo form.[24-27] In each enzyme, the hydroxo ligand plays a critical functional role. In order to efficiently disproportionate superoxide, the $Mn^{III/II}$ reduction potential of MnSOD must lie midway between the potentials for superoxide reduction to hydrogen peroxide and oxidation to molecular oxygen (0.89 and -0.16 V vs. NHE, respectively).[25, 28, 29] Since the $Mn^{III/II}$ reduction potential of aqueous Mn is quite high (1.51 V vs. NHE), the MnSOD protein must suppress the potential by over 1 V.[30] This suppression is facilitated to a large degree by hydrogen bonding interactions between the hydroxo ligand and

a glutamine residue in the second coordination sphere (Figure 1, right).[25, 28, 29] In MnLOX, the Mn^{III}-hydroxo unit initiates oxidation of the unsaturated fatty acid substrate by a concerted proton-electron transfer (CPET) reaction, where the Mn^{III} center accepts an electron and the hydroxo ligand serves as the proton acceptor.[27] Thus, redox reactions of a Mn^{III}-hydroxo unit are critical to the function of both enzymes. (CPET is a sub-class of PCET, where the proton and electron are transferred in the same kinetic step).[19, 31]

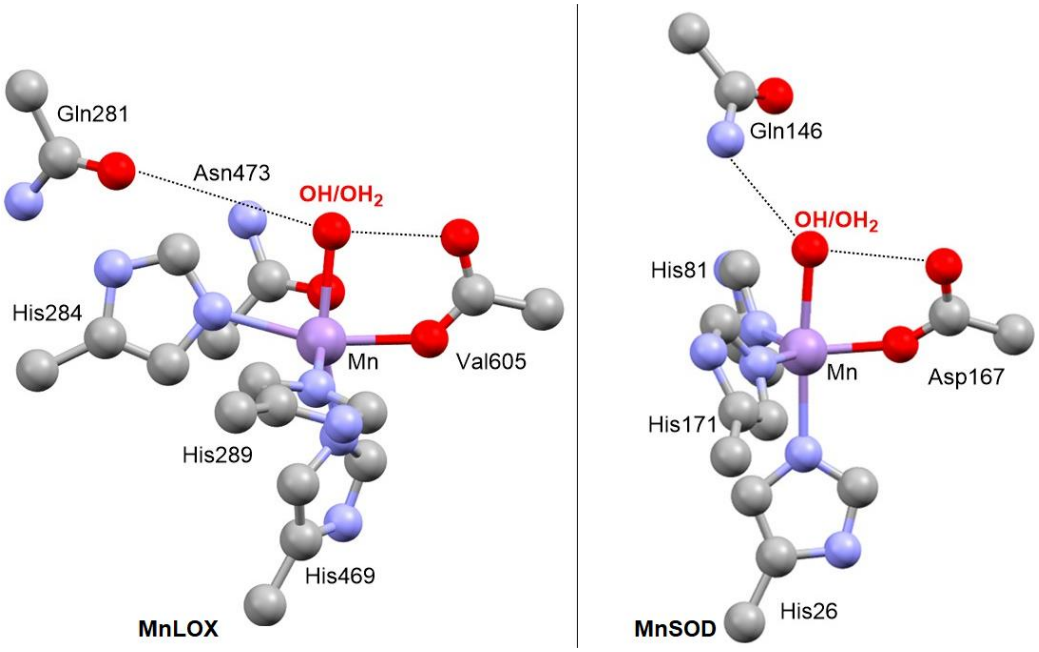

Figure 2.1. Active-site structures of MnLOX (left) and MnSOD (right) from PDB files 5FNO and 1VEW, respectively. Important hydrogen-bonding interactions with the coordinated solvent ligand are shown with dotted lines. The coordinated carboxylate of MnLOX is labeled according to the C-terminal amino acid from which it derives.

Although the active sites of MnSOD and MnLOX are distinct in several ways, in each case a coordinated carboxylate is *cis* to the solvent ligand (Figure 2.1).[32, 33] Structures of the active site of Mn^{III}SOD from DFT computations typically show the hydroxo ligand donating a hydrogen bond to the carbonyl group of this *cis* aspartate ligand.[28, 34, 35] A similar hydrogen bond may be inferred

for the Mn^{III}LOX active site (Figure 2.1, left). While there are numerous studies discussing the importance of the hydrogen bond between coordinated solvent and the second-sphere glutamine ligand in MnSOD,[20] comparatively less attention has been paid to the consequences of the putative hydrogen bond between the hydroxo and carboxylate ligands in either MnSOD or MnLOX.

Our group has sought to understand the reactivity of Mn^{III}-hydroxo complexes using synthetic model complexes. For example, using the $[Mn^{III}(OH)(dpaq)]^{+}$ complex and its derivatives (see Figure 2.2, top), we have shown that Mn^{III}-hydroxo complexes with more electron-deficient ligands show an increased rate for CPET reactions.[36-39] These rate variations were related to the increased oxidizing power of the Mn^{III} center, as marked by a $Mn^{III/II}$ reduction potential. However, the ligand variations explored in this work have effected changes only in the primary coordination sphere. As can be inferred from the MnSOD and MnLOX active sites in Figure 2.1, the utilized extensive hydrogen bonding in the extended coordination sphere must also modulate reactivity of the Mn^{III}-hydroxo unit.

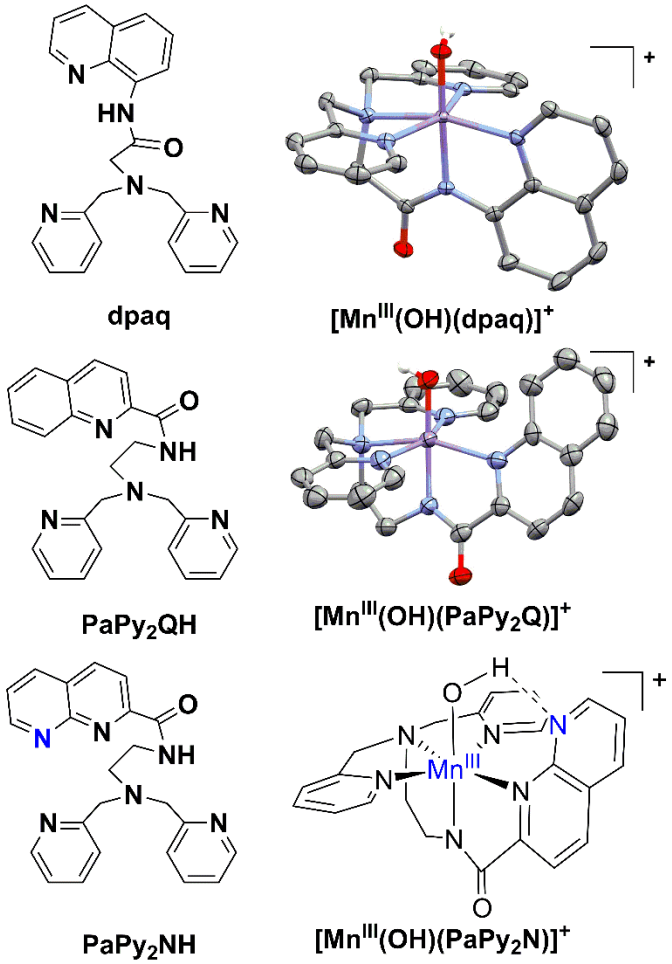

Figure 2.2. Structures of dpaq, $PaPy_2QH$ and $PaPy_2NH$ ligands (left) and corresponding Mn^{III}-hydroxo complexes (right). The structures for $[Mn^{III}(OH)(dpaq)]^+$ and $[Mn^{III}(OH)(PaPy_2Q)]^+$ are ORTEP renderings using the crystal structure of the triflate and perchlorate salts, respectively (see ref. [39] and [40]). Hydrogen atoms (except for the hydroxo proton) and counteranions were removed for clarity.

Our understanding of the roles of hydrogen-bonds in stabilizing unusual ligands and in contributing to particular reactions has benefitted greatly from model complexes that mimic interactions observed in metalloenzyme active sites.[41, 42] For example, Borovik and co-workers have utilized a variety of tripodal ligands with intramolecular hydrogen-bond networks to demonstrate how hydrogen bonding can modulate the properties of oxo ligands for metals in moderate (Fe^{III} and Mn^{III})[43, 44] to high (Fe^{IV}, Mn^{IV}, and Mn^{V})[45-47] oxidation states. The importance

of the hydrogen-bond network of these tripodal ligands on O_2 activation has also been examined.[48, 49] Fout and co-workers have employed an azafulvene-amine-based tripodal ligand with a second-coordination sphere cavity that tautomerize between hydrogen-bond donating to hydrogen-bond accepting configurations.[50] Metal complexes of these ligands have been employed to stabilize oxo adducts for metals in moderate oxidation states (Fe^{III} and Mn^{III})[51, 52] and to support catalysts for nitrite and perchlorate reduction.[53] Employing a variety of ligands with hydrogen-bonding capabilities in the secondary coordination sphere, Szymczak and co-workers have explored the role of intramolecular hydrogen-bonding interactions on the properties and reactivity of late transition-metal complexes.[54-61] Additionally, Karlin *et al.* have reported that the introduction of an intermolecular hydrogen-bonding interaction to a synthetic, heme Fe^{IV}-oxo complex enhances the reactivity of this complex towards oxidizing C–H bonds.[62]

Of most pertinence to the MnSOD and MnLOX systems, Borovik and co-workers recently determined the influence of variations in the strength of a hydrogen-bond donor on the properties and chemical reactivity of Mn^{III}-oxo complexes.[63] These studies employed a modified tripodal ligand with a single phenylurea arm capable of donating a hydrogen bond to the oxo ligand. The strength of this hydrogen bond was modulated using phenyl substituents *para* to the HN_{urea} group. In this series, it was found that reaction rates with 9,10-dihydroanthracene (DHA) varied by more than 10-fold, with faster rates observed for complexes with electron-rich *para* substituents. On the basis of a comprehensive analysis of kinetic and thermodynamic data, it was concluded that variations in the basicity of the oxo ligand, caused by the differences in hydrogen-bond strengths, led to the observed changes in reaction rates.[63]

In the majority of these recent studies, the intramolecular hydrogen-bonding network places a hydrogen-bond donor adjacent to an oxo or hydroxo ligand. This situation is distinct from the

putative hydroxo-carboxylate interaction in the Mn^{III}SOD and Mn^{III}LOX active sites, where the carboxylate acts as a hydrogen-bond acceptor for the hydroxo ligand (Figure 1). What effects does this hydrogen-bond acceptor have on the properties and reactivity of the Mn^{III}-hydroxo unit? In this present work, we address this question using a pair of Mn^{III}-hydroxo complexes, one of which contains a hydrogen-bond accepting group adjacent to the hydroxo ligand, and one of which does not. We employed the $[Mn^{III}(OH)(PaPy_2Q)]^+$ complex, previously reported by Mascharak and co-workers,[40] as the complex lacking a hydrogen-bond. The crystal structure for this complex shows an aryl ring of a quinolinyl group adjacent to the hydroxo ligand (Figure 2.2). To introduce a hydrogen-bond acceptor, we developed a new ligand ($PaPy_2NH$), where we have substituted the quinolinyl group in $PaPy_2QH$ with a 1,8-naphthyridinyl group (Figure 2.2, bottom). Spectroscopic studies of $[Mn^{III}(OH)(PaPy_2Q)]^+$ and $[Mn^{III}(OH)(PaPy_2N)]^+$ confirm similar ligand binding modes in these complexes, but the consequences of the putative hydrogen-bonding interaction in the latter complex are manifested through perturbations in the electronic absorption spectrum. These conclusions are further supported by structural and spectroscopic characterization of the corresponding Mn^{III}-methoxy complexes. An assessment of the reactivities of the Mn^{III}-hydroxo complexes using a variety of substrates shows that $[Mn^{III}(OH)(PaPy_2N)]^+$ displays far more rapid rates in CPET reactions (*ca.* 15- to 100-fold rate enhancements relative to $[Mn^{III}(OH)(PaPy_2Q)]^+$. A thermodynamic analysis of the contributions to the CPET rates of these complexes provides strong support that the increased basicity of $[Mn^{III}(OH)(PaPy_2N)]^+$ leads to the enhanced reactivity of this complex. Accordingly, these studies suggest that one role of the hydroxo-carboxylate hydrogen-bonding interaction in the Mn^{III}SOD and Mn^{III}LOX systems is to enhance the oxidizing ability of the Mn^{III}-hydroxo unit by increasing the basicity of the hydroxo ligand.

2.2 Materials and Methods.

All chemicals and solvents used were ACS reagent grade or higher and were obtained from commercial vendors. These chemicals were used without further purification unless otherwise stated. Anhydrous and degassed acetonitrile, methanol, dichloromethane and ether were obtained from the Pure Solv (2010) solvent purification system. Iodosobenzene (PhIO) was prepared using a literature procedure.[64] Phenolic substrates and Bu_4NPF_6 for electrochemistry were purified by recrystallizations in hot ethanol.[65] TEMPOH (2,2′-6,6′-tetramethylpiperidine-1-ol) was synthesized according to literature procedure.[66] The *N*,*N*-Bis(2-pyridylmethyl)amine-N-ethyl-2-quinolinecarboxamide ($PaPy_2QH$) ligand was synthesized using a procedure reported by Mascharak *et al*.[40] ^{1}H NMR and ESI-MS data supporting the formation of this ligand are provided in Figures A1.1 and A1.2. Electronic absorption data were collected on Varian Cary 50 Bio UV−visible spectrophotometer equipped with a Unisoku (USP-203-A) cryostat. ^{1}H NMR were collected on a Bruker AVIIIHD 400 MHz spectrometer. ^{1}H NMR data acquisitions for the Mn^{III}-hydroxo complexes were collected with a spectral width of 150 to -150 ppm with 1000 scans to provide sufficient signal-to-noise ratio. Spectra were processed in the MestReNova software. ESI-MS experiments were performed using on an LCT Premier – a quadrupole and time of flight tandem mass analyzer with an electrospray ion source. Electron paramagnetic resonance (EPR) experiments were performed on a Bruker EMXPlus spectrometer with a dual-mode cavity and an Oxford instruments cryostat. Electrochemical measurements were performed using a Basi® PalmSens EmStat3+ potentiostat.

Synthesis of $PaPy_2NH$ ligand. The $PaPy_2NH$ ligand was synthesized in a stepwise proceses, as described below.

1,8-naphthyridine-2-carboxylic acid. The 1,8-naphthyridine-2-carboxylic acid was synthesized using a modification of a route from Bera *et al.*[67] In a glovebox, 3.0 g (24.6 mmol) of 2-amino-3-pyridinecarboxaldehyde were weighed into a Schlenk flask equipped with a magnetic stir bar and wrapped with aluminum foil to exclude light. The flask was stoppered with a pierceable rubber septum and wrapped with Parafilm. The flask was taken out of the glovebox and transferred to a dark fume hood. 4.40 mL methyl pyruvate were added to the Schlenk flask by syringe under dynamic N_2 flow and vigorous stirring. 30 mL ethanol were also added by syringe, followed by the addition of 5.0 mL deionized H_2O. The mixture was placed in an ice bath for 30 minutes. 30 mL 3.0 M NaOH were added dropwise to the mixture by an addition funnel under dynamic N_2 flow. After complete addition, the ice bath was removed, the mixture was warmed to room temperature and stirred for 16 hours under static N_2. A clear, orange solution was obtained. The orange solution was placed in an ice bath and brought to pH 1.0 using concentrated HCl. A cream precipitate was formed. This solid was filtered using a fine-frit Buchner funnel, then washed with cold ethanol and cold acetone. The solid residue was then dried in vacuo. (4.214 g, 98% yield). ^{1}H NMR (400 MHz, D_2O) δ 8.99 (dd, J = 4.4, 1.9 Hz, 1H), 8.49 – 8.27 (m, 2H), 7.98 (d, J = 8.4 Hz, 1H), 7.60 (dd, J = 8.2, 4.4 Hz, 1H) (Figure A1.3).

Ethyl 1,8-naphthyridine-2-carboxylate. A mixture of 1.18 g (6.8 mmol) 1,8-naphthyridine-2-carboxylic acid and 45 mL EtOH with 1.6 mL of concentrated sulfuric acid was refluxed under vigorous stirring for 24 hours. The EtOH was removed using a rotary evaporator, leaving a red, oily residue. This oily residue was neutralized with excess saturated sodium bicarbonate until effervescence was longer observed. The product was extracted several times with 25 mL chloroform until the chloroform layer became almost colorless. The chloroform extract was washed successively with deionized H_2O (5 × 50 mL), dried over anhydrous Na_2SO_4 for *ca.* 2

hours, and then filtered by gravity filtration. The filtrate was dried in vacuo to yield an orange solid (1.098 g, 92% yield). ^{1}H NMR (400 MHz, $CDCl_3$) δ 9.25 (dd, *J* = 4.2, 2.0 Hz, 1H), 8.38 (d, *J* = 8.4 Hz, 1H), 8.33 – 8.25 (m, 2H), 7.61 (dd, *J* = 8.2, 4.2 Hz, 1H), 4.54 (qd, *J* = 7.1, 1.1 Hz, 2H), 1.49 (td, *J* = 7.1, 1.0 Hz, 3H) (Figure A1.4).

N-(2-aminoethyl)-1,8-naphthyridine-2-carboxamide. 1.63 g (27.12 mmol) ethylenediamine was added to a round-bottom flask containing 1.098 g (5.43 mmol) ethyl 1,8-naphthyridine-2-carboxylate, followed by the addition of 1.0 mL pyridine. The mixture was heated to 100°C for 4 hours under a N_2 atmosphere. The solvent was removed using a rotary evaporator, leaving an orange oil. The oil was acidified to pH 5 with concentrated HCl and was then washed with chloroform (2 × 50 mL). The aqueous layer was made basic with 15 mL pH 10 NaOH solution and extracted with chloroform (5 × 50 mL). The chloroform layer was dried over anhydrous Na_2SO_4 and filtered by gravity filtration. The solvent was removed in vacuo to yield an orange solid. (0.982 g, yield: 84%). ^{1}H NMR (400 MHz, $CDCl_3$) δ 9.13 (dd, *J* = 4.2, 2.0 Hz, 1H), 8.55 (s, 1H), 8.39 (d, *J* = 8.4 Hz, 1H), 8.33 (d, *J* = 8.4 Hz, 1H), 8.24 (dd, *J* = 8.2, 2.0 Hz, 1H), 7.54 (dd, *J* = 8.2, 4.2 Hz, 1H), 3.54 (q, *J* = 6.2 Hz, 2H), 2.93 (t, *J* = 6.1 Hz, 2H) (Figure A1.5).

N-(2-(bis(pyridin-2-ylmethyl)amino)ethyl)-1,8-naphthyridine-2-carboxamide ($PaPy_2NH$). 0.982 g (4.54 mmol) *N*-(2-aminoethyl)-1,8-naphthyridine-2-carboxamide were placed in a round-bottom flask with 1.489 g (9.08 mmol) 2-(chloromethyl)pyridine hydrochloride. 2.7 mL of deionized H_2O and 2.2 mL 10 M NaOH were added to this solution. The mixture was heated to 70°C for 4 hours. 40 mL saturated NaOH were added to the mixture, and then the solution was extracted using chloroform (8 × 50 mL). The reddish-brown solution was then washed with aqueous HCl solution (pH 5) until the aqueous extract became light brown (8 × 100 mL). The chloroform extract was dried over anhydrous Na_2SO_4, filtered, and the solvent was removed in

vacuo. (1.653 g, yield: 91%). ^{1}H NMR (500 MHz, Chloroform-*d*) δ 9.25 (dd, *J* = 4.2, 2.0 Hz, 1H), 8.89 (d, *J* = 5.8 Hz, 1H), 8.61 – 8.52 (m, 2H), 8.45 – 8.36 (m, 2H), 8.31 (dd, *J* = 8.1, 2.0 Hz, 1H), 7.67 (d, *J* = 7.8 Hz, 2H), 7.63 – 7.58 (m, 3H), 7.11 (ddd, *J* = 7.2, 5.1, 1.3 Hz, 2H), 3.95 (s, 4H), 3.67 (q, *J* = 6.1 Hz, 2H), 2.88 (t, *J* = 6.3 Hz, 2H) (Figure A1.6). ^{13}C NMR (126 MHz, Chloroform-*d*) δ 154.71, 149.25, 138.92, 137.29, 136.80, 123.38, 123.28, 122.21, 120.34, 60.53, 52.96, 37.67 (Figure A1.7). ^{1}H-^{13}C HSQC (Figure A1.8) ESI-MS *m/z* 399.19 $[M+H]^{+}$ (Calc: 399.19) (Figure A1.9).

Synthesis of $[Mn^{II}(PaPy_2Q)](OTf)$. In a glovebox, 0.374 g (0.94 mmol) $PaPy_2QH$ were dissolved in 20 mL of CH_3OH. A solution of 0.091 g (0.94 mmol) NaO^tBu dissolved in 20 mL of CH_3OH was added dropwise to the solution of $PaPy_2QH$ under vigorous stirring. The mixture was stirred continuously for 15 minutes. 0.410 g of (0.94 mmol) $Mn^{II}(OTf)_2\cdot(CH_3CN)_2$ in 20 mL of CH_3OH was added dropwise to the mixture. A clear, brown solution was obtained. The mixture was stirred continuously for 24 hours. The solution was concentrated in vacuo until a beige colored precipitate was observed. The concentrated solution was layered with ether and allowed to stand for 24 hours. The solvent was carefully decanted leaving a beige precipitate. The precipitate was dried in vacuo, washed with ether and dried (these processes were performed twice). Repeated recrystallization of this beige precipitate in CH_3CN produced orange microcrystals (0.452 g, 80% yield). Crystals suitable for X-ray crystallography were obtained by slow vapor diffusion of ether into concentrated acetonitrile solution of $[Mn^{II}(PaPy_2Q)](OTf)$. We note that, in solution, the $[Mn^{II}(PaPy_2Q)](OTf)$ reacts with ambient O_2 over the course of *ca.* 50 minutes to yield the $[Mn^{III}(OH)PaPy_2Q]^{+}$. Because of this reactivity, we stored $[Mn^{II}(PaPy_2Q)](OTf)$ as a solid in a glovebox.

The perpendicular mode X-band EPR spectrum of a 3 mM CH_3CN solution of $[Mn^{II}(PaPy_2Q)](OTf)$ at 10 K shows a broad signal at $g \approx 2.0$ that we attribute to a mononuclear Mn^{II} center (Figure A1.12). Evans NMR data for $[Mn^{II}(PaPy_2Q)](OTf)$ in CD_3CN further supporting this assignment, yielding μ_{eff} = 5.67 BM (Figure A1.13). ESI-MS analysis of a CH_3CN solution of $[Mn^{II}(PaPy_2Q)](OTf)$ shows a peak at *m/z* = 451.12 (calc for $[Mn^{II}(PaPy_2Q)]^+$: 451.12) (Figure A1.14).

$[Mn^{II}(PaPy_2N)](OTf)\cdot CH_3CN$. In a glovebox, 0.695 g (1.75 mmol) $PaPy_2NH$ ligand was dissolved in 30 mL of CH_3OH. A solution of 0.168 g (1.75 mmol) of NaO^tBu dissolved in 20 mL of CH_3OH was added dropwise to the solution of $PaPy_2NH$ under vigorous stirring. The mixture was stirred continuously for 15 minutes. 0.762 g (1.75 mmol) of $Mn^{II}(OTf)_2\cdot(CH_3CN)_2$ dissolved in 20 mL of CH_3OH was added dropwise to the ligand and NaO^tBu mixture until complete addition. A clear, reddish-brown solution was obtained. The mixture was stirred continuously for 24 hours. The solution was concentrated in vacuo until an orange precipitate was observed. The concentrated solution was layered with ether and allowed to stand for 24 hours. The solvent was carefully decanted leaving an orange solid. The precipitate was dried in vacuo, washed with ether and dried again (these processes were repeated twice). Repeated recrystallization of this orange material produced crystals suitable for X-ray crystallographic analysis (1.002 g, 95% yield). Because the $[Mn^{II}(PaPy_2N)](OTf)\cdot CH_3CN$ showed some reactivity with O_2 when in solution, this material was stored as a solid in the glovebox.

Perpendicular mode X-band EPR spectrum of frozen 3 mM CH_3CN solution of $[Mn^{II}(PaPy_2N)](OTf)\cdot CH_3CN$, at 10 K shows a broad signal at $g \approx 2.0$, consistent with a mononuclear Mn^{II} center (Figure A1.15). Evans NMR data in CD_3CN yield μ_{eff} = 5.58 BM (Figure

A1.16). ESI-MS data for a CH_3CN solution of $[Mn^{II}(PaPy_2N)](OTf)\cdot CH_3CN$ reveal a *m/z* peak at 452.11 (calc for $[Mn^{II}(PaPy_2N)]^+$: 452.11) (Figure A1.17).

Syntheses of $[Mn^{III}(OH)(PaPy_2Q)](OTf)$ and $[Mn^{III}(OH)(PaPy_2N)](OTf)$. The Mn^{III}-hydroxo complexes $[Mn^{III}(OH)(PaPy_2Q)](OTf)$ and $[Mn^{III}(OH)(PaPy_2N)](OTf)$ were generated using the same synthetic procedure. In a glovebox, 2.0 mL of a 1.25 mM solution of $[Mn^{II}(PaPy_2Q)](OTf)$ (or $[Mn^{II}(PaPy_2N)](OTf)\cdot CH_3CN$) was prepared by dissolving 1.6 mg (2.5 μmol) of the Mn^{II} salt in 1.40 mL of CH_3CN to give an orange solution. The solution was transferred to a gastight cuvette sealed with a pierceable septum. A stock solution of PhIO was generated by dissolving 1.8 mg (8.2 μmol) of PhIO in 4.0 mL of CH_3CN in the glovebox. A 0.6 mL aliquot of this PhIO solution was added to the solution of the Mn^{II} complex in the cuvette, delivering 0.5 equiv. PhIO. The PhIO solution was added using a gastight syringe that was purged three times with inert gas. The formation of the Mn^{III}-hydroxo product was monitored by electronic absorption spectroscopy and was complete in *ca.* 10 minutes. The $[Mn^{III}(OH)(PaPy_2Q)](OTf)$ and $[Mn^{III}(OH)(PaPy_2N)](OTf)$ products were characterized by ESI-MS and a variety of spectroscopic methods (Figures A1.18 - 21), as discussed in the Results and Analysis section. The perpendicular-mode X-band EPR spectra of 5 mM CH_3CN solutions of $[Mn^{III}(OH)(PaPy_2Q)](OTf)$ and $[Mn^{III}(OH)(PaPy_2N)](OTf)$ at 10 K showed no signals (Figure A1.12 and A1.15).

Synthesis of $[Mn^{III}(OMe)(PaPy_2Q)](OTf)$ and $[Mn^{III}(OMe)(PaPy_2N)](OTf)$. The Mn^{III}-methoxy complexes $[Mn^{III}(OMe)(PaPy_2Q)](OTf)$ and $[Mn^{III}(OMe)(PaPy_2Q)](OTf)$ were prepared using the same procedure to generate the Mn^{III}-hydroxo adducts, with the exception that CH_3OH was used as the solvent. Suitable crystals of $[Mn^{III}(OMe)(PaPy_2Q)](OTf)$ for X-ray crystallography were obtained at room temperature by layering of the concentrated methanolic solution of $[Mn^{III}(OMe)(PaPy_2Q)](OTf)$ with ether in a scintillation vial. Suitable crystals of

$[Mn^{III}(OMe)(PaPy_2N)](OTf)$ for X-ray crystallography was obtained at room temperature by layering of the concentrated methanolic solution of $[Mn^{III}(OMe)(PaPy_2N)](OTf)$ with ether at in an NMR tube. The formulations of these complexes are supported by Evans NMR and ESI-MS data (Figures A1.22 – A1.25), as discussed in the Results and Analysis section.

X-ray Crystallographic Studies for $[Mn^{II}(PaPy_2Q)](OTf)$, $[Mn^{II}(PaPy_2N)](OTf)\cdot CH_3CN$, $[Mn^{III}(OMe)(PaPy_2Q)](OTf)$, $[Mn^{III}(OMe)(PaPy_2N)](OTf)$ and $[Mn^{II}(PaPy_2N)](PF_6)\cdot CH_3CN$. Complete sets of unique reflections were collected with monochromated CuKα radiation for single-domain crystals of all four compounds. Totals of 1967 ($[Mn^{II}(PaPy_2Q)](OTf)$), 4351 ($[Mn^{III}(OMe)(PaPy_2Q)](OTf)$), and 4021 ($[Mn^{III}(OMe)(PaPy_2N)](OTf)$) 1°-wide ω- or ϕ-scan frames were collected with a Bruker APEX II CCD area detector. Frame counting times of 10-30 seconds were used for $[Mn^{II}(PaPy_2Q)](OTf)$, 4-6 seconds for $[Mn^{III}(OMe)(PaPy_2Q)](OTf)$, 8-15 seconds for $[Mn^{III}(OMe)(PaPy_2N)](OTf)$, and 5-8 seconds for $[Mn^{II}(PaPy_2N)](PF_6)\cdot CH_3CN$. A total of 1941 1°-wide ω- or ϕ-scan frames with counting times of 8-30 seconds were collected with a Bruker Platinum 135 CCD area detector for $[Mn^{II}(PaPy_2N)](OTf)\cdot CH_3CN$. X-rays for all four structures were provided by a Bruker MicroStar microfocus rotating anode operating at 45kV and 60 mA and equipped dual CCD detectors and Helios multilayer x-ray optics. Preliminary lattice constants were obtained with the Bruker program SMART.[68] Integrated reflection intensities for all crystals were produced using the Bruker program SAINT.[69] All four data sets were corrected empirically for variable absorption effects using equivalent reflections. The Bruker software package SHELXTL was used to solve each structure using "direct methods" techniques. All stages of weighted full-matrix least-squares refinement were conducted using Fo^2 data with the SHELXTL v2014 software package.[70]

The final structural model for all five structures incorporated anisotropic thermal parameters for all nonhydrogen atoms and isotropic thermal parameters for all included hydrogen atoms. The methoxy methyl groups in $[Mn^{III}(OMe)(PaPy_2Q)](OTf)$, and $[Mn^{III}(OMe)(PaPy_2N)](OTf)$ and the CH_3CN methyl group in $[Mn^{II}(PaPy_2N)](OTf)\cdot CH_3CN$ were included in their structural models as idealized riding model sp^3-hybridized rigid rotors (with a C-H bond length of 0.98 Å) that were allowed to rotate freely about their C-O or C-C bonds in least-squares refinement cycles. All ligand hydrogen atoms in $[Mn^{II}(PaPy_2N)](OTf)\cdot CH_3CN$ and the hydrogen atoms bonded to C2 atoms in $[Mn^{II}(PaPy_2Q)](OTf)$ and $[Mn^{III}(OMe)(PaPy_2Q)](OTf)$ were located from a difference Fourier and included in the structural model as independent isotropic atoms whose parameters were allowed to vary in least-squares refinement cycles. The remaining hydrogen atoms in all ligands (except H2 in $[Mn^{II}(PaPy_2Q)](OTf)$ and $[Mn^{III}(OMe)(PaPy_2Q)](OTf)$) were placed at idealized riding model sp^2- or sp^3-hybridized positions with C-H bond lengths of 0.95 - 0.99 Å. The isotropic thermal parameters of idealized hydrogen atoms in all five structures were fixed at values 1.2 (non-methyl) or 1.5 (methyl) times the equivalent isotropic thermal parameter of the carbon atom to which they are covalently bonded.

Whereas $[Mn^{III}(OMe)(PaPy_2Q)](OTf)$ and $[Mn^{III}(OMe)(PaPy_2N)](OTf)$ are essentially isomorphous with a C-H group in $[Mn^{III}(OMe)(PaPy_2Q)](OTf)$ being replaced by a nitrogen atom in $[Mn^{III}(OMe)(PaPy_2N)](OTf)$, $[Mn^{II}(PaPy_2Q)](OTf)$ and $[Mn^{II}(PaPy_2N)](OTf)\cdot CH_3CN$ are not isomorphous. In order to experimentally distinguish between $PaPy_2Q$ and $PaPy_2N$ ligands, the hydrogen atoms bonded to the C2 atoms in the $PaPy_2Q$ ligands of $[Mn^{II}(PaPy_2Q)](OTf)$ and $[Mn^{III}(OMe)(PaPy_2Q)](OTf)$ were located from a difference Fourier and included in the structural model as independent isotropic atoms whose parameters were allowed to vary in least-squares refinement cycles. No significant electron density was observed at reasonable sp^2-hybridized

positions around the corresponding nitrogen atoms in the $PaPy_2N$ ligands. The relevant crystallographic and structure refinement data for all five compounds are given in Tables A1.1 and A1.2.

Water O1W oxygen atoms in $[Mn^{III}(OMe)(PaPy_2Q)](OTf)$ and $[Mn^{III}(OMe)(PaPy_2N)](OTf)$ are only 1.94 - 1.98 Å away from an inversion-center-related O1W and therefore only present part of the time. Their equivalent isotropic thermal parameters became reasonable when their occupancy factors were reduced to 0.30. Mild restraints were also applied to the anisotropic thermal parameters for O1W in $[Mn^{III}(OMe)(PaPy_2Q)](OTf)$.

The triflate anion in $[Mn^{III}(OMe)(PaPy_2N)](OTf)$ is 58/42 disordered with two orientations in the asymmetric unit. The bond lengths and angles for both orientations were idealized by restraining them to be appropriate multiples of the S-O bond length which was incorporated into least-squares refinement cycles as a free variable that refined to a final value of 1.404(3) Å.

The second acetonitrile solvent molecule of crystallization for $[Mn^{II}(PaPy_2N)](PF_6)\cdot CH_3CN$ is disordered with two orientations in the lattice. Since both orientations utilize C3S, it was assigned an occupancy factor of 1.00. One orientation utilizes positions for (covalently bonded) atoms C4S-C3S-C4S' (bond angle: 162°) and the second one uses C3S-N2S-N2S*(bond angle: 167°; N2S* is an inversion-related N2S). The occupancy factor for N2S was set to 0.50 and the (normalized) occupancy factors for C4S and C4S' refined to 0.61 and 0.39. Hydrogen atoms on solvent molecules were not included in the structural model for $[Mn^{II}(PaPy_2N)](PF_6)\cdot CH_3CN$.

Kinetic studies of TEMPOH oxidation by Mn^{III}-hydroxo and Mn^{III}-methoxy complexes. A common kinetic procedure was employed to investigate TEMPOH oxidation by the Mn^{III}-hydroxo or Mn^{III}-methoxy complex ($[Mn^{III}(OH)(PaPy_2Q)]^+$, $[Mn^{III}(OH)(PaPy_2N)]^+$, $[Mn^{III}(OMe)(PaPy_2Q)]^+$, and $[Mn^{III}(OMe)(PaPy_2N)]^+$. The only difference in the procedure was

the use of CH_3CN for the Mn^{III}-hydroxo complexes and the use of CH_3OH for the Mn^{III}-methoxy complexes. For each experiment, 2.0 mL of a 1.25 mM solution of the Mn^{III}-hydroxo or Mn^{III}-methoxy complex was prepared in a nitrogen filled glovebox, placed in a gastight cuvette, sealed with a pierceable septum, and wrapped with Parafilm to maintain an inert atmosphere. An appropriate amount of TEMPOH (10 - 40 equiv.) was dissolved in 100 μL CH_3CN (or CH_3OH) in a vial in the glovebox, sealed with a pierceable septum, and wrapped with Parafilm. The cuvette was equilibrated to -35°C on the spectrometer for 10 minutes before injection of the substrate. The gastight syringe used to inject the TEMPOH was purged three times with inert gas before each injection. Kinetic measurements were performed on a Varian Cary 50 Bio UV−visible spectrophotometer connected to a Unisoku (USP-203-A) cryostat. Activation parameters were determined for TEMPOH oxidation by the Mn^{III}-hydroxo complexes by performing the same kinetic procedure at different temperatures.

Kinetic studies of phenol oxidation by $[Mn^{III}(OH)(PaPy_2Q)]^+$ and $[Mn^{III}(OH)(PaPy_2N)]^+$. We investigated phenol oxidation using a protocol nearly identical to that employed for TEMPOH oxidation. Each experiment involved 2.0 mL of a 1.25 mM solution of $[Mn^{III}(OH)(PaPy_2Q)]^+$ or $[Mn^{III}(OH)(PaPy_2N)]^+$ in CH_3CN, to which was added an excess of the phenol substrate (*e.g.*, 10–200 equiv. of 4-^{t}Bu-2,6- DTBP for $[Mn^{III}(OH)(PaPy_2Q)]^+$ and 10-50 equiv. 4-^{t}Bu-2,6- DTBP for $[Mn^{III}(OH)(PaPy_2N)]^+$). The range of substrate concentrations chosen was based on the rates of reactions.

Cyclic Voltammetry. Cyclic voltammograms were recorded using Basi® PalmSens EmStat3+ potentiostat. The working electrode was a glassy carbon electrode with a Pt wire as the counter electrode. A 0.01 M AgCl solution was prepared using 0.1 M Bu_4NPF_6 electrolyte solution in CH_3CN. The 0.01 M AgCl solution was used for the Ag/AgCl quasi-reference electrode. Fc^+/Fc

potential was measured as an external reference. 2 mM solutions of $[Mn^{III}(OH)(PaPy_2Q)]^+$ and $[Mn^{III}(OH)(PaPy_2N)]^+$ were prepared from 10 mL of a degassed 0.1 M Bu_4NPF_6 electrolyte solution in CH_3CN. These sample solutions were sparged with nitrogen gas with the aid of Teflon tubing for 15 minutes before measurement. The Teflon tubing was placed above the surface of the solution to continue flushing the headspace, while not disturbing the solution in the electrochemical cell during measurement. All measurements were performed at room temperature.

DFT Calculations for Thermodynamic Parameters. DFT calculations were performed using the ORCA 4.2.1 software.[71] Geometry optimizations were performed using the B3LYP[72, 73] functional with the def2-TZVP basis set for Mn, N and O atoms, while the def2-SVP basis set was used for the C and H atoms.[74, 75] Grimme's D3 dispersion correction[76-79] was also applied with a fine integration grid (Grid6) and exchange grid (GridX6). Analytical frequency calculations were performed using the same level of theory. The frequency calculations provided the zero point energy, thermal corrections, and entropy, and verified that the structures were minima. Single point energies were obtained for all structures by using the larger def2-TZVPP basis set on all atoms with a finer integration grid (Grid7) and exchange grid (GridX7), as well as the Grimme's D3 dispersion correction.[76-79] In all cases, solvation was accounted for by using the SMD solvation model with default parameter for acetonitrile or DMSO.[80] The RIJCOSX approximation together with def2/J auxiliary basis set was used for all the calculations.[81, 82]

Calculated pK_a values, reduction potentials, and BDFEs were determined following an approach we previously employed for Mn^{III}-hydroxo complexes.[37] This procedure, which was inspired by the work of Solis and Hammes-Schiffer,[83] relies on the use of a reference complex, for which experimental pK_a and reduction potential values are known. We utilized the $[Mn^{III}(OH_2)(dpaq)]^{2+}$ complex as our reference, with pK_a = 6.8 and $E_{1/2}$ = 0.65 (versus Fc^+/Fc).[84]

The calculated p*K*a and $E_{1/2}$ parameters were determined using the optimized structures of the Mn^{III}-hydroxo, Mn^{III}-aqua, Mn^{II}-hydroxo, and Mn^{II}-aqua complexes. Single-point energy and analytical frequency calculations for these optimized structures provided the data for the determination of $\Delta\Delta G$ for the proton- and electron-transfer reactions between the reference compound and the compound of interest (Table A1.3). These $\Delta\Delta G$ values were then converted to pK_a and $E_{1/2}$ values relative to the reference complex (Table A1.4). From these values, the BDFEs for the $[Mn^{II}(OH_2)(PaPy_2Q)]^+$ and *trans*-$[Mn^{II}(OH_2)(PaPy_2N)]^+$ complexes were calculated using the Bordwell equation.[85]

Calculated O-H BDEs of the phenolic substrates were obtained using an approach we previously applied to calculate C-H BDEs of hydrocarbon substrates.[86] This DFT-based approach developed by Cramer and Que[87] was validated relative to the highly accurate *jun-jun* method of Truhlar *et al.*[88, 89] Geometry optimizations and frequency calculations of the phenolic substrates were performed Using the M06-2X functional, def2-TZVPP basis set for all atoms and a fine integration grid (Grid6). Single-point energy calculations were performed using the same functional and basis set with a finer integration grid (Grid7). Solvation was accounted for by using the SMD solvation model with default parameter for acetonitrile.[80] The bond dissociation enthalpies were computed using the zero-point corrected electronic energies. The thermoynamic parameters (pK_a values and reduction potentials) for the substrates were calculated using the method outlined by Solis and Hammes-Schiffer.[83] We utilized 4-^{t}Bu-2,6- DTBP as our reference, with pK_a in CH_3CN = 28 and $E_{1/2}$ = 0.93 (versus Fc^+/Fc).[90, 91]

2.3 Results and Discussion

Structures and Properties of [Mn^{II}($PaPy_2Q$)](OTf) and [Mn^{II}($PaPy_2N$)](OTf) Complexes.

The crystal structure of [Mn^{II}($PaPy_2Q$)](OTf) shows a Mn^{II} center in a distorted octahedral environment (Figure 2.3, left). The $PaPy_2Q$ ligand is bound in a pentadentate fashion, with *trans* pyridyl moieties and the tertiary amine and quinolinyl moieties also bound in a *trans* orientation (N4-Mn-N5 and N3-Mn-N1 angles of 145.40(9)° and 146.32(8)°, respectively; see Figure 2.3 for atom labels). This ligand binding mode is the same as that observed in crystal structures of corresponding Mn^{III}-hydroxo and Mn-NO complexes of the $PaPy_2Q$ ligand.[40] In the crystal structure of [Mn^{II}($PaPy_2Q$)](OTf), the quinolinyl group is tilted towards the N5-pyridine, as illustrated by the N5-Mn-N1 and N4-Mn-N1 angles of 97.04(9)° and 116.29(8)°, respectively. This tilt is likely caused by a triflate counterion that occupies a pocket between the quinolinyl and N4-pyridyl groups (Figure A1.10). The Mn^{II} coordination sphere of [Mn^{II}($PaPy_2Q$)](OTf) is completed by an amide oxygen, derived from a separate [Mn^{II}($PaPy_2Q$)]$^+$ cation, *trans* to the amide nitrogen (Figure 2.3, left). Similar polymeric structures have been observed for other solid-state Mn^{II} complexes supported by N_5^- ligands with carboxamido functions.[38, 92] Compared to [Mn^{II}(dpaq)](OTf) (Figure 2.2),[39] which we take as a representative example of such N_5^--ligated Mn^{II} complexes, [Mn^{II}($PaPy_2Q$)](OTf) shows an elongated Mn–N bond length for the quinolinyl donor (Mn–N1 in Table 2.1). This elongation could reflect the different disposition of the carboxamido function in the $PaPy_2Q$ and dpaq ligands, or could be caused by the presence of the triflate anion positioned between the pyridyl and quinolinyl groups (Figure A1.10).

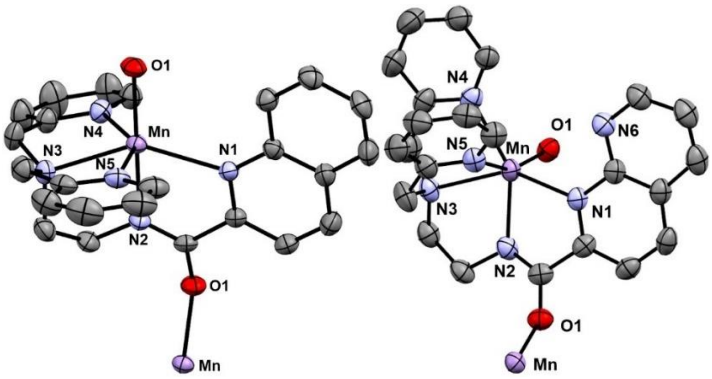

Figure 2.3. X-ray crystal structures of [Mn^{II}($PaPy_2Q$)](OTf) (left) and [Mn^{II}($PaPy_2N$)](OTf) (right) showing 50% probability thermal ellipsoids. The triflate counter ions, solvent molecules, and hydrogen atoms were removed for clarity.

Table 2.1. Manganese-Ligand Bond Lengths (Å) and Angles (°) from the Crystal Structures of [Mn^{II}($PaPy_2Q$)](OTf), [Mn^{II}($PaPy_2N$)](OTf), and [Mn^{II}(dpaq)](OTf).

	[Mn^{II}(L)](OTf)		
	L = $PaPy_2Q$	L = $PaPy_2N$	L = dpaq[a]
Mn–N1 (Å)	2.357(2)	2.228(3)	2.214(3)
Mn–N2 (Å)	2.148(2)	2.187(4)	2.191(3)
Mn–N3 (Å)	2.347(2)	2.344(4)	2.314(3)
Mn–N4 (Å)	2.299(2)	2.276(4)	2.244(3)
Mn–N5 (Å)	2.305(2)	2.298(4)	2.286(3)
Mn–O1 (Å)	2.0633(19)	2.119(3)	2.079(2)
O1–Mn–N2 (°)	174.49(9)	101.06(13)	164.88(10)
N4–Mn–N5 (°)	145.40(9)	75.68(14)	147.89(11)
N1–Mn–N3 (°)	146.32(8)	141.70(14)	151.40(10)
N4–Mn–N2 (°)	84.21(9)	147.36(14)	94.97(10)
N1–Mn–N2 (°)	72.75(8)	73.95(13)	74.46(10)
N3–Mn–N2 (°)	76.93(9)	73.52(14)	77.52(10)

[a] Data from ref. [39].

In the crystal structure of [Mn^{II}($PaPy_2N$)](OTf), the $PaPy_2N$ ligand is bound in a pentadentate fashion; however, the orientation of this N_5^- ligand differs from that observed for [Mn^{II}($PaPy_2Q$)](OTf) (Figure 2.3). In the structure of [Mn^{II}($PaPy_2N$)](OTf), the N donors from the quinolinyl, carboxamido, tertiary amine, and N4-pyridyl group are all in roughly the same plane. Thus, unlike in the structure of [Mn^{II}($PaPy_2Q$)](OTf), the pyridyl moieties of [Mn^{II}($PaPy_2N$)](OTf)

are in a *cis* orientation, with a N4-Mn-N5 angle of 75.7° (Table 2.1). This relatively acute angle could be enforced by a π-stacking interaction between the pyridyl rings (Figure 2.3, right). With the unique binding mode of the $PaPy_2N$ ligand, the amide oxygen that completes the Mn^{II} coordination sphere lies *trans* to the N5-pyridyl nitrogen. Despite the different binding modes of the $PaPy_2Q$ and $PaPy_2N$ ligands, the complexes have comparable Mn^{II}-ligand bond lengths (Table 2.1). The two exceptions are the Mn-N1(quinolinyl/naphthyridinyl) and Mn–O1 distances, which are shorter and longer, respectively, for the $[Mn^{II}(PaPy_2N)](OTf)$ complex.

The unexpected binding mode of the $PaPy_2N$ ligand might reduce steric interactions between the adjacent $[Mn^{II}(PaPy_2N)]^+$ cations in the solid state, or might reflect different crystal packing forces caused by a MeCN solvent of crystallization in the solid-state structure. To determine if a different sixth ligand would change the solid-state structure of $[Mn^{II}(PaPy_2N)](OTf)$, we attempted to grow crystals of $[Mn^{II}(PaPy_2N)](OTf)$ in the presence of water and with different counter ions. The structure $[Mn^{II}(PaPy_2N)](PF_6)$ is essentially identical to that of the triflate salt. Attempts to crystallize this complex in the presence of water were unsuccessful.

When $[Mn^{II}(PaPy_2Q)](OTf)$ or $[Mn^{II}(PaPy_2N)](OTf)$ are dissolved in MeCN, the solutions lack any defined electronic absorption bands in the visible region but show the onset of absorption intensity near 600 nm (Figure A1.11). These spectra are reminiscent of those of $[Mn^{II}(dpaq)](OTf)$ and related complexes[37-39] and are consistent with the lack of any spin-allowed *d-d* transitions for these high-spin Mn^{II} centers. X-band EPR, ESI-MS, and solution-phase magnetic susceptibility measurements for $[Mn^{II}(PaPy_2Q)](OTf)$ and $[Mn^{II}(PaPy_2N)](OTf)$ in MeCN are consistent with mononuclear Mn^{II} centers (Figures A1.12 – A1.17). Thus, the polymeric structures observed in the solid-state (Figure 2.3) are not retained in solution. From the available spectroscopic data for

the Mn^{II} complexes, we are unable to determine if the coordination mode of either the $PaPy_2Q$ or $PaPy_2N$ ligands change in solution.

Formation and Properties of Mn^{III}-hydroxo Complexes. The addition of iodosobenzene (PhIO) to either $[Mn^{II}(PaPy_2Q)](OTf)$ or $[Mn^{II}(PaPy_2N)](OTf)$ in MeCN at 25 °C results in the formation of oxidation products with electronic absorption bands in the visible region (Figure 2.4). For each reaction, these new chromophores are maximally formed with a minimum of 0.5 equiv. PhIO. The pink oxidation product from $[Mn^{II}(PaPy_2Q)](OTf)$ shows well-defined absorption bands at 485 and 734 nm (ε = 320 and 120 M^{-1} cm^{-1}, respectively). The energies and intensities of these electronic absorption bands are essentially identical to those of the Mn^{III}-hydroxo adduct $[Mn^{III}(OH)(PaPy_2Q)](ClO_4)$, reported by Masharak and co-workers (Figure 2.2).[40] ESI-MS data for the oxidized product show a prominent ion peak at an *m/z* value consistent with $[Mn^{III}(OH)(PaPy_2Q)]^+$ (Figure A1.18). An analysis of the solution magnetic moment by the NMR method of Evans yielded μ_{eff} = 4.9 BM, which is close to that expected for an S = 2 system (Figure A1.19). On the basis of these data, we formulate the product of the reaction of PhIO and $[Mn^{II}(PaPy_2Q)](OTf)$ in MeCN as the triflate salt of $[Mn^{III}(OH)(PaPy_2Q)]^+$.

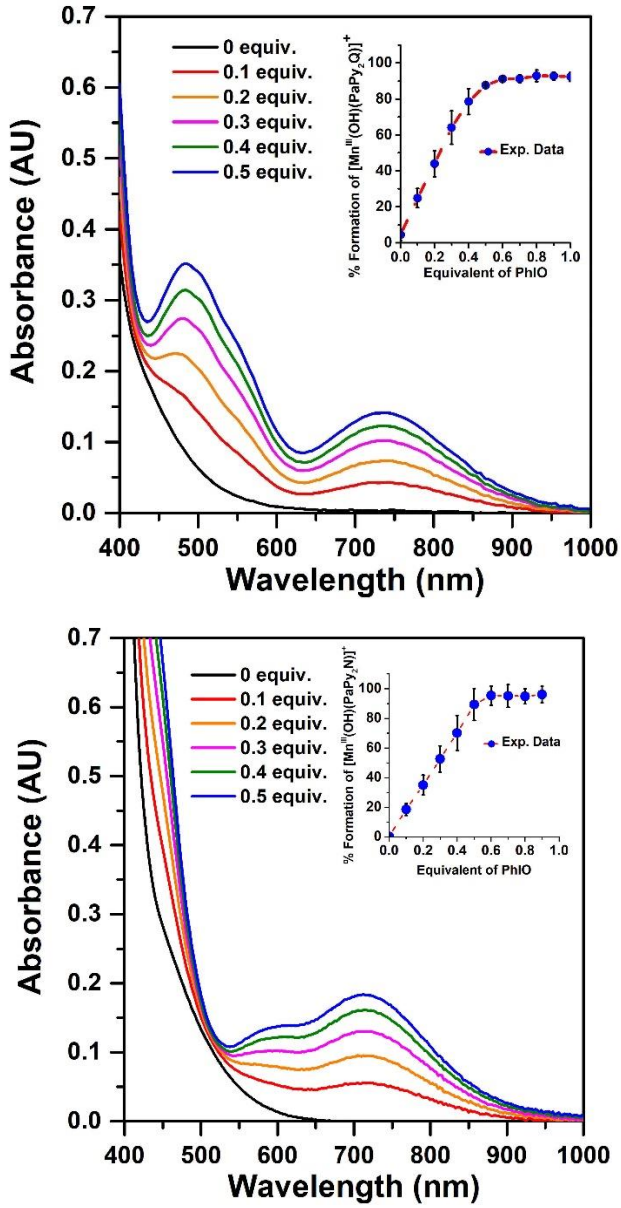

Figure 2.4. Electronic absorption spectroscopic titrations of $[Mn^{II}(PaPy_2Q)](OTf)$ (top) and $[Mn^{II}(PaPy_2N)](OTf)$ (bottom) with 0 - 1.0 equiv. PhIO in MeCN at 25 °C. The insets show the percent formation of product vs. equiv. added PhIO.

Mascharak and co-workers previously reported the X-ray structure of the perchlorate salt of $[Mn^{III}(OH)(PaPy_2Q)]^+$ (Figure 2.2).[40] This structure is very similar to that of $[Mn^{II}(PaPy_2Q)](OTf)$, but with the hydroxo ligand replacing the amide oxygen. In addition, the Mn^{II}-ligand bond lengths in $[Mn^{II}(PaPy_2Q)](OTf)$ are all longer than the corresponding distances in

$[Mn^{III}(OH)(PaPy_2Q)](ClO_4)$. We summarize the reaction of $[Mn^{II}(PaPy_2Q)](OTf)$ with PhIO to generate the Mn^{III}-hydroxo product in Figure 2.5.

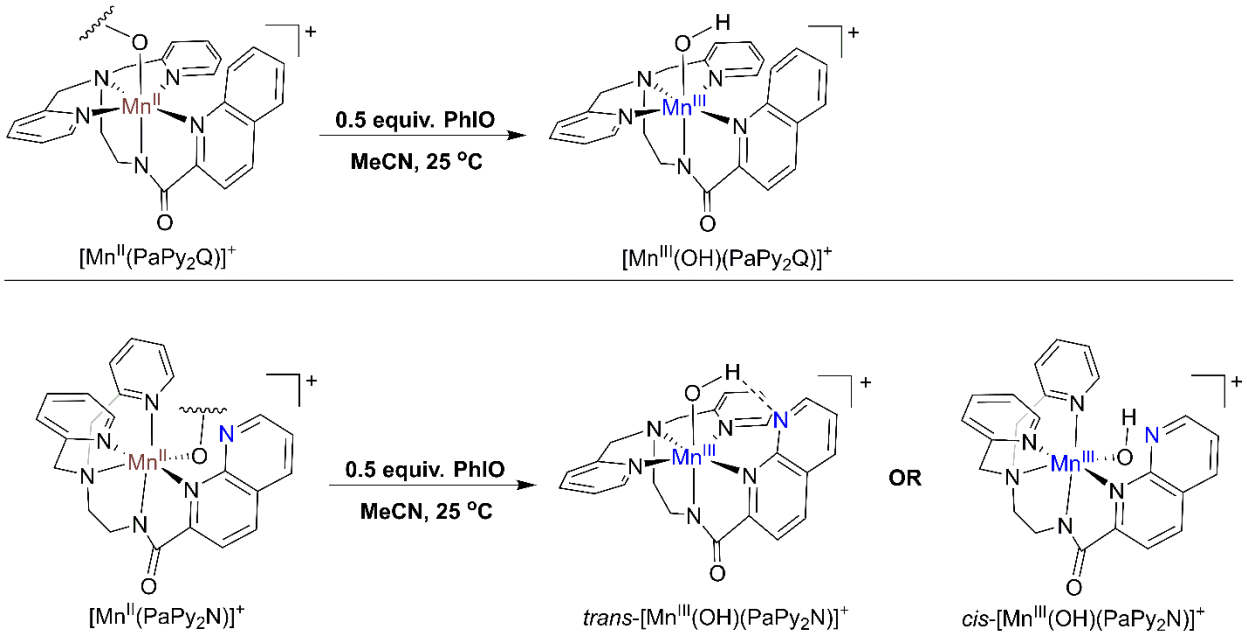

Figure 2.5. Schematic representation of the reactions of $[Mn^{II}(PaPy_2Q)]^+$ and $[Mn^{II}(PaPy_2N)]^+$ with PhIO to generate the Mn^{III}-hydroxo complexes $[Mn^{III}(OH)(PaPy_2Q)]^+$ and $[Mn^{III}(OH)(PaPy_2N)]^+$. Two potential structures for $[Mn^{III}(OH)(PaPy_2N)]^+$ are shown.

While the reaction of PhIO with $[Mn^{II}(PaPy_2Q)](OTf)$ yields a pink solution, the addition of PhIO to $[Mn^{II}(PaPy_2N)](OTf)$ gives rise to a green solution characterized by an electronic absorption band at 730 nm (ε = 130 M^{-1} cm^{-1}) and a shoulder at 580 nm (Figure 2.4). The use of the NMR method of Evans to investigate this solution yields a magnetic moment (μ_{eff}) of 4.9 BM, supportive of the formation of a mononuclear, S = 2 Mn^{III} species (Figure A2.20). ESI-MS data for the green solution show a prominent ion peak at *m/z* of 469.12, which is as expected for the Mn^{III}-hydroxo adduct $[Mn^{III}(OH)(PaPy_2N)]^+$ (Figure A1.21).

Our data for the PhIO oxidation products of $[Mn^{II}(PaPy_2Q)](OTf)$ or $[Mn^{II}(PaPy_2N)](OTf)$ in MeCN provide support for the formation of Mn^{III}-hydroxo complexes in each reaction. While the solution structure of $[Mn^{III}(OH)(PaPy_2Q)]^+$ can be reasonably inferred from the structure of the crystallographically-characterized perchlorate salt,[40] the structure of $[Mn^{III}(OH)(PaPy_2N)]^+$ is uncertain. We propose two hypothetical structures, which we distinguish by the orientation of the pyridyl groups (*trans* or *cis*; see Figure 2.5, bottom-right). In *cis*-$[Mn^{III}(OH)(PaPy_2N)]^+$, the $PaPy_2N$ ligand has the same binding mode as in the corresponding Mn^{II} complex (Figure 2.3, right), which places the hydroxo ligand *trans* to the N5-pyridyl group. In the structure of *trans*-$[Mn^{III}(OH)(PaPy_2N)]^+$, the $PaPy_2N$ ligand has the same binding mode as the $PaPy_2Q$ ligand (Figure 2.5), which places the hydroxo ligand *trans* to the amide function. In *trans*-$[Mn^{III}(OH)(PaPy_2N)]^+$, the hydroxo ligand can serve as a hydrogen-bond donor to a nitrogen atom of the adjacent naphthyridinyl group. Either structure could result in structural perturbations relative to $[Mn^{III}(OH)(PaPy_2Q)]^+$ that would change the Mn^{III} *d-d* transition energies (*vide infra*). Thus, either structure could be consistent with the clear differences in the electronic absorption spectra of $[Mn^{III}(OH)(PaPy_2Q)]^+$ and $[Mn^{III}(OH)(PaPy_2N)]^+$ (Figure 2.4).

Formation and X-ray Crystal Structures of the Mn^{III}-Methoxy Complexes $[Mn^{III}(OMe)(PaPy_2Q)](OTf)$ and $[Mn^{III}(OMe(PaPy_2N)](OTf)$. To better understand any structural differences between $[Mn^{III}(OH)(PaPy_2Q)]^+$ and $[Mn^{III}(OH)(PaPy_2N)]^+$, we generated the corresponding Mn^{III}-methoxy complexes. As shown in Figure 2.6, the reaction of 0.5 equiv. PhIO with either $[Mn^{II}(PaPy_2Q)](OTf)$ or $[Mn^{II}(PaPy_2N)](OTf)$ in MeOH at 25° C leads to the formation of chromophores with electronic absorption bands at 511 and 768 nm (ε = 480 and 120 $M^{-1}cm^{-1}$ respectively) for $[Mn^{III}(OMe)(PaPy_2Q)]^+$ and 485 and 768 nm (ε = 380 and 120 $M^{-1}cm^{-1}$ respectively) for $[Mn^{III}(OMe)(PaPy_2N)]^+$. The positions and relative intensities of these bands are

very similar to those observed for $[Mn^{III}(OMe)(dpaq)]^+$ (λ_{max} = 510 and 760 nm, with ε = 330 and 130 $M^{-1}cm^{-1}$, respectively; see Table 2).[92] ESI-MS data for these complexes show peaks at *m/z* values consistent with the $[Mn^{III}(OMe)(PaPy_2Q)]^+$ and $[Mn^{III}(OMe)(PaPy_2N)]^+$ cations (Figure A1.22 – A1.23), and magnetic moments by the NMR method of Evans are 4.9 and 5.0 BM, respectively (Figure A1.24 – A1.25), consistent with high-spin (S = 2) Mn^{III} centers.

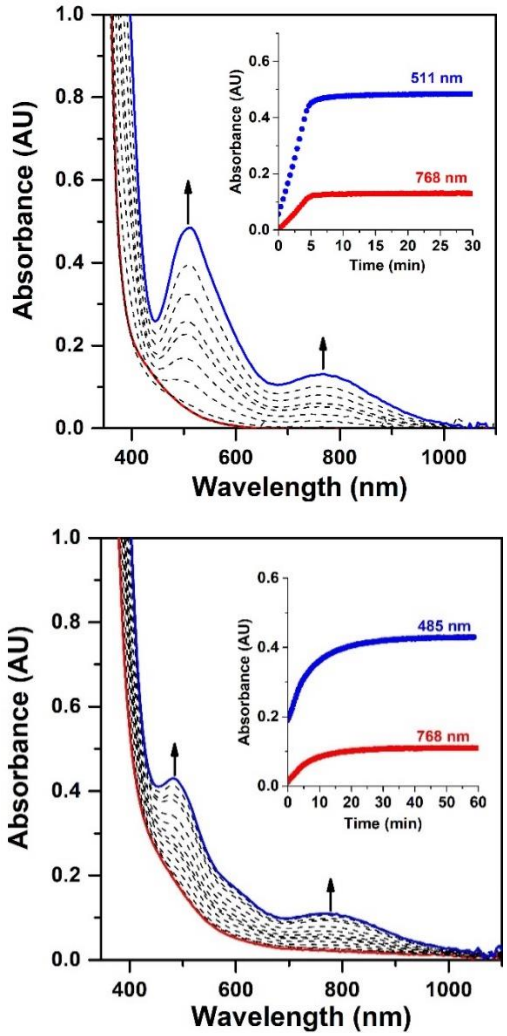

Figure 2.6. Electronic absorption spectra showing the reaction of 1.0 mM $[Mn^{II}(PaPy_2Q)]^+$ (top, red trace) and $[Mn^{II}(PaPy_2N)]^+$ (bottom, red trace) with 0.5 equiv. of PhIO at 25 °C in MeOH. The reactions yield $[Mn^{III}(OMe)(PaPy_2Q)]^+$ (top, blue trace) and $[Mn^{III}(OMe)(PaPy_2N)]^+$ (bottom, blue trace). Inset: Time evolution of absorption signals at specified wavelengths at different time ranges.

The oxidation products of both [Mn^{II}($PaPy_2Q$)](OTf) or [Mn^{II}($PaPy_2N$)](OTf) were amenable to structural characterization by X-ray crystallography, and the solid-state structures are shown in Figure 2.7. In each case, the crystal structures are of mononuclear Mn^{III}-methoxy complexes, with the methoxy ligand bound *trans* to the carboxamido nitrogen. The Mn–OMe distances of 1.826(3) and 1.815(2) Å are similar to those of other Mn^{III}-methoxy complexes (Table 2.2).[92]

The similar geometries of [Mn^{III}(OMe)($PaPy_2Q$)](OTf) and [Mn^{III}(OMe)($PaPy_2N$)](OTf) are in accord with their nearly identical electronic absorption spectra (Figure 2.6), which require very similar ligand-field geometries. For [Mn^{III}(OMe)($PaPy_2Q$)](OTf), the observed binding mode of the $PaPy_2Q$ ligand is the same as that observed for the Mn^{II} and Mn^{III}-hydroxo structures. A comparison of the [Mn^{III}(OMe)($PaPy_2Q$)](OTf) and [Mn^{III}(OH)($PaPy_2Q$)](ClO_4) structures reveals nearly identical Mn^{III}-ligand bond lengths (Table 2.2). Surprisingly, the binding mode of the $PaPy_2N$ ligand in the crystal structure of [Mn^{III}(OMe)($PaPy_2N$)](OTf) is distinct from that observed in the [Mn^{II}($PaPy_2N$)](OTf) structure (cf. Figures 2.7 and 2.3). Relative to [Mn^{II}($PaPy_2N$)](OTf), the pyridyl groups of the Mn^{III}-methoxy complex have moved to a *trans* orientation, placing the methoxy opposite the carboxamido donor. This alternate binding mode for the $PaPy_2N^-$ ligand provides strong evidence that this ligand can change coordination around the Mn ion in solution and suggests that the [Mn^{III}(OH)($PaPy_2N$)](OTf) complex (Figure 2.5) could have a geometry similar to that of its Mn^{III}-methoxy analogue.

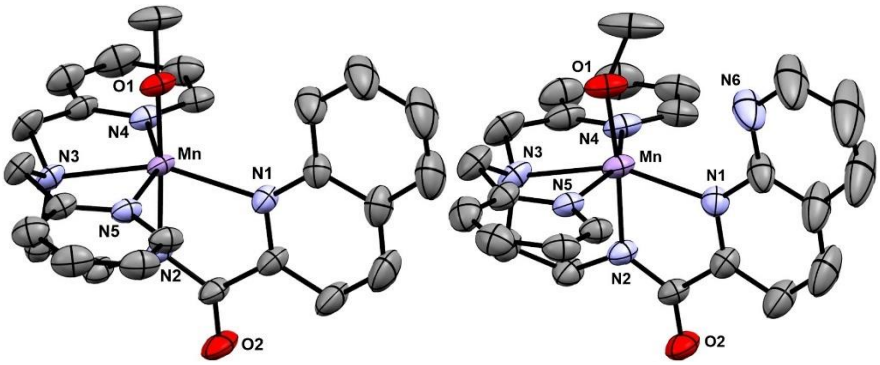

Figure 2.7. X-ray crystal structures of [Mn^{III}(OMe)($PaPy_2Q$)](OTf) (left) and [Mn^{III}(OMe)($PaPy_2N$)](OTf) (right) showing 50% probability thermal ellipsoid. The triflate counter ions, solvent molecules, and hydrogen atoms were removed for clarity.

Table 2.2. Manganese-Ligand Bond Lengths (Å) from the Crystal Structures of [Mn^{III}(OMe)$PaPy_2Q$)](OTf), [Mn^{III}(OMe)($PaPy_2N$)](OTf), [Mn^{III}(OH)($PaPy_2Q$)](ClO_4), and [Mn^{III}(OMe)(dpaq)](OTf) and Electronic Absorption Band Maxima (nm) and Extinction Coefficients ($M^{-1}cm^{-1}$).

	[Mn^{III}(OMe)(L)](OTf)			[Mn^{III}(OH)($PaPy_2Q$)](ClO_4)[b]
	L = $PaPy_2Q$	L = $PaPy_2N$	L = dpaq[a]	
Mn–N1	2.189(3)	2.186(3)	2.051(5)	2.1945(19)
Mn–N2	1.943(3)	1.961(2)	1.979(5)	1.9680(18)
Mn–N3	2.226(3)	2.232(3)	2.175(5)	2.2415(19)
Mn–N4	2.122(3)	2.127(3)	2.203(6)	2.171(2)
Mn–N5	2.199(3)	2.184(3)	2.212(6)	2.138(2)
Mn–O2	1.826(3)	1.815(2)	1.825(4)	1.8180(16)
λ (ε)	511 (480)	485 (380)	510 (330)	485 (280)
	768 (120)	768 (120)	760 (130)	740 (120)

[a] Data from ref. [92]. [b] Data from ref. [40].

Comparison of ^{1}H NMR Spectra for Mn^{III}-hydroxo and Mn^{III}-methoxy Complexes. To further probe the geometries of the Mn^{III}-hydroxo and Mn^{III}-methoxy complexes, we collected room-temperature ^{1}H NMR data for each species. We will begin our discussion of the ^{1}H NMR data by focusing on [Mn^{III}(OMe)($PaPy_2Q$)](OTf) and [Mn^{III}(OMe)($PaPy_2N$)](OTf), as solid-state structures are available for each of these complexes (Figure 2.7). The ^{1}H NMR spectra of 15 mM solutions of [Mn^{III}(OMe)($PaPy_2Q$)](OTf) and [Mn^{III}(OMe)($PaPy_2N$)](OTf) in CD_3OD are very

similar, each showing a set of four downfield signals from *ca.* 120 to 40 ppm, and two upfield signals near -10 and -25 ppm (Figure 2.8 and Table 2.3). The large hyperfine shifts of many of these peaks are similar to those observed for other high-spin, mononuclear Mn^{III} complexes.[93, 94] The ^1H NMR spectrum of $[Mn^{III}(OMe)(PaPy_2Q)](OTf)$ shows an additional broad resonance at -86.5 ppm that is absent in the ^1H NMR spectrum of $[Mn^{III}(OMe)(PaPy_2Q)](OTf)$. However, the spectrum of $[Mn^{III}(OMe)(PaPy_2N)](OTf)$ contains a broad, poorly-resolved peak near -14 ppm, which could correspond to the broad signal for $[Mn^{III}(OMe)(PaPy_2Q)](OTf)$ at -86.5 ppm. Overall, the pattern of hyperfine-shifted peaks for $[Mn^{III}(OMe)(PaPy_2Q)](OTf)$ and $[Mn^{III}(OMe)(PaPy_2N)](OTf)$ are very similar, suggesting that the similarities in the solid-state structures are retained in solution.

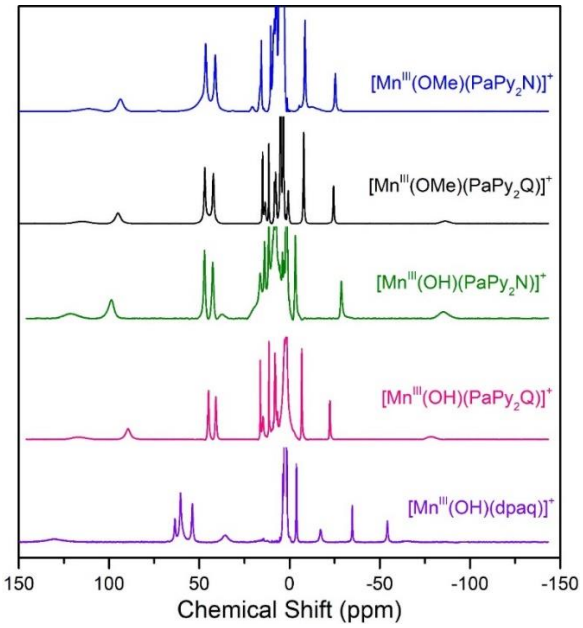

Figure 2.8. ^1H NMR spectra of 15 mM solutions of $[Mn^{III}(OH)(PaPy_2Q)]^+$ (pink) and $[Mn^{III}(OH)(PaPy_2N)]^+$ (green) in CD_3CN, and $[Mn^{III}(OMe)(PaPy_2Q)]^+$ (black) and $[Mn^{III}(OMe)(PaPy_2N)]^+$ (blue) in CD_3OD. All spectra are at 298 K. The spectrum of $[Mn^{III}(OH)(dpaq)]^+$ in 400 µL CD_3CN with 45 µL D_2O (purple) from ref. [36] is included for comparison.

Table 2.3. ^{1}H NMR Chemical Shifts (ppm) for $[Mn^{III}(OMe)(L)]^+$ Complexes in CD_3OD and $Mn^{III}(OH)(L)]^+$ Complexes in CD_3CN.

$[Mn^{III}(OMe)(L)]^+$			$[Mn^{III}(OH)(L)]^+$		
L = $PaPy_2Q$	L = $PaPy_2N$	L = dpaq[a]	L = $PaPy_2Q$	L = $PaPy_2N$	L = dpaq[a]
114.2	111.4	127.5 (py)	116.4	121.7	130.5 (py)
95.0	93.7	60.8 (py)	88.7	97.3	62.7 (qn)
		59.9 (qn)	44.8	47.0	60.9 (py)
		57.2 (qn)	40.8	42.4	54.3 (py)
46.9	46.4	53.9 (py)		37.4	40.5 (ND)
42.2	41.2	38.5 (CH_2)	-6.7	-3.2	-4.6 (py)
		2.54 (ND)	-22.8	-28.8	-15.5 (qn)
		-4.2 (py)	-77.0	-84.5	-33.7 (qn)
-7.9	-9.6	-15.7 (qn)			-53.8 (qn)
-24.4	-13.9	-33.6 (qn)			-63.4 (qn)
-86.2	-25.4	-52.7 (qn)			
		-66.3 (qn)			

[a] From ref. [36].

The ^{1}H NMR spectra of the Mn^{III}-hydroxo complexes $[Mn^{III}(OH)(PaPy_2Q)](OTf)$ and $[Mn^{III}(OH)(PaPy_2N)](OTf)$ in CD_3CN at 25 °C are nearly identical. Each spectrum shows four downfield resonances at *ca.* 120, 90, 45, and 40 ppm, and three upfield peaks at *ca.* -5, -25, and -80 ppm (Figure 8). A peak-to-peak comparison of the corresponding resonances of these two complexes reveals only modest shifts of *ca.* 2 – 9 ppm (Table 2.3). The only notable difference between the ^{1}H NMR spectra of $[Mn^{III}(OH)(PaPy_2Q)](OTf)$ and $[Mn^{III}(OH)(PaPy_2N)](OTf)$ is the low intensity peak at 37.4 ppm that is present only in the spectrum of the latter complex (Figure 8 and Table 2.3). In previous studies of Mn^{III}-hydroxo complexes, we have observed shifts in proton resonances caused by the addition of a small amount of water to the CD_3CN solution. In this present case, the addition of 20 μL D_2O to the 400 μL sample of $[Mn^{III}(OH)(PaPy_2Q)](OTf)$ led to the resolution of a weak peak near 52.5 ppm (Figure A1.26). Similarly, the addition of D_2O to $[Mn^{III}(OH)(PaPy_2N)](OTf)$ caused the disappearance of the weak signal at 37.4 ppm. Presumably,

the presence of D_2O causes this peak to shift downfield such that it now overlaps with the more intense resonances near 45 ppm (Figure A1.26).

The ^{1}H NMR data for [Mn^{III}(OH)($PaPy_2N$)](OTf) allow us to reasonably infer the solution structure of this complex. If the binding mode of the $PaPy_2N$ ligand in this complex followed that of [Mn^{II}($PaPy_2N$)](OTf), with *cis* pyridyl ligands (Figure 2.3), the protons of the two pyridyl groups would be inequivalent. In that case, we would expect [Mn^{III}(OH)($PaPy_2N$)](OTf) to show more resonances than [Mn^{III}(OH)($PaPy_2Q$)](OTf), [Mn^{III}(OMe)($PaPy_2Q$)](OTf), and [Mn^{III}(OMe)($PaPy_2N$)](OTf). Not only does the ^{1}H NMR spectrum of [Mn^{III}(OH)($PaPy_2N$)](OTf) lack more proton resonances than the spectra of the other complexes, the spectra of all four complexes are strikingly similar (Figure 2.8 and Table 2.3), suggesting that the ligands for these four complexes have nearly identical structures in solution. On this basis, we propose that the solution structure of [Mn^{III}(OH)($PaPy_2N$)](OTf) has the hydroxo group *trans* to the carboxamido function, with *trans* pyridyl groups (*i.e.*, *trans*-[Mn^{III}(OH)($PaPy_2N$)]$^+$ in Figure 2.5).

Relative to [Mn^{III}(OH)(dpaq)]$^+$, the ^{1}H NMR spectra of [Mn^{III}(OH)($PaPy_2Q$)]$^+$ and [Mn^{III}(OH)($PaPy_2N$)]$^+$ show far fewer peaks in the upfield region. The four peaks for [Mn^{III}(OH)(dpaq)]$^+$ from -15.5 to -63.4 ppm all arise from quinolinyl protons. In addition, the 62.7 ppm resonance of [Mn^{III}(OH)(dpaq)]$^+$ was also attributed to a quinolinyl proton, and there is no corresponding peak observed for either [Mn^{III}(OH)($PaPy_2Q$)]$^+$ or [Mn^{III}(OH)($PaPy_2N$)]$^+$. Given the difference in the position of the quinolinyl (or 1,8-naphthyridinyl) moieties for these complexes, it is not unexpected that these peaks would be perturbed. Many of the quinolinyl and naphthyridinyl protons for [Mn^{III}(OH)($PaPy_2Q$)]$^+$ and [Mn^{III}(OH)($PaPy_2N$)]$^+$ are relatively far from the Mn^{III} center (the longest H···Mn separation in the X-ray structure of [Mn^{III}(OH)($PaPy_2Q$)]$^+$ is *ca.* 6.7 Å, whereas the longest distance in [Mn^{III}(OH)(dpaq)]$^+$ is 6.1 Å).[39,

[40] Thus, the resonances for some quinolinyl protons for $[Mn^{III}(OH)(PaPy_2Q)]^+$ might contract towards the 10 – 0 ppm range. In contrast to the large perturbations in quinolinyl resonances for these complexes, the pyridyl resonances of $[Mn^{III}(OH)(dpaq)]^+$ (at 130.5, 60.9, 54.3, and -4.6 ppm) have corresponding peaks (shifted by *ca.* 10 – 15 ppm) in the spectra of $[Mn^{III}(OH)(PaPy_2Q)]^+$ and $[Mn^{III}(OH)(PaPy_2N)]^+$. A comparison of the ^{1}H NMR spectra of the Mn^{III}-methoxy complex $[Mn^{III}(OMe)(PaPy_2Q)]^+$ and $[Mn^{III}(OMe)(PaPy_2N)]^+$ with $[Mn^{III}(OMe)(dpaq)]^+$ also reveals minor perturbations in the positions of pyridyl protons and large changes for protons associated with the quinolinyl (or 1,8-naphthyridinyl) groups (Table 2.3).

Potential Structures of $[Mn^{III}(OH)(PaPy_2N)]^+$ from DFT Computations. Due to the lack of a crystal structure for $[Mn^{III}(OH)(PaPy_2N)]^+$, we used DFT computations to develop structures for the *trans*- and *cis*-$[Mn^{III}(OH)(PaPy_2N)]^+$ isomers presented in Figure 2.5. The structures are shown in Figure 2.9 (top). A DFT-computed structure for $[Mn^{III}(OH)(PaPy_2Q)]^+$ in the crystallographically-characterized *trans* conformation gives Mn–ligand bond lengths within *ca.* 0.02 Å of the experimental distances (Table 2.4), supporting the use of our theoretical approach. The Mn–ligand bonds lengths in the *trans*-$[Mn^{III}(OH)(PaPy_2N)]^+$ isomer are very similar to those in the X-ray and DFT-derived structures of $[Mn^{III}(OH)(PaPy_2Q)]^+$ (Table 2.4). The Mn–N1 bond length involving one nitrogen of the naphthyridine group is slightly shorter in *trans*-$[Mn^{III}(OH)(PaPy_2N)]^+$ than the corresponding Mn–N1 distance in $[Mn^{III}(OH)(PaPy_2Q)]^+$. This variation might reflect the strong hydrogen-bond between the hydroxo and naphthyridine groups. This interaction is marked by a short (hydroxo)OH···N(naphthyridine) distance of 1.952 Å. The heavy atom (hydroxo)O···N(naphthyridine) separation of 2.862 Å is just slightly longer than that observed for (oxo)O···N(urea) distances in X-ray crystal structures of Mn^{III}-oxo and Mn^{III}-hydroxo

adducts with intramolecular hydrogen bonds (2.613 Å).[63] Overall, the similarities between the structures of *trans*-$[Mn^{III}(OH)(PaPy_2N)]^+$ and $[Mn^{III}(OH)(PaPy_2Q)]^+$ are in accordance with the nearly identical ^1H NMR spectra of these complexes (Figure 2.8).

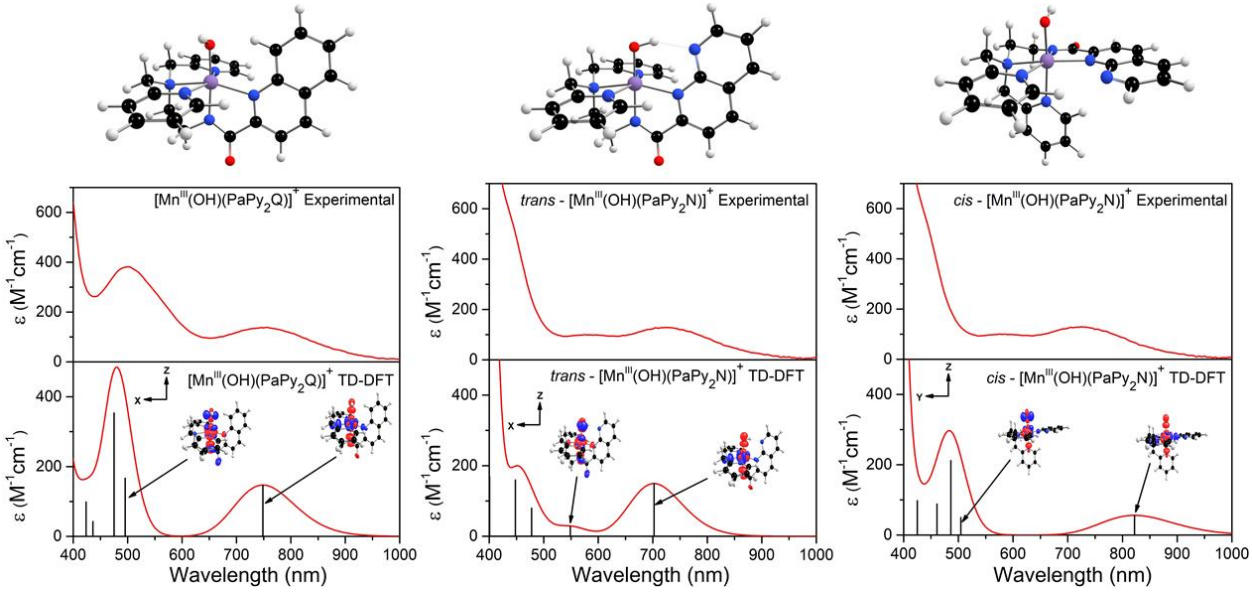

Figure 2.9. TD-DFT computed absorption spectrum for $[Mn^{III}(OH)(PaPy_2Q)]^+$ (left), *trans*-$[Mn^{III}(OH)(PaPy_2N)]^+$ (center) and *cis*-$[Mn^{III}(OH)(PaPy_2N)]^+$ (right). The sticks indicate electronic transitions; EDDMs of selected transitions are included as an inset. Red and blue colors in the EDDMs denotes gain and loss of electron density, respectively. The DFT-computed structures of the Mn^{III}-hydoxo complexes are shown above the absorption spectra.

In the structure of *cis*-$[Mn^{III}(OH)(PaPy_2N)]^+$, the hydroxo group is *trans* to a pyridyl donor and *cis* to the carboxamide function (Figure 2.9, top-right). This disposition of the hydroxo group in *cis*-$[Mn^{III}(OH)(PaPy_2N)]^+$ prevents any intramolecular hydrogen bonding with the naphthyridinyl ligand. The Mn–N(pyridyl) (N4 and N5) distances in this structure are shorter than those of the *trans* isomer by 0.1 Å. All other Mn-ligand bond lengths are elongated in the *cis* structure.

To further evaluate the *trans*- and *cis*-$[Mn^{III}(OH)(PaPy_2N)]^+$ structures on the basis of experimental data, we performed TD-DFT calculations to predict electronic absorption spectra for

each isomer. Although TD-DFT calculations have known drawbacks, this method has performed quite well for mononuclear Mn^{III} complexes,[95-99] potentially because the electronic absorption spectra of these complexes are dominated by ligand-field transitions. In support, the TD-DFT absorption spectrum for $[Mn^{III}(OH)(PaPy_2Q)]^+$ is in excellent agreement with experimental data, with both spectra showing features at *ca.* 750 and 500 nm (Figure 2.9, left). An analysis of the electron-density difference maps for the states contributing to these bands readily supports their assignments as Mn^{III} ligand-field transitions. Using a coordinate system where the *z*-axis lies along the Mn–OH bond and the *x*- and *y*-axes coincide with the equatorial Mn-ligand bonds, $[Mn^{III}(OH)(PaPy_2Q)]^+$ has a $(d_{xy})^1(d_{yz})^1(d_{xz})^1(d_{x^2-y^2})^1(d_{z^2})^0$ ground configuration. The highest-energy d_{z^2} MO is strongly destabilized by σ-antibonding interactions with the hydroxo and carboxamido donors, while the $d_{x^2-y^2}$ MO is σ-antibonding with respect to the equatorial ligands. The d_{xz} and d_{yz} MOs have weak π-antibonding interactions with the hydroxo ligand, and the d_{xy} MO is essentially non-bonding. From the TD-DFT calculations for $[Mn^{III}(OH)(PaPy_2Q)]^+$, the lower-energy band at 750 nm is due to a one-electron $d_{x^2-y^2} \rightarrow d_{z^2}$ transition, while the higher-energy band near 500 nm contains contributions from one-electron $d_{xz} \rightarrow d_{z^2}$ and $d_{yz} \rightarrow d_{z^2}$ transitions. Electron-density difference maps (EDDMs) for the $d_{x^2-y^2} \rightarrow d_{z^2}$ and $d_{yz} \rightarrow d_{z^2}$ transitions are shown in Figure 2.9.

The TD-DFT absorption spectrum for *trans*-$[Mn^{III}(OH)(PaPy_2N)]^+$ has bands at 700, 550 and 450 nm, which are in excellent agreement with the experimental features at 730, 580, and 450 nm (Figure 2.9, center). The TD-DFT calculations for *trans*-$[Mn^{III}(OH)(PaPy_2N)]^+$ also reproduce the spectral changes relative to $[Mn^{III}(OH)(PaPy_2Q)]^+$. First, the TD-DFT calculations predict the lowest-energy band of *trans*-$[Mn^{III}(OH)(PaPy_2N)]^+$ (from a $d_{x^2-y^2} \rightarrow d_{z^2}$ excitation) to be blue-shifted compared to that of $[Mn^{III}(OH)(PaPy_2Q)]^+$ (700 and 750 nm, respectively), which is in

excellent agreement with the experimental bandshift (730 and 750 nm, respectively). Second, the $d_{xz} \rightarrow d_z^2$ transition of *trans*-$[Mn^{III}(OH)(PaPy_2N)]^+$ is red-shifted compared to that of $[Mn^{III}(OH)(PaPy_2Q)]^+$ (Figure 2.9). This shift accounts for the weak feature observed near 600 nm for $[Mn^{III}(OH)(PaPy_2N)]^+$ that is absent in the corresponding spectrum of $[Mn^{III}(OH)(PaPy_2Q)]^+$. Accordingly, the TD-DFT absorption spectrum of *trans*-$[Mn^{III}(OH)(PaPy_2N)]^+$ reproduces all the spectral perturbations observed experimentally.

In contrast, the TD-DFT absorption spectrum for *cis*-$[Mn^{III}(OH)(PaPy_2N)]^+$ is in poorer agreement with the experimental spectrum and does not reproduce the spectral perturbations relative to $[Mn^{III}(OH)(PaPy_2Q)]^+$ (Figure 2.9). The lowest-energy transition for *cis*-$[Mn^{III}(OH)(PaPy_2N)]^+$ is at *ca.* 830 nm, which is significantly lower than the experimental band (720 nm). In addition, the $d_{xz} \rightarrow d_z^2$ transition in *cis*-$[Mn^{III}(OH)(PaPy_2N)]^+$ is essentially unchanged relative to that of $[Mn^{III}(OH)(PaPy_2Q)]^+$. On the basis of these results, only the *trans*-$[Mn^{III}(OH)(PaPy_2N)]^+$ isomer can account for the spectral perturbations relative to $[Mn^{III}(OH)(PaPy_2Q)]^+$. The TD-DFT computation for the Mn^{III}-methoxy complexes were also performed, and the results nicely reproduced the experimental electronic spectra of the methoxy complexes (Figure A1.27).

Table 2.4. Structural Properties for $[Mn^{III}(OH)(PaPy_2Q)]^+$ from X-ray Crystallography and DFT Computations and Structural Properties for isomers of $[Mn^{III}(OH)(PaPy_2N)]^+$ from DFT Computations.

	$[Mn^{III}(OH)(PaPy_2Q)]^+$		$[Mn^{III}(OH)(PaPy_2N)]^+$	
	XRD	DFT	***trans***	***cis***
Mn–N1 (Å)	2.1945(19)	2.211	2.172	2.259
Mn–N2 (Å)	1.9680(18)	1.956	1.970	2.010
Mn–N3 (Å)	2.2415(19)	2.260	2.261	2.308
Mn–N4 (Å)	2.171(2)	2.166	2.191	2.093
Mn–N5 (Å)	2.138(2)	2.136	2.161	2.093
Mn–O2 (Å)	1.8180(16)	1.843	1.822	1.832
OH···N (Å)			1.952	
N2-Mn-O2 (°)	174.21	176.2	176.7	173.54

TEMPOH Oxidation by Mn^{III}-hydroxo complexes. The reactivity of $[Mn^{III}(OH)(PaPy_2Q)]^+$ and $[Mn^{III}(OH)(PaPy_2N)]^+$ were compared using the substrate TEMPOH, which is known for its thermochemical preference to react by a CPET mechanism.[90] This preference stems from the relatively weak O–H bond dissociation free energy of TEMPOH (BDFE = 66.5 kcal mol^{-1} in MeCN at 298 K) compared to its poor acidity (pK_a = 41 in MeCN) and difficulty in oxidation ($TEMPOH^{+/\bullet}$ $E_{p,a}$ = 0.71 V vs. $Fc^{+/0}$). In addition, TEMPOH has been previously employed to assess reactivity differences for Mn^{III}-hydroxo complexes and thus provides an excellent point of reference.[16, 37-39, 100]

The addition of excess TEMPOH to MeCN solutions of either $[Mn^{III}(OH)(PaPy_2Q)]^+$ or $[Mn^{III}(OH)(PaPy_2N)]^+$ at -35 °C led to the disappearance of the electronic absorption signals characteristic of these Mn^{III}-hydroxo adducts (Figure 2.10). In each case, the decay of the absorption bands could be fit to a pseudo-first order process to at least five half-lives to give k_{obs} values. When using 10 equiv. TEMPOH relative to the Mn^{III}-hydroxo concentration, the electronic absorption signals of $[Mn^{III}(OH)(PaPy_2Q)]^+$ decayed completely over the course of *ca.* 200 seconds (Figure 2.10, top). In contrast, when the same reaction was performed with

$[Mn^{III}(OH)(PaPy_2N)]^+$, the signals associated with the Mn^{III}-hydroxo adduct disappeared within *ca.* 15 seconds (Figure 2.10, center). In each case, the absorption spectra of the product solutions were consistent with the formation of the Mn^{II} starting complexes (Figure 2.10). X-band EPR experiments of the product solutions in perpendicular mode are dominated by signals associated with the TEMPO radical (Figure A1.12 and A1.15). Collectively, these results support a reaction where the Mn^{III}-hydroxo adduct abstracts a hydrogen atom from TEMPOH to yield the corresponding Mn^{II}-aqua species and TEMPO radical.

To more thoroughly compare the rate differences for $[Mn^{III}(OH)(PaPy_2Q)]^+$ and $[Mn^{III}(OH)(PaPy_2N)]^+$, we collected k_{obs} values at different TEMPOH concentrations. For each complex, a plot of k_{obs} versus substrate concentration was linear (Figure 2.10, bottom), and the slope was taken as the second-order rate constant (k_2). Using this procedure, we determined k_2 values of 1.7(1) and 27(3) $M^{-1}s^{-1}$ for TEMPOH oxidation by $[Mn^{III}(OH)(PaPy_2Q)]^+$ and $[Mn^{III}(OH)(PaPy_2N)]^+$, respectively, at -35 °C. Thus, the latter complex shows a 15-fold rate enhancement. Table 2.5 compares these second-order rate constants with those determined for $[Mn^{III}(OH)(dpaq)]^+$ and its derivatives. The rate constant for TEMPOH oxidation for $[Mn^{III}(OH)(PaPy_2N)]^+$ is nearly four-fold faster than that of the previously reported $[Mn^{III}(OH)(dpaq^{5NO2})]^+$ complex (k_2 = 27(3) and 7(1) $M^{-1}s^{-1}$, respectively), which has the fastest TEMPOH oxidation rate of the $[Mn^{III}(OH)(dpaq^R)]^+$ series.[37] The k_2 value observed for $[Mn^{III}(OH)(PaPy_2Q)]^+$ is nearly identical to that reported for the unmodified $[Mn^{III}(OH)(dpaq)]^+$ complex (1.1(1) $M^{-1}s^{-1}$).[36]

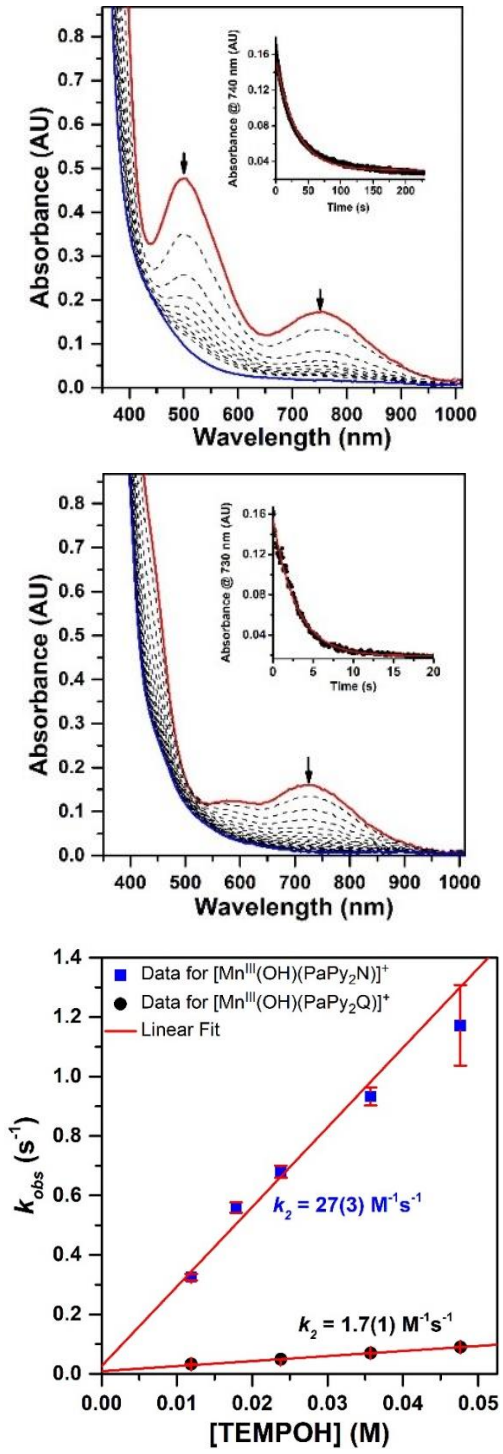

Figure 2.10. Reactions of 1.25 mM $[Mn^{III}(OH)(PaPy_2Q)]^+$ (top) and $[Mn^{III}(OH)(PaPy_2N)]^+$ (center) with 10 equiv. TEMPOH in MeCN at -35 °C. The inset shows the decay of the electronic absorption signal over time (black dots) and a fit (red trace) to a first-order decay. Bottom: Plot of first-order rate constants versus TEMPOH concentration. The error bars represent +/- one standard deviation.

Table 2.5. Second-Order Rate Constants (k_2) and Experimental Activation Parameters for TEMPOH Oxidation by Mn^{III}-hydroxo complexes and DFT-Calculated Thermodynamic Parameters.

	experimental				DFT-calculated		
complex	k_2 ($M^{-1}s^{-1}$)	$\Delta H^{\ddagger a}$	$\Delta S^{\ddagger b}$	$\Delta G^{\ddagger a}$	Mn^{III}/Mn^{II} $E_{1/2}$[c]	Mn^{II}-OH_2 pK_a	BDFE[a]
$[Mn^{III}(OH)(PaPy_2Q)]^+$	1.7(1)	6.1(9)	-40(4)	18(1)	-0.75	29.6	78.3
$[Mn^{III}(OH)(PaPy_2N)]^+$	27(3)	6.0(9)	-35(3)	16(1)	-1.01	38.2	84.0
$[Mn^{III}(OH)(dpaq)]^+$ [d]	1.1(1)	5.3(9)	-43(4)	18(1)	-0.70	29.3	79.1
$[Mn^{III}(OH)(dpaq^{2Me})]^+$ [d]	3.9(3)	5.7(3)	-41(1)	17.9(9)	-0.58	28.7	80.9
$[Mn^{III}(OH)(dpaq^{5NO2})]^+$ [d]	7(1)	5.1(5)	-42(2)	18(1)	-0.51	27.8	81.2

[a] In kcal mol^{-1}. [b] In cal $mol^{-1}K^{-1}$. [c] In V relative to Fc^+/Fc. [d] From ref. [37].

Activation parameters for the reaction of TEMPOH with $[Mn^{III}(OH)(PaPy_2Q)]^+$ and $[Mn^{III}(OH)(PaPy_2N)]^+$ were obtained by collecting k_{obs} values (using 10 equiv. TEMPOH) from -35 to 15 °C for the former complex and -35 to 0 °C for the latter complex (the rate of TEMPOH oxidation by $[Mn^{III}(OH)(PaPy_2N)]^+$ was too fast at 15 °C to obtain reliable kinetic data). These data are shown in Figure 2.11 (top). An Eyring analysis of the variable-temperature rate data yield the free energy of activation ($\Delta G^{\ddagger}$), enthalpy of activation ($\Delta H^{\ddagger}$), and entropy of activation ($\Delta S^{\ddagger}$) values shown in Table 2.5 and summarized in Figure 11 (bottom). Activation parameters for Mn^{III}-hydroxo complexes in similar coordination spheres are included for comparison. For this series, the $\Delta H^{\ddagger}$ values fall within the narrow range of 5.1 – 6.1 kcal mol^{-1}, with the $[Mn^{III}(OH)(PaPy_2Q)]^+$ and $[Mn^{III}(OH)(PaPy_2N)]^+$ complexes being on the higher end of this range. The $\Delta S^{\ddagger}$ values show more variation (-43 to -35 cal mol^{-1} K^{-1}), with $[Mn^{III}(OH)(PaPy_2N)]^+$ having the lowest value. The combination of activation enthalpies and entropies give $\Delta G^{\ddagger}$ values from 16 to 18 kcal mol^{-1}, with the most reactive $[Mn^{III}(OH)(PaPy_2N)]^+$ having the lowest free energy of activation for the series. The small variation of activation enthalpies for the reactivity of this series of Mn^{III}-hydroxo complexes with TEMPOH is quite similar to that observed for DHA oxidation by a set of Mn^{III}-oxo complexes.[63] In that case, the $\Delta H^{\ddagger}$ values varied from 13(1) to 15(1) kcal mol^{-1}.

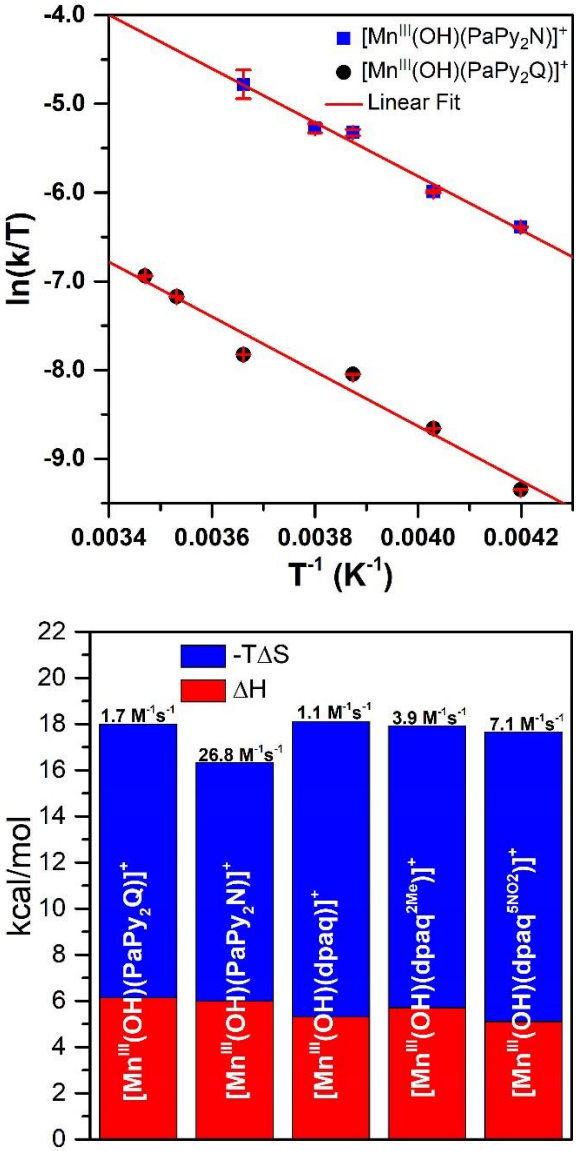

Figure 2.11. Top: Eyring plot of variable-temperature kinetic data for TEMPOH oxidation by $[Mn^{III}(OH)(PaPy_2Q)]^+$ and $[Mn^{III}(OH)(PaPy_2N)]^+$ in MeCN. Bottom: Bar graph showing the activation parameters and second-order rate constants for TEMPOH oxidation by various Mn^{III}-hydroxo complexes.

TEMPOH Oxidation by Mn^{III}-methoxy complexes. Since Mn^{III}-methoxy complexes have been previously shown to be capable of effecting CPET reactions with TEMPOH,[92] we investigated the reactions of $[Mn^{III}(OMe)(PaPy_2Q)]^+$ and $[Mn^{III}(OMe)(PaPy_2N)]^+$ with TEMPOH. When either of these Mn^{III}-methoxy complexes is treated with TEMPOH in MeOH at -35 °C, the

electronic absorption bands associated with the Mn^{III}-methoxy adduct undergo a rapid decay (Figure A1.28). Using an analysis similar to that employed for the Mn^{III}-hydroxo complexes, we determined second-order rate constants for TEMPOH oxidation by $[Mn^{III}(OMe)(PaPy_2Q)]^+$ and $[Mn^{III}(OMe)(PaPy_2N)]^+$ of 0.68(8) and 2.9(1) $M^{-1}s^{-1}$, respectively (Figure A1.28). The four-fold rate enhancement for $[Mn^{III}(OMe)(PaPy_2N)]^+$ relative to $[Mn^{III}(OMe)(PaPy_2Q)]^+$ is far less than the 15-fold enhancement observed for the corresponding Mn^{III}-hydroxo complexes (Table 2.5). One cause of this difference could be that substitution of the methoxy ligand for a hydroxo in the $PaPy_2N$-containing complexes would eliminate any potential intramolecular hydrogen-bonding interaction. An additional difference between the Mn^{III}-methoxy and Mn^{III}-hydroxo reactions with TEMPOH is that MeOH and MeCN were the respective solvents. This change in solvent could influence the reaction rates to some extent. All attempts to measure TEMPOH oxidation rates for $[Mn^{III}(OMe)(PaPy_2N)]^+$ relative to $[Mn^{III}(OMe)(PaPy_2Q)]^+$ in MeCN were complicated by the reaction of the Mn^{III}-methoxy complexes with trace water to give the Mn^{III}-hydroxo species, even when using dried MeCN.

Thermodynamic Analysis of TEMPOH Oxidation Using Experimental and Computational Methods. To address the basis for the rate enhancement of $[Mn^{III}(OH)(PaPy_2N)]^+$ compared to $[Mn^{III}(OH)(PaPy_2Q)]^+$, we turned to a thermodynamic analysis of the CPET reaction. CPET reactions often show a correlation between the thermodynamic driving force and the activation barrier,[101, 102] as shown, for example, in our previous investigation of rate variations in TEMPOH oxidation reactions by the series of $[Mn^{III}(OH)(dpaq^{5R})]^+$ complexes.[37] Before extending this treatment to the reaction of TEMPOH with $[Mn^{III}(OH)(PaPy_2Q)]^+$ and $[Mn^{III}(OH)(PaPy_2N)]^+$, we first discuss the thermodynamic framework for CPET reactions.

For the reaction of a Mn^{III}-hydroxo adduct with TEMPOH, the driving force is given by the difference in O–H BDFEs of the Mn^{II}-aqua product and the TEMPOH reactant (eqn. 1). For a set of reactions of different Mn^{III}-hydroxo adducts with TEMPOH, the variation of the O–H BDFE of the Mn^{II}-aqua complex is the cause for the change in the reaction driving force, as the TEMPO–H BDFE is a constant. In this case, a stronger O–H bond in the Mn^{II}-aqua product is associated with faster reaction rates, with $\ln(k_2)$ linearly correlated with the Mn^{II}-aqua BDFE.[37]

$$\Delta G = \text{BDFE}(Mn^{II}O(H)–H) – \text{BDFE}(\text{TEMPO–H}) \quad (1)$$

In many instances, it is helpful to use a square scheme to deconstruct the O–H BDFE of the Mn^{II}-aqua complex into individual proton- and electron-transfer steps.[103] Scheme 1.1 shows this deconstruction, where the CPET step is along the diagonal and the edges represent proton transfer (vertical) and electron transfer (horizontal). The O–H BDFE is related to the electron- and proton-transfer steps using the modified Bordwell equation (eqn. 2),[85] where pK_a is for the Mn^{II}-aqua product, the potential is for the Mn^{III}-OH/Mn^{II}-OH couple, and $C_{G,sol}$ is a constant for a given solvent and reaction conditions. In our previous investigation of $[Mn^{III}(OH)(dpaq^{5R})]^+$ complexes, we observed that both the reduction potential and pK_a changed as a function of the R substitution, but changes in the potential were the larger and, therefore, dominant contribution to the change in O–H BDFE.[37]

$$\text{BDFE}(Mn^{II}O(H)–H) = 1.37\text{p}K_a + 23.06E° + C_{G,sol} \quad (2)$$

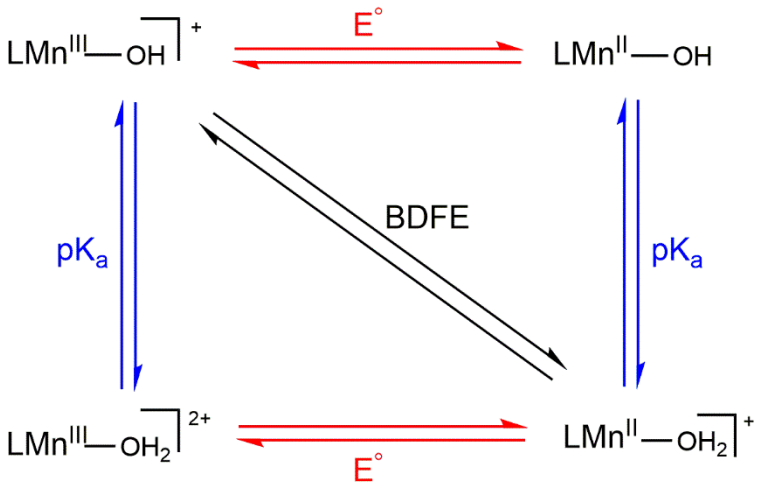

Scheme 1.1. Thermodynamic Square Scheme for Decomposing the O–H BDFE of a Mn^{III}–OH/Mn^{II}–OH_2 Complex.

On the basis of these thermodynamic considerations, the rate enhancement observed for $[Mn^{III}(OH)(PaPy_2N)]^+$ over $[Mn^{III}(OH)(PaPy_2Q)]^+$ and other Mn^{III}-hydroxo complexes very likely arises from differences in the O-H BDFEs of the Mn^{II}-aqua products. In particular, the nitrogen atom from the naphthyridinyl moiety in $[Mn^{II}(OH_2)(PaPy_2N)]^+$ could stabilize the Mn^{II}-aqua product through hydrogen bonding, whereas this type of interaction is unavailable in $[Mn^{II}(OH_2)(PaPy_2Q)]^+$. Consequently, we would expect the $[Mn^{II}(OH_2)(PaPy_2N)]^+$ product to be significantly more basic (higher pK_a) than $[Mn^{II}(OH_2)(PaPy_2Q)]^+$. It is also possible that the significant difference in the observed rate of reaction arises from differences in the $Mn^{III/II}$ reduction potentials. To evaluate these possibilities, we combined CV experiments with DFT computations.

CV experiments for $[Mn^{III}(OH)(PaPy_2Q)]^+$ and $[Mn^{III}(OH)(PaPy_2N)]^+$ in MeCN at 25 °C each reveal irreversible reduction waves with negative peak potentials ($E_{p,c}$ = -0.86 and -1.10 V vs. Fc/Fc^+, respectively) (Figure A1.29). The peak potentials for both $[Mn^{III}(OH)(PaPy_2Q)]^+$ and $[Mn^{III}(OH)(PaPy_2N)]^+$ are more negative than those of $[Mn^{III}(OH)(dpaq)]^+$ and its derivatives ($E_{p,c}$

= -0.73 to -0.54 V).[37, 39] Remarkably, $[Mn^{III}(OH)(PaPy_2N)]^+$ has the lowest peak potential of this series of Mn^{III}-hydroxo complexes, but also shows the fastest rate of reaction for TEMPOH oxidation. Thus, these CV data reveal that $[Mn^{III}(OH)(PaPy_2N)]^+$ reacts rapidly with TEMPOH in spite of its very negative potential.

As we have been unable to obtain experimental insight into either the basicity of the Mn^{III}-hydroxo reactants or the acidity of the Mn^{II}-aqua products, we turned to DFT computations to obtain reasonable approximations for these parameters. We also used computations to calculate the thermodynamic $E_{1/2}$ values for the Mn^{III}-OH/Mn^{II}-OH couples, which differ slightly from the peak potentials observed by CV. The results are collected in Table 2.5, which also includes values for $[Mn^{III}(OH)(dpaq^R)]^+$ complexes.[37]

The calculated $E_{1/2}$ values mirror the trend in the experimental $E_{p,c}$ values, with $[Mn^{III}(OH)(PaPy_2N)]^+$ showing a more negative potential by *ca.* 250 mV (calculated $E_{1/2}$ values for $[Mn^{III}(OH)(PaPy_2Q)]^+$ and $[Mn^{III}(OH)(PaPy_2N)]^+$ are -0.75 and -1.01 V, respectively). Thus, the computations reinforce the conclusion that $[Mn^{III}(OH)(PaPy_2N)]^+$ is a significantly poorer one-electron oxidant than $[Mn^{III}(OH)(PaPy_2Q)]^+$. The p$K_a$ calculations indicate that $[Mn^{II}(OH_2)(PaPy_2N)]^+$ is considerably less acidic than $[Mn^{II}(OH_2)(PaPy_2Q)]^+$ (pK_a = 38.2 and 29.6, respectively). The basis for this large difference comes from the strong hydrogen-bond in the former complex that is lacking in the latter. The DFT structures for the Mn^{II}-aqua complexes (Figure A1.30) reveal a short OH···N(naphthyridinyl) distance of 1.64 Å in $[Mn^{II}(OH_2)(PaPy_2N)]^+$. This interaction causes a distortion in the aqua binding position, giving an N1-Mn-O2 angle of 159°, with the aqua ligand tilted toward the naphthyridinyl group. In contrast, the corresponding angle in $[Mn^{II}(OH_2)(PaPy_2Q)]^+$, which lacks any hydrogen bond with the aqua ligand, is 170°, with the aqua angled slightly away from the quinolinyl moiety.

When combined, the calculated $E_{1/2}$and pK_a values give O-H BDFEs for $[Mn^{II}(OH_2)(PaPy_2Q)]^+$ and $[Mn^{II}(OH_2)(PaPy_2N)]^+$ of 78.3 and 84.0 kcal mol^{-1}, respectively (Table 2.5 and Figure 2.12). The larger BDFE for $[Mn^{II}(OH_2)(PaPy_2N)]^+$ explains the higher reactivity with TEMPOH observed for the corresponding Mn^{III}-hydroxo complex. The stronger bond formed in $[Mn^{II}(OH_2)(PaPy_2N)]^+$ creates a larger driving force for the CPET reaction. The BDFE of $[Mn^{II}(OH_2)(PaPy_2Q)]^+$ is comparable to that of $[Mn^{II}(OH_2)(dpaq)]^+$ (79.1 kcal/mol), which explains their observed similar reaction rates with TEMPOH (1.7(1) and 1.1(1) $M^{-1}s^{-1}$, respectively; see Table 2.5).

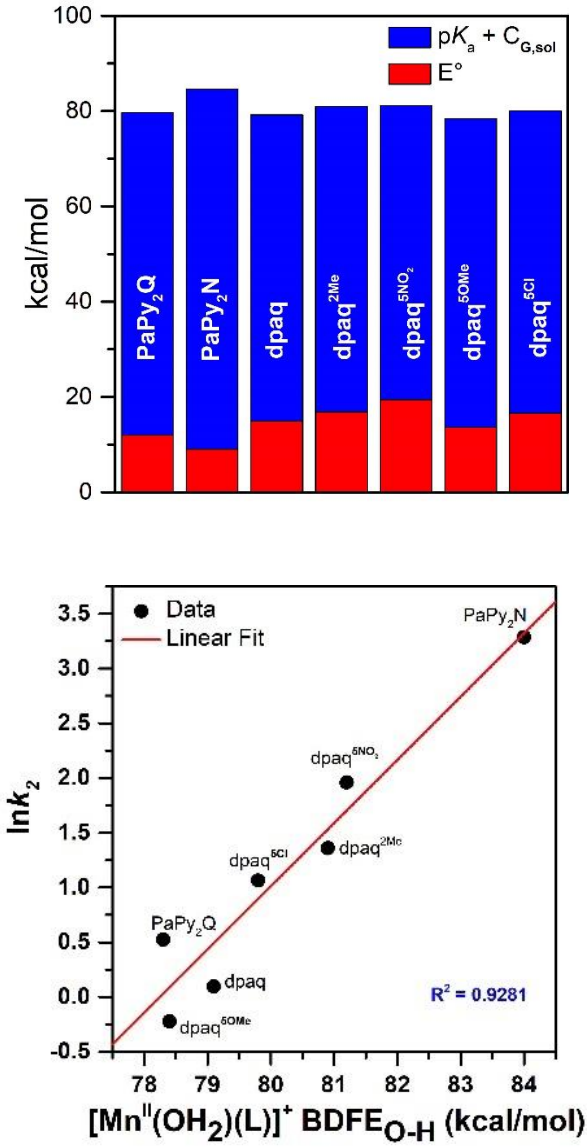

Figure 2.12. Top: Thermodynamic contributions to the O–H BDFE of Mn^{II}-aqua complexes from the Mn^{III}-OH/Mn^{II}-OH reduction potentials and Mn^{II}-aqua pK_a values. Bottom: Comparison of ln(k_2) for TEMPOH oxidation by Mn^{III}-hydroxo complexes as a function of the O–H BDFE of corresponding Mn^{II}-aqua complexes.

When considering the reactivity of a broader series of Mn^{III}-hydroxo complexes with TEMPOH,[37] a plot of the ln(k_2) vs the O–H BDFE of Mn^{II}-aqua complexes shows a linear correlation, albeit with some scatter (Figure 2.12, bottom). These results reinforce the conclusion that higher O–H BDFEs in the Mn^{II}-aqua products lowers the activation barrier and increases

reactivity. The $[Mn^{III}(OH)(PaPy_2N)]^+$ and $[Mn^{III}(OH)(dpaq^{OMe})]^+$ complexes provide the extremes of this series, where the *ca.* 35-fold difference in rate constants is in line with the *ca.* 5 kcal mol^{-1} difference in O–H BDFE. What is remarkable for this series is that the basis for the higher reactivities of $[Mn^{III}(OH)(PaPy_2N)]^+$ and $[Mn^{III}(OH)(dpaq^{NO2})]^+$ are of a different origin. While $[Mn^{III}(OH)(PaPy_2N)]^+$ shows a rapid reaction with TEMPOH on the basis of the basicity of this complex, it is the relatively high reduction potential of $[Mn^{III}(OH)(dpaq^{NO2})]^+$ that causes this species to be a good CPET agent. This difference is illustrated in the bar graph in Figure 2.12 (top), which readily displays the large contribution to the Mn^{II}-aqua BDFE from the pK_a term of $[Mn^{III}(OH)(PaPy_2N)]^+$ and the large contribution to the BDFE from the more positive reduction potential of $[Mn^{III}(OH)(dpaq^{NO2})]^+$.

Variation in CPET Reaction Rates of Mn^{III}-hydroxo Complexes Using Substituted Phenols. We further assessed reactivity differences between $[Mn^{III}(OH)(PaPy_2Q)]^+$ and $[Mn^{III}(OH)(PaPy_2N)]^+$ using 4-X-2,6-di-*tert*-butylphenols (4-X-2,6-DTBP), where X denotes various substituents (X = OMe, Me, ^{t}Bu, H, and Cl). By exploring reactions with these *para*-substituted phenols, we are able to correlate changes in the thermodynamic properties of the substrate with the reactivity of the Mn^{III}-hydroxo unit. In Figure 2.13, we show the decay of $[Mn^{III}(OH)(PaPy_2Q)]^+$ (top) and $[Mn^{III}(OH)(PaPy_2N)]^+$ (center) upon the addition of 10 equiv. 4-^{t}Bu-2,6-DTBP at 50 °C. In each case, we observe the disappearance of the electronic absorption signals associated with the Mn^{III}-hydroxo complexes and the appearance of bands at 380 nm, 400 nm, and 628 nm. These bands are characteristic of the 2,4,6-tri-*tert*-butylphenoxyl radical,[104] which forms as a product of this reaction in *ca.* 60 and 97% yield relative to the Mn^{III}-hydroxo concentration of $[Mn^{III}(OH)(PaPy_2Q)]^+$ and $[Mn^{III}(OH)(PaPy_2N)]^+$, respectively. X-band EPR experiments of the product solutions in perpendicular mode are dominated by signals associated

with the 2,4,6-tri-*tert*-butylphenoxyl radical (Figure A1.12 and A1.15). The electronic absorption and EPR data thus indicate that both $[Mn^{III}(OH)(PaPy_2Q)]^+$ and $[Mn^{III}(OH)(PaPy_2N)]^+$ react with 4-^{t}Bu-2,6-DTBP to form the corresponding phenoxyl radical and Mn^{II} products. Reactions using different concentrations of the 4-^{t}Bu-2,6-DTBP substrate allowed us to determined k_2 values of 5.2(2) and 0.08(1) $M^{-1}s^{-1}$ for $[Mn^{III}(OH)(PaPy_2N)]^+$ and $[Mn^{III}(OH)(PaPy_2Q)]^+$, respectively. Thus, we observe a remarkable 65-fold rate acceleration for the former complex. On the basis of our thermodynamic analysis discussed in the previous section, we infer that this rate increase comes from the enhanced thermodynamic capabilities of $[Mn^{III}(OH)(PaPy_2N)]^+$ in CPET reactions.

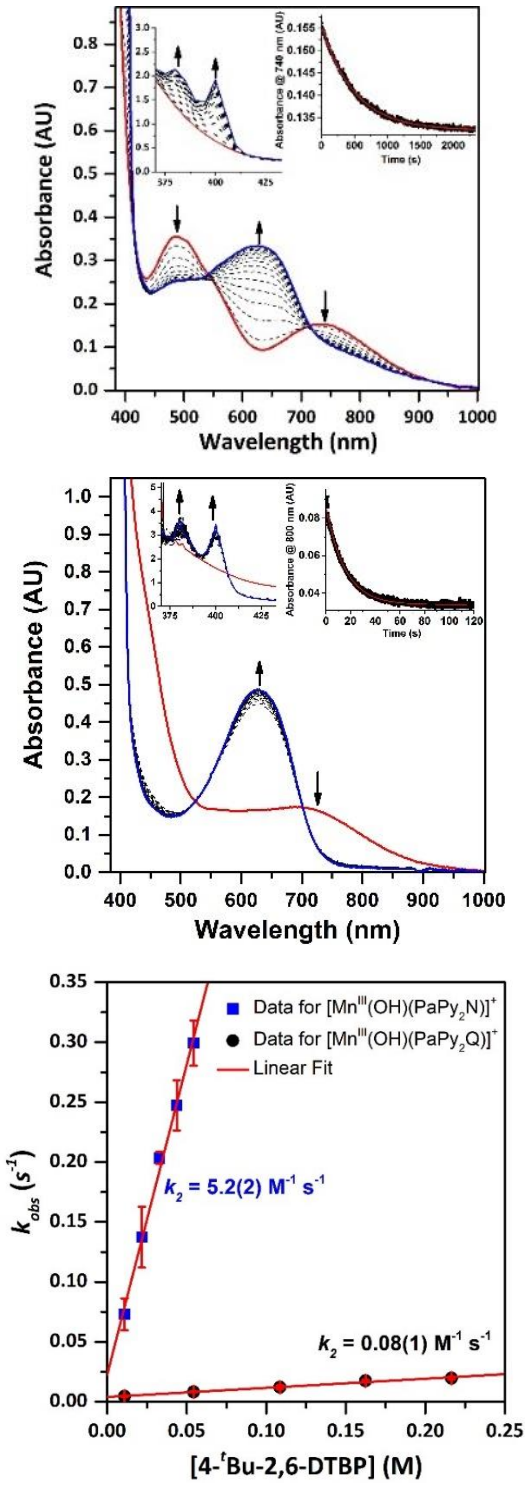

Figure 2.13. Reactions of 1.25 mM $[Mn^{III}(OH)(PaPy_2Q)]^+$ (top) and $[Mn^{III}(OH)(PaPy_2N)]^+$ with 10 equiv. 4-^{t}Bu-2,6-DTBP in MeCN at 50 °C. The inset shows the decay of the electronic absorption signal over time (black dots) and a fit (red trace) to a first-order decay. Bottom: Plot of first-order rate constants versus 4-^{t}Bu-2,6-DTBP concentration. The error bars represent +/- one standard deviation.

We performed similar experiments for the remaining 4-X-2,6-DTBP (X = OMe, Me, H, and Cl), and the data are shown in the Supporting Information (Figure A1.31). Second-order rate constants for each reaction are collected in (Table 2.6). From these data, it is immediately apparent that the k_2 for phenol oxidation by $[Mn^{III}(OH)(PaPy_2N)]^+$ is always significantly larger than that of $[Mn^{III}(OH)(PaPy_2Q)]^+$. The reactions with 4-H-2,6-DTBP provide the extreme example, where a 100-fold rate enhancement is observed. Thus, for this set of phenol substrates, $[Mn^{III}(OH)(PaPy_2N)]^+$ shows rate enhancements of 40- to 100-fold relative to $[Mn^{III}(OH)(PaPy_2Q)]^+$.

Table 2.6. Second-order Rate Constants (k_2) for the Oxidation of 4-X-2,6-DTBP Substrates by $[Mn^{III}(OH)(PaPy_2Q)]^+$ and $[Mn^{III}(OH)(PaPy_2N)]^+$ with DFT-Computed Thermodynamic Parameters for the Phenol Substrates.

substrate	k_2 ($M^{-1}s^{-1}$)		O–H		
	$[Mn^{III}(OH)(PaPy_2Q)]^+$	$[Mn^{III}(OH)(PaPy_2N)]^+$	BDE[a]	pK_a	$E_{1/2}$[b]
4-MeO-2,6-DTBP	2.3(1)	127(2)	77.3	28.1	0.58
4-Me-2,6-DTBP	0.165(4)	8.0(4)	81.6	27.5	0.86
4-^{t}Bu-2,6-DTBP	0.08(1)	5.2(2)	82.3	28.0	0.93
4-Cl-2,6-DTBP	0.0323(1)	2.4(2)	83.5	25.4	1.17
4-H-2,6-DTBP	0.012(1)	0.99(2)	83.9	26.8	1.15

[a] In kcal mol^{-1}. [b] In V relative to Fc^+/Fc.

When the rates of 4-X-2,6-DTBP oxidation by $[Mn^{III}(OH)(PaPy_2Q)]^+$ and $[Mn^{III}(OH)(PaPy_2N)]^+$ are considered with respect to the phenol BDE, we observe a uniform decrease in the reaction rate with increasing BDE of the phenol O–H bond (Table 2.6). (In this analysis, we have used DFT-calculated O–H bond dissociation enthalpies, as experimental values in MeCN are not known for all the phenols considered.) A plot of ln(k_2) for phenol oxidation by both $[Mn^{III}(OH)(PaPy_2Q)]^+$ and $[Mn^{III}(OH)(PaPy_2N)]^+$ shows a linear correlation with the calculated phenol O–H bond strength (Figure 2.14). This behavior supports a common reaction

mechanism for all phenols. The unitless slope, α, for these correlations (which was obtained by correcting the slope in the ln(k_2) versus BDE plot for thermal energy in kcal mol^{-1}; see the caption of Figure 2.14) is *ca*. -0.5, which is common for such linear-free energy correlations.

Plots of ln(k_2) versus the calculated reduction potentials ($E_{1/2}$) of the phenols are also quite linear, showing faster reaction rates for phenols with more negative potentials (Figure A1.32, top left). In the comparison of rate versus potential, we can determine a unitless slope of *ca*. -0.2 from plots of (RT/F)ln(k_2) versus $E_{1/2}$ (Figure A1.32, top right). This small slope indicates that the reaction rates are far less sensitive to the potential of the substrate than the O–H BDE. Tolman, Mayer, and co-workers observed similarly small slopes when investigating phenol oxidation by a pair of Cu^{III}-hydroxo complexes.[11] An analysis of the reaction rates, as ln(k_2) versus the phenol pK_a shows more significant scatter (Figure A1.32, bottom), although there is a general trend that more acidic phenols (*i.e.*, 4-Cl-2,6-DTBP) show slower reaction rates. This trend tends to rule out mechanisms involving rate-limiting proton transfer, as then we would expect faster reaction rates with more acidic phenols. We therefore conclude that both $[Mn^{III}(OH)(PaPy_2Q)]^+$ and $[Mn^{III}(OH)(PaPy_2N)]^+$ perform phenol oxidation by a CPET mechanism, with rates determined by the BDE of the substrate O–H bond.

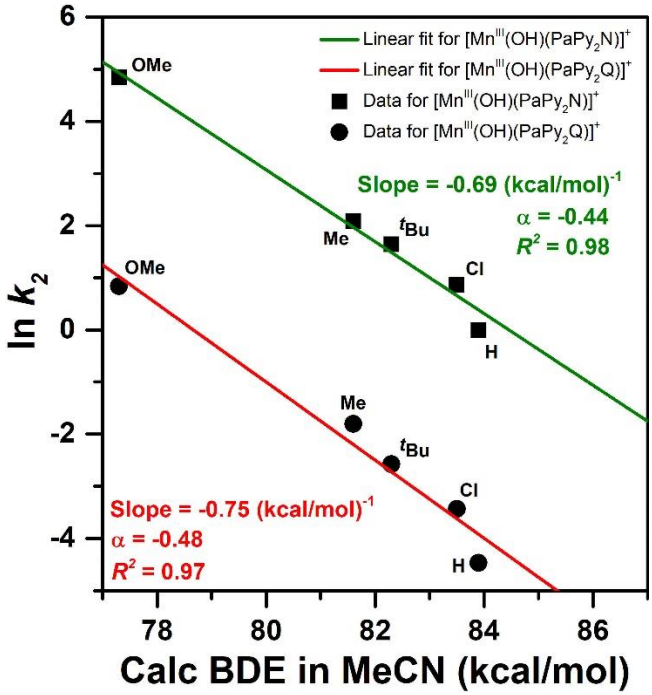

Figure 2.14. Plot of ln(k_2) for the oxidation of 4-X-2,6-DTBP by $[Mn^{III}(OH)(PaPy_2Q)]^+$ and $[Mn^{III}(OH)(PaPy_2N)]^+$ versus the DFT-calculated O–H BDE of the phenol substrate. The □ parameter is related to the slope by the equation □ = slope·RT, where R is the gas constant and T is the reaction temperature of 50°C.

2.4 Conclusions

The extended coordination environments of metal catalysts play a significant role in modulating reactivity. In metalloenzymes, this extended coordination environment is created by second- and third-sphere amino acid residues that can influence reactivity in several ways;[41] *i.e.*, creating substrate-binding pockets, promoting coordination of exogenous ligands, or forming hydrogen bonds with first-coordination sphere amino acid residues. A prominent feature of the active sites of the MnSOD and MnLOX enzymes in the Mn^{III} state is a hydrogen bond between a coordinated hydroxo ligand and a *cis* carboxylate ligand (Figure 2.1).

In this present study, we have examined a pair of Mn^{III}-hydroxo complexes that differ only in one functional group of the supporting ligand. One of these complexes, $[Mn^{III}(OH)(PaPy_2N)]^+$,

contains a naphthyridinyl moiety capable of forming an intramolecular hydrogen bond with the hydroxo ligand. The second complex, $[Mn^{III}(OH)(PaPy_2Q)]^+$ contains a quinolinyl moiety that does not permit any intramolecular hydrogen bonding. Using a variety of spectroscopic and computational methods, we propose that the $[Mn^{III}(OH)(PaPy_2N)]^+$ complex has the same coordination geometry and ligand-binding configuration as $[Mn^{III}(OH)(PaPy_2Q)]^+$, but that the latter complex contains an intramolecular hydrogen bond. In particular, the strong similarities of the ^1H NMR spectra of $[Mn^{III}(OH)(PaPy_2Q)]^+$ and $[Mn^{III}(OH)(PaPy_2N)]^+$ support a common ligand-binding configuration (Figure 2.8). In addition, computational studies of a model of $[Mn^{III}(OH)(PaPy_2N)]^+$ containing an intramolecular hydrogen bond nicely reproduce the experimental electronic absorption spectrum of this complex and reproduce spectral shifts relative to $[Mn^{III}(OH)(PaPy_2Q)]^+$ (Figure 2.9).

Despite their very similar structures, the $[Mn^{III}(OH)(PaPy_2N)]^+$ reacts with substrates with activated O–H bonds far more rapidly than $[Mn^{III}(OH)(PaPy_2Q)]^+$ (Figures 2.10 and 2.13). Using various substrates, we observe rate enhancements for $[Mn^{III}(OH)(PaPy_2N)]^+$ over $[Mn^{III}(OH)(PaPy_2Q)]^+$ of between 15- and 100-fold. A detailed analysis of the thermodynamic contributions to CPET reactions of $[Mn^{III}(OH)(PaPy_2Q)]^+$ and $[Mn^{III}(OH)(PaPy_2N)]^+$ reveals that the latter complex is significantly more basic. This increased basicity more than counteracts the more negative reduction potential of this complex, leading to a stronger O–H BDFE in the $[Mn^{II}(OH_2)(PaPy_2N)]^+$ product. Thus, the differences in reactivity between $[Mn^{III}(OH)(PaPy_2Q)]^+$ and $[Mn^{III}(OH)(PaPy_2N)]^+$ can be understand on the basis of thermodynamic considerations, which are strongly influenced by the ability of the latter complex to form an intramolecular hydrogen bond. Accordingly, this work suggests that the hydrogen-bond inferred in the active-site structures of MnSOD and MnLOX likely serves a functional role by increasing the basicity of the

hydroxo ligand. In the case of MnLOX, this increased basicity would activate the Mn^{III}-hydroxo unit towards CPET reactions involving the biological substrate.

2.5 Acknowledgments

This work was supported by the U.S. National Science Foundation (CHE-1900384 to T.A.J). Support for the NMR instrumentation was provided by NIH Shared Instrumentation Grant # S10OD016360. The U.S. NSF is also acknowledged for funds used for the purchase of X-ray instruments (CHE-0079282) and the EPR spectrometer (CHE-0946883).

2.6 References

1. V. A. Larson, B. Battistella, K. Ray, N. Lehnert and W. Nam, *Nature Reviews Chemistry*, 2020, **4**, 404-419.
2. D. B. Rice, A. A. Massie and T. A. Jackson, *Accounts of Chemical Research*, 2017, **50**, 2706-2717.
3. K. Ray, F. F. Pfaff, B. Wang and W. Nam, *J. Am. Chem. Soc.*, 2014, **136**, 13942-13958.
4. M. Puri and L. Que, Jr., *Acc. Chem. Res.*, 2015, **48**, 2443-2452.
5. M. Guo, T. Corona, K. Ray and W. Nam, *ACS Central Science*, 2019, **5**, 13-28.
6. A. S. Borovik, *Chemical Society Reviews*, 2011, **40**, 1870-1874.
7. R. A. Baglia, J. P. T. Zaragoza and D. P. Goldberg, *Chemical Reviews*, 2017, **117**, 13320-13352.
8. M. Mandal, C. E. Elwell, C. J. Bouchey, T. J. Zerk, W. B. Tolman and C. J. Cramer, *Journal of the American Chemical Society*, 2019, **141**, 17236-17244.
9. P. Paolo and M. A. R., *European Journal of Inorganic Chemistry*, 2018, **2018**, 547-560.
10. H. Gao and J. T. Groves, *Journal of the American Chemical Society*, 2017, **139**, 3938-3941.
11. D. Dhar, G. M. Yee, T. F. Markle, J. M. Mayer and W. B. Tolman, *Chemical Science*, 2017, **8**, 1075-1085.
12. W.-M. Ching, A. Zhou, J. E. M. N. Klein, R. Fan, G. Knizia, C. J. Cramer, Y. Guo and L. Que, *Inorganic Chemistry*, 2017, **56**, 11129-11140.
13. D. Dhar, G. M. Yee, A. D. Spaeth, D. W. Boyce, H. Zhang, B. Dereli, C. J. Cramer and W. B. Tolman, *Journal of the American Chemical Society*, 2016, **138**, 356-368.
14. J. A. Kovacs, *Accounts of Chemical Research*, 2015, **48**, 2744-2753.
15. J. P. T. Zaragoza, M. A. Siegler and D. P. Goldberg, *Journal of the American Chemical Society*, 2018, **140**, 4380-4390.
16. J. R. Mayfield, E. N. Grotemeyer and T. A. Jackson, *Chemical Communications*, 2020, **56**, 9238-9255.
17. J. Donghyun, Y. J. J., N. Hyeonju, H. Britt, H. K. O., S. E. I. and C. Jaeheung, *Angewandte Chemie International Edition*, 2018, **57**, 7764-7768.

18. A. K. Holley, V. Bakthavatchalu, J. M. Velez-Roman and D. K. St Clair, *International journal of molecular sciences*, 2011, **12**, 7114-7162.
19. W. Zhu and N. G. J. Richards, *Essays In Biochemistry*, 2017, **61**, 259-270.
20. Y. Sheng, I. A. Abreu, D. E. Cabelli, M. J. Maroney, A.-F. Miller, M. Teixeira and J. S. Valentine, *Chemical Reviews*, 2014, **114**, 3854-3918.
21. Y. Chen, A. Wennman, S. Karkehabadi, Å. Engström and E. H. Oliw, *Journal of Lipid Research*, 2016, **57**, 1574-1588.
22. R. A. Edwards, H. M. Baker, M. M. Whittaker, J. W. Whittaker, G. B. Jameson and E. N. Baker, *Journal of Biological Inorganic Chemistry*, 1998, **3**, 161-171.
23. A. Wennman, E. H. Oliw, S. Karkehabadi and Y. Chen, *Journal of Biological Chemistry*, 2016, **291**, 8130-8139.
24. A.-F. Miller, F. Padmakumar, D. Sorkin, A. Karapetian and C. K. Vance, *J. Inorg. Biochem.*, 2003, **93**, 71-83.
25. A.-F. Miller, *Curr. Opin. Chem. Biol.*, 2004, **8**, 162-168.
26. C. Su, M. Sahlin and E. H. Oliw, *Journal of Biological Chemistry*, 2000, **275**, 18830-18835.
27. A. Wennman, S. Karkehabadi and E. H. Oliw, *Archives of Biochemistry and Biophysics*, 2014, **555–556**, 9-15.
28. T. A. Jackson, C. T. Gutman, J. Maliekal, A.-F. Miller and T. C. Brunold, *Inorganic Chemistry*, 2013, **52**, 3356-3367.
29. C. K. Vance and A. F. Miller, *Biochemistry*, 2001, **40**, 13079-13087.
30. T. A. Jackson and T. C. Brunold, *Acc. Chem. Res.*, 2004, **37**, 461-470.
31. J. Azadmanesh, W. E. Lutz, L. Coates, K. L. Weiss and G. E. O. Borgstahl, *Nature Communications*, 2021, **12**, 2079.
32. A. Wennman, E. H. Oliw, S. Karkehabadi and Y. Chen, *Journal of Biological Chemistry*, 2016, **291**, 8130-8139.
33. R. Edwards, H. Baker, M. Whittaker, J. W. Whittaker, G. Jameson and E. Baker, *JBIC Journal of Biological Inorganic Chemistry*, 1998, **3**, 161-171.
34. T. A. Jackson, J. Xie, E. Yikilmaz, A.-F. Miller and T. C. Brunold, *J. Am. Chem. Soc.*, 2002, **124**, 10833-10845.
35. W.-G. Han, T. Lovell and L. Noodleman, *Inorganic Chemistry*, 2002, **41**, 205-218.
36. D. B. Rice, S. D. Jones, J. T. Douglas and T. A. Jackson, *Inorganic Chemistry*, 2018, **57**, 7825-7837.
37. D. B. Rice, A. Munasinghe, E. N. Grotemeyer, A. D. Burr, V. W. Day and T. A. Jackson, *Inorganic Chemistry*, 2019, **58**, 622-636.
38. D. B. Rice, G. B. Wijeratne, A. D. Burr, J. D. Parham, V. W. Day and T. A. Jackson, *Inorganic Chemistry*, 2016, **55**, 8110-8120.
39. G. B. Wijeratne, B. Corzine, V. W. Day and T. A. Jackson, *Inorganic Chemistry*, 2014, **53**, 7622-7634.
40. A. A. Eroy-Reveles, Y. Leung, C. M. Beavers, M. M. Olmstead and P. K. Mascharak, *Journal of the American Chemical Society*, 2008, **130**, 4447-4458.
41. S. A. Cook, E. A. Hill and A. S. Borovik, *Biochemistry*, 2015, **54**, 4167-4180.
42. A. S. Borovik, *Accounts of Chemical Research*, 2004, **38**, 54-61.
43. C. E. MacBeth, A. P. Golombek, V. G. Young, C. Yang, K. Kuczera, M. P. Hendrich and A. S. Borovik, *Science*, 2000, **289**, 938-941.

44. Z. Shirin, B. S. Hammes, V. G. Young and A. S. Borovik, *Journal of the American Chemical Society*, 2000, **122**, 1836-1837.
45. T. H. Parsell, M.-Y. Yang and A. S. Borovik, *Journal of the American Chemical Society*, 2009, **131**, 2762-2763.
46. T. H. Parsell, R. K. Behan, M. T. Green, M. P. Hendrich and A. S. Borovik, *J. Am. Chem. Soc.*, 2006, **128**, 8728-8729.
47. R. Gupta, T. Taguchi, B. Lassalle-Kaiser, E. L. Bominaar, J. Yano, M. P. Hendrich and A. S. Borovik, *Proceedings of the National Academy of Sciences*, 2015, **112**, 5319-5324.
48. R. L. Shook and A. S. Borovik, *Inorganic Chemistry*, 2010, **49**, 3646-3660.
49. R. L. Shook, S. M. Peterson, J. Greaves, C. Moore, A. L. Rheingold and A. S. Borovik, *Journal of the American Chemical Society*, 2011, **133**, 5810-5817.
50. E. M. Matson, J. A. Bertke and A. R. Fout, *Inorganic Chemistry*, 2014, **53**, 4450-4458.
51. Z. Gordon, T. J. Miller, C. A. Leahy, E. M. Matson, M. Burgess, M. J. Drummond, C. V. Popescu, C. M. Smith, R. L. Lord, J. Rodríguez-López and A. R. Fout, *Inorganic Chemistry*, 2019, **58**, 15801-15811.
52. Y. J. Park, E. M. Matson, M. J. Nilges and A. R. Fout, *Chemical Communications*, 2015, **51**, 5310-5313.
53. C. L. Ford, Y. J. Park, E. M. Matson, Z. Gordon and A. R. Fout, *Science*, 2016, **354**, 741-743.
54. J. R. Wilson, M. Zeller and N. K. Szymczak, *Chemical Communications*, 2021, **57**, 753-756.
55. J. P. Shanahan, D. M. Mullis, M. Zeller and N. K. Szymczak, *Journal of the American Chemical Society*, 2020, **142**, 8809-8817.
56. E. W. Dahl, J. J. Kiernicki, M. Zeller and N. K. Szymczak, *Journal of the American Chemical Society*, 2018, **140**, 10075-10079.
57. E. W. Dahl, H. T. Dong and N. K. Szymczak, *Chemical Communications*, 2018, **54**, 892-895.
58. E. W. Dahl and N. K. Szymczak, *Angewandte Chemie International Edition*, 2016, **55**, 3101-3105.
59. C. M. Moore and N. K. Szymczak, *Chemical Science*, 2015, **6**, 3373-3377.
60. C. M. Moore and N. K. Szymczak, *Chemical Communications*, 2015, **51**, 5490-5492.
61. C. M. Moore, D. A. Quist, J. W. Kampf and N. K. Szymczak, *Inorganic Chemistry*, 2014, **53**, 3278-3280.
62. M. A. Ehudin, D. A. Quist and K. D. Karlin, *Journal of the American Chemical Society*, 2019, **141**, 12558-12569.
63. S. K. Barman, J. R. Jones, C. Sun, E. A. Hill, J. W. Ziller and A. S. Borovik, *Journal of the American Chemical Society*, 2019, **141**, 11142-11150.
64. H. Saltzman and J. G. Sharefkin, *Org. Synth.*, 1963, **43**.
65. W. L. F. Armarego and D. D. Perrin, *Purification of Laboratory Chemicals*, Butterworth-Heinemann: Oxford, U.K, 1997.
66. E. A. Mader, E. R. Davidson and J. M. Mayer, *Journal of the American Chemical Society*, 2007, **129**, 5153-5166.
67. M. Sarkar, P. Pandey and J. K. Bera, *Inorganica Chimica Acta*, 2019, **486**, 518-528.
68. .
69. .
70. .

71. F. Neese, F. Wennmohs, U. Becker and C. Riplinger, *The Journal of Chemical Physics*, 2020, **152**, 224108.
72. C. Lee, W. Yang and R. G. Parr, *Physical Review B*, 1988, **37**, 785-789.
73. A. D. Becke, *The Journal of Chemical Physics*, 1993, **98**, 5648-5652.
74. F. Weigend and R. Ahlrichs, *Physical Chemistry Chemical Physics*, 2005, **7**, 3297-3305.
75. F. Weigend, *Physical Chemistry Chemical Physics*, 2006, **8**, 1057-1065.
76. S. Grimme, S. Ehrlich and L. Goerigk, *Journal of Computational Chemistry*, 2011, **32**, 1456-1465.
77. S. Grimme, J. Antony, S. Ehrlich and H. Krieg, *The Journal of Chemical Physics*, 2010, **132**, 154104.
78. S. Grimme, *Journal of Computational Chemistry*, 2006, **27**, 1787-1799.
79. S. Grimme, *Journal of Computational Chemistry*, 2004, **25**, 1463-1473.
80. A. V. Marenich, C. J. Cramer and D. G. Truhlar, *The Journal of Physical Chemistry B*, 2009, **113**, 6378-6396.
81. R. Izsák and F. Neese, *The Journal of Chemical Physics*, 2011, **135**, 144105.
82. T. Petrenko, S. Kossmann and F. Neese, *The Journal of Chemical Physics*, 2011, **134**, 054116.
83. B. H. Solis and S. Hammes-Schiffer, *Inorganic Chemistry*, 2014, **53**, 6427-6443.
84. M. Sankaralingam, Y.-M. Lee, D. G. Karmalkar, W. Nam and S. Fukuzumi, *Journal of the American Chemical Society*, 2018, **140**, 12695-12699.
85. F. G. Bordwell, J. Cheng, G. Z. Ji, A. V. Satish and X. Zhang, *Journal of the American Chemical Society*, 1991, **113**, 9790-9795.
86. A. A. Massie, A. Sinha, J. D. Parham, E. Nordlander and T. A. Jackson, *Inorganic Chemistry*, 2018, **57**, 8253-8263.
87. J. E. M. N. Klein, B. Dereli, L. Que and C. J. Cramer, *Chemical Communications*, 2016, **52**, 10509-10512.
88. E. Papajak and D. G. Truhlar, *The Journal of Chemical Physics*, 2012, **137**, 064110.
89. J. Zheng, P. Seal and D. G. Truhlar, *Chemical Science*, 2013, **4**, 200-212.
90. J. J. Warren, T. A. Tronic and J. M. Mayer, *Chemical Reviews*, 2010, **110**, 6961-7001.
91. J. Y. Lee, R. L. Peterson, K. Ohkubo, I. Garcia-Bosch, R. A. Himes, J. Woertink, C. D. Moore, E. I. Solomon, S. Fukuzumi and K. D. Karlin, *Journal of the American Chemical Society*, 2014, **136**, 9925-9937.
92. G. B. Wijeratne, V. W. Day and T. A. Jackson, *Dalton Transactions*, 2015, **44**, 3295-3306.
93. J. A. Bonadies, M. J. Maroney and V. L. Pecoraro, *Inorganic Chemistry*, 1989, **28**, 2044-2051.
94. Y. Ciringh, S. W. Gordon-Wylie, R. E. Norman, G. R. Clark, S. T. Weintraub and C. P. Horwitz, *Inorganic Chemistry*, 1997, **36**, 4968-4982.
95. T. A. Jackson, A. Karapetian, A.-F. Miller and T. C. Brunold, *Biochemistry*, 2005, **44**, 1504-1520.
96. T. A. Jackson, A. Karapetian, A.-F. Miller and T. C. Brunold, *J. Am. Chem. Soc.*, 2004, **126**, 12477-12491.
97. R. A. Geiger, S. Chattopadhyay, V. W. Day and T. A. Jackson, *Journal of the American Chemical Society*, 2010, **132**, 2821-2831.
98. H. E. Colmer, A. W. Howcroft and T. A. Jackson, *Inorganic Chemistry*, 2016, **55**, 2055-2069.

99. H. E. Colmer, R. A. Geiger, D. F. Leto, G. B. Wijeratne, V. W. Day and T. A. Jackson, *Dalton Transactions*, 2014, **43**, 17949-17963.
100. M. K. Coggins, L. M. Brines and J. A. Kovacs, *Inorganic Chemistry*, 2013, **52**, 12383-12393.
101. J. M. Mayer, *Acc. Chem. Res.*, 2011, **44**, 36-46.
102. J. W. Darcy, B. Koronkiewicz, G. A. Parada and J. M. Mayer, *Accounts of Chemical Research*, 2018, **51**, 2391-2399.
103. R. Tyburski, T. Liu, S. D. Glover and L. Hammarström, *Journal of the American Chemical Society*, 2021, **143**, 560-576.
104. V. W. Manner, T. F. Markle, J. H. Freudenthal, J. P. Roth and J. M. Mayer, *Chemical Communications*, 2008, DOI: 10.1039/B712872J, 256-258.

Chapter 3

Characterization and Chemical Reactivity of Room-Temperature-Stable Mn^{III}-alkylperoxo Complexes

This chapter has been submitted to *Chem. Sci.* and is undergoing revisions.

3.1 Introduction

Metal-alkylperoxo adducts are essential species in industrial and biological oxidation reactions.[1-3] For example, Co^{III}-alkylperoxo adducts are proposed as intermediates in the industrial oxidation of cyclohexane to adipic acid.[1, 4-7] In the oxidation mechanism, homolytic cleavage of the O–O bond of a Co^{III}-cyclohexylperoxo species leads to the production of cyclohexanol and cyclohexanone.[4, 8] Further radical-induced oxidation of cyclohexanone by C–C bond cleavage yields adipic acid.[4] In biological systems, metal-alkylperoxo adducts are common intermediates in a variety of oxygenase enzymes, where they can be directly involved in substrate oxidation or precede the formation of high-valent metal-oxo species.[9, 10] Given the importance of metal-alkylperoxo species in such reactions, there are now many examples of synthetic Fe-,[11, 12] Co-,[1, 4, 5] and Cu-alkylperoxo[3, 13, 14] adducts, and these complexes are capable of oxidizing substrates such as 1,4-cyclohexadiene, 2-phenylpropionaldehyde, and triphenylphosphine.

While such studies of synthetic model complexes have probed the properties and reactivity of many types of metal-alkylperoxo complexes, examples of Mn-alkylperoxo adducts are more limited, and there remain many open questions concerning the factors governing the decay and reactivity of these complexes. Kovacs and co-workers have performed pioneering investigations of Mn^{III}-alkylperoxo adducts, including structural characterization of a family of complexes by X-ray crystallography.[15, 16] These studies employed pentadentate, thiolate-containing N_4S^- ligands, which in the corresponding $[Mn^{III}(OOR)(N_4S)]^+$ complexes placed the thiolate donor *cis* to the alkylperoxo ligand, with bulky quinolinyl or 6-methylpyridyl substituents *trans* to each other and *cis* to the alkylperoxo moiety (Figure 3.1, left).[15, 16] The crystallographically observed Mn–N distances for the quinolinyl and 6-methylpyridyl donors range from 2.35 to 2.52 Å, which are quite long for Mn^{III}–N interactions. Interestingly, these long Mn–N distances are correlated with the

alkylperoxo O–O bond lengths, which vary from 1.43 to 1.47 Å.[16] As shorter Mn–N distances gave longer O–O bonds, it was proposed that less Lewis acidic Mn^{III} centers yielded more activated Mn^{III}-alkylperoxo adducts. By using variable-temperature kinetic studies, the O-O bond lengths for these Mn^{III}-alkylperoxo complexes were in turn related to their thermal decay rates. Mn^{III}-alkylperoxo adducts with longer O–O bonds decayed more rapidly, with lower $\Delta H^{\ddagger}$ values and $\Delta S^{\ddagger}$ values that were more negative.[16] Because of the correlation between the Mn–N distances and the O–O bond lengths, these results suggest that activation of Mn^{III}-alkylperoxo complexes can be controlled by the donor strength of groups *cis* to the alkylperoxo unit. Thermal decomposition studies and analysis of the decay products of the Mn^{III}-cumylperoxo adduct supported a decay by homolytic cleavage of the alkylperoxo O–O bond.[16]

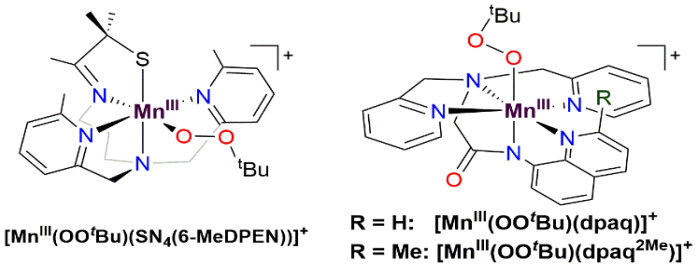

Figure 3.1. Schematic structures of $[Mn^{III}(OO^tBu)(SN_4(6\text{-MeDPEN}))]^+$ (left) and $[Mn^{III}(OO^tBu)(dpaq^R)]^+$ (right). The $[Mn^{III}(OO^tBu)(SN_4(6\text{-MeDPEN}))]^+$ complex is a representative example of a Mn^{III}-alkylperoxo adduct supported by an N_4S^- ligand.

While these studies provide structure-reactivity correlations with regards to the thermal decay pathway, the Mn^{III}-alkylperoxo adducts of the N_4S^- ligands failed to show any direct reaction towards a range of substrates.[16] Product analysis of the reaction solutions provided evidence of the oxidation of a variety of substrate (i.e., PEt_3, TEMPOH, and cyclohexane carboxaldehyde) following decay of the Mn^{III}-alkylperoxo adducts, implying that a product of the decay pathway is

a capable oxidant. In contrast, Mn^{III}-hydroperoxo complexes supported by neutral, macrocyclic N_4 ligands are known to react directly with aldehydes, sulfides, and hydrocarbons possessing weak C–H bonds.[17, 18] Given that metal-alkylperoxo adducts are often taken as analogues of metal-hydroxoperoxo species,[17-24] the stark difference in reactivity between Mn^{III}-alkylperoxo and Mn^{III}-hydroperoxo adducts in substrate oxidation reactions is striking. The disparate reactivities of these complexes might reflect the differences in the properties of the supporting ligands employed (N_4S^- for Mn^{III}-alkylperoxo versus neutral N_4 for Mn^{III}-hydroperoxo). There is a clear need to understand better the role of non-thiolate-containing supporting ligands in influencing the properties and reactivity of Mn^{III}-alkylperoxo complexes.

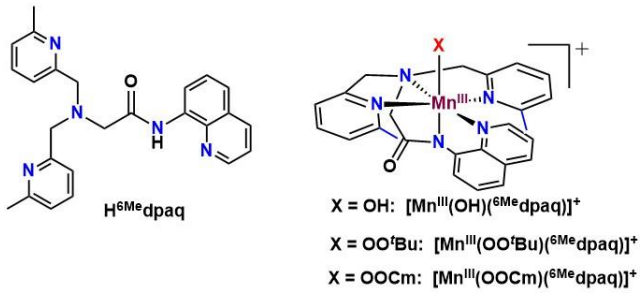

Figure 3.2. H^{6Me}dpaq ligand (left), and $[Mn^{III}(OH)(^{6Me}dpaq)]^+$, $[Mn^{III}(OO^tBu)(^{6Me}dpaq)]^+$, and $[Mn^{III}(OOCm)(^{6Me}dpaq)]^+$ complexes (right). The 6-Me-pyridyl substituents have been highlighted in blue in the structure of the metal complexes.

We previously generated a pair of Mn^{III}-alkylperoxo complexes with ligands lacking thiolate ligation.[25] These Mn^{III}-alkylperoxo complexes were supported by the pentadentate dpaq and $dpaq^{2Me}$ ligands, both of which feature strongly donating amide groups trans to the alkylperoxo moiety (Fig. 3.1, right; dpaq = 2-[bis(pyridin-2-ylmethyl)]amino-N-quinolin-8-yl-acetamidate, $dpaq^{2Me}$ = 2-[bis(pyridin-2-ylmethyl)]amino-N-2-methyl-quinolin-8-yl-acetamidate).[25] Both $[Mn^{III}(OO^tBu)(dpaq)]^+$ and $[Mn^{III}(OO^tBu)(dpaq^{2Me})]^+$ were unstable ($t_{1/2}$ = 3200 and 3600 s,

respectively, for 2 mM solution in CH_3CN at -15 °C) but were characterized by electronic absorption, Mn K-edge X-ray absorption, and FT-IR spectroscopies.[25] The observation of tBuOO• in EPR spectra of the complexes following their thermal decay provided support for a decay pathway involving Mn–O bond homolysis.[25] While these data suggest differences in decay pathways for the thiolate- versus non-thiolate-ligand complexes, the large excess of ^{t}BuOOH (*ca.* 100 equiv.) required to form the $[Mn^{III}(OO^tBu)(dpaq)]^+$ and $[Mn^{III}(OO^tBu)(dpaq^{2Me})]^+$ complexes made a complete analysis of their reactivity and decay pathways unfeasible. The large excess of ^{t}BuOOH also complicated any investigations of substrate oxidation.

Given the limitations of the Mn^{III}-alkylperoxo complexes of the dpaq and $dpaq^{2Me}$ ligands, we sought to develop a derivative of the dpaq ligand that would better stabilize the Mn^{III}-alkylperoxo adduct. Herein, we report Mn^{III}-alkylperoxo adducts supported by ^{6Me}dpaq (Figure 3.2). This new ligand incorporates steric bulk at the 6 position of the pyridyl substituents in the equatorial plane. This choice was inspired by the higher stability of the Mn^{III}-alkylperoxo complexes supported by N_4S^- ligands with two bulky N-donor ligands *cis* to the alkylperoxo ligand (Figure 3.1, left). X-ray crystallographic characterization of the Mn^{III}-hydroxo adduct $[Mn^{III}(OH)(^{6Me}dpaq)](OTf)$ reveals that the 6-methylpyridyl groups cause elongations in the Mn–N distance of 0.11 Å relative to $[Mn^{III}(OH)(dpaq)](OTf)$.[26] The $[Mn^{III}(OH)(^{6Me}dpaq)](OTf)$ complex reacts with stoichiometric amounts of ^{t}BuOOH and CmOOH in CH_3CN to generate the $[Mn^{III}(OO^tBu)(^{6Me}dpaq)]^+$ and $[Mn^{III}(OOCm)(^{6Me}dpaq)]^+$ complexes. These Mn^{III}-alkylperoxo complexes are stable in solution at room temperature with half-lives of *ca.* 5 and 8 days, respectively. Structural characterization for $[Mn^{III}(OOCm)(^{6Me}dpaq)]^+$ was obtained by X-ray crystallography. Despite their relatively high thermal stabilities, kinetic studies of $[Mn^{III}(OO^tBu)(^{6Me}dpaq)]^+$ and $[Mn^{III}(OOCm)(^{6Me}dpaq)]^+$ provide evidence for the direct reaction of these Mn^{III}-alkylperoxo adducts with phosphines. These

results show that the ligand sphere of Mn^{III}-alkylperoxo adducts is critically important in governing their reactivity in substrate oxidation reactions.

3.2 Experimental Details and Methods.

General Methods:

All chemicals were used as obtained from commercial sources unless noted otherwise. Acetonitrile, diethyl diethyl ether, and methanol were dried and degassed using a PureSolv Micro solvent purification system. 1,4-Benzoquine was purified by sublimation. Bis((6-methylpyridin-2-yl)methyl)amine was synthesized according to a reported procedure.[27] The concentration of *tert*-butyl hydroperoxide (^{t}BuOOH) in decane stock solution was found to be 4.3 M by iodometric titration.[28] Experiments were performed under dinitrogen atmosphere in a glovebox unless otherwise noted.

Instrumentation:

Electronic absorption experiments were performed using a Varian Cary 50 Bio UV−visible spectrophotometer equipped with a Unisoku cryostat and stirrer. Vibrational data were obtained using a PerkinElmer Spectrum100 FTIR spectrometer with samples sealed in 0.1 mm gastight NaCl cells. Electrospray ionization mass spectrometry (ESI-MS) experiments were performed using an LCT Premier MicroMass electrospray time-of-flight instrument. X-band EPR experiments were performed using a Bruker EMXplus with Oxford ESR900 continuous-flow liquid helium cryostat and an Oxford ITC503 temperature system. ^{1}H and ^{31}P NMR spectra were obtained on a Bruker DRX 400 MHz NMR spectrometer. ^{13}C and HSQC NMR spectra were obtained on an Avance AVIII 500 MHz NMR spectrometer. Hyperfine shifted ^{1}H NMR data were collected within the spectra width of 150 to -100 ppm with 1000 scans to provide sufficient S/N. Spectra were baseline subtracted with the multipoint fitting procedure using the spline functions

in the MestReNova program. GC analysis was performed on the Agilent 6890N gas chromatograph coupled to a triple quadrupole mass analyzer with both electron impact and chemical ionization sources. X-ray crystallography experiments were performed on a Bruker diffractometer equipped with Helios high-brilliance multilayer optics, a platinum CCD detector and a Bruker MicroStar microfocus rotating anode X-ray source operating at 45 kV and 60 mA.

Synthesis of 2-(bis((6-methylpyridin-2-yl)methyl)amino)-N-(quinolin-8-yl)acetamide (H^{6Me}dpaq). The H^{6Me}dpaq ligand was synthesized according to a modified literature procedure.[29] Under an inert atmosphere in a Schlenk flask, 0.879 g (6.1 mmol) 8-aminoquinoline and 1.238 g (11.7 mmol) sodium carbonate were dissolved in 20 mL CH_3CN. The solution was cooled to 273 K in an ice bath, and 1.231 g (6.1 mmol) bromoacetyl bromide was added dropwise to the cooled solution. The reaction was stirred for one hour at 273 K. The reaction mixture was filtered through an ultrafine frit, and the solvent was removed under vacuum. The resulting orange solid was combined in a flask with 1.002 g (9.5 mmol) sodium carbonate and dissolved in 40 mL CH_3CN under an inert atmosphere. The solution was cooled to 273 K in an ice bath. 1.387 g (6.1 mmol) of bis((6-methylpyridin-2-yl)methyl)amine was added slowly while stirring, and the reaction mixture was stirred overnight at 273 K. After *ca.* 20 hours, the reaction mixture was filtered through an ultrafine frit, and the solvent was removed under vacuum. The resulting red solid was purified through column chromatography on neutral alumina as the stationary phase and 99:1% vol:vol CH_2Cl_2:MeOH as the mobile phase. The purification was completed with 98:2% vol:vol CH_2Cl_2:MeOH. The final product was obtained as a dark yellow solid in 80% yield and characterized by ^1H, ^{13}C, and HSQC NMR methods (Figure A2.1 – A2.3). ^1H NMR data (400 MHz) for H^{6Me}dpaq ($CDCl_3$, δ) = 11.61 (s, 1H), 8.94 (dd; *J* = 4.2, 1.7 Hz;1H), 8.75 (dd; *J* = 6.1, 2.9 Hz; 1H), 8.19 (dd; *J* = 8.3, 1.7 Hz; 1H), 7.82 (d; *J* = 7.7 Hz; 2H), 7.52 (m, 5H), 7.02 (m, 2H),

3.99 (s, 4H), 3.52 (s, 2H), 2.47 (s, 6H) ppm. ^{13}C NMR data (125 MHz) for H^{6Me}dpaq ($CDCl_3$, δ) = 169.92 (s, C=O), 157.88 (s, Py), 157.80 (s, Py), 148.19 (s, Qu), 139.02 (s, Qu), 137.01 (s, Qu), 136.42 (s, Qu), 134.58 (s, Qu), 128.22 (s, Qu), 127.58 (s; Qu), 121.98 (s; Py), 121.73 (d; Py,Qu), 120.30 (s, Py), 116.65 (s, Qu), 61.48 (-CH_2Py), 59.39 (-CH_2CO-), 24.50 (CH_3Py) ppm.

Synthesis and Characterization of [Mn^{II}(OH$_2$)(^{6Me}dpaq)](OTf). The reaction of 0.545 g (1.3 mmol) H^{6Me}dpaq with 0.577 g (1.3 mmol) Mn^{II}(OTf)$_2$·2CH_3CN in 40 mL MeOH under an inert atmosphere using 0.128 g (1.3 mmol) NaO^{t}Bu as a base stirred for 18 hours yields a bright orange solution. The MeOH was removed completely in vacuo leaving behind an orange powder. The orange powder was dissolved in a minimal amount of CH_3CN and layered with diethyl ether. This procedure led to the formation of an orange precipitate. The solvent was decanted, and the orange solid was dried, washed with diethyl ether, and dried again. The recrystallization procedures were repeated two more times and orange microcrystalline solid was obtained. The microcrystalline material was dissolved in a minimal amount of CH_3CN and set-up for crystal growth by slow vapor diffusion of diethyl ether into the CH_3CN solution. Single crystals suitable for X-ray crystallographic analysis were obtained by this method.

X-band, perpendicular-mode EPR data obtained for a *ca.* 2 mM solution of [Mn^{II}(H_2O)(^{6Me}dpaq)]OTf in CH_3CN reveals a 6-line signal (g = 2.00, A = 93.9G; Figure A2.5). The g-value and hyperfine splitting observed in this EPR spectrum are similar to those reported for the high-spin [Mn^{II}(N4S)]$^+$ complexes (g = 1.98 - 2.00, A = 90 – 100 G) and [Mn^{II}(NCMe)(dpaq^{2Me})]$^+$ (g = 2.04).[30, 31] Thus, we conclude that the monomeric structure observed in the X-ray structure of [Mn^{II}(H_2O)(^{6Me}dpaq)](OTf) is retained in solution. In addition, a determination of the magnetic moment for this complex by the Evans method yielded a value of 5.7 μ_B, which is consistent with the assignment of this species as a high-spin Mn^{II} complex (the

calculated spin-only value for an $S = 5/2$ species is 5.91 μ_B). Mass-spectral analysis of a CH_3CN solution of $[Mn^{II}(H_2O)(^{6Me}dpaq)](OTf)$ revealed a peak at *m/z* = 465.12, consistent with the $[Mn^{II}(^{6Me}dpaq)]^+$ ion (calculated *m/z* = 465.14; Figure A2.6). The ESI-MS data also show an *m/z* peak at 482.14, which is consistent with $[Mn^{III}(OH)(^{6Me}dpaq)]^+$ (calculated *m/z* = 482.15). The appearance of $[Mn^{III}(OH)(^{6Me}dpaq)]^+$ indicates the oxidation of $[Mn^{II}(H_2O)(^{6Me}dpaq)]OTf$ by ambient oxygen in air to form $[Mn^{III}(OH)(^{6Me}dpaq)]^+$. This phenomenon has been observed in other Mn^{II} complexes with similar ligands.[26, 30]

X-ray diffraction data collection and analysis for $[Mn^{II}(H_2O)(^{6Me}dpaq)](OTf)$. Complete sets of unique reflections were collected with monochromated CuKα radiation for a crystal sample of the $[Mn^{II}(H_2O)(^{6Me}dpaq)](OTf)$ compound. The $[Mn^{II}(H_2O)(^{6Me}dpaq)](OTf)$ crystal was a 95/5 racemic twin. Totals of 1639 1.0°-wide ω- or ϕ-scan frames with counting times of 4-6 seconds were collected for $[Mn^{II}(H_2O)(^{6Me}dpaq)](OTf)$ with a Bruker APEX II CCD area detector. X-rays were provided by a Bruker MicroStar microfocus rotating anode operating at 45kV and 60 mA and equipped with Helios multilayer x-ray optics. Preliminary lattice constants were obtained with the Bruker program SMART.[8] Integrated reflection intensities were produced using the Bruker program SAINT.[9] Data sets were corrected empirically for variable absorption effects using equivalent reflections. The Bruker software package SHELXTL was used to solve the structure using "direct methods" techniques. All stages of weighted full-matrix least-squares refinement were conducted using Fo^2 data with the SHELXTL v2014 software package.[10]

The final structural model incorporated anisotropic thermal parameters for all nonhydrogen atoms and isotropic thermal parameters for all hydrogen atoms. Hydrogen atoms in the ^{6Me}dpaq ligands and acetonitrile molecules of crystallization were fixed at idealized riding model sp^2- or sp^3-hybridized positions with C-H bond lengths of 0.95 - 0.99 Å. Both hydrogen atoms for the

water molecule were located from a difference Fourier and included in the structural model as independent isotropic atoms whose parameters were allowed to refine in least-squares refinement cycles. All methyl groups were refined as idealized rigid rotors (with a C-H bond length of 0.98 Å) that were allowed to rotate freely about their C-C bonds in least-squares refinement cycles. The isotropic thermal parameters of idealized hydrogen atoms were fixed at values 1.2 (non-methyl) or 1.5 (methyl) times the equivalent isotropic thermal parameter of the carbon atom to which they are covalently bonded. The relevant crystallographic and structure refinement data for $[Mn^{II}(H_2O)(^{6Me}dpaq)](OTf)$ are given in Table A2.1.

Synthesis and Characterization of $[Mn^{III}(OH)(^{6Me}dpaq)](OTf)$. The $[Mn^{II}(H_2O)(^{6Me}dpaq)]OTf$ complex reacts very slowly with dioxygen to produce $[Mn^{III}(OH)(^{6Me}dpaq)]OTf$ (Figure A2.7, left). A more ready method for obtaining $[Mn^{III}(OH)(^{6Me}dpaq)]OTf$ was identified through oxidation of $[Mn^{II}(H_2O)(^{6Me}dpaq)]OTf$ in CH_3CN using 0.5 equiv. PhIO (Figure A2.7, right). The oxidation reaction led to a change in color from the bright orange color CH_3CN solution of $[Mn^{II}(H_2O)(^{6Me}dpaq)]OTf$ to dark bronze color. Mass spectral analysis of CH_3CN solutions of $[Mn^{III}(OH)(^{6Me}dpaq)](OTf)$ reveal a prominent peak at *m/z* = 482.14, in good agreement with the predicted *m/z* for $[Mn^{III}(OH)(^{6Me}dpaq)]^+$ (calculated *m/z* = 482.14, Figure A2.8). The ESI-MS data also show a peak associated with the Na^+ cation of the $H^{6Me}dpaq$ ligand (Figure A2.8). The solution-phase magnetic moment of $[Mn^{III}(OH)(^{6Me}dpaq)]^+$, as determined using the Evans ^1H NMR method with diamagnetic correction, support the assignment of this species as a high-spin Mn^{III} center (μ_{eff} = 4.5 μ_B, expected spin-only value of μ_{eff} = 4.9 μ_B). ^1H NMR characterization suggests that the dissolution of $[Mn^{III}(OH)(^{6Me}dpaq)](OTf)$ in CD_3CN does not result in the formation of (μ-

oxo)dimanganese(III, III) species.[32] Presumably the steric bulk of the additional 6-methyl moiety is sufficient to prohibit formation of a (μ-oxo)dimanganese(III, III) complex.

X-ray quality crystals of $[Mn^{III}(OH)(^{6Me}dpaq)](OTf)$ were obtained by crystallization of the concentrated bronze color solution resulting from the oxidation of $[Mn^{II}(H_2O)(^{6Me}dpaq)]OTf$ by slow vapor diffusion of diethyl ether into the CH_3CN solution at room temperature.

X-ray diffraction data collection and analysis for $[Mn^{III}(OH)(^{6Me}dpaq)](OTf)$. A set of 4121 unique reflections were collected[33] for a 92/8 racemically-twinned crystal of $[Mn(C_{25}H_{24}N_5O)(OH)][O_3SCF_3]$ using 1.0º-wide ω- or ϕ-scan frames with scan times of 8-30 seconds and monochromated CuKα radiation (λ = 1.54178 Å) on a Bruker Proteum Single Crystal Diffraction System equipped with dual CCD area detectors. Data collection utilized a Platinum 135 CCD detector and Helios high-brilliance multilayer optics. X-rays were provided with a Bruker MicroStar microfocus Cu rotating anode x-ray source operating at 45 kV and 60 mA. The integrated data[34] were corrected empirically for variable absorption effects using equivalent reflections. The Bruker software package SHELXTL was used to solve the structure using "direct methods" techniques. All stages of weighted full-matrix least-squares refinement were conducted using F_o^2 data with the SHELXTL XL v2014 software package[35].

The asymmetric unit of $[Mn(C_{25}H_{24}N_5O)(OH)][O_3SCF_3]$ contains an ordered $[Mn(C_{25}H_{24}N_5O)(OH)]^+$ cation and an ordered triflate anion. All nonhydrogen atoms of $[Mn(C_{25}H_{24}N_5O)(OH)][O_3SCF_3]$ were included in the structural model with anisotropic thermal parameters that were allowed to vary along with their positional parameters in least-squares refinement cycles. The hydrogen atom of the coordinated hydroxyl group was located from a difference Fourier and included in the structural model as an independent isotropic atom whose parameters was also allowed to vary. Methyl groups for $[Mn(C_{25}H_{24}N_5O)(OH)][O_3SCF_3]$ were

incorporated into the structural model as idealized rigid rotors (using sp^3-hybridized geometry and a C–H bond length of 0.98 Å) that were permitted to rotate freely about their C–C bonds in least-squares refinement cycles. The remaining non-methyl hydrogen atoms for $[Mn(C_{25}H_{24}N_5O)(OH)][O_3SCF_3]$ were included in the structural model as idealized riding-model atoms (assuming sp^2- or sp^3-hybridization of the carbon atoms with C–H bond lengths of 0.95 or 0.99 Å). The isotropic thermal parameters of all idealized hydrogen atoms were fixed at values 1.2 (nonmethyl) or 1.5 (methyl) times the equivalent isotropic thermal parameter of the carbon atom to which they are covalently bonded.

Synthesis and Characterization of $[Mn^{III}(OO^tBu)(^{6Me}dpaq)]^+$ and $[Mn^{III}(OOCm)(^{6Me}dpaq)]^+$. $[Mn^{III}(OO^tBu)(^{6Me}dpaq)]^+$ and $[Mn^{III}(OOCm)(^{6Me}dpaq)]^+$ were prepared by the reaction of $[Mn^{II}(H_2O)(^{6Me}dpaq)]OTf$ in CH_3CN with 1.5 equiv. of ^{t}BuOOH and CmOOH, respectively, at 298 K (Amount determined by titration, see Figure A 2.9). The formation of $[Mn^{III}(OO^tBu)(^{6Me}dpaq)]^+$ and $[Mn^{III}(OOCm)(^{6Me}dpaq)]^+$ were monitored by electronic absorption spectroscopy. These data show the appearance of an electronic absorption feature at around 650 nm. This feature increased in intensity with time, and the formation was deemed complete after there was no change in intensity with time. The formation of $[Mn^{III}(OO^tBu)(^{6Me}dpaq)]^+$ and $[Mn^{III}(OOCm)(^{6Me}dpaq)]^+$ was also performed by the reaction of $[Mn^{III}(OH)(^{6Me}dpaq)]^+$ in CH_3CN with 1.0 equiv. ^{t}BuOOH and CmOOH, respectively, at 298 K. In thi case, the formation was evident by the decrease in the intensity of the 510 nm feature of $[Mn^{III}(OH)(^{6Me}dpaq)]^+$ and the appearance of a 650 nm feature. The formation was deemed complete after there was no change in intensity of the 650 nm feature with time. Mass spectral analysis of a CH_3CN solution of $[Mn^{III}(OO^tBu)(^{6Me}dpaq)]^+$ shows a peak at *m/z* = 554.19 that is consistent with the formulation of this species as $[Mn^{III}(OO^tBu)(^{6Me}dpaq)]^+$ (calculated *m/z* =

554.20, Figure A2.10, left). The magnetic moment of $[Mn^{III}(OO^tBu)(^{6Me}dpaq)]^+$, as determined using the Evans ^1H NMR method with diamagnetic correction, supports the assignment of this species as a high-spin Mn^{III} center (μ_{eff} = 4.5 μ_B, which compares well with the free-ion value for an S = 2 system of 4.9 μ_B). ESI-MS data collected for $[Mn^{III}(OOCm)(^{6Me}dpaq)]^+$ show a characteristic peak at m/z = 616.18 that agrees with that expected for this complex (calculated *m/z* = 616.21, Figure A2.10, right). X-ray quality crystals of the $[Mn^{III}(OOCm)(^{6Me}dpaq)]^+$ were obtained by layering of concentrated CH_3CN solution of $[Mn^{III}(OOCm)(^{6Me}dpaq)]^+$ with cold diethyl ether. The set-up was kept in a freezer at 233 K and green crystalline material used for X-ray crystallography studies were obtained after 2 days.

X-ray diffraction data collection and analysis for $[Mn^{III}(OOCm)(^{6Me}dpaq)](OTf)$. Complete sets of unique reflections were collected with monochromated CuKα radiation for a crystal sample of the $[Mn^{III}(OOCm)(^{6Me}dpaq)](OTf)$ with single domain. Totals of 4998 1.0°-wide ω- or ϕ-scan frames with counting times of 10-15 seconds were collected for $[Mn^{III}(OOCm)(^{6Me}dpaq)](OTf)$ with a Bruker APEX II CCD area detector. X-rays were provided by a Bruker MicroStar microfocus rotating anode operating at 45kV and 60 mA and equipped with Helios multilayer x-ray optics. Preliminary lattice constants were obtained with the Bruker program SMART.[8] Integrated reflection intensities were produced using the Bruker program SAINT.[9] Data sets were corrected empirically for variable absorption effects using equivalent reflections. The Bruker software package SHELXTL was used to solve the structure using "direct methods" techniques. All stages of weighted full-matrix least-squares refinement were conducted using Fo^2 data with the SHELXTL v2014 software package.[10]

The final structural model incorporated anisotropic thermal parameters for all nonhydrogen atoms and isotropic thermal parameters for all hydrogen atoms. Hydrogen atoms in the ^{6Me}dpaq

ligands and acetonitrile molecules of crystallization were fixed at idealized riding model sp^2- or sp^3-hybridized positions with C-H bond lengths of 0.95 - 0.99 Å. All methyl groups were refined as idealized rigid rotors (with a C-H bond length of 0.98 Å) that were allowed to rotate freely about their C-C bonds in least-squares refinement cycles. The isotropic thermal parameters of idealized hydrogen atoms were fixed at values 1.2 (non-methyl) or 1.5 (methyl) times the equivalent isotropic thermal parameter of the carbon atom to which they are covalently bonded. The relevant crystallographic and structure refinement data for $[Mn^{III}(OOCm)(^{6Me}dpaq)](OTf)$ are given in Table A2.1.

Decay kinetics. 1.25 mM sample solutions of the $[Mn^{II}(OOR)(^{6Me}dpaq)]^+$ complexes (R = ^{t}Bu and Cm) in CH_3CN were prepared in the glovebox, dispensed into a quartz cuvette and covered with a rubber septum. The septum was wrapped with Parafilm. The cuvette was taken out of the glovebox, and the decay kinetics were monitored on a Varian Cary 50 Bio UV−visible spectrophotometer equipped with a temperature controller and stirrer.

PPh_3 reaction kinetics and Eyring analysis. Samples of the $[Mn^{III}(OOR)(^{6Me}dpaq)]^+$ complexes in CH_3CN were prepared in the glovebox and dispensed into a quartz cuvette, covered with a rubber septum and wrapped with Parafilm. 300 μL of dichloromethane was added to an amount of PPh_3 in a 4.0 mL vial. The vial was covered with a rubber septum and wrapped with Parafilm. The cuvette and the vial containing the substrate were taken outside the glovebox. The cuvette was placed on the UV-vis spectrometer and equilibrated at 298 K for 10 minutes before the PPh_3 solution was added using a gastight syringe that was purged five times with nitrogen gas. For variable temperature kinetic experiments, the same procedure was repeated using 1.25 mM $[Mn^{III}(OOR)(^{6Me}dpaq)]^+$ and 100 equiv. PPh_3 in the temperature range of 288 - 313 K.

Reactivity of $[Mn^{III}(OO^tBu)(^{6Me}dpaq)]^+$ and $[Mn^{III}(OOCm)(^{6Me}dpaq)]^+$ with DHA. The reaction of $[Mn^{III}(OO^tBu)(^{6Me}dpaq)]^+$ with 9,10-dihydroanthracene (DHA) was performed by adding 100 equiv. DHA, dissolved in 100 μL of CH_2Cl_2 to a cuvette containing a 1.75 mM solution of $[Mn^{III}(OO^tBu)(^{6Me}dpaq)]^+$ in CH_3CN in the glovebox. The cuvette was sealed with a rubber septum and wrapped with Parafilm. The reaction mixture was brought out of the glovebox and the reaction was heated to 323 K while monitoring the reaction by electronic absorption spectroscopy. After the reaction was completed, evident by the disappearance of the 650 nm feature, the reaction mixture was passed through a 2-inch silica plug and the eluate was dried in vacuo. The solid residue was analyzed by ^1H NMR spectroscopy for characterization and quantification. Quantification was performed with 1,4-benzoquinone as an internal standard (Figure A2.11). At first, quantification showed 2.4 equiv. DHA converted to anthracene. However, control experiments without the $[Mn^{III}(OO^tBu)(^{6Me}dpaq)]^+$ also showed the conversion of DHA to anthracene (Figure A2.12). Another control experiment was conducted where UV-light from the spectrometer was isolated from a reaction solution. In this case, the control experiment lacking $[Mn^{III}(OO^tBu)(^{6Me}dpaq)]^+$ revealed no oxidation of DHA. This result revealed that UV-light from the spectrometer contributes to the observed 2.4 equiv. conversion of DHA to anthracene. In subsequent procedures, we isolation the reaction mixture from the interference from the UV-light and quenched the reaction after 7 hours. These experiments revealed that 1.4 equiv. DHA were converted to anthracene. A similar reaction performed at 298 K over the course of 13 hours revealed only trace amounts of anthracene. Under these conditions, the final solution was still green, indicating the lack of full consumption of $[Mn^{III}(OO^tBu)(^{6Me}dpaq)]^+$. Similar conditions were used to explore the reaction of $[Mn^{III}(OOCm)(^{6Me}dpaq)]^+$ with DHA. In this reaction, we also found *ca.* 1.4 equiv. DHA converted to anthracene. The decay rate of $[Mn^{III}(OOCm)(^{6Me}dpaq)]^+$ was 0.0188 min^{-1},

which is comparable to that of $[Mn^{III}(OO^tBu)(^{6Me}dpaq)]^+$ under the same conditions (0.0141 min^{-1}). These decay rates are indistinguishable from the thermal decays rates of these complexes. The presence of O_2 also had an effect on the product distribution. Aerobic studies of this reaction gave mixtures of products, including anthracene and the oxygenated products anthraquinone and anthrone. The same experimental procedure was repeated for the reaction of $[Mn^{III}(OO^tBu)(^{6Me}dpaq)]^+$ with d_4-DHA, and no change in the decay rate of the Mn^{III}-alkylperoxo species was observed (Figure A2.13).

3.3 Results and Analysis

Formation and Characterization of $[Mn^{II}(OH_2)(^{6Me}dpaq)](OTf)$ and $[Mn^{III}(OH)(^{6Me}dpaq)](OTf)$.

$[Mn^{II}(H_2O)(^{6Me}dpaq)]OTf$ was prepared by the metalation of $H^{6Me}dpaq$ with $Mn^{II}(OTf)_2$. The X-ray crystal structure of $[Mn^{II}(H_2O)(^{6Me}dpaq)]OTf$ reveals a monomeric, six-coordinate Mn^{II} center coordinated by the pentadentate $^{6Me}dpaq$ ligand and a water molecule (Figure 3.3, left). Previous X-ray crystal structures for $[Mn^{II}(dpaq)](OTf)$[26] and $[Mn^{II}(dpaq^{2Me})](OTf)$[30] showed polymeric species, where the coordination site trans to the amide function was occupied by a carbonyl oxygen from a second $[Mn^{II}(dpaq)]^+$ (or $[Mn^{II}(dpaq^{2Me})]^+$) cation (Figure A2.14). The 6-Me-pyridyl functions in $[Mn^{II}(H_2O)(^{6Me}dpaq)]OTf$ give rise to elongated bonds (Mn–N4 and Mn–N5) when compared to those of $[Mn^{II}(dpaq)](OTf)$ and $[Mn^{II}(dpaq)^{2Me}](OTf)$ (Tables 3.1 and A2.2). The bonds involving the amide and amine functions (Mn–N2 and Mn–N3, respectively) of $[Mn^{II}(H_2O)(^{6Me}dpaq)]OTf$ are slightly contracted compared to the corresponding distances in $[Mn^{II}(dpaq)](OTf)$ and $[Mn^{II}(dpaq)^{2Me}](OTf)$ (Table 3.1), which could reflect some compensation for the longer bond lengths with the 6-Me-pyridyl donors. In the solid-state structure, the aqua

ligand of [$Mn^{II}(H_2O)(^{6Me}dpaq)$]OTf hydrogen bonds with both an amide oxygen of a neighboring [$Mn^{II}(H_2O)(^{6Me}dpaq)$]OTf molecule in the unit cell and with an oxygen of a triflate counter anion (H···O separations of 1.79(7) and 1.86(6) Å, respectively). Solution-phase characterization of [$Mn^{II}(H_2O)(^{6Me}dpaq)$]OTf in CH_3CN by EPR (Figure A2.4), ESI-MS (Figure A2.6), and Evans NMR provide evidence that the mononuclear structure observed in the solid state is retained in solution.

[$Mn^{II}(H_2O)(^{6Me}dpaq)$]OTf reacts very slowly with dioxygen. Electronic absorption data collected during the oxygenation of a 2.5 mM solution of [$Mn^{II}(H_2O)(^{6Me}dpaq)$]OTf in CH_3CN shows the appearance of a single feature at 510 nm, but this new chromophore is still forming even after 48 hours (Figure A2.7, left). This reactivity contrasts with that of [Mn^{II}(dpaq)](OTf) and the majority of its derivatives, as these Mn^{II} complexes reacted with dioxygen with full conversion to Mn^{III} products over the course of several hours.[26, 30, 32] Presumably, the elongation of the Mn–N4 and Mn–N5 bonds in [$Mn^{II}(H_2O)(^{6Me}dpaq)$]OTf leads to a more electron-deficient Mn^{II} center with muted reactivity with dioxygen. In contrast, the reaction between [$Mn^{II}(H_2O)(^{6Me}dpaq)$]OTf and 0.5 equiv. PhIO is rapid, resulting in the formation of a bronze colored solution with a single electronic absorption feature at *ca*. 510 nm (Figure A2.7, right).

X-ray diffraction studies of crystals obtained from this dark orange solution establish the oxidation product as [Mn^{III}(OH)(^{6Me}dpaq)](OTf) (Figure 3.3, right). In this complex, a six-coordinate Mn^{III} center is coordinated in a distorted octahedral geometry with the hydroxo ligand *trans* to the amide function. This coordination mode is identical to that observed in Mn^{III}-hydroxo complexes of dpaq and its derivatives.[26, 30, 32] The Mn–OH distance of 1.806(6) Å is within error of that observed for [Mn^{III}(OH)(dpaq)](OTf) (1.806(13); see Table 3.1)[26] and is on the low end of

the range of Mn–OH bond lengths reported for other Mn^{III}-hydroxo complexes (1.81 - 1.86 Å).[30, 36-44] Further comparisons of the X-ray structure of [Mn^{III}(OH)(^{6Me}dpaq)](OTf) with those of related Mn^{III}-hydroxo species reveals that the 6-Me-pyridyl groups give rise to substantial bond elongations. Specifically, the Mn–N4 and Mn–N5 distances of [Mn^{III}(OH)(^{6Me}dpaq)](OTf) are 2.322(6) and 2.381(7) Å, while the corresponding distances in [Mn^{III}(OH)(dpaq)](OTf) are 2.260(14) and 2.216(15) Å (Table 3.1).[26] Mn^{III} complexes of the N_4S^- class of ligands (Figure 3.1) with 6-Me-pyridyl or quinolinyl substituents in the equatorial field had Mn–N distances ranging from 2.352 – 2.581 Å.[16, 31] The 6-Me-pyridyl Mn–N distances of [Mn^{III}(OH)(^{6Me}dpaq)](OTf) are thus on the short end of this range. For [Mn^{III}(OH)(^{6Me}dpaq)](OTf), the longer Mn–N4 and Mn–N5 distances are accompanied by modest contractions of Mn–N1, Mn–N2, and Mn–N3 by 0.031, 0.013, and 0.043 Å, respectively, relative to [Mn^{III}(OH)(dpaq)](OTf) (Table 3.1). The extended X-ray structure of [Mn^{III}(OH)(^{6Me}dpaq)](OTf) reveals a hydrogen bond between the hydroxo ligand and the amide oxygen of a neighboring [Mn^{III}(OH)(^{6Me}dpaq)]$^+$ cation (H···O distance of 2.008 Å, see Figure A2.14). This kind of interaction was also observed in the crystal structure of [Mn^{III}(OH)(^{2Me}dpaq)](OTf) (H···O distance of 1.982 Å, see Figure A2.14).[30] A free triflate ion is also present in the asymmetric unit of [Mn^{III}(OH)(^{6Me}dpaq)](OTf), though there is no interaction with the Mn center (closest Mn–O distance of *ca.* 7.5 Å).

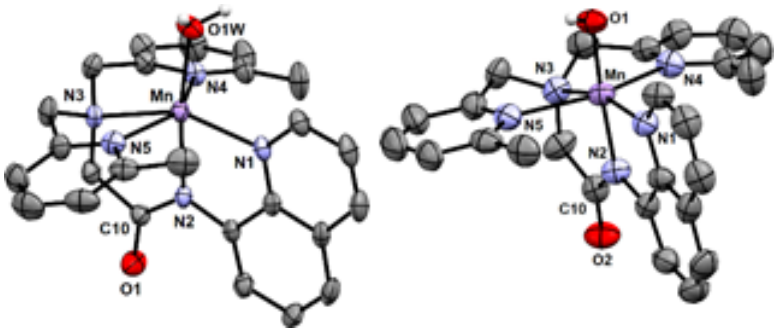

Figure 3.3. X-ray crystal structures of $[Mn^{II}(H_2O)(^{6Me}dpaq)]OTf$ and $[Mn^{III}(OH)(^{6Me}dpaq)](OTf)$ showing 50% probability thermal ellipsoid. Triflate counter ion and non-aqua and non-hydroxo hydrogen atoms were removed for clarity.

Previous investigations of $[Mn^{III}(OH)(dpaq)](OTf)$ and a subset of its derivatives have shown that dissolution of the salts of these Mn^{III}-hydroxo complexes in dried CH_3CN leads to the formation of an equilibrium mixture of Mn^{III}-hydroxo and (μ-oxo)dimanganese(III,III) complexes that can both be detected by ^1H NMR spectroscopy.[32, 45] The ^1H NMR spectrum of $[Mn^{III}(OH)(^{6Me}dpaq)](OTf)$ in CD_3CN at 298 K exhibits seven hyperfine-shifted peaks that lie well outside 0 - 20 ppm (the diamagnetic region), as well as two well-resolved peaks in the 0 - 10 ppm region (Figure 3.4, red trace). The lack of a large number of peaks in the diamagnetic region suggests that dissolution of $[Mn^{III}(OH)(^{6Me}dpaq)](OTf)$ in CD_3CN does not result in the formation of (μ-oxo)dimanganese(III, III) species. The chemical shifts for the ^1H NMR signals of $[Mn^{III}(OH)(^{6Me}dpaq)]^+$ are quite similar to those of $[Mn^{III}(OH)(dpaq)]^+$ (Figure 3.4 and Table 3.2).[32, 45] The four most upfield-shifted peaks in the ^1H NMR spectrum of $[Mn^{III}(OH)(dpaq)]^+$ were assigned to protons from the quinolinyl moiety.[45] The upfield region of the ^1H NMR spectrum of $[Mn^{III}(OH)(^{6Me}dpaq)]^+$ shows three sharp peaks at -19.3, -45.0, and -61.6 ppm that resemble the peaks of $[Mn^{III}(OH)(dpaq)]^+$ at -15.5, -33.7, -53.8 ppm (Figure 3.4). The ^1H NMR spectrum of $[Mn^{III}(OH)(^{6Me}dpaq)]^+$ lacks a broad, highly upfield-shifted peak analogous to the weak, broad -63.4 ppm signal of $[Mn^{III}(OH)(dpaq)]^+$, but the breadth of this signal renders it difficult to resolve.

The overall similarities between the upfield regions of the ^{1}H NMR spectra of $[Mn^{III}(OH)(^{6Me}dpaq)]^{+}$ and $[Mn^{III}(OH)(dpaq)]^{+}$ are expected given the lack of changes to the quinolinyl group in the former complex. The downfield ^{1}H NMR signals of $[Mn^{III}(OH)(dpaq)]^{+}$ and the resonance at -4.6 ppm were attributed to pyridyl protons.[45] Consequently, the larger relative perturbations in the downfield regions of the ^{1}H NMR spectra of $[Mn^{III}(OH)(dpaq)]^{+}$ and $[Mn^{III}(OH)(^{6Me}dpaq)]^{+}$ can be rationalized by changes in chemical shifts of pyridyl protons. The peak at 130.5 ppm for $[Mn^{III}(OH)(dpaq)]^{+}$ was assigned to the **α**-H of the pyridine substituent.[45] The lack of a corresponding peak in the ^{1}H NMR spectrum of $[Mn^{III}(OH)(^{6Me}dpaq)]^{+}$ is consistent with the functionalization of the pyridyl functions in the 6-position. The ^{1}H NMR spectrum of $[Mn^{III}(OH)(^{6Me}dpaq)]^{+}$ contains a broad, upfield peak at -9.5 ppm, lacking in the ^{1}H NMR spectrum of $[Mn^{III}(OH)(dpaq)]^{+}$, that we attribute to protons of the 6-methyl-substituents. Overall, the ^{1}H NMR spectra of $[Mn^{III}(OH)(^{6Me}dpaq)]^{+}$ and $[Mn^{III}(OH)(dpaq)]^{+}$ are quite similar, and the observed differences can be rationalized in terms of the presence of the 6-Me-pyridyl groups in the former complex.

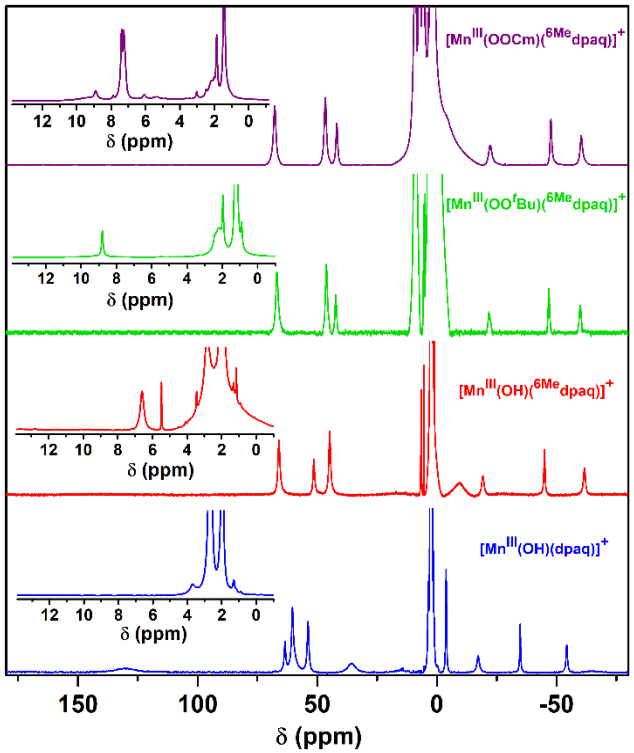

Figure 3.4. ^{1}H NMR spectra of 20 mM solutions of $[Mn^{III}(OH)(^{6Me}dpaq)]^+$ (red), 15 mM $[Mn^{III}(OO^tBu)(^{6Me}dpaq)]^+$ (green), 15 mM $[Mn^{III}(OOCm)(^{6Me}dpaq)]^+$ (purple), and 15 mM solutions of $[Mn^{II}(OH)(dpaq)]^+$ (blue) with 45 µL D_2O. All samples were prepared in CD_3CN at 298 K. The Mn^{III}-alkylperoxo complexes were prepared by treating $[Mn^{III}(OH)(^{6Me}dpaq)]^+$ with 1 equiv. ^{t}BuOOH (green) or CmOOH (purple). Inset: expanded view of the 0 to 13 ppm region.

Table 3.1 Manganese-ligand bond lengths (Å) and angles from X-ray crystal structures of $[Mn^{II}(OH_2)(^{6Me}dpaq)](OTf)$, $[Mn^{II}(dpaq)](OTf)$, $[Mn^{III}(OH)(^{6Me}dpaq)](OTf)$, $[Mn^{III}(OH)(dpaq)](OTf)$, and $[Mn^{III}(OOCm)(^{6Me}dpaq)](OTf)$.

Bond	$[Mn^{II}(OH_2)(L)](OTf)$	$[Mn^{II}(L)](OTf)$	$[Mn^{III}(OH)(L)](OTf)$		$[Mn^{III}(OOCm)(L)](OTf)$
	L = ^{6Me}dpaq	L = dpaq	L = ^{6Me}dpaq	L = dpaq	L = ^{6Me}dpaq
Mn–O1	2.108(3)	2.079(2)[a]	1.806(6)	1.806(13)	1.849(3)
Mn–N1	2.233(3)	2.214(3)	2.041(7)	2.072(14)	2.044(4)
Mn–N2	2.152(4)	2.191(3)	1.962(6)	1.975(14)	1.955(4)
Mn–N3	2.280(3)	2.314(3)	2.130(6)	2.173(14)	2.100(4)
Mn–N4	2.354(4)	2.244(3)	2.322(6)	2.260(14)	2.284(4)
Mn–N5	2.417(3)	2.286(3)	2.381(7)	2.216(15)	2.394(4)
O1–O2					1.466(4)
Mn–O1–O2					110.4(2)

[a] For $[Mn^{II}(dpaq)](OTf)$, the oxygen atom derives from a carbonyl unit of a separate $[Mn^{II}(dpaq)]^+$ cation

Formation of $[Mn^{III}(OO^tBu)(^{6Me}dpaq)]^+$ and $[Mn^{III}(OOCm)(^{6Me}dpaq)]^+$

The addition of a slight excess of ^{t}BuOOH to $[Mn^{II}(H_2O)(^{6Me}dpaq)]OTf$ in CH_3CN at 298 K results in the formation of a green chromophore with a prominent electronic absorption band at 650 nm (ε = 240 $M^{-1}cm^{-1}$) and a shoulder near 500 nm (ε = 263 $M^{-1}cm^{-1}$; see Figure 3.5, left) (Extinction coefficients were determined assuming full conversion under these conditions.) Maximal formation of the green chromophore from $[Mn^{II}(H_2O)(^{6Me}dpaq)]OTf$ requires 1.5 equiv. ^{t}BuOOH (Figure A2.9). A similar reaction is observed upon the addition of CmOOH to $[Mn^{II}(H_2O)(^{6Me}dpaq)]OTf$ (Figure A2.15). Spectroscopic data provided below support the formulation of these green chromophores as $[Mn^{III}(OO^tBu)(6Medpaq)]^+$ and $[Mn^{III}(OOCm)(^{6Me}dpaq)]^+$. The half-lives of the 2 mM solutions of the $[Mn^{III}(OO^tBu)(^{6Me}dpaq)]^+$ and $[Mn^{III}(OOCm)(^{6Me}dpaq)]^+$ are *ca.* 5 and 8 days, respectively, in CH_3CN at 298 K.

The time course for the formation of $[Mn^{III}(OO^tBu)(^{6Me}dpaq)]^+$ from $[Mn^{II}(H_2O)(^{6Me}dpaq)]^+$ shows an initial rise in absorbance intensity at 510 nm that maximizes near *ca*. 60 minutes and then drops and levels by 120 minutes. In contrast, the absorbance intensity at 650 nm shows a steep rise from 0 to 40 minutes, grows more slowly from 40 – 100 minutes, and then rises quickly and levels by 120 minutes (Figure 3.5, left inset). On the basis of this reaction profile, we propose the formation of the Mn^{III}-hydroxo adduct $[Mn^{III}(OH)(^{6Me}dpaq)]^+$ as an intermediate in this reaction, as this species shows an absorption maximum at 510 nm. This proposal is consistent with the 1.5:1 ^{t}BuOOH:Mn^{II} stoichiometry, where initial oxidation of $[Mn^{II}(H_2O)(^{6Me}dpaq)]OTf$ to $[Mn^{III}(OH)(^{6Me}dpaq)]^+$ consumes 0.5 equiv. ^{t}BuOOH, and the remaining 1.0 equiv. ^{t}BuOOH converts $[Mn^{III}(OH)(^{6Me}dpaq)]^+$ to $[Mn^{III}(OO^tBu)(^{6Me}dpaq)]^+$ by a ligand substitution reaction that yields water as a co-product (Scheme 3.1). To test this mechanism, we added 1.0 equiv. ^{t}BuOOH

to $[Mn^{III}(OH)(^{6Me}dpaq)]^+$ in CH_3CN at 298 K and observed the formation of $[Mn^{III}(OO^tBu)(^{6Me}dpaq)]^+$ in maximal yield (Figure 3.5, Right). In this case, the conversion is accompanied with isosbestic points at 505 and 555 nm, indicating the lack of an accumulating intermediate. The formation of a Mn^{III}-hydroxo intermediate during the reaction of ^{t}BuOOH with $[Mn^{II}(dpaq)](OTf)$ and $[Mn^{II}(dpaq^{2Me})](OTf)$ was observed previously.[25]

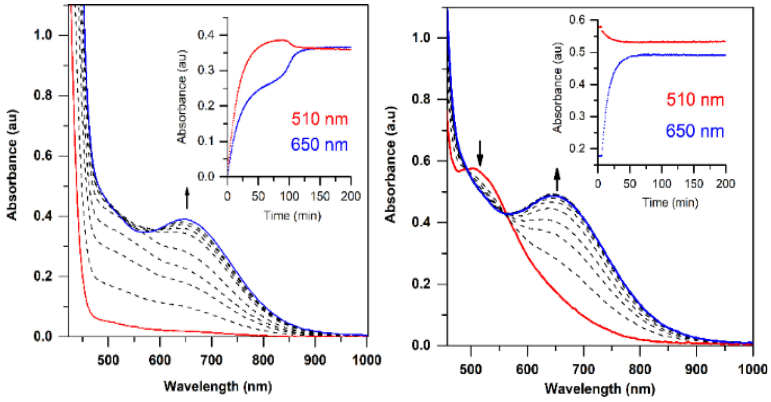

Figure 3.5. Left: Electronic absorption spectra showing the formation of the green 1.5 mM $[Mn^{III}(OO^tBu)(^{6Me}dpaq)]^+$ species (blue trace) from the oxidation of $[Mn^{II}(H_2O)(^{6Me}dpaq)]OTf$ (red trace) with 1.5 equiv. ^{t}BuOOH. Right: Electronic absorption spectra showing the formation of 2.0 mM $[Mn^{III}(OO^tBu)(^{6Me}dpaq)]^+$ from the reaction of $[Mn^{III}(OH)(^{6Me}dpaq)]^+$ (red trace) with 1.0 equiv. ^{t}BuOOH (blue trace is the final spectrum). Time courses for each reaction are shown in the insets.

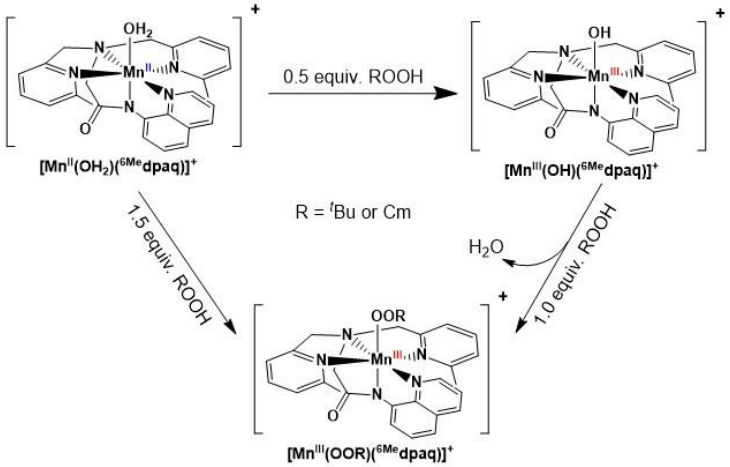

Scheme 3.1. Synthetic route for the preparation of $[Mn^{III}(OOR)(^{6Me}dpaq)]^+$.

Structural Properties of $[Mn^{III}(OOCm)(^{6Me}dpaq)]^{+}$

While all attempts at obtaining crystalline material for $[Mn^{III}(OO^{t}Bu)(^{6Me}dpaq)](OTf)$ were unsuccessful, we were able to obtain diffraction-quality crystals for $[Mn^{III}(OOCm)(^{6Me}dpaq)](OTf)$, which confirmed the formulation of this complex (Figure 3.6). The cumylperoxo ligand of $[Mn^{III}(OOCm)(^{6Me}dpaq)](OTf)$ is bound *trans* to the amide nitrogen (N2-Mn-O1 angle of 176.6°), occupying the position of the hydroxo ligand in $[Mn^{III}(OH)(^{6Me}dpaq)](OTf)$. The Mn-O1 bond length for $[Mn^{III}(OOCm)(^{6Me}dpaq)](OTf)$ is longer than the Mn–O1 bond in the Mn^{III}-hydroxo analogue (1.849(3) and 1.806(6) Å, respectively), but similar to crystallographic Mn–OOCm distances for the $[Mn^{III}(OOCm)(N_4S)]^{+}$ complexes (1.848(4) and1.84(1) Å).[15, 16] The O1-O2 bond is oriented such that the projection of this bond onto the equatorial plane bisects the N1-Mn-N4 bond angle. The aryl ring of the cumyl moiety is parallel to the plane of the pyridines coordinated to the Mn^{III} center, as opposed to the out-of-plane orientation observed in the $[Mn^{III}(S^{Me2}N_4(6\text{-Me-DPEN}))(OOCm)](BPh_4)$ complex.[16] This orientation of the cumyl moiety is stabilized by π-CH interactions between the aryl ring and a methylene group of the ^{6Me}dpaq ligand, as evidenced by short H···C contacts of *ca.* 2.8 Å. The O1-O2 bond length of 1.466(4) Å for $[Mn^{III}(OOCm)(^{6Me}dpaq)](OTf)$ is consistent with that expected for an alkylperoxo moiety[4, 5, 46, 47] and is within the range of values observed for the $[Mn^{III}(OOCm)(N_4S)]^{+}$ complexes (1.457(5) and 1.51(2) Å).[15, 16] The nitrogen atoms of the 6-Me-pyridyl groups (N4 and N5 of $[Mn^{III}(OOCm)(^{6Me}dpaq)](OTf)$) are 2.284(4) and 2.394(4) Å, respectively, from the Mn center.

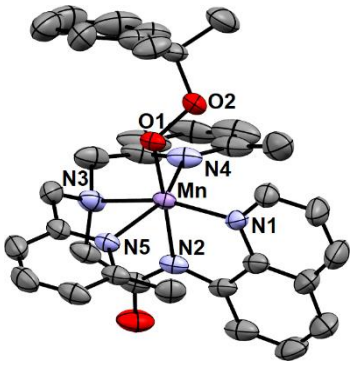

Figure 3.6. ORTEP diagram of cationic portion of [Mn^{III}(OOCm)(^{6Me}dpaq)](OTf) showing 50% probability thermal ellipsoids. Hydrogen atoms of the ^{6Me}dpaq ligand, solvent of crystallization, and the triflate counterion were omitted for clarity.

Spectroscopic Properties of [Mn^{III}(OO^{t}Bu)(^{6Me}dpaq)]$^+$ and [Mn^{III}(OOCm)(^{6Me}dpaq)]$^+$

Although we were unable to obtain crystallographic information concerning [Mn^{III}(OO^{t}Bu)(^{6Me}dpaq)]$^+$, the ^{1}H NMR spectrum of this species in CD_3CN is essentially identical to that of [Mn^{III}(OOCm)(^{6Me}dpaq)]$^+$ (Figure 3.4 and Table 3.2). Each spectrum shows six peaks outside the diamagnetic region, three downfield and three upfield. The only notable difference between the spectra of [Mn^{III}(OO^{t}Bu)(^{6Me}dpaq)]$^+$ and [Mn^{III}(OOCm)(^{6Me}dpaq)]$^+$ are the number of peaks from 10 – 5 ppm (Table 3.2). While [Mn^{III}(OO^{t}Bu)(^{6Me}dpaq)]$^+$ shows a single prominent peak at 9.2 ppm, [Mn^{III}(OOCm)(^{6Me}dpaq)]$^+$ shows five peaks in this region. We tentatively attributed these peaks to protons from the t-butyl and cumyl moieties, respectively. The ^{1}H NMR spectra of [Mn^{III}(OOCm)(^{6Me}dpaq)]$^+$ and [Mn^{III}(OO^{t}Bu)(^{6Me}dpaq)]$^+$ are also very similar to that of [Mn^{III}(OH)(^{6Me}dpaq)]$^+$ (Figure 3.4 and Table 3.2), which is consistent with the same binding mode of the ^{6Me}dpaq ligand in each of these complexes. In particular, the three upfield peaks of the Mn^{III}-alkylperoxo adducts at *ca.* -22, -47, and -60 ppm have chemical shifts very similar to the upfield resonances observed for [Mn^{III}(OH)(^{6Me}dpaq)]$^+$ (-19.3, -45, and -61.6 ppm; see Table 3.2). Similarly, the downfield peaks at *ca.* 67, 46, and 42 ppm in the ^{1}H NMR spectrum of the Mn^{III}-

alkylperoxo adducts show only slight deviations from the corresponding resonances of $[Mn^{III}(OH)(^{6Me}dpaq)]^+$ (66.0, 51.4, and 44.8 ppm; see Table 3.2).The solution FT-IR spectra of $[Mn^{III}(OO^tBu)(^{6Me}dpaq)]^+$ and $[Mn^{III}(OOCm)(^{6Me}dpaq)]^+$ show features at 877 cm^{-1} and 861 cm^{-1}, respectively, that are absent in the FT-IR spectrum of $[Mn^{III}(OH)(^{6Me}dpaq)]^+$ (Figure 3.7). These bands have energies similar to those of O-O vibrations reported for Mn^{III}-alkylperoxo complexes (872 – 895 cm^{-1}; Table A2.3).[15, 16, 25] As such, we assign these features as the O-O stretches of $[Mn^{III}(OO^tBu)(^{6Me}dpaq)]^+$ and $[Mn^{III}(OOCm)(^{6Me}dpaq)]^+$. EPR analysis of frozen 5 mM CH_3CN solutions of $[Mn^{III}(OO^tBu)(^{6Me}dpaq)]^+$ and $[Mn^{III}(OOCm)(^{6Me}dpaq)]^+$ collected at 10 K showed no signals in either perpendicular- or parallel-mode (Figure A2.16). This observation is consistent with the lack of X-band EPR signals for many Mn^{III} complexes due to moderate to large zero-field splitting relative to the microwave energy.[48-52] Additional ESI-MS data and solution-phase magnetic moments further support the formulations for these Mn^{III}-alkylperoxo complexes (Supporting Information).

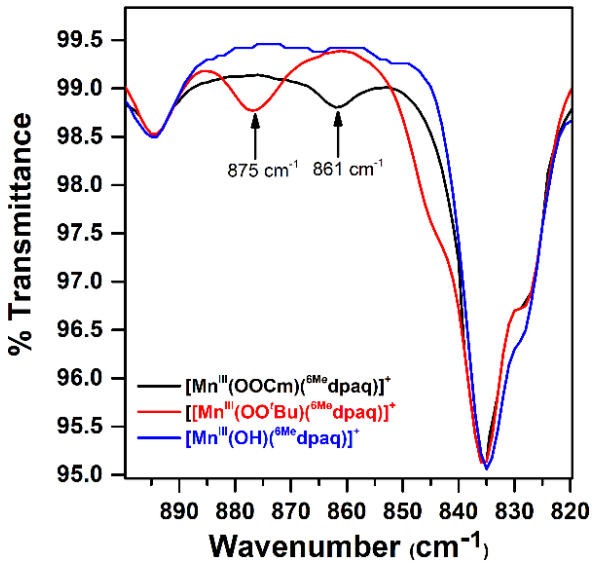

Figure 3.7. Solution FT-IR spectra obtained following the reactions of 2 mM solutions of $[Mn^{III}(OH)(^{6Me}dpaq)]^+$ in CH_3CN and with 1.0 equiv. ^{t}BuOOH (red trace) and 1.0 equiv. CmOOH (black trace). The FT-IR spectrum of $[Mn^{III}(OH)(^{6Me}dpaq)]^+$ (blue trace) is shown for comparison.

Table 3.2 ^{1}H NMR Chemical Shifts (ppm) for $[Mn^{III}(OH)(^{6Me}dpaq)]^+$, $[Mn^{III}(OO^tBu)(^{6Me}dpaq)]^+$, $[Mn^{III}(OOCm)(^{6Me}dpaq)]^+$, and $[Mn^{III}(OH)(dpaq)]^+$ in CD_3CN at 298 K.

$[Mn^{III}(OH)(^{6Me}dpaq)]^+$	$[Mn^{III}(OO^tBu)(^{6Me}dpaq)]^+$	$[Mn^{III}(OOCm)(^{6Me}dpaq)]^+$	$[Mn^{III}(OH)(dpaq)]^+$
			130.5 (H-py)
66.0	66.8	67.8	62.7 (H-qn)
51.4	46.1	46.7	60.9 (H-py)
44.8	42.2	41.8	54.3 (H-py)
			40.5
8.9	9.2	8.9, 7.38, 7.26	
5.5		6.05, 5.3	
-9.6			-4.6 (H-py)
-19.3	-22	-22.3	-15.5 (H-qn)
			-33.7 (H-qn)
-45	-46.9	-47.6	-53.8 (H-qn)
-61.6	-60	-60.3	-63.4 (H-qn)

Data and assignments (in parentheses) for $[Mn^{III}(OH)(dpaq)]^+$ in CD_3CN with 880 equiv. of D_2O from reference 39 (py = pyridine, qn = quinoline).

Thermal Decay Pathways of $[Mn^{III}(OO^tBu)(^{6Me}dpaq)]^+$ and $[Mn^{III}(OOCm)(^{6Me}dpaq)]^+$

The thermal decay of $[Mn^{III}(OO^tBu)(^{6Me}dpaq)]^+$ and $[Mn^{III}(OOCm)(^{6Me}dpaq)]^+$ in CH_3CN at 323 K under anaerobic conditions was monitored by electronic absorption spectroscopy. Each decay reaction progressed with the disappearance of the 650 nm feature associated with the Mn^{III}-

alkylperoxo adduct and the appearance of a feature at 510 nm (Figure 3.8). The feature at 510 nm, along with ESI-MS analyses of the product solutions (Figure A2.17), marks $[Mn^{III}(OH)(^{6Me}dpaq)]^+$ as the major product of these decay reactions (99 and 92% formation from $[Mn^{III}(OOCm)(^{6Me}dpaq)]^+$ and $[Mn^{III}(OO^tBu)(^{6Me}dpaq)]^+$, respectively, on the basis of the extinction coefficient of the Mn^{III}-hydroxo complex). For $[Mn^{III}(OOCm)(^{6Me}dpaq)]^+$, the decay proceeds with isosbestic behavior, and the respective decay and formation rates of the 650 and 510 nm electronic absorption signals are identical (Figure 3.8, right; k_{obs} = 0.016 min^{-1} for both processes). In contrast, the thermal decay for $[Mn^{III}(OO^tBu)(^{6Me}dpaq)]^+$ is not isosbestic, and the rate of formation of the 510 nm chromophore lags behind the decay of the 650 nm band (Figure 3.8, left). We tentatively attribute this difference to the higher purity of $[Mn^{III}(OOCm)(^{6Me}dpaq)]^+$ used in these experiments, as this complex was obtained as a recrystallized solid. In support, thermal decay studies of crude $[Mn^{III}(OOCm)(^{6Me}dpaq)]^+$ also failed to show isosbestic behavior (Figure A2.18). Additional product analysis following the thermal decay of 18 mM $[Mn^{III}(OOCm)(^{6Me}dpaq)]^+$ in CH_3CN at 323 K revealed 61.3 ± 0.1% 2-phenyl-2-propanol and 25.7 ± 0.1% acetophenone formed relative to the initial $[Mn^{III}(OOCm)(^{6Me}dpaq)]^+$ concentration. (The organic products from the thermal decay of $[Mn^{III}(OO^tBu)(^{6Me}dpaq)]^+$ were not quantified, because the volatility of acetone, a potential product, renders quantification unreliable.)

When the decay of 6 mM $[Mn^{III}(OOCm)(^{6Me}dpaq)]^+$ was performed in CD_3CN, we observed 50 ± 0.3% 2-phenyl-2-propanol and 40 ± 0.3% acetophenone relative to the initial $[Mn^{III}(OOCm)(^{6Me}dpaq)]^+$, a marked change in the product distribution. The implications of these results with respect to the decay mechanism are explored in the Discussion section (*vide infra*).

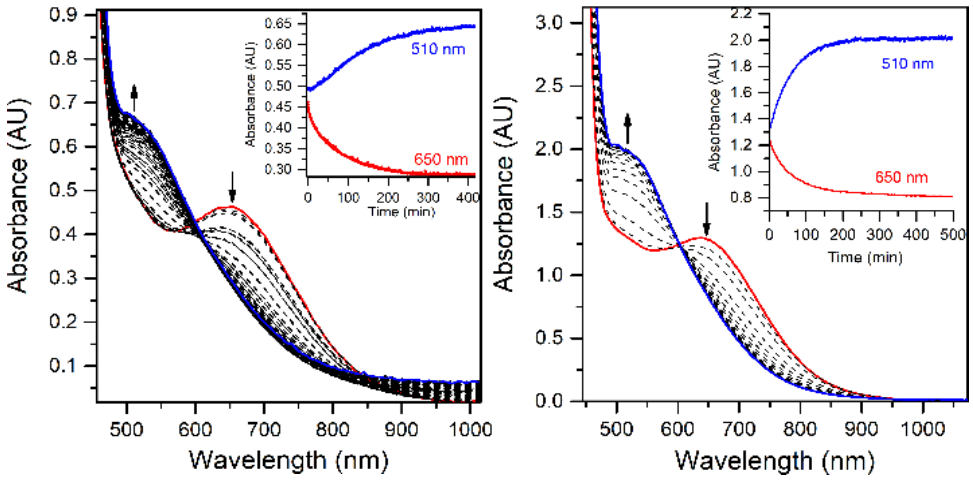

Figure 3.8 Electronic absorption spectra showing the decay of anaerobic CH_3CN solutions of 2 mM $[Mn^{III}(OO^tBu)(^{6Me}dpaq)]^+$ and 6 mM $[Mn^{III}(OOCm)(^{6Me}dpaq)]^+$ (red traces) at 323 K to give $[Mn^{III}(OH)(^{6Me}dpaq)]^+$ (blue traces). The inset shows the change in absorbance at 650 and 510 nm over the course of the decay reaction.

To further probe the decay reactions, we monitored decay kinetics for 1.25 mM CH_3CN solutions of each complex from 303-348 K in CH_3CN under anaerobic conditions. At each temperature, the decay could be fit to a pseudo- first-order process, and the k_{obs} values at different temperatures were fit to the Eyring equation to obtain activation parameters (Figure 3.9). This analysis yielded $\Delta H^{\ddagger}$ = 21.4 ± 1.5 kcal/mol, $\Delta S^{\ddagger}$ = -9.5 ± 4.9 cal/mol·K, and $\Delta G^{\ddagger}$ = 24.2 ± 3.0 kcal/mol at 298 K for $[Mn^{III}(OO^tBu)(^{6Me}dpaq)]^+$; and $\Delta H^{\ddagger}$ = 23.5 ± 1.2 kcal/mol, $\Delta S^{\ddagger}$ = -1.5 ± 3.6 cal/mol·K, and $\Delta G^{\ddagger}$ = 23.9 ± 2.2 kcal/mol at 298 K for $[Mn^{III}(OOCm)(^{6Me}dpaq)]^+$. Both complexes display $\Delta H^{\ddagger}$ values significantly higher than those of the $[Mn^{III}(OOR)(N_4S)]^+$ complexes ($\Delta H^{\ddagger}$ = 15.9 - 10.5 kcal/mol),[16] which is in line with the greater thermal stabilities of $[Mn^{III}(OO^tBu)(^{6Me}dpaq)]^+$ and $[Mn^{III}(OOCm)(^{6Me}dpaq)]^+$. The entropies of activation of $Mn^{III}(OO^tBu)(^{6Me}dpaq)]^+$ and $[Mn^{III}(OOCm)(^{6Me}dpaq)]^+$ are slightly negative and smaller in magnitude than those of the $[Mn^{III}(OOR)(N_4S)]^+$ complexes ($\Delta S^{\ddagger}$ = -15 to -34 cal mol^{-1} K^{-1}).

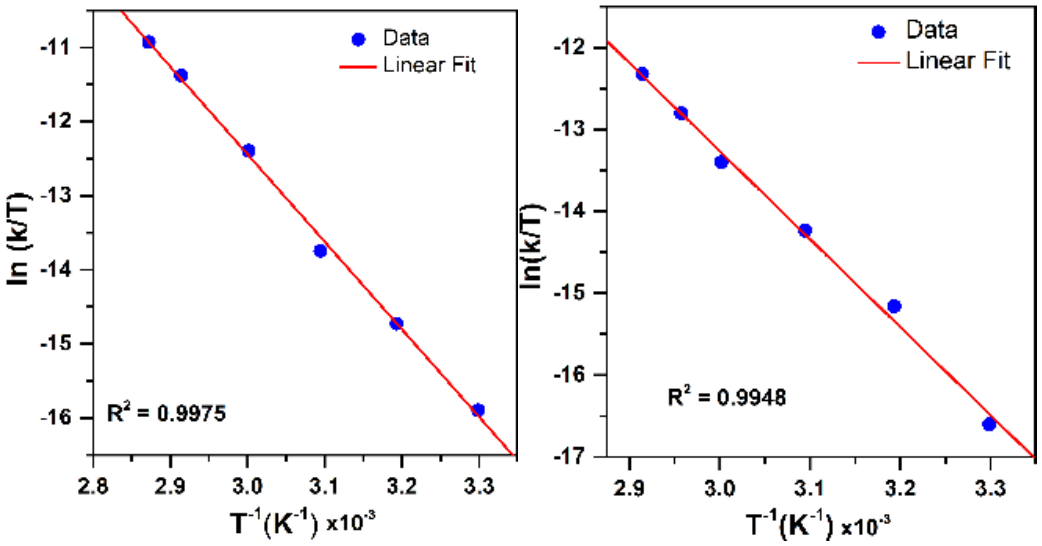

Figure 3.9. Eyring plot from variable-temperature thermal decay kinetics of $[Mn^{III}(OO^tBu)(^{6Me}dpaq)]^+$ (left) and $[Mn^{III}(OOCm)(^{6Me}dpaq)]^+$ (right) in CH_3CN.

Substrate Oxidation by Mn^{III}-alkylperoxo Adducts.

Direct Oxidation of Triphenylphosphine

The addition of 100 equiv. PPh_3 to an anaerobic solution of $[Mn^{III}(OO^tBu)(^{6Me}dpaq)]^+$ (2.0 mM in CH_3CN) at 298 K resulted in the loss of intensity at 650 nm over the course of two hours, resulting in an electronic absorption spectrum consistent with the generation of Mn^{II} products (Figure 3.10, left). The decay of the 650 nm absorption signal could be well-fit to a first-order model, yielding a pseudo-first- order rate constant k_{obs} (Figure 3.10, left inset). A ^{31}P NMR analysis of the organic products revealed the formation of Ph_3PO (Figure A2.19). EPR analysis of the reaction mixture shows a signal centered at g = 2.03 that is similar in appearance to that of the $[Mn^{II}(H_2O)(^{6Me}dpaq)]OTf$ starting material, albeit with the lack of apparent hyperfine splitting (Figure A2.20). [30, 31] This evidence is in accordance with the featureless UV-vis spectrum of the final reaction mixture, which is characteristic of a Mn^{II} product (Figure 3.10, left). The rate of decay of $[Mn^{III}(OO^tBu)(^{6Me}dpaq)]^+$ increased linearly with increasing concentrations of PPh_3

(Figure 3.10, right). A linear fit of k_{obs} versus PPh_3 concentration yields a second-order rate constant for PPh_3 oxidation by $[Mn^{III}(OO^tBu)(^{6Me}dpaq)]^+$ of 0.0035 $M^{-1}s^{-1}$ at 298 K in CH_3CN. The $[Mn^{III}(OOCm)(^{6Me}dpaq)]^+$ complex displayed similar reactivity with PPh_3 (k_2 = 0.0033 $M^{-1}s^{-1}$ at 298 K; see Figure A2.21). These rates show that the nature of the alkylperoxo group does not have a significant influence on the reactivity with PPh_3.

Further insight into the reaction of PPh_3 with $[Mn^{III}(OO^tBu)(^{6Me}dpaq)]^+$ was obtained through an Eyring analysis of variable-temperature kinetic experiments (Figure 3.11). These experiments yielded $\Delta H^{\ddagger}$ = 17.6 ± 1.4 kcal/mol, $\Delta S^{\ddagger}$ = -12.6 ± 4.6 cal/mol·K, and $\Delta G^{\ddagger}$ = 21.3 ± 2.8 kcal/mol at 298 K. The high activation enthalpy and Gibbs free energy of activation account for the sluggishness of this reaction, and the negative entropy of activation is consistent with a bimolecular reaction.

Mechanistic insight into the reaction between PPh_3 and the Mn^{III}-alkylperoxo was obtained by the reaction of 22 mM $[Mn^{III}(OOCm)(^{6Me}dpaq)]^+$ with 5 equiv. of PPh_3 in CH_3CN at 298 K. Quantification of the organic products of this reaction by GC-MS revealed 88.5 ± 0.3% 2-phenyl-2-propanol and 1.5 ± 0.3% acetophenone based on the initial concentration of $[Mn^{III}(OOCm)(^{6Me}dpaq)]^+$. ESI-MS analysis of the final reaction mixtures for the reaction of $[Mn^{III}(OOCm)(^{6Me}dpaq)]^+$ with PPh_3 showed the presence of peaks at *m/z* = 465.14, 482.14 and 743.23, which are consistent with expected *m/z* values for $[Mn^{II}(^{6Me}dpaq)]^+$, $[Mn^{III}(OH)(^{6Me}dpaq)]^+$ and $[Mn^{III}(OPPh_3)(^{6Me}dpaq)]^+$, respectively (Figure A2.22).

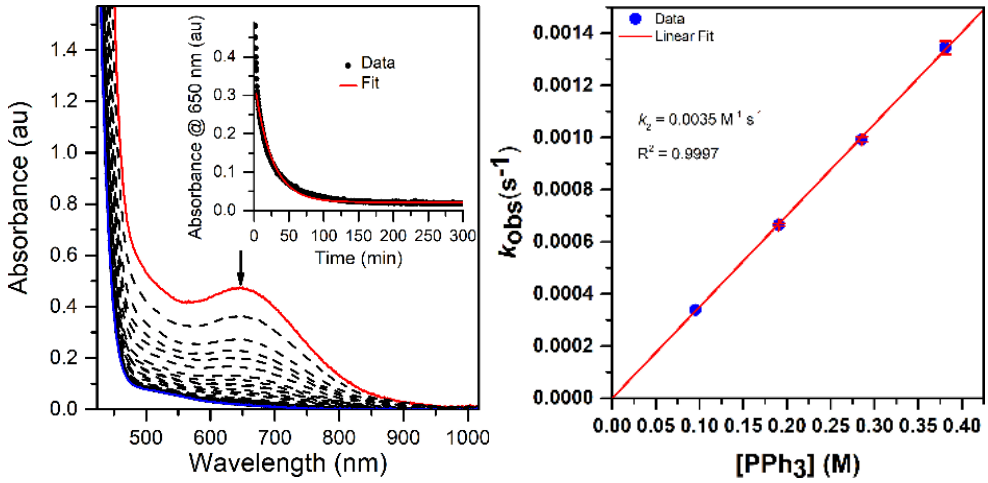

Figure 3.10. Left: Electronic absorption spectra monitoring the reaction of a 2.0 mM anaerobic solution of $[Mn^{III}(OO^tBu)(^{6Me}dpaq)]^+$ (red trace) in CH_3CN with 100 equiv of PPh_3 at 298 K. Left Inset: time course for the spectral changes. Right: Pseudo-first-order rate constants, k_{obs} (s^{-1}), versus PPh_3 concentration (M) for a 1.25 mM solution of $[Mn^{III}(OO^tBu)(^{6Me}dpaq)]^+$ at 298 K.

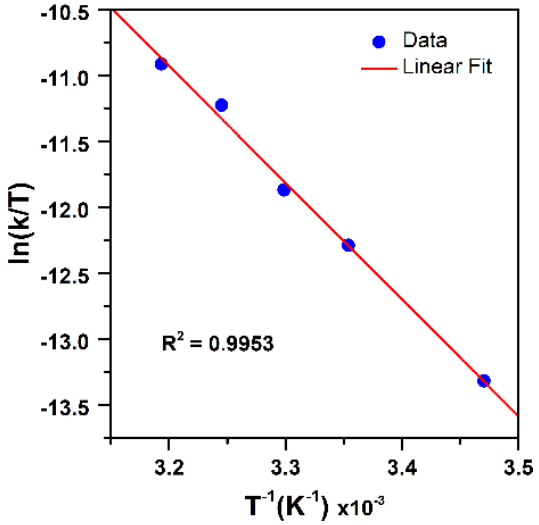

Figure 3.11. Eyring plot from variable-temperature reaction kinetics of $[Mn^{III}(OO^tBu)(^{6Me}dpaq)]^+$ with PPh_3 in CH_3CN.

Indirect Oxidation of 9,10-Dihydroanthracene (DHA)

The reaction of the Mn^{III}-alkylperoxo complexes with the hydrogen-atom donor DHA was also explored. In this case, the addition of a large excess of DHA (100 equiv. relative to Mn^{III})

to[Mn^{III}(OO^{t}Bu)(^{6Me}dpaq)]$^+$ or [Mn^{III}(OOCm)(^{6Me}dpaq)]$^+$ in CH_3CN at 323 K did not result in any change in the rate of decay of the Mn^{III}-alkylperoxo complexes (Figure A2.23). We also observed no change in the thermal decay rate with d_4-DHA (Figure A2.13). Nonetheless, an analysis of the reaction solution following the full thermal decay of [Mn^{III}(OO^{t}Bu)(^{6Me}dpaq)]$^+$ or [Mn^{III}(OOCm)(^{6Me}dpaq)]$^+$ (after *ca.* 7 hours) revealed the formation of *ca.* 1.4 equiv. anthracene relative to the starting Mn^{III}-alkylperoxo concentration (Figure A2.11). Thus, while neither [Mn^{III}(OO^{t}Bu)(^{6Me}dpaq)]$^+$ nor [Mn^{III}(OOCm)(^{6Me}dpaq)]$^+$ is capable of direct oxidation of DHA, a product of the thermal decay of each complex is an effective oxidant of DHA.

3.4 Discussion

Ligand-Sphere Influence on the Structure-Property Correlations of Mn^{III}-alkylperoxo Complexes

The generation of the room-temperature stable [Mn^{III}(OO^{t}Bu)(^{6Me}dpaq)]$^+$ and [Mn^{III}(OOCm)(^{6Me}dpaq)]$^+$ complexes relied upon previous observations that Mn^{III} centers with higher Lewis acidity give rise to corresponding Mn^{III}-alkylperoxo adducts with shorter and more stable O-O bonds.[16] The basis of this correlation rests on the π-donating properties of the alkylperoxo ligand. A more Lewis acidic Mn^{III} center fosters greater π-donation from the alkylperoxo π* MO, which strengths the O-O bond. The 6-Me-pyridyl groups of the structurally characterized [Mn^{III}(OOCm)(^{6Me}dpaq)]$^+$ complex give two elongated Mn-N distances of 2.284(4) and 2.394(4) Å. These weak metal-ligand interactions increase the Lewis acidity of the Mn^{III} center, stabilizing the Mn^{III}-alkylperoxo unit.

The crystal structure of [Mn^{III}(OOCm)(^{6Me}dpaq)]$^+$ allows us to determine how closely this complex follows previously observed correlations based on the [Mn^{III}(OOR)(N_4S)]$^+$ complex. The

$[Mn^{III}(OOR)(N_4S)]^+$ complexes showed a linear correlation between the elongated Mn-N distances and the O-O bond lengths, with the shortest Mn-N distances of *ca.* 2.40 Å giving rise to the longest O-O bonds of *ca.* 1.47 Å (Figure 3.12). The metric parameters for $[Mn^{III}(OOCm)(^{6Me}dpaq)]^+$ follow the spirit of this correlation; that is, this complex has a short average Mn-N distance of 2.34 Å and an O-O bond of 1.466(4) Å, on the long end of that observed for Mn^{III}-alkylperoxo adducts (1.43 – 1.47 Å). However, if we use the previous correlation as a guide, the Mn-N distances observed for $[Mn^{III}(OOCm)(^{6Me}dpaq)]^+$ would predict a O-O bond length far longer than that observed, making this complex a clear outlier (Figure 3.12). It is not completely surprising that the markedly different coordination spheres of $[Mn^{III}(OOCm)(^{6Me}dpaq)]^+$ and the $[Mn^{III}(OOR)(N_4S)]^+$ series would cause such a deviation, as the O-O distance should be a reporter of the entire coordination sphere. It is additionally possible that there is a limit to the extent to which the O-O bond can be elongated in Mn^{III}-OOR complexes, and that the limit is near 1.47 Å.

The $[Mn^{III}(OOCm)(^{6Me}dpaq)]^+$ complex also breaks the previously observed correlation that Mn^{III}-alkylperoxo adducts with longer O-O bonds are less stable than those with shorter O-O bonds.[15] $[Mn^{III}(OOCm)(^{6Me}dpaq)]^+$ has an O-O distance at the long end of the$[Mn^{III}(OOR)(N_4S)]^+$ series but has a room-temperature half-life of *ca*. 5 days. In contrast, the most stable $[Mn^{III}(OOR)(N_4S)]^+$ complex has a half-life of *ca.* 5 minutes at 293 K.[16] One caveat that must be noted in comparing the thermal stability of $[Mn^{III}(OOCm)(^{6Me}dpaq)]^+$ with the $[Mn^{III}(OOR)(N_4S)]^+$ series is the difference in solvents (CH_3CN and CH_2Cl_2, respectively).[16] To address this complication, we determined the half-life of $[Mn^{III}(OOCm)(^{6Me}dpaq)]^+$ in CH_2Cl_2 at 298 K. The $[Mn^{III}(OOCm)(^{6Me}dpaq)]^+$ complex did decay more rapidly in CH_2Cl_2 than in CH_3CN (half-life of 3 vs. 8 days, respectively). While solvent does have some effect on the stability of the Mn^{III}-alkylperoxo complex, the solvent change alone cannot account for the dramatic increase in

stability of the $[Mn^{III}(OOR)(^{6Me}dpaq)]^+$ complexes relative to the $[Mn^{III}(OOR)(N_4S)]^+$ series. On this basis, while also noting the limited sample size, it is tempting to speculate that the presence of thiolate ligands in the $[Mn^{III}(OOR)(N_4S)]^+$ series severely reduces the stability of the Mn^{III}-alkylperoxo adducts. This conclusion makes it all the more remarkable that the first isolable Mn^{III}-alkylperoxo adducts contained thiolate ligands.

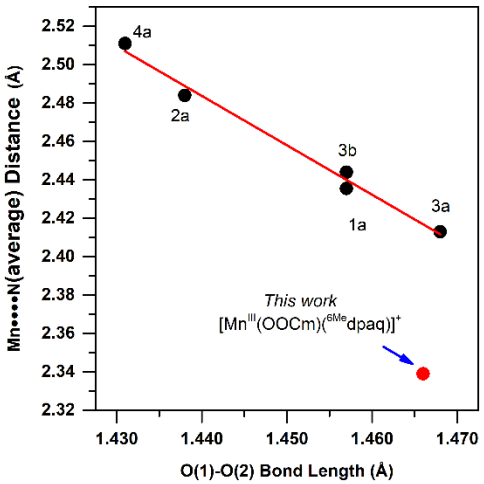

Figure 3.12 Correlation between average Mn-distance and alkylperoxo O-O bond length for $[Mn^{III}(OOR)(N_4S)]^+$ complexes (see ref. 16) and corresponding point for $[Mn^{III}(OOCm)(^{6Me}dpaq)](OTf)$ described in this work.

Thermal decay mechanism of $[Mn^{III}(OOCm)(^{6Me}dpaq)]^+$

The organic products observed upon the decay of cumylperoxo-metal complexes are often used to infer the nature of the decay pathway.[53] Homolytic cleavage of the O-O bond produces cumyloxyl radical that can rearrange by β-scission to produce acetophenone and $\cdot CH_3$ (Scheme 3.2, path b). Alternatively, heterolytic cleavage of the O-O bond produces cumyl oxyanion that can deprotonate solvent to produce 2-phenyl-2-propanol (Scheme 3.2, path a).[53-55] Previous studies of Mn^{III}-alkylperoxo[16] and some Fe^{III}-alkylperoxo[12] complexes showed organic products exclusively attributable to O-O homolysis. In contrast, there are examples of Cu^{II}-alkylperoxo[56]

adducts that decay exclusively by heterolytic cleavage of the O-O bond, and there are a handful of examples where the decay of a metal-alkylperoxo adduct yields a mixture of products characteristic of both pathways.[2, 5, 11, 13, 57]

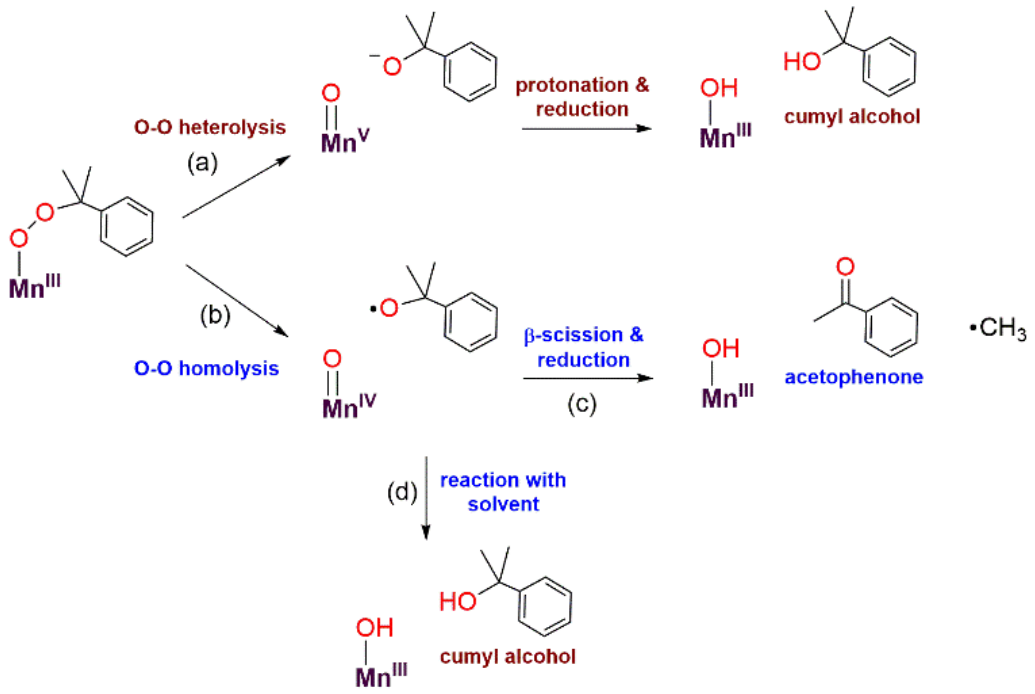

Scheme 3.2. Possible Decay pathways for $[Mn^{III}(OOCm)(^{6Me}dpaq)](OTf)$.

Analysis of the organic decay products of $[Mn^{III}(OOCm)(^{6Me}dpaq)]^{+}$ reveal both 2-phenyl-2-propanol and acetophenone (61 and 26% yield relative to the $[Mn^{III}(OOCm)(^{6Me}dpaq)]^{+}$adduct). Electronic absorption, ^{1}H NMR, and ESI-MS data identify $[Mn^{III}(OH)(^{6Me}dpaq)]^{+}$ as a dominant decay product (Figure A2.17 and Figure A2.24*)*. The distribution of 2-phenyl-2-propanol and acetophenone could suggest that both homolysis and heterolysis of the O-O bond occur in the thermal decay of $[Mn^{III}(OOCm)(^{6Me}dpaq)]^{+}$ in CH_3CN, with a slight preference for the heterolytic pathway. Either O-O cleavage pathway would yield a high-valent Mn-oxo intermediate that could be reduced to the observed Mn^{III}-hydroxo product. There are recent reports of Mn^{IV}-oxo adducts of the closely related dpaq ligand that react with C-H bonds to yield a Mn^{III}-hydroxo product.[58, 59]

To clarify the decay pathway of $[Mn^{III}(OOCm)(^{6Me}dpaq)]^+$, we examined the products formed when the complex decayed in CD_3CN. In this case, we observed increased formation of acetophenone and decreased formation of 2-phenyl-2-propanol (40:50%) compared to the decay in CH_3CN (26:61%). A change in product distribution in deuterated solvent was also observed by Cho *et al*.[13] Itoh[2, 3] and others[53, 54] have rationalized a change in the acetophenone: 2-phenyl-2-propanol product distribution in terms of solvent involvement in the decay pathway. In CH_3CN, the cumyloxyl radical decays by competing reactions: 1) □-scission to yield acetophenone and methyl radical, and 2) hydrogen-atom abstract from solvent to yield 2-phenyl-2-propanol (Scheme 2, paths c and d).[2, 3, 53, 56, 57, 60] In CD_3CN, the rate of the hydrogen-atom abstraction reaction from the solvent is decreased, yielding a marked increase in acetophenone formation by □-scission. Consequently, the change in the distribution of acetophenone: 2-phenyl-2-propanol in CD_3CN is strong evidence for homolysis of the O-O bond of $[Mn^{III}(OOCm)(^{6Me}dpaq)]^+$. Whether or not some of the 2-phenyl-2-propanol product derives from a minor heterolytic pathway is unclear at present.

A second line of evidence for the production of cumyloxyl radicals by O-O homolysis of $[Mn^{III}(OOCm)(^{6Me}dpaq)]^+$ comes from changes to the decay kinetics of $[Mn^{III}(OOCm)(^{6Me}dpaq)]^+$ in CH_3CN and CD_3CN. The $[Mn^{III}(OOCm)(^{6Me}dpaq)]^+$ complex decays slowly in CH_3CN, and this rate of decay matches the rate of formation of the $[Mn^{III}(OH)(^{6Me}dpaq)]^+$ product (Figure 3.8). In contrast, the decay rate of $[Mn^{III}(OOCm)(^{6Me}dpaq)]^+$ increases in CD_3CN by about eight-fold relative to that in CH_3CN (Figure A2.25). In addition, the decay rate of $[Mn^{III}(OOCm)(^{6Me}dpaq)]^+$ in CD_3CN is five-fold faster than the rate of formation of $[Mn^{III}(OH)(^{6Me}dpaq)]^+$. These observations are consistent with our proposal that $[Mn^{III}(OOCm)(^{6Me}dpaq)]^+$ decays by homolytic O-O cleavage to give a Mn^{IV}-oxo adduct and cumyloxyl radical. In CH_3CN, the cumyloxyl radical

and Mn^{IV}-oxo intermediates react rapidly and preferentially with solvent to give the observed $[Mn^{III}(OH)(^{6Me}dpaq)]^+$ and 2-phenyl-2-propanol products. Under these conditions, a relatively small amount of cumyloxyl radical undergoes β-scission to yield acetophenone. In CD_3CN, the Mn^{IV}-oxo adduct and cumyloxyl radical decay products have slower rates of reaction with solvent, allowing for reaction with $[Mn^{III}(OOCm)(^{6Me}dpaq)]^+$, which hastens its decay.

Reaction mechanism of $[Mn^{III}(OOCm)(^{6Me}dpaq)]^+$ with PPh_3

To the best of our knowledge, the reactions of $[Mn^{III}(OO^tBu)(^{6Me}dpaq)]^+$ and $[Mn^{III}(OOCm)(^{6Me}dpaq)]^+$ with PPh_3 at 298 K are the first observations of direct substrate oxidation by Mn^{III}-alkylperoxo complexes. The reaction of $[Mn^{III}(OOCm)(^{6Me}dpaq)]^+$ with PPh_3 showed the near exclusive formation of 2-phenyl-2-propanol, with only a trace amount of acetophenone (Figure A2.26). This distribution suggests a change to O-O heterolysis under these conditions. An Eyring analysis for the reaction of $[Mn^{III}(OO^tBu)(^{6Me}dpaq)]^+$ with PPh_3 gives $\Delta S^{\ddagger}$ = -12.6 ± 4.6 cal/mol·K, which is consistent with a bimolecular reaction involving the association of $[Mn^{III}(OO^tBu)(^{6Me}dpaq)]^+$ with PPh_3 to form the activated complex. The change in reaction rate as a function of PPh_3 concentration is further evidence of a direct reaction between the $[Mn^{III}(OOR)(^{6Me}dpaq)]^+$ complexes and PPh_3. We propose a reaction mechanism where $[Mn^{III}(OOR)(^{6Me}dpaq)]^+$ and PPh_3 form an activated complex, with PPh_3 interacting with the proximal oxygen of the alkylperoxo ligand (Scheme 3.3). Recent reports show that Brønsted and Lewis acids, or the introduction of secondary coordination interaction through pendant amines which act as hydrogen-bond acceptor in an Fe^{III}-OOR (R = H, acyl) adduct could direct heterolytic cleavage.[11, 61-63] This interaction between $[Mn^{III}(OOR)(^{6Me}dpaq)]^+$ and PPh_3 may also be able to instigate heterolytic cleavage of the Mn^{III}-alkylperoxo O-O bond. For the $[Mn^{III}(OOCm)(^{6Me}dpaq)]^+$ complex, this decay will lead to the formation of cumyloxy anion,

which gives 2-phenyl-2-propanol after protonation[2, 56, 57] and a Mn^{III}-species that is reduced to the Mn^{II} product observed by UV-vis and EPR spectroscopy (Scheme 3.3). The identity of the reductant for the Mn^{III} center is unclear.

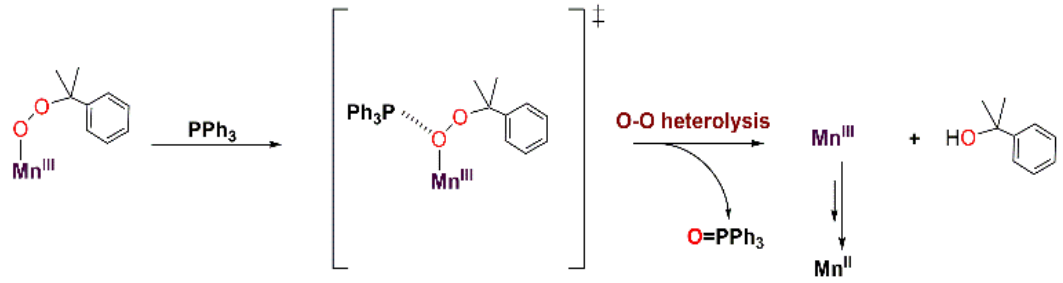

Scheme 3.3. Proposed mechanisms for PPh_3 oxidation by $[Mn^{III}(OOCm)(^{6Me}dpaq)]^+$.

Reaction mechanism of $[Mn^{III}(OOCm)(^{6Me}dpaq)](OTf)$ with DHA

In contrast to the direct oxidation of PPh_3, the reaction of $[Mn^{III}(OO^tBu)(^{6Me}dpaq)]^+$ and $[Mn^{III}(OOCm)(^{6Me}dpaq)]^+$ with DHA is an indirect oxidation caused by products of the Mn^{III}-alkylperoxo decay process (Scheme 3.4). Neither $[Mn^{III}(OOR)(^{6Me}dpaq)]^+$ complex shows any change in decay rate in the presence of an excess amount of DHA (Figure A2.13), although the decay solutions reveal the formation of 1.4 equiv. anthracene relative to the initial Mn^{III}-OOR concentration. The notion that the reaction is indirect is further supported by the lack of any change in decay rate when d_4-DHA is used as substrate (Figure A2.13).

The formation of 1.4 equiv. anthracene is consistent with the thermal decay of the $[Mn^{III}(OOR)(^{6Me}dpaq)]^+$ complexes by O-O homolysis (Scheme 3.4). The Mn^{IV}-oxo decay product should be capable of DHA oxidation, as observed for several oxo-manganese complexes.[58, 59] This reaction will result in a Mn^{II}-aqua complex, consistent with the observation of a Mn^{II} signal in the EPR spectrum of the final reaction mixture (Figure A2.27). The cumyloxyl radical also generated by O-O homolysis could be responsible for the remaining 0.4 equiv. anthracene.

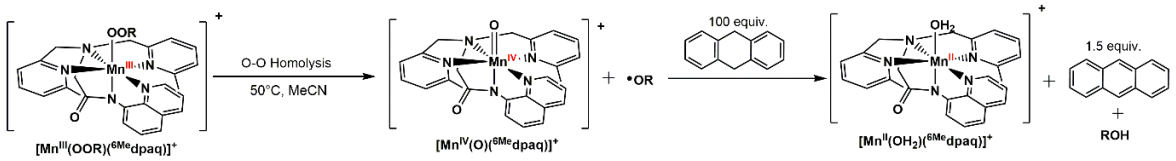

Scheme 3.4. Mechanistic proposal for the reaction of DHA with $[Mn^{III}(OO^{t}Bu)(^{6Me}dpaq)]^{+}$.

3.5 Conclusions

Inspired by previously developed structure-reactivity correlations, we developed a new ligand derivative (^{6Me}dpaq) that provides remarkable stability to Mn^{III}-alkylperoxo complexes. A simple change of two pyridyl groups to 6-Me-pyridyl groups results in new Mn^{III}-alkylperoxo complexes that i) can be generated using stoichiometric amounts of oxidant rather than large excesses, and ii) are stable at room temperature. This enhanced stability allowed us to structurally characterize a Mn^{III}-cumylperoxo adduct by X-ray diffraction. In spite of the unusual stability of these Mn^{III}-alkylperoxo adducts, these complexes are the first members of their class to show direct reactivity with a substrate (triphenylphosphine). This result demonstrates that the ligand-sphere of Mn^{III}-alkylperoxo adducts has great control over reactivity. These N_5^--ligated Mn^{III}-alkylperoxo adducts show a dominant decay pathway by homolytic O-O bond cleavage, similar to that observed for Mn^{III}-alkylperoxo adducts bound by thiolate-containing N_4S^- ligands. While the basis of the enhanced stability of $[Mn^{III}(OO^{t}Bu)(^{6Me}dpaq)]^{+}$ and $[Mn^{III}(OO^{t}Bu)(^{6Me}dpaq)]^{+}$ will be the subject of future investigations, it is tempting to speculate that the thiolate ligands in the $[Mn^{III}(OOR)(N_4S)]^{+}$ complexes serve to lower the activation energy for decay. In addition, while the new Mn^{III}-alkylperoxo adducts generally follow a previously identified structural correlation between Mn-N and O-O distances, the observed O-O distance for the Mn^{III}-cumylperoxo adduct is far shorter than expected on the basis of the Mn-N distances. Thus, perturbations to the primary coordination sphere not only affect reactivity but also render this complex an outlier compared to

previous compounds. Future work will be aimed at understanding the basis for this outlier status in terms of both structural correlations and chemical reactivity.

3.6 Acknowledgements

This work was supported by the U.S. National Science Foundation (CHE-1565661 to T.A.J). Support for the NMR instrumentation was provided by NIH Shared Instrumentation Grant # S10OD016360. The U.S. NSF is also acknowledged for funds used for the purchase of X-ray instruments (CHE-0079282) and the EPR spectrometer (CHE-0946883). We will also want to acknowledge Samuel R. Crowell for the provision of some [Mn^{III}(OH)(^{6Me}dpaq)](OTf) complex.

3.7 References

1. F. A. Chavez and P. K. Mascharak, *Accounts of Chemical Research*, 2000, **33**, 539-545.
2. T. Tano, M. Z. Ertem, S. Yamaguchi, A. Kunishita, H. Sugimoto, N. Fujieda, T. Ogura, C. J. Cramer and S. Itoh, *Dalton Transactions*, 2011, **40**, 10326-10336.
3. S. Itoh, *Accounts of Chemical Research*, 2015, **48**, 2066-2074.
4. F. A. Chavez, C. V. Nguyen, M. M. Olmstead and P. K. Mascharak, *Inorganic Chemistry*, 1996, **35**, 6282-6291.
5. F. A. Chavez, J. M. Rowland, M. M. Olmstead and P. K. Mascharak, *Journal of the American Chemical Society*, 1998, **120**, 9015-9027.
6. R. Chakrabarty, P. Sarmah, B. Saha, S. Chakravorty and B. K. Das, *Inorganic Chemistry*, 2009, **48**, 6371-6379.
7. G. W. Parshall and S. D. Ittel, *Homogeneous Catalysis. The applications and Chemistry of Catalysis by Soluble Transition Metal Complexes* Wiley-Interscience, New York, 1992.
8. J. Ebner and D. Riley, 1995, 205-248.
9. P. F. Fitzpatrick, *Biochemistry*, 2003, **42**, 14083-14091.
10. S. C. Peck and W. A. van der Donk, *JBIC Journal of Biological Inorganic Chemistry*, 2017, **22**, 381-394.
11. I. Ghosh, S. Banerjee, S. Paul, T. Corona and T. K. Paine, *Angewandte Chemie International Edition*, 2019, **58**, 12534-12539.
12. S. Hong, Y.-M. Lee, K.-B. Cho, M. S. Seo, D. Song, J. Yoon, R. Garcia-Serres, M. Clémancey, T. Ogura, W. Shin, J.-M. Latour and W. Nam, *Chemical Science*, 2014, **5**, 156-162.
13. B. Kim, D. Jeong and J. Cho, *Chemical Communications*, 2017, **53**, 9328-9331.
14. H. Oh, W.-M. Ching, J. Kim, W.-Z. Lee and S. Hong, *Inorganic Chemistry*, 2019, **58**, 12964-12974.

15. M. K. Coggins and J. A. Kovacs, *Journal of the American Chemical Society*, 2011, **133**, 12470-12473.
16. M. K. Coggins, V. Martin-Diaconescu, S. DeBeer and J. A. Kovacs, *Journal of the American Chemical Society*, 2013, **135**, 4260-4272.
17. M. Sankaralingam, Y.-M. Lee, S. H. Jeon, M. S. Seo, K.-B. Cho and W. Nam, *Chemical Communications*, 2018, **54**, 1209-1212.
18. H. So, Y. J. Park, K.-B. Cho, Y.-M. Lee, M. S. Seo, J. Cho, R. Sarangi and W. Nam, *Journal of the American Chemical Society*, 2014, **136**, 12229-12232.
19. N. Lehnert, F. Neese, R. Y. N. Ho, L. Que and E. I. Solomon, *Journal of the American Chemical Society*, 2002, **124**, 10810-10822.
20. P. Chen, K. Fujisawa and E. I. Solomon, *Journal of the American Chemical Society*, 2000, **122**, 10177-10193.
21. B. Kim, D. Jeong, T. Ohta and J. Cho, *Communications Chemistry*, 2019, **2**, 81.
22. A. S. Faponle, M. G. Quesne, C. V. Sastri, F. Banse and S. P. de Visser, *Chemistry (Weinheim an der Bergstrasse, Germany)*, 2015, **21**, 1221-1236.
23. L. R. Widger, Y. Jiang, A. C. McQuilken, T. Yang, M. A. Siegler, H. Matsumura, P. Moënne-Loccoz, D. Kumar, S. P. de Visser and D. P. Goldberg, *Dalton Transactions*, 2014, **43**, 7522-7532.
24. A. W. Stubbs and M. Dincă, *Inorganic Chemistry*, 2019, **58**, 13221-13228.
25. J. D. Parham, G. B. Wijeratne, D. B. Rice and T. A. Jackson, *Inorganic Chemistry*, 2018, **57**, 2489-2502.
26. G. B. Wijeratne, B. Corzine, V. W. Day and T. A. Jackson, *Inorganic Chemistry*, 2014, **53**, 7622-7634.
27. H. Nagao, N. Komeda, M. Mukaida, M. Suzuki and K. Tanaka, *Inorganic Chemistry*, 1996, **35**, 6809-6815.
28. V. R. Kokatnur and M. Jelling, *Journal of the American Chemical Society*, 1941, **63**, 1432-1433.
29. Y. Hitomi, K. Arakawa, T. Funabiki and M. Kodera, *Angew. Chem., Int. Ed.*, 2012, **51**, 3448-3452.
30. D. B. Rice, G. B. Wijeratne, A. D. Burr, J. D. Parham, V. W. Day and T. A. Jackson, *Inorganic Chemistry*, 2016, **55**, 8110-8120.
31. M. K. Coggins, S. Toledo, E. Shaffer, W. Kaminsky, J. Shearer and J. A. Kovacs, *Inorganic chemistry*, 2012, **51**, 6633-6644.
32. D. B. Rice, A. Munasinghe, E. N. Grotemeyer, A. D. Burr, V. W. Day and T. A. Jackson, *Inorganic Chemistry*, 2019, **58**, 622-636.
33. Data Collection: SMART Software in APEX2 v2014.11-0 Suite. Bruker-AXS, 5465 E. Cheryl Parkway, Madison, WI 53711-5373 USA.
34. Data Reduction: SAINT Software in APEX2 v2014.11-0 Suite. Bruker-AXS, 5465 E. Cheryl Parkway, Madison, WI 53711-5373 USA.
35. Refinement: SHELXTL Software in APEX2 v2014.11-0 Suite. Bruker-AXS, 5465 E. Cheryl Parkway, Madison, WI 53711-5373 USA.
36. C. R. Goldsmith, A. P. Cole and T. D. P. Stack, *Journal of the American Chemical Society*, 2005, **127**, 9904-9912.
37. S. El Ghachtouli, B. Lassalle-Kaiser, P. Dorlet, R. Guillot, E. Anxolabéhère-Mallart, C. Costentin and A. Aukauloo, *Energy & Environmental Science*, 2011, **4**, 2041-2044.

38. Z. Shirin, B. S. Hammes, V. G. Young and A. S. Borovik, *Journal of the American Chemical Society*, 2000, **122**, 1836-1837.
39. B. Cheng, P. H. Fries, J.-C. Marchon and W. R. Scheidt, *Inorganic Chemistry*, 1996, **35**, 1024-1032.
40. A. A. Eroy-Reveles, Y. Leung, C. M. Beavers, M. M. Olmstead and P. K. Mascharak, *Journal of the American Chemical Society*, 2008, **130**, 4447-4458.
41. D. M. Eichhorn and W. H. Armstrong, *Journal of the Chemical Society, Chemical Communications*, 1992, DOI: 10.1039/C39920000085, 85-87.
42. T. J. Hubin, J. M. McCormick, N. W. Alcock and D. H. Busch, *Inorganic Chemistry*, 2001, **40**, 435-444.
43. M. K. Coggins, L. M. Brines and J. A. Kovacs, *Inorganic Chemistry*, 2013, **52**, 12383-12393.
44. Z. Shirin, A. S. Borovik and V. G. Young Jr, *Chemical Communications*, 1997, DOI: 10.1039/A703395H, 1967-1968.
45. D. B. Rice, S. D. Jones, J. T. Douglas and T. A. Jackson, *Inorganic Chemistry*, 2018, **57**, 7825-7837.
46. C. Fontaine, K. N. V. Duong, C. Merienne, A. Gaudemer and C. Giannotti, *Journal of Organometallic Chemistry*, 1972, **38**, 167-178.
47. L. Saussine, E. Brazi, A. Robine, H. Mimoun, J. Fischer and R. Weiss, *Journal of the American Chemical Society*, 1985, **107**, 3534-3540.
48. A. Abragam and B. Bleaney, *Electron Paramagnetic Resonance of Transition Ions*, Dover Publications Inc., New York, 1986.
49. A.-L. Barra, D. Gatteschi, R. Sessoli, G. L. Abbati, A. Cornia, A. C. Fabretti and M. G. Uytterhoeven, *Angewandte Chemie International Edition in English*, 1997, **36**, 2329-2331.
50. D. P. Goldberg, J. Telser, J. Krzystek, A. G. Montalban, L.-C. Brunel, A. G. M. Barrett and B. M. Hoffman, *Journal of the American Chemical Society*, 1997, **119**, 8722-8723.
51. J. Krzystek, J. Telser, B. M. Hoffman, L.-C. Brunel and S. Licoccia, *Journal of the American Chemical Society*, 2001, **123**, 7890-7897.
52. J. Limburg, J. S. Vrettos, R. H. Crabtree, G. W. Brudvig, J. C. de Paula, A. Hassan, A.-L. Barra, C. Duboc-Toia and M.-N. Collomb, *Inorganic Chemistry*, 2001, **40**, 1698-1703.
53. D. V. Avila, C. E. Brown, K. U. Ingold and J. Lusztyk, *Journal of the American Chemical Society*, 1993, **115**, 466-470.
54. I. Chodák, D. Bakoš and V. Mihálov, *Journal of the Chemical Society, Perkin Transactions 2*, 1980, DOI: 10.1039/P29800001457, 1457-1459.
55. R. Oyama and M. Abe, *The Journal of Organic Chemistry*, 2020, **85**, 8627-8638.
56. T. Tano, K. Mieda, H. Sugimoto, T. Ogura and S. Itoh, *Dalton Transactions*, 2014, **43**, 4871-4877.
57. T. Tano, H. Sugimoto, N. Fujieda and S. Itoh, *European Journal of Inorganic Chemistry*, 2012, **2012**, 4099-4103.
58. S. Biswas, A. Mitra, S. Banerjee, R. Singh, A. Das, T. K. Paine, P. Bandyopadhyay, S. Paul and A. N. Biswas, *Inorganic Chemistry*, 2019, **58**, 9713-9722.
59. M. Sankaralingam, Y.-M. Lee, Y. Pineda-Galvan, D. G. Karmalkar, M. S. Seo, S. H. Jeon, Y. Pushkar, S. Fukuzumi and W. Nam, *Journal of the American Chemical Society*, 2019, **141**, 1324-1336.

60. E. Baciocchi, M. Bietti, M. Salamone and S. Steenken, *The Journal of Organic Chemistry*, 2002, **67**, 2266-2270.
61. S. Kal, A. Draksharapu and L. Que, *Journal of the American Chemical Society*, 2018, **140**, 5798-5804.
62. J. Serrano-Plana, F. Acuña-Parés, V. Dantignana, W. N. Oloo, E. Castillo, A. Draksharapu, C. J. Whiteoak, V. Martin-Diaconescu, M. G. Basallote, J. M. Luis, L. Que Jr., M. Costas and A. Company, *Chemistry – A European Journal*, 2018, **24**, 5331-5340.
63. K. Cheaib, M. Q. E. Mubarak, K. Sénéchal-David, C. Herrero, R. Guillot, M. Clémancey, J.-M. Latour, S. P. de Visser, J.-P. Mahy, F. Banse and F. Avenier, *Angewandte Chemie International Edition*, 2019, **58**, 854-858.

Chapter 4

Modulating CPET Reactivity of Mn^{III}-Hydroxo Unit by Steric Perturbation and The Reactivity of its Mn^{III}-Alkylperoxo with Protic Solvent

4.1 Introduction

Coupled proton electron transfer (CPET) reactions are a subclass of proton-coupled electron transfer (PCET) reaction, where the proton and electron are transferred in the same kinetic step.[1-3] CPET reactions are used by biological enzymes such manganese lipoxygenase (MnLOX) to oxidize unactivated C-H bonds of a polyunsaturated fatty acid into its hydroperoxide. The hydroperoxides are metabolized into oxylipins like leukotrienes and jasmonates, which act as inflammatory mediators and reproductive/growth regulators in plants.[4, 5] High-valent Mn-oxo species are well reckoned to promote CPET reactions.[6-10] However, current interests have been directed towards the exploration of Mn^{III}-hydroxo species as well. For example, in the MnLOX, the Mn^{III}-hydroxo unit acts as the CPET agent to initiate substrate oxidation. Despite this established reaction, only few synthetic Mn^{III}-hydroxo complexes are known that oxidizes C-H bonds.[2, 11-17]

A notable example among the few synthetic Mn^{III}-OH complexes that are capable of CPET reactions with hydrocarbons is the Mn^{III}-hydroxo complex of a neutral pentadentate ligand – $[Mn^{III}(PY5)(OH)]^{2+}$ (PY5 = 2,6-bis(bis(2-pyridyl)- methoxymethane)pyridine) by Goldsmith *et al.* that oxidizes toluene, a hydrocarbon with a relatively strong C-H bond (C-H BDE = 88 ± 2 kcal/mol) by a CPET mechanism.[13] Our lab also reported Mn^{III}-hydroxo complexes – $[Mn^{III}(OH)(dpaq)]^{+}$ and $[Mn^{III}(OH)(dpaq^{2Me})]^{+}$ (dpaq = 2-[bis(pyridin-2ylmethyl)]amino-N-quinolin-8-yl-acetamidate) that are capable of CPET reactivity with xanthene.[18, 19] The $[Mn^{III}(OH)(dpaq^{2Me})]^{+}$ is a $[Mn^{III}(OH)(dpaq)]^{+}$ complex with a methyl substituent on the second position of the quinoline ring. The observed rate constants (k_{obs}) for the reaction of 250 equiv. of xanthene with 1.25 mM solution of the $[Mn^{III}(OH)(dpaq)]^{+}$ and $[Mn^{III}(OH)(dpaq^{2Me})]^{+}$ in MeCN at 50 °C are 8×10^{-3} s^{-1} and 2.5×10^{-3} s^{-1} respectively.[18] DFT calculation revealed that the slower

reactivity of the $[Mn^{III}(OH)(dpaq^{2Me})]^{+}$ with xanthene relative to that of the $[Mn^{III}(OH)(dpaq)]^{+}$ is due to the steric encumbrance created by the 2-methyl substituent on the quinoline ring of the $[Mn^{III}(OH)(dpaq^{2Me})]^{+}$, which mitigates reactivity by requiring a different orientation of the xanthene with the $[Mn^{III}(OH)(dpaq^{2Me})]^{+}$, compared to that in the $[Mn^{III}(OH)(dpaq)]^{+}$.[18] Calculations show that this reorientation in the $[Mn^{III}(OH)(dpaq^{2Me})]^{+}$ introduced a destabilizing effect that caused the transition state of the $[Mn^{III}(OH)(dpaq^{2Me})]^{+}$ to be higher than that of the $[Mn^{III}(OH)(dpaq^{2Me})]^{+}$ by about 3 kcal/mol.[18]

To gain some insight into how the reactivity of $[Mn^{III}(OH)(dpaq)]^{+}$ and $[Mn^{III}(OH)(dpaq^{2Me})]^{+}$ complexes with xanthene compare to that of the $[Mn^{III}(PY5)(OH)]^{2+}$, A second-order rate constant for xanthene oxidation by $[Mn^{III}(PY5)(OH)]^{2+}$ was extrapolated to 250 equiv. of xanthene used in the studies of $[Mn^{III}(OH)(dpaq)]^{+}$ and $[Mn^{III}(OH)(dpaq^{2Me})]^{+}$ complexes, and a k_{obs} of 8×10^{-2} s^{-1} was estimated. This revealed that the xanthene reactivity of $[Mn^{III}(PY5)(OH)]^{2+}$ is *ca.*10 and 30 fold faster than those of $[Mn^{III}(OH)(dpaq)]^{+}$ and $[Mn^{III}(OH)(dpaq^{2Me})]^{+}$ respectively.[12, 13, 20] The relative enhancement in the rate of $[Mn^{III}(PY5)(OH)]^{2+}$ vs. $[Mn^{III}(OH)(dpaq)]^{+}$ and $[Mn^{III}(OH)(dpaq^{2Me})]^{+}$ can be explained to stem from the higher $Mn^{III/II}$ reduction potential of the $[Mn^{III}(PY5)(OH)]^{2+}$ (+0.14 V vs Fc/Fc^{+} in MeCN) compared to those of the $[Mn^{III}(OH)(dpaq)]^{+}$ and $[Mn^{III}(OH)(dpaq^{2Me})]^{+}$ (-0.73 V and -0.62 V respectively, vs Fc/Fc^{+} in MeCN).[13, 18] This difference of 760-870 mV explains why $[Mn^{III}(PY5)(OH)]^{2+}$ is a better oxidant than the $[Mn^{III}(OH)(dpaq)]^{+}$ and $[Mn^{III}(OH)(dpaq^{2Me})]^{+}$. The experimental p$K_a$ of 13 ± 0.5 of the $[Mn^{II}(PY5)(OH_2)]^{2+}$ relative to the calculated pK_a of the $[Mn^{II}(OH_2)(dpaq)]^{+}$ and $[Mn^{II}(OH_2)(dpaq^{2Me})]^{+}$ (29.3 and 28.7 respectively) revealed and suggested that the reactivity of $[Mn^{III}(PY5)(OH)]^{2+}$ is even suppressed by its lower proton affinity.[12, 13, 20]

An alternative means of investigating CPET reactivity in metal complexes is by using TEMPOH. TEMPOH is a hydroxylamine, and it does not model a typical biological PCET substrate. However, it is desirable for studying biomimetic PCET reactions because of its relatively weaker O-H bond (BDFE = 66.5 kcal mol^{-1} in MeCN at 298 K)[21] which allows reactivity studies of metal complexes with BDFE of 60 to >80 kcal/mol[22], poor Bronsted acidity (pK_a = 41 in MeCN) and the difficulty of oxidation ($TEMPOH^{+/\bullet}$ $E_{p,a}$ = 0.71 V vs. $Fc^{+/0}$).[1] Therefore, it strongly prefers to react by CPET. Kovacs *et al.* reported a Mn^{III}-hydroxo thiolate complex – $[Mn^{III}(OH)(S^{Me2}N_4(tren))]^+$ that is capable of CPET reactivity with TEMPOH substrate at a very fast rate with a second-order rate constant (k_2) of 2.1 x 10^3 $M^{-1}s^{-1}$ at 25 °C.[2] However, this complex shows no activity towards hydrocarbons.[2] The $[Mn^{III}(OH)(dpaq)]^+$ and $[Mn^{III}(OH)(dpaq^{2Me})]^+$ also displays activity toward TEMPOH (k_2 = 1.1 and 3.9 $M^{-1}s^{-1}$ respectively at -35 °C).[18] The higher reactivity of $[Mn^{III}(OH)(dpaq^{2Me})]^+$ vs. $[Mn^{III}(OH)(dpaq)]^+$ originates from the steric bulkiness introduced by the methyl substituent in $[Mn^{III}(OH)(dpaq^{2Me})]^+$ which leads to the elongation of the $Mn–N_{quinoline}$ bond by 0.11 Å relative to $[Mn^{III}(OH)(dpaq)]^+$. As a result of this elongation, the Mn^{III} center becomes more Lewis acidic, leading to the $Mn^{III/II}$ reduction potential of the $[Mn^{III}(OH)(dpaq^{2Me})]^+$ being higher than that of the $[Mn^{III}(OH)(dpaq)]^+$ (-0.62 V and -0.73 V respectively, vs. Fc/Fc^+ in MeCN).[18, 20] This increase in reduction potential enhanced the rate of reaction of $[Mn^{III}(OH)(dpaq^{2Me})]^+$ relative to $[Mn^{III}(OH)(dpaq)]^+$. A comparison of their reactivity with that of the $[Mn^{III}(OH)(S^{Me2}N_4(tren))]^+$ complex revealed that they are slower by *ca.* two orders of magnitude.

We went further in our studies to investigate how electronic modulation controls the reactivity of $[Mn^{III}(OH)(dpaq)]^+$ through a series of substitutions at the 5-position of the quinoline by synthesizing a series of complexes – $[Mn^{III}(OH)(dpaq^{5R})]^+$ (R = H, NO_2, OMe, and Cl)[20], but the

modifications only provide limited enhancement of CPET reactivity (The largest rate constant was obtained for the most electron deficient complex – $[Mn^{III}(OH)(dpaq^{5NO2})]^+$ (k_2 = 7(1) M^{-1} s^{-1}), and the smallest rate constant obtained for the least electron deficient complex – $[Mn^{III}(OH)(dpaq^{5OMe})]^+$ (k_2 = 0.8(1) M^{-1} s^{-1}).[20]

Since we have observed how steric perturbation of the quinoline moiety modulates the reactivity of the dpaq complex through the comparative studies between $[Mn^{III}(OH)(dpaq)]^+$ and $[Mn^{III}(OH)(dpaq^{2Me})]^+$. We understand that the elongation of the Mn-N bond increases the $Mn^{III/II}$ reduction potential which foster reactivity, but this was at the expense of steric hinderance which also affects the reactivity. We want to investigate further the influence of steric perturbation around the reaction center by exploring the extent to which the elongation of the equatorial Mn-$N_{pyridine}$ bond will modulate the $Mn^{III/II}$ reduction potential and how steric encumbrance around the pyridine donor rings will compare to the results from the studies of $[Mn^{III}(OH)(dpaq^{2Me})]^+$, where steric hinderance was introduced by the methyl substituent on the quinoline ring. Kovacs *et al*. already reported using a thiolate N_4S^- ligand scaffold, that an introduction of steric encumbrance around the equatorial pyridine ring donors lead to a significant elongation the Mn-$N_{pyridine}$ bonds.[23, 24] Motivated by this, we describe here the modification of the dpaq ligand by the introduction of methyl substituents at the 6-positions of the pyridines rings that are *trans* to each other in the $[Mn^{III}(OH)(dpaq)]^+$ to obtain a new complex – $[Mn^{III}(OH)(^{6Me}dpaq)]^+$.

The $[Mn^{III}(OH)(^{6Me}dpaq)]^+$ display some interesting spectroscopic and reactivity as compared to the other dpaq complexes studied previously. Firstly, an attempt to prepare the $[Mn^{III}(OH)(^{6Me}dpaq)]^+$ by oxidizing the $[Mn^{II}(^{6Me}dpaq)]^+$ with dioxygen showed a considerable lengthening in the time taken for complete formation of the $[Mn^{III}(OH)(^{6Me}dpaq)]^+$ complex as compared to other dpaq complexes. Secondly, the electronic absorption spectrum of

$[Mn^{III}(OH)(^{6Me}dpaq)]^+$ looks different from that of the other $[Mn^{III}(OH)(dpaq^R)]^+$ (R = H, 2Me, $5NO_2$, 5OMe, and 5Cl) complexes. The $[Mn^{III}(OH)(dpaq^R)]^+$ complexes exhibit similar electronic absorption spectra with a feature around 770 nm that has been assigned to the Mn^{III} $dx^2\text{-}y^2 \rightarrow dz^2$ transition.[19, 20, 25] The structural modification in the $[Mn^{III}(OH)(^{6Me}dpaq)]^+$ leads to an expected elongation of the Mn-$N_{pyridine}$ bond that results in a change in the electronic absorption spectrum. We explained this change in the electronic absorption feature by TD-DFT calculation. Thirdly, the structural modification in $[Mn^{III}(OH)(^{6Me}dpaq)]^+$ also leads to an increase in reactivity with TEMPOH relative to the $[Mn^{III}(OH)(dpaq)]^+$, and almost a similar rate with $[Mn^{III}(OH)(dpaq^{2Me})]^+$. However, what is more interesting is that this modification turns off the reactivity of the $[Mn^{III}(OH)(^{6Me}dpaq)]^+$ with xanthene. Finally, the $[Mn^{III}(OH)(^{6Me}dpaq)]^+$ reacts with alkylperoxides – *tert*-butyl hydroperoxide (^{t}BuOOH) and cumyl hydroperoxide (CmOOH) to produce a room-temperature stable $[Mn^{III}(OOR)(^{6Me}dpaq)]^+$ (R = ^{t}Bu and Cm) complexes and the $[Mn^{III}(OOR)(^{6Me}dpaq)]^+$ complexes were found to undergo hydrolysis in the presence of protic solvents.

4.2 Materials and Methods

All chemicals obtained from commercial sources were of ACS grade or better and were used as obtained, unless noted otherwise. Acetonitrile, diethyl ether, and methanol were dried and degassed using a PureSolv Micro solvent purification system. The $H^{6Me}dpaq$ ligand and the $[Mn^{II}(OH_2)(^{6Me}dpaq)](OTf)$, $[Mn^{III}(OH)(^{6Me}dpaq)](OTf)$, $[Mn^{III}(OO^tBu)(^{6Me}dpaq)](OTf)$ and $[Mn^{III}(OOCm)(^{6Me}dpaq)](OTf)$ complexes were synthesized according to a reported procedure. (see chapter 3). Experiments were performed under dinitrogen atmosphere in a glovebox unless otherwise noted. Electronic absorption experiments were performed using a Varian Cary 50 Bio

UV−visible spectrophotometer equipped with a Unisoku cryostat and stirrer (for low temperature experiments) or a Quantum Northwest temperature controller equipped with a stirrer (for high temperature experiments). Electrospray ionization mass spectrometry (ESI-MS) experiments were performed using an LCT Premier MicroMass electrospray time-of-flight instrument. ^{1}H NMR spectra were obtained on a Bruker DRX 400 MHz NMR spectrometer.

Kinetic studies of TEMPOH and xanthene oxidation by [Mn^{III}(OH)(^{6Me}dpaq)](OTf). A 1.25 mM solution of [Mn^{III}(OH)(^{6Me}dpaq)]$^{+}$ was prepared in 2.0 mL of MeCN in a nitrogen-filled glovebox and transferred to a quartz cuvette that was sealed with a rubber septum. The cuvette was removed from the glovebox and allowed to equilibrate at -35 °C for 10 minutes on the Uv-vis spectrometer. A 100 μL solution of TEMPOH, with concentrations ranging from 10-60 equiv. relative to [Mn^{III}(OH)(^{6Me}dpaq)]$^{+}$, was added to the cuvette using a gastight syringe that had been purged with N_2 gas. The addition of TEMPOH led to the disappearance of the 510 nm electronic absorption feature of [Mn^{III}(OH)(^{6Me}dpaq)]$^{+}$. The change in absorbance as a function of time was fit to obtain a pseudo-first-order rate constant (k_{obs}). The reported k_{obs} represent an average from three separate measurements. A linear fit of the plot of k_{obs} vs the concentration of TEMPOH provided the second-order rate constant (k_2).

The reactivity of [Mn^{III}(OH)(^{6Me}dpaq)]$^{+}$ with xanthene was investigated using a similar approach. In this case, 250 equiv. xanthene was prepared anaerobically in 300 μL dichloromethane in a 400 mL vial. The solution of xanthene was added to 2 mL of a 1.25 mL solution of [Mn^{III}(OH)(^{6Me}dpaq)]$^{+}$ that had equilibrate at 50°C for 10 minutes on the spectrometer. The decay of the 510 nm feature of the [Mn^{III}(OH)(^{6Me}dpaq)]$^{+}$ was monitored by electronic absorption spectroscopy over a period of 1000 minutes.

Reaction of $[Mn^{III}(OO^tBu)(^{6Me}dpaq)]^+$ with protic solvents (water, trifluoroethanol and methanol). The propensity for $[Mn^{III}(OO^tBu)(^{6Me}dpaq)]^+$ to undergo ligand substitution reactions was first discovered when trying to prepare the complex in various protic solvents. In a representative procedure, $[Mn^{III}(OO^tBu)(^{6Me}dpaq)]^+$ was prepared in MeCN and then dried in vacuo to remove the solvent, leaving behind an oily film. The oily film was taken into the glovebox and dissolved in trifluoroethanol (TFE). The solution was transferred to a quartz cuvette, sealed with a rubber septum, and wrapped with Parafilm. The sample was then removed from the glovebox, inserted in the UV-vis spectrometer, and heated to 50 °C. Initial absorption spectra collected under these conditions revealed the electronic absorption band of $[Mn^{III}(OO^tBu)(^{6Me}dpaq)]^+$ at 650 nm. This band decayed over the course of 60 minutes, with the concomitant formation of a band at 510 nm. An ESI-MS analysis of the product solution revealed a prominent ion peak at 564.07 *m/z*, consistent with $[Mn^{III}(OCH_3CF_3)(^{6Me}dpaq)]^+$ (*m/z* = 564.14; see Figure A3.1 and Figure A3.2). Thus, while $[Mn^{III}(OO^tBu)(^{6Me}dpaq)]^+$ is initially formed upon dissolution of the $[Mn^{III}(OO^tBu)(^{6Me}dpaq)](OTf)$ salt in TFE, a ligand substitution reaction occurs that replaces the alkylperoxo ligand with a $CF_3CH_2O^-$ ligand. This ligand substitution reaction with TFE was only observed at 50 °C. A similar, albeit far more rapid, ligand substitution reaction occurs upon dissolution of $[Mn^{III}(OO^tBu)(^{6Me}dpaq)](OTf)$ in MeOH at 25 °C.

To determine rate constants for ligand substitution reactions of $[Mn^{III}(OO^tBu)(^{6Me}dpaq)]^+$, an acetonitrile solution of $[Mn^{III}(OO^tBu)(^{6Me}dpaq)]^+$ was prepared in the glovebox and transferred into a quartz cuvette sealed with a pierceable rubber septum and wrapped with Parafilm. The cuvette was removed from the glovebox and 100 equiv. degassed H_2O were injected while monitoring the reaction by electronic absorption spectroscopy at 25 °C. The same procedure was

performed for ligand substitution reaction with MeOH using 100 μL of MeOH (Figure A3.3 and Figure A3.4).

It is also important to note that attempts to form the $[Mn^{III}(OO^{t}Bu)(^{6Me}dpaq)]^{+}$ and $[Mn^{III}(OOCm)(^{6Me}dpaq)]^{+}$ in protic solvents using the preparation methods described above were not successful due to ligand substitution competing with $[Mn^{III}(OOR)(^{6Me}dpaq)]^{+}$ formation. An example is where we tried to form $[Mn^{III}(OO^{t}Bu)(^{6Me}dpaq)]^{+}$ from $[Mn^{III}(OH)(^{6Me}dpaq)]^{+}$ in TFE and MeOH by reacting each solution with 1.0 equiv of ^{t}BuOOH at 25 °C. This results in the decay of the *ca.* 500 nm features to feature reminiscent of the $[Mn^{II}(H_2O)(^{6Me}dpaq)]^{+}$ complex. On the other hand, attempt to make $[Mn^{III}(OO^{t}Bu)(^{6Me}dpaq)]^{+}$ by the reaction of $[Mn^{II}(H_2O)(^{6Me}dpaq)]^{+}$ and 1.5 equiv of ^{t}BuOOH in TFE as discussed in previous studies where MeCN was used as a solvent (Chapter 3) led to the formation of a mixture of products containing the $[Mn^{III}(OO^{t}Bu)(^{6Me}dpaq)]^{+}$ and $[Mn^{III}(OCH_2CF_3)(^{6Me}dpaq)]^{+}$ complex results from the substitution of the ^{t}butylperoxo ligand with trifluoroethoxy ligand) (Figure A3.5, left). Also an attempt to form $[Mn^{III}(OO^{t}Bu)(^{6Me}dpaq)]^{+}$ in MeOH using $[Mn^{II}(H_2O)(^{6Me}dpaq)]^{+}$ and 1.5 equiv. of ^{t}BuOOH led to the formation of the $[Mn^{III}(OMe)(^{6Me}dpaq)]^{+}$ complex (Figure A3.5, right), with no change to the absorption feature even after addition of additional amount of ^{t}BuOOH up to 5 equiv.
These studies show the sensitive of the alkylperoxo complexes towards protic solvent and revealed that the alkylperoxo cannot be prepared in protic solvents.

Cyclic Voltammetry. Cyclic voltammograms were recorded using Basi® PalmSens EmStat3+ potentiostat. The working electrode was a glassy carbon electrode with a Pt wire as the counter electrode. A 0.01 M AgCl solution was prepared using 0.1 M Bu_4NPF_6 electrolyte solution in CH_3CN. The 0.01 M AgCl solution was used for the Ag/AgCl quasi-reference electrode. Fc^{+}/Fc potential was measured as an external reference. 2 mM solutions of $[Mn^{III}(OH)(^{6Me}dpaq)](OTf)$

was prepared from 10 mL of a degassed 0.1 M Bu_4NPF_6 electrolyte solution in CH_3CN. These sample solutions were sparged with nitrogen gas with the aid of Teflon tubing for 15 minutes before measurement. The Teflon tubing was placed above the surface of the solution to continue flushing the headspace, while not disturbing the solution in the electrochemical cell during measurement. All measurements were performed at room temperature. Data was referenced to the cathodic peak potential for Fc^+/Fc in MeCN.

Electronic Structure Calculations. All DFT calculations were performed using ORCA 4.2.1.[26] Geometry optimizations used the B3LYP[27, 28] functional with the def2-TZVP basis set for Mn, N and O atoms, while the def2-SVP basis set was used for C and H atoms.[29, 30] Grimme's D3 dispersion correction[31-34] was also applied with a fine integration grid (Grid6 and GridX6 in ORCA). Analytical frequency calculations were performed using the same level of theory. The zero-point energies, thermal corrections, and entropies were obtained from the analytical frequency calculations. Single point energies were obtained for all structures using the same B3LYP-D3 functional but with the larger def2-TZVPP basis set on all atoms and a finer integration grid (Grid7 and GridX7). In all cases, solvation was accounted for by using the SMD solvation model with default parameters for acetonitrile.[35] The RIJCOSX approximation together with def2/J auxiliary basis set was used for all calculations.[36, 37]

4.3 Results and Discussions

Summary of previous characterization of [Mn^{III}(OH)(^{6Me}dpaq)](OTf)

Previous studies have discussed the preparation and established the molecular structure and spectroscopic properties of [Mn^{III}(OH)(^{6Me}dpaq)](OTf). (Chapter 3) The XRD structure revealed a mononuclear six-coordinate Mn^{III}-center coordinated in a distorted octahedral geometry with an

hydroxo ligand in *trans* configuration to the amide moiety. ^{1}H NMR spectroscopy of the [Mn^{III}(OH)(^{6Me}dpaq)](OTf) solution in CD_3CN confirmed the presence of monomeric species and the absence of the (μ-oxo)dimanganese(III, III) species in solution, due to the absence of a large number of peaks in the diamagnetic region. The chemical shifts for the ^{1}H NMR signals of [Mn^{III}(OH)(^{6Me}dpaq)]$^{+}$ (see chapter 3) are quite similar to those of [Mn^{III}(OH)(dpaq)]$^{+}$.[20, 38] Electron spray ionization mass spectrometry (ESI-MS) analysis of [Mn^{III}(OH)(^{6Me}dpaq)]$^{+}$ showed an ion peak with *m/z* ratio that matched the expected value for the [Mn^{III}(OH)(^{6Me}dpaq)]$^{+}$ and Evans NMR gave a 4.89 BM value expected for an S=2 d^4 system. (See Chapter 3) All these data confirmed the formation of mononuclear [Mn^{III}(OH)(^{6Me}dpaq)](OTf) in solid state and in MeCN solution. However, the electronic absorption spectrum of the [Mn^{III}(OH)(^{6Me}dpaq)](OTf) in MeCN showed just a broad feature from *ca.* 800 nm to 470 nm with λ_{max} at 510 nm (ε = 250 M^{-1} cm^{-1}) (Chapter 3). This is different from the electronic absorption spectroscopic features of the [Mn^{III}(OH)(dpaq^{R})](OTf) (R = 5H, 5OMe, 5Cl, 5NO_2 and 2Me) in MeCN which show absorptions with λ_{max} values at *ca.* 500 and 770 nm.[18-20, 38]

Structural comparism of [Mn^{III}(OH)(^{6Me}dpaq)](OTf) and [Mn^{III}(OH)(dpaq)](OTf).

The coordination mode of the of [Mn^{III}(OH)(^{6Me}dpaq)](OTf) and [Mn^{III}(OH)(dpaq)](OTf) are similar (Figure 4.1) and their Mn–OH distances are within error range (1.806(6) and 1.806(13) Å respectively Table 4.1). These Mn–OH bond lengths are in the low end of the values reported for other Mn^{III}-hydroxo complexes (1.81 - 1.86 Å).[2, 18, 39-46] The most striking structural differences between these two Mn^{III}-hydroxo complexes arises from the Mn-$N_{pyridine}$ bonds (Mn-N4 and Mn-N5, see Table 4.1 & Figure 4.1). It can be seen that these bonds are comparatively elongated in the [Mn^{III}(OH)(^{6Me}dpaq)](OTf). These elongations are comparatively compensated by slight

contractions of the Mn-N2 and Mn-N3 bonds in the [Mn^{III}(OH)(^{6Me}dpaq)](OTf) (see Table 4.1). The elongations of the Mn-$N_{pyridine}$ bonds in [Mn^{III}(OH)(^{6Me}dpaq)](OTf) relative to [Mn^{III}(OH)(dpaq)](OTf) is due to steric perturbation resulting from the methyl substituent at the 6-positions of the pyridine rings (Figure 4.1, left).

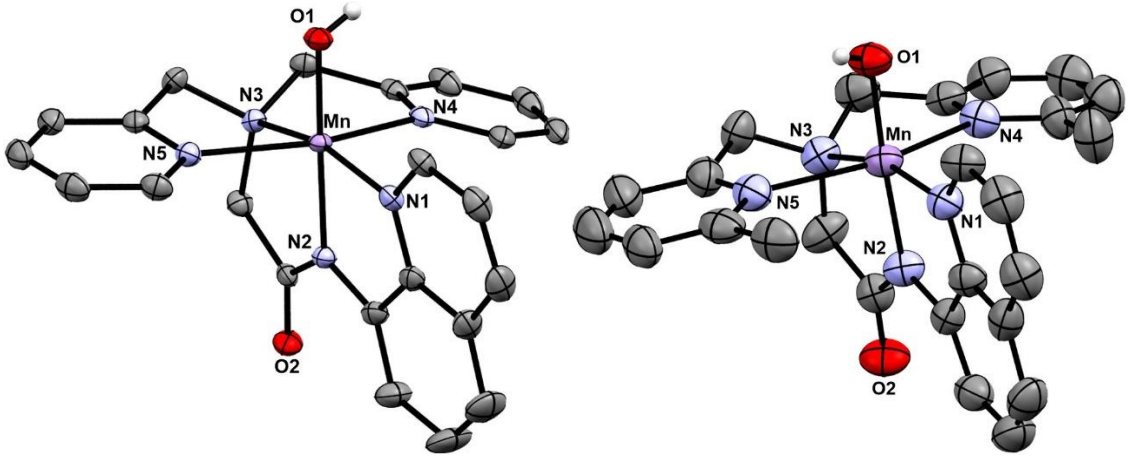

Figure 4.1. Crystal structure of [Mn^{III}(OH)(dpaq)](OTf) (left), and [Mn^{III}(OH)(^{6Me} dpaq)](OTf) (right) showing 50% probability thermal ellipsoid. Triflate counter ion, solvent of crystallization and non-hydroxo hydrogen atoms were removed for clarity.

Table 4.3. Manganese-ligand bond lengths (Å) from XRD structures of [Mn^{II}(OH_2)(^{6Me}dpaq)](OTf), [Mn^{II}(dpaq)]$^+$and [Mn^{III}(OH)(L)](OTf) (L = ^{6Me}dpaq and dpaq).

Bond	[Mn^{II}(OH_2)(^{6Me}dpaq)](OTf)	[Mn^{II}(dpaq)](OTf)	[Mn^{III}(OH)(L)](OTf)	
			L = ^{6Me}dpaq	L = dpaq
Mn–O1	2.108(3)	2.079(2)[a]	1.806(6)	1.806(13)
Mn–N1	2.233(3)	2.214(3)	2.041(7)	2.072(14)
Mn–N2	2.152(4)	2.191(3)	1.962(6)	1.975(14)
Mn–N3	2.280(3)	2.314(3)	2.130(6)	2.173(14)
Mn–N4	2.354(4)	2.244(3)	2.322(6)	2.260(14)
Mn–N5	2.417(3)	2.286(3)	2.381(7)	2.216(15)

[a] For [Mn^{II}(dpaq)]$^+$, the oxygen atom derives from a carbonyl unit of a separate [Mn^{II}(dpaq)]$^+$ cation.

$[Mn^{III}(OH)(^{6Me}dpaq)]^+$ reacts with stoichiometric amount (1.0 equiv.) of ROOH (R = ^{t}Bu or cumyl) to produce the alkylperoxo complexes $[Mn^{III}(OOR)(^{6Me}dpaq)]^+$ (see chapter 3). Similar but non-stoichiometric reaction have been reported for the $[Mn^{III}(OH)(dpaq)]^+$ and $[Mn^{III}(OH)(dpaq^{2Me})]^+$ where large excess of ^{t}BuOOH is needed to form the $[Mn^{III}(OOR)(dpaq^R)]^+$ complex.[47]

Properties and O_2 Reactivity of $[Mn^{II}(H_2O)(^{6Me}dpaq)]^+$

The crystal structure and chemical reactivity of $[Mn^{II}(H_2O)(^{6Me}dpaq)](OTf)$ was briefly presented in Chapter 3. Here we compare this structure to that of other Mn^{II} complexes with similar ligands, and we provide additional information concerning the reactivity of this complex. The Mn^{II} center in $[Mn^{II}(H_2O)(^{6Me}dpaq)](OTf)$ is six-coordinate, with a pentadentate ^{6Me}dpaq ligand and an axial aqua ligand in the sixth coordination site (Figure 4.2, left). This structure is generally similar to those of $[Mn^{II}(dpaq)](OTf)$[19] and $[Mn^{II}(dpaq^{2Me})](OTf)$,[18] with the exception that the crystal structures of those complexes revealed polymers of the respective $[Mn^{II}(dpaq)]^+$ and $[Mn^{II}(dpaq^{2Me})]^+$ cations. These polymeric structures were achieved by having the sixth coordination position of the Mn^{II} centers occupied by the carbonyl oxygen atom of the amide group of another $[Mn^{II}(dpaq)]^+$ or $[Mn^{II}(dpaq^{2Me})]^+$ cation (Figure 4.2, right).

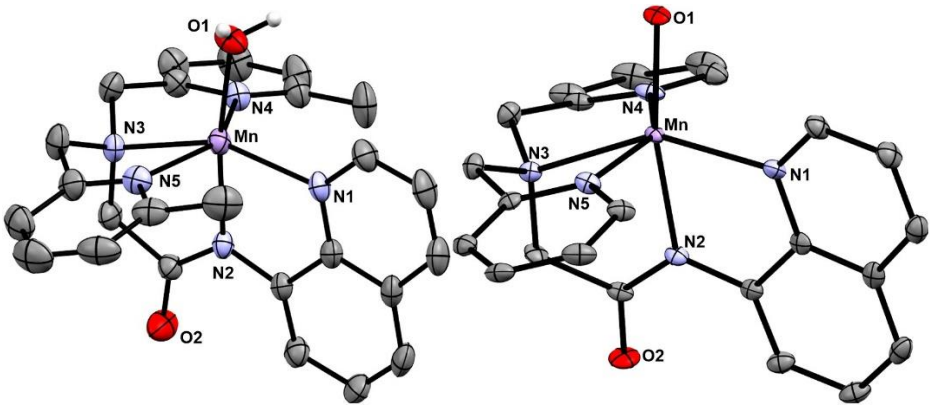

Figure 4.2. Crystal structure of $[Mn^{II}(OH_2)(^{6Me}dpaq)](OTf)$ (left), and $[Mn^{II}(dpaq)](OTf)$ (right) showing 50% probability thermal ellipsoid. Triflate counter ion, solvent of crystallization and non-hydroxo hydrogen atoms were removed for clarity.

When dissolved in MeCN, the $[Mn^{II}(H_2O)(^{6Me}dpaq)](OTf)$ complex shows a weak electronic absorption band at from *ca.* 600 nm to 490 nm (Figure 4.3). Exposure of an MeCN solution of this complex to O_2 results in the eventual growth of a band at *ca.* 510 nm that is attributed to $[Mn^{III}(OH)(^{6Me}dpaq)]^+$. This reaction is very slow, such that only partial oxidation is observed after 48 hours (Figure 4.3). In contrast, other $[Mn^{II}(dpaq)]^+$ complexes show complete formation within 0.5 – 5 hours.[18-20] The sluggish nature of the reaction of $[Mn^{II}(H_2O)(^{6Me}dpaq)]^+$ with O_2 could be caused by having a more electron-deficient Mn^{II} center. The 6-Me-pyridyl groups in $[Mn^{II}(H_2O)(^{6Me}dpaq)]^+$ give rise to elongated Mn-$N_{Pyridine}$ bonds when compared to $[Mn^{II}(dpaq)](OTf)$ and its derivatives by 0.02 – 0.04 Å.[18, 19] These longer bonds presumably mitigate electron donation from the pyridyl ligands to the Mn^{II} center, leading to a less electron rich metal. Along similar lines, the $[Mn^{II}(dpaq^{5NO2})](OTf)$ complex, which contains a strongly electron-donating nitro group on the quinolinyl moiety, shows essentially no reactivity with dioxygen.[20] While the formation of the $[Mn^{III}(OH)(^{6Me}dpaq)]^+$ complex from O_2 oxidation of $[Mn^{II}(H_2O)(^{6Me}dpaq)]^+$ is very slow, the Mn^{III}-hydroxo complex can be rapidly formed from the reaction of $[Mn^{II}(H_2O)(^{6Me}dpaq)]^+$ and PhIO, as previously described (see Chapter 3).

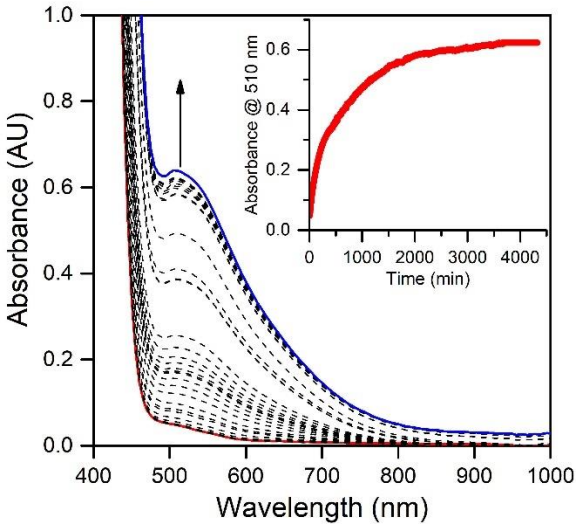

Figure 4.3. Electronic absorption spectra showing the reaction of a 2.5 mM solution of $[Mn^{II}(H_2O)(^{6Me}dpaq)]OTf$ in CH_3CN (red trace) with dioxygen at 298 K. The dashed traces show the reaction progress and the blue trace is the final spectrum.

Spectroscopic Properties and Electronic Structure of $[Mn^{III}(OH)(^{6Me}dpaq)]^+$

The electronic absorption spectrum of $[Mn^{III}(OH)(^{6Me}dpaq)]^+$ in MeCN at 25 °C shows a single broad absorption feature from *ca.* 800 to 470 nm with λ_{max} at 510 nm (ε = 250 M^{-1} cm^{-1}) (Figure 4.4). This spectrum deviates significantly from that observed for $[Mn^{III}(OH)(dpaq)]^+$ and its derivatives (Figure 4.4). The electronic absorption spectra of those complexes showed two absorption maxima with λ_{max} values at *ca.* 500 and 770 nm (Figure 4.4).[18-20, 38] To understand the origin of the spectral perturbations for $[Mn^{III}(OH)(^{6Me}dpaq)](OTf)$, we used time-dependent density functional theory (TD-DFT) calculations. Although TD-DFT calculations have known drawbacks, this method has performed exceptionally well for mononuclear Mn^{III} complexes,[48-52] potentially because ligand-field transitions dominate the electronic absorption spectra of these complexes.

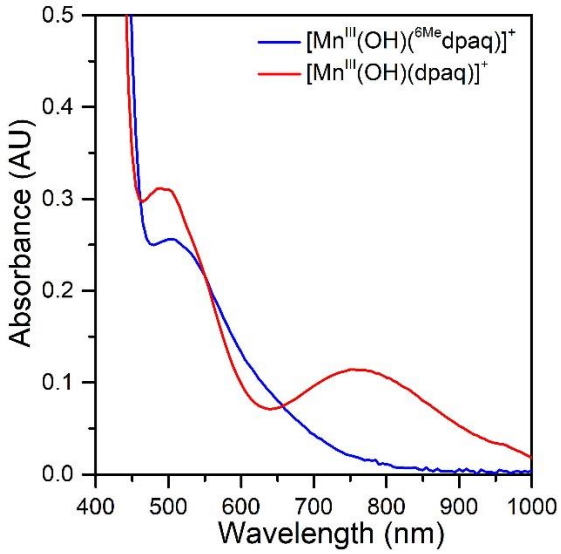

Figure 4.4. The electronic absorption spectrum of 1.0 mM $[Mn^{III}(OH)(^{6Me}dpaq)]^+$ (blue trace) and 1.0 mM $[Mn^{III}(OH)(dpaq)]^+$ in MeCN at 25°C shown for comparison (red trace).

DFT geometry optimization for $[Mn^{III}(OH)(^{6Me}dpaq)]^+$ and $[Mn^{III}(OH)(dpaq)]^+$ reproduced the trends in metric parameters obtained from XRD analysis of the complexes (Table 4.1). The Mn^{III}-hydroxo distances (Mn–O1) for these complexes are essentially identical, while the largest difference is in the Mn-$N_{pyridine}$ distances (Mn–N4 and Mn–N5), which are elongated by 0.08 to 0.2 Å in $[Mn^{III}(OH)(^{6Me}dpaq)]^+$. DFT calculations predict a $(d_{xy})^1(d_{yz})^1(d_{xz})^1(d_{x^2-y^2})^1(d_{z^2})^0$ ground configuration for each complex. (In the DFT computations for $[Mn^{III}(OH)(^{6Me}dpaq)]^+$ and $[Mn^{III}(OH)(dpaq)]^+$, we chose a coordinate system where the *z*-axis lies along the Mn–O(H) bond and the *x*- and *y*-axes coincide with the equatorial Mn-ligand bonds. Accordingly, the d_{z^2} and $d_{x^2-y^2}$ MO are the σ-antibonding MOs, and the d_{xy}, d_{yz}, and d_{xz} MOs are capable of π-interactions.) With this ground configuration, each spin-allowed ligand-field transition can be reasonably approximated by a one-electron excitation from a singly-occupied Mn^{III} *d*-based MO to the unoccupied d_{z^2}-based MO. Consequently, the ligand-field electronic transition energies can be directly related to the Mn^{III} *d*-orbital splitting pattern. We will therefore briefly discuss the

compositions and energies of the *d*-based MOs of $[Mn^{III}(OH)(^{6Me}dpaq)]^+$ and $[Mn^{III}(OH)(dpaq)]^+$, as differences in these orbitals can account for all perturbations in the electronic absorption spectra of these complexes.

Table 4.1. Selected Manganese−Ligand Bond Lengths (Å) for $[Mn^{III}(OH)(dpaq)]^+$ and $[Mn^{III}(OH)(^{6Me}dpaq)]^+$from X-ray Crystallography and DFT Computations.

	$[Mn^{III}(OH)(dpaq)]^+$		$[Mn^{III}(OH)(^{6Me}dpaq)]^+$	
	XRD	DFT	XRD	DFT
Mn–O1 (Å)	1.806(13)	1.829	1.806(6)	1.830
Mn–N1 (Å)	2.072(14)	2.089	2.041(7)	2.048
Mn–N2 (Å)	1.975(14)	1.980	1.962(6)	1.968
Mn–N3 (Å)	2.173(14)	2.222	2.130(6)	2.134
Mn–N4 (Å)	2.260(14)	2.213	2.322(6)	2.339
Mn–N5 (Å)	2.216(15)	2.209	2.381(7)	2.422

In each complex the highest-energy d_z^2 MO is strongly destabilized by σ-antibonding interactions with both the hydroxo and carboxamido donors (Figure 4.5). These d_z^2 MO in each complex have ligand contributions from the $2p_x$ orbital of the equatorial N donor atoms, $2p_z$ orbital of the carboxamido nitrogen atom and $2p_z$ orbital of the oxygen atom of the hydroxo ligand (Table A3.1 and A3.2). The DFT calculations actually predict nearly identical energies (*ca.* -2.2 eV; see Figure 4) for the d_z^2 MOs of $[Mn^{III}(OH)(^{6Me}dpaq)]^+$ and $[Mn^{III}(OH)(dpaq)]^+$. Thus, any differences in the spectroscopic or chemical properties of these complexes are not related to differences in Mn^{III}-hydroxo or Mn^{III}-amide bonding interactions. This DFT-based prediction is in full accordance with the nearly identical Mn^{III}-$O_{hydroxo}$ (Mn–O1) and Mn^{III}-N_{amide} (Mn–N2) bond

lengths observed in both the experimental and DFT-computed structures of these complexes (Table 4.1). The energy and composition of the $d_{x^2-y^2}$ MOs of $[Mn^{III}(OH)(^{6Me}dpaq)]^+$ and $[Mn^{III}(OH)(dpaq)]^+$ show significantly more variation (Figure 4.5). The $d_{x^2-y^2}$ MO is σ-antibonding with respect to the equatorial ligands and is therefore sensitive to the longer Mn-$N_{pyridine}$ bond lengths in $[Mn^{III}(OH)(^{6Me}dpaq)]^+$ (Mn–N4 and Mn–N5; see Table 4.1). These longer, and therefore weaker, Mn-$N_{pyridine}$ bonds lead to a stabilization of the $d_{x^2-y^2}$ MO by *ca.* 0.3 eV relative to $[Mn^{III}(OH)(dpaq)]^+$ (Figure 4.5). The d_{xz} and d_{yz} MOs of each complex have weak π-antibonding interactions with the hydroxo ligand. The nearly identical Mn-hydroxo distances for the $[Mn^{III}(OH)(^{6Me}dpaq)]^+$ and $[Mn^{III}(OH)(dpaq)]^+$ give rise to similar Mn-hydroxo □-interactions, causing the d_{xz} and d_{yz} MOs of these complexes to lie at similar energies. The d_{xy} MO of each complex is non-bonding.

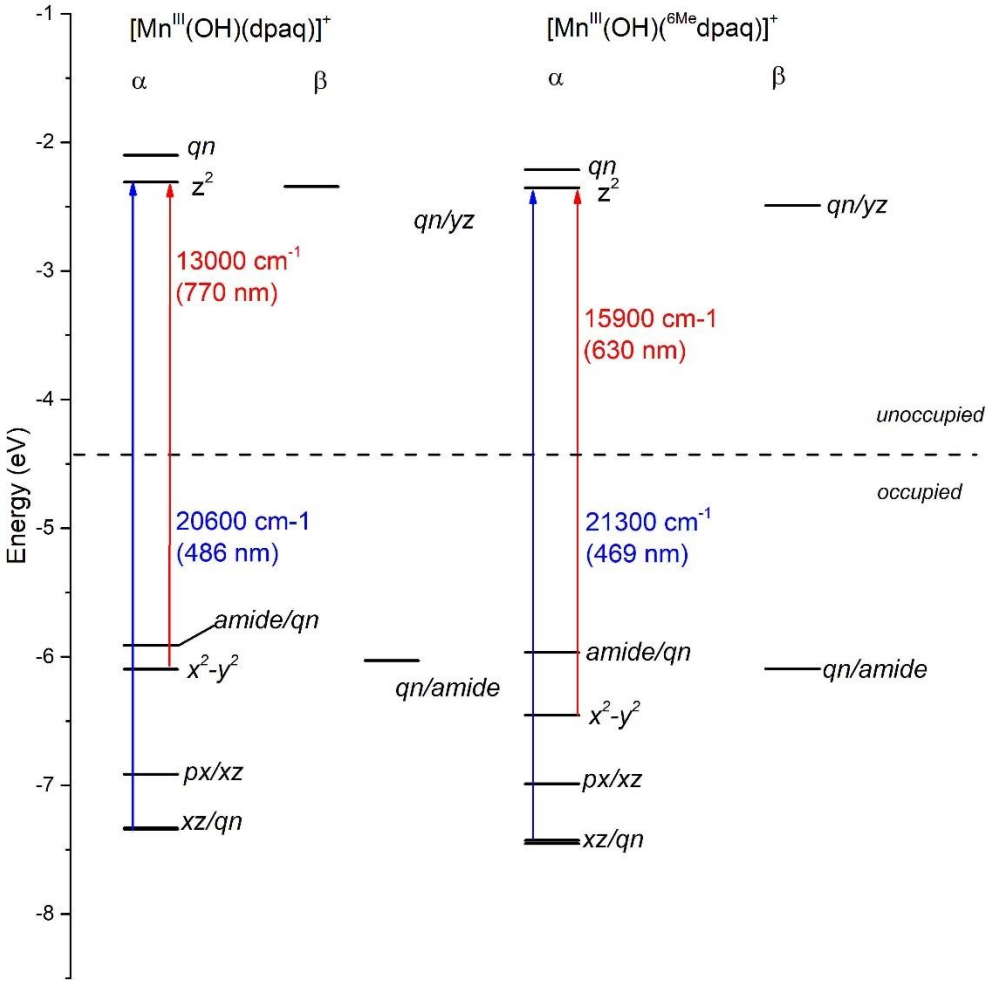

Figure 4.5. MO energy level diagram for $[Mn^{III}(OH)(dpaq)]^+$ and $[Mn^{III}(OH)(^{6Me}dpaq)]^+$ based on the Kohn-Sham orbitals from DFT calculations. α and β refer to spin-up and spin-down MOs, respectively.

The TD-DFT-computed electronic absorption spectra of both $[Mn^{III}(OH)(^{6Me}dpaq)]^+$ and $[Mn^{III}(OH)(dpaq)]^+$ are in excellent agreement with their experimental counterparts (Figure 4.6). Starting with $[Mn^{III}(OH)(dpaq)]^+$, the calculated spectrum shows two bands at *ca.* 770 nm and 500 nm, which nearly perfectly reproduce the experimental spectrum (Figure 4.6, left). An analysis of the electron-density difference maps (EDDMs) for the states contributing to these bands shows that each band derives from Mn^{III} ligand-field transitions. The lower-energy band at 770 nm is due to a one-electron $d_{x^2-y^2} \rightarrow d_{z^2}$ transition. The band at *ca.* 500 nm contains contributions from two

ligand-field transitions - a $d_{yz} \rightarrow d_z^2$ transition at 505 nm and a $d_{xz} \rightarrow d_z^2$ transition near 486 nm. Given these assignments, the position of the lower-energy band reflects the difference between Mn-ligand σ-interactions with the axial and equatorial ligands, while the energy of the higher-energy band reports differences between Mn-hydroxo σ- and π-interactions.

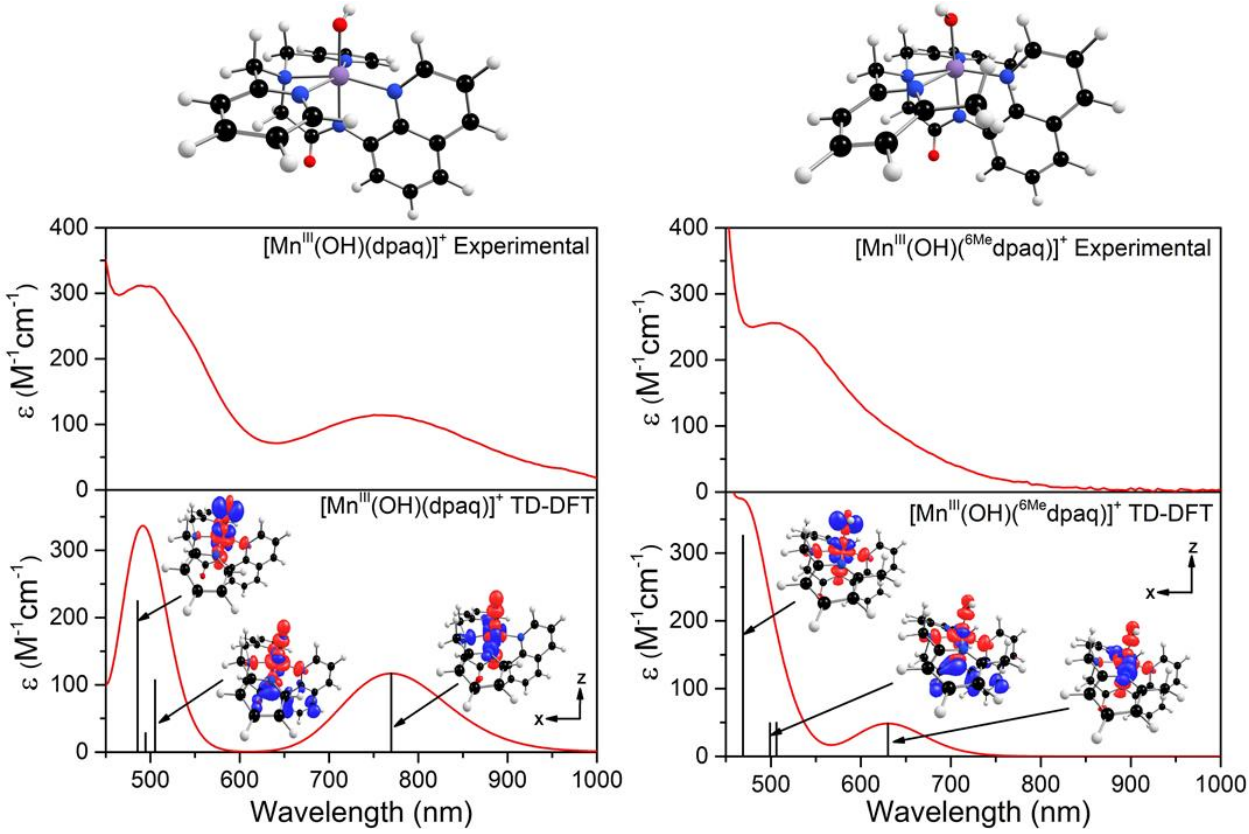

Figure 4.6. TD-DFT computed electronic absorption spectra for $[Mn^{III}(OH)(dpaq)]^+$ (left) and $[Mn^{III}(OH)(^{6Me}dpaq)]^+$ (right). The sticks indicate electronic transitions; EDDMs of selected transitions are included as an inset. Red and blue colors in the EDDMs denotes gain and loss of electron density, respectively. The DFT-computed structures of the Mn^{III}-hydoxo complexes are shown above the absorption spectra.

The TD-DFT-computed electronic absorption spectrum of $[Mn^{III}(OH)(^{6Me}dpaq)]^+$ also nicely reproduces the experimental spectrum. The computed spectrum shows a weak feature near 630 nm that corresponds with the distinct rise in absorption intensity in the experimental spectrum. The

calculated spectrum also shows more intensity at wavelengths less than 550 nm, in good agreement with experiment (Figure 4.6, right). Importantly, the TD-DFT-computed spectrum of $[Mn^{III}(OH)(^{6Me}dpaq)]^+$ reproduces all the major differences and similarities relative to $[Mn^{III}(OH)(dpaq)]^+$; *i.e.*, the lowest-energy band has a pronounced blue-shift, while the higher-energy bands are relatively unperturbed. The lowest-energy band of $[Mn^{III}(OH)(^{6Me}dpaq)]^+$ at 630 nm arise from a one-electron $d_{x^2-y^2} \rightarrow d_{z^2}$ transition. The pronounced blue-shift relative to that of $[Mn^{III}(OH)(dpaq)]^+$ (770 to 630 nm) can be nicely rationalized on the basis of the stabilization of $d_{x^2-y^2}$ MO of $[Mn^{III}(OH)(^{6Me}dpaq)]^+$ caused by the longer Mn-$N_{pyridine}$ bond lengths (Figure 4.5 and Table 4.1). The higher-energy band in the TD-DFT-computed spectrum of $[Mn^{III}(OH)(^{6Me}dpaq)]^+$ contains the $d_{yz} \rightarrow d_{z^2}$ and $d_{xz} \rightarrow d_{z^2}$ transitions. The wavelengths of these transitions are only slightly blue-shifted relative to the corresponding transitions in $[Mn^{III}(OH)(dpaq)]^+$ (505 vs 499 nm, and 486 vs 469 nm, respectively; see Figure 4.6). Overall, the TD-DFT computations reveal that the spectral perturbations between $[Mn^{III}(OH)(dpaq)]^+$ and $[Mn^{III}(OH)(^{6Me}dpaq)]^+$ can be understood on the basis of the elongated Mn-$N_{pyridine}$ bonds in the latter complex.

Oxidative reactivity of $[Mn^{III}(OH)(^{6Me}dpaq)](OTf)$

To evaluate the effect of the Mn-$N_{pyridine}$ bond elongations of $[Mn^{III}(OH)(^{6Me}dpaq)]^+$ on chemical reactivity, we explored the reaction of this complex with TEMPOH and xanthene. Both substrates have been employed previously to assess the reactivity of Mn^{III}-hydroxo adducts.[18, 19] TEMPOH has an unusually small O-H bond dissociation free energy (BDFE = 66.5 kcal/mol, in MeCN at 25 °C) and therefore participates in CPET reactions with a range of compounds.[1] Xanthene has relatively activated bis-benzylic C–H bonds, which provide a reasonable approximation of the bis-allylic C–H bonds of the native substrate of MnLOX.

The addition of 10 equiv. TEMPOH to a 1.25 mM solution of $[Mn^{III}(OH)(^{6Me}dpaq)]^{+}$ in MeCN at -35 °C led to the disappearance of the electronic absorption features of the Mn^{III}-hydroxo complex within 100 s, giving a final spectrum identical to that of $[Mn^{II}(H_2O)(^{6Me}dpaq)]^{+}$ with *ca.* 100 % yield (Figure 4.7). The observed products are consistent with a CPET reaction between the Mn^{III}-hydroxo center and TEMPOH, which would afford TEMPO radical and $[Mn^{II}(H_2O)(^{6Me}dpaq)]^{+}$. Kinetic experiment to obtain the second-order rate constant (k_2) were performed at -35 °C using 10 - 60 equiv. TEMPOH. A plot of k_{obs} vs the concentration of TEMPOH is linear, and a fit to these data provided the second-order rate constant (k_2) of 3.4(2) $M^{-1}s^{-1}$ at -35 °C (Figure 4.8).

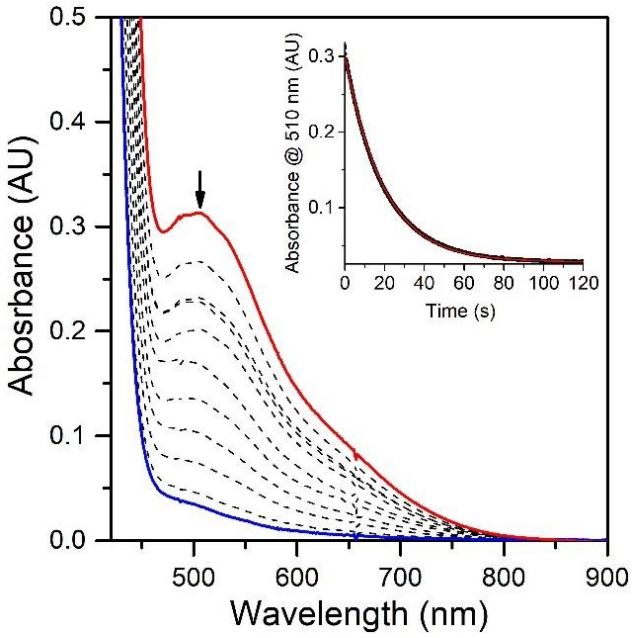

Figure 4.7. Reactions of 1.25 mM $[Mn^{III}(OH)(^{6Me}dpaq)](OTf)$ with 10 equiv. TEMPOH at -35 °C in MeCN (initial and final spectra are the red and blue traces, respectively). Inset: The decay of the 510 nm band over time (black trace) and fit to pseudo-first-order kinetic model (red trace).

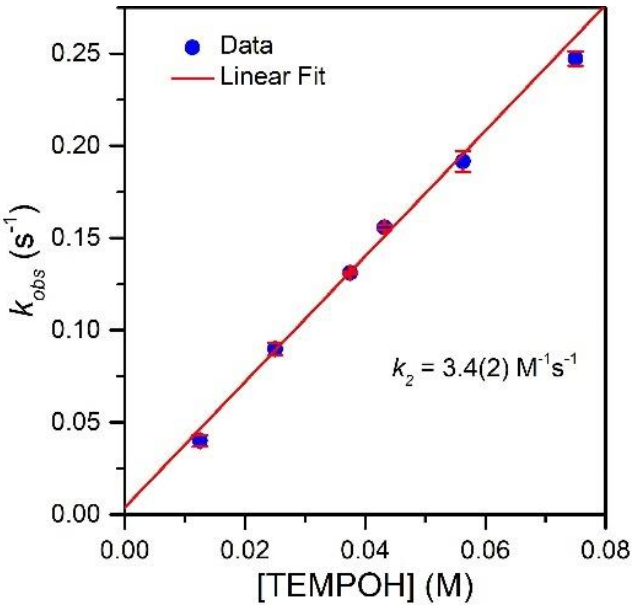

Figure 4.8. Pseudo-first-order rate constants k_{obs} (s^{-1}) as a function of TEMPOH concentration for a 1.25 mM solution of [Mn^{III}(OH)(^{6Me}dpaq)](OTf) in MeCN at -35 °C. The second-order rate constant (k_2) was calculated from the slope of the linear fit.

Table 4.2 compares the second-order rate constant for TEMPOH oxidation by [Mn^{III}(OH)(^{6Me}dpaq)]$^+$ with those determined for [Mn^{III}(OH)(dpaq)]$^+$ and its derivatives. The rate constant for TEMPOH oxidation for [Mn^{III}(OH)(^{6Me}dpaq)]$^+$ is nearly three-fold faster than that of [Mn^{III}(OH)(dpaq)]$^+$ (k_2 = 1.1(1) $M^{-1}s^{-1}$) and almost the same as that determined for [Mn^{III}(OH)(dpaq^{2Me})]$^+$ (k_2 = 3.9(3) $M^{-1}s^{-1}$).[18, 20] Thus, Me substituents on the pyridyl or quinolinyl groups have similar consequences on reactivity.

We also investigated the reactivity of [Mn^{III}(OH)(^{6Me}dpaq)]$^+$ with xanthene by treating a 1.25 mM solution of this Mn^{III}-hydroxo complex in MeCN with 250 equiv. xanthene at 50 °C. In this case, the absorbance band of [Mn^{III}(OH)(^{6Me}dpaq)]$^+$ at 510 nm decayed by only 10% over the course of 1000 minutes, which is within the range of self-decay rate for [Mn^{III}(OH)(^{6Me}dpaq)]$^+$ at this temperature. This apparent lack of reactivity is somewhat unexpected, as [Mn^{III}(OH)(dpaq)]$^+$ reacts with xanthene under similar conditions, albeit at a slow rate (0.0008 s^{-1}). It is possible that

the decreased reactivity for $[Mn^{III}(OH)(^{6Me}dpaq)]^+$ might be due to the steric bulk of the 6-methyl substituents, which could hinder the approach of xanthene to the Mn^{III}-hydroxo unit. Notably, $[Mn^{III}(OH)(dpaq^{2Me})]^+$ reacts with xanthene *ca.* three times slower than $[Mn^{III}(OH)(dpaq)]^+$ (0.00025 s^{-1} vs 0.0008 s^{-1} respectively).[18] In that case, DFT computations demonstrated that the steric bulk of the 2-Me-quinoline moiety in $[Mn^{III}(OH)(dpaq^{2Me})]^+$ caused the xanthene to orientate differently in the transition state from when compared to $[Mn^{III}(OH)(dpaq)]^+$. This reorientation introduced a destabilizing effect that caused the transition state of the $[Mn^{III}(OH)(dpaq^{2Me})]^+$ to be higher than that of the $[Mn^{III}(OH)(dpaq)]^+$ by about 3 kcal/mol. A similar situation caused by the 6-Me-pyridyl groups of $[Mn^{III}(OH)(^{6Me}dpaq)]^+$ could hamper the reaction of this complex with xanthene.

Table 4.2. Second-Order Rate Constants (k_2) for TEMPOH Oxidation by Mn^{III}-hydroxo complexes experimental $E_{1/2}$ and DFT-Calculated Thermodynamic Parameters.

	Experimental	DFT-calculated			
complex	k_2 ($M^{-1}s^{-1}$)	$Mn^{III/II}$ $E_{p,c}$[c]	$Mn^{III/II}$ $E_{1/2}$[c]	Mn^{II}-OH_2 pK_a	BDFE[a]
$[Mn^{III}(OH)(^{6Me}dpaq)]^+$	3.4(2)	-0.63	-0.60	28.6	80.2
$[Mn^{III}(OH)(dpaq)]^+$ [b]	1.1(1)	-0.70	-0.70	29.3	79.1
$[Mn^{III}(OH)(dpaq^{2Me})]^+$ [b]	3.9(3)[d]	-0.62	-0.58	28.7	80.9
$[Mn^{III}(OH)(dpaq^{5NO2})]^+$ [b]	7(1)	-0.57	-0.51	27.8	81.2
$[Mn^{III}(OH)(dpaq^{5Cl})]^+$ [b]	2.8(2)	-0.66	-0.62	28.7	79.8
$[Mn^{III}(OH)(dpaq^{5OMe})]^+$ [b]	0.8(1)	-0.72	-0.73	29.5	78.4

[a] In kcal mol^{-1}. [b] From ref. [20]. [c] In V relative to Fc^+/Fc. [d] From ref.[18].

Thermodynamic Driving Force for TEMPOH Oxidation Using Experimental and Computational Methods.

In our previous investigation of the CPET reactivity of a series of Mn^{III}-hydroxo complexes, we observed a strong correlation between the CPET reaction rate and the variation in the

thermodynamic driving force.[20] The driving force for these reactions is the difference between the BDFE of the $Mn^{II}O(H)$-H bond being formed and the TEMPO-H bond being broken (eqn. 1).

$$\Delta G = \text{BDFE}(Mn^{II}O(H)–H) – \text{BDFE}(\text{TEMPO}–H) \quad (\mathbf{1})$$

Thus, the variation in driving force among a set of Mn^{III}-hydroxo complexes comes from the O–H BDFE of the Mn^{II}-aqua complex. To understand the basis for changes in the O–H BDFE, it is convenient to deconstruct the BDFE into individual proton- and electron-transfer steps, as represented by a square diagram (Scheme 4.1). The horizontal lines in this diagram represent single electron transfer steps, and vertical lines represent single proton transfer steps. The diagonal line represents CPET. The square scheme also illustrates that the O–H BDFE of a Mn^{II}-aqua complex can be calculated using the one-electron reduction potential of the $Mn^{III/II}$-OH couple and the pK_a of the Mn^{II}-OH_2 product using the modified Bordwell equation (eqn. 2).[53]

$$\text{BDFE}(Mn^{II}O(H)–H) = 1.37\text{p}K_a + 23.06E_{1/2} + C_{G,sol} \quad (\mathbf{2})$$

In this equation, $C_{G,sol}$ is a constant for a given solvent ($C_{G,sol,\ MeCN}$ = 54.9 kcal/mol). In our previous investigation of $[Mn^{III}(OH)(dpaq^{5R})]^+$ complexes, we observed that both the reduction potential and pK_a changed as a function of the R substituent, but changes in the potential were the larger and, therefore, dominate contribution to the change in O–H BDFE.[20] A stronger O–H bond in the Mn^{II}-aqua product was associated with faster reaction rates.[20]

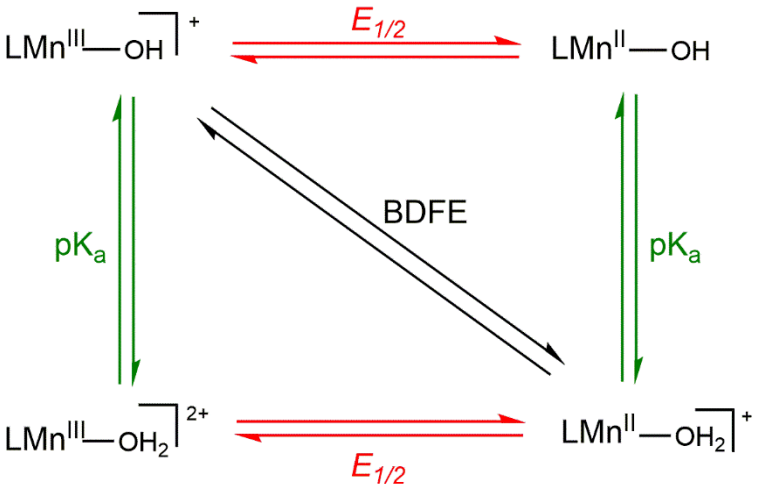

Scheme 4.1. Thermodynamic Square Scheme for Decomposing the O–H BDFE of a Mn^{III}–OH/Mn^{II}–OH_2 Couple.

As a first step in understanding thermodynamic contributions to the CPET reactivity of $[Mn^{III}(OH)(^{6Me}dpaq)]^+$, we performed cyclic voltammetry (CV) experiments to measure the $Mn^{III/II}$-OH peak potential. The $Mn^{III/II}$-OH peak potential was measured to be -0.63 V Fc^+/Fc (Figure A3.6). This potential is between those of $[Mn^{III}(OH)(dpaq^{2Me})]^+$ and $[Mn^{III}(OH)(dpaq^{5Cl})]^+$ (-0.62 V and -0.66 V vs. Fc^+/Fc respectively).[20]The $Mn^{III/II}$-OH peak potentials previously measured for $[Mn^{III}(OH)(dpaq)]^+$ and its derivatives are presented in Table 4.2.

Following a previous approach,[20] we also calculated the pK_a and $E_{1/2}$ values associated with the $[Mn^{III}(OH)(^{6Me}dpaq)]^+/[Mn^{II}(OH_2)(^{6Me}dpaq)]^+$ couple. With this method, which was inspired by Hammes-Schiffer and Solis,[54] intrinsic errors in the calculations should be comparable, and largely cancel, among the series of similar complexes being compared. The details of these calculations are discussed in the appendix and the calculated values are presented in Table 4.2. The $E_{1/2}$ value of $[Mn^{III}(OH)(^{6Me}dpaq)]^+/[Mn^{II}(OH_2)(^{6Me}dpaq)]^+$ couple is 30 mV higher than the experimental $Mn^{III/II}$-OH peak potential. The calculated $E_{1/2}$ value of -0.60 V for $[Mn^{III}(OH)(^{6Me}dpaq)]^+$ is 100 mV more positive than that of $[Mn^{III}(OH)(dpaq)]^+$ (-0.70 V) but

nearly the same as that of $[Mn^{III}(OH)(dpaq^{2Me})]^+$ (-0.58 V). Thus, $[Mn^{III}(OH)(^{6Me}dpaq)]^+$ is a better one-electron oxidant than $[Mn^{III}(OH)(dpaq)]^+$ and is on par with $[Mn^{III}(OH)(dpaq^{2Me})]^+$. The origin of the increased $Mn^{III/II}$ reduction potential in $[Mn^{III}(OH)(^{6Me}dpaq)]^+$ relative to $[Mn^{III}(OH)(dpaq)]^+$ results from the longer Mn-$N_{pyridine}$ bonds (Mn–N4 and Mn–N5, see Table 4.1). This elongation reduces the interaction between the Mn center and the pyridine ligands, which consequentially leads to a more Lewis acidic Mn center with a higher propensity to undergo one-electron reduction. The DFT calculations predict a pK_a value of 28.6 for $[Mn^{II}(OH_2)(^{6Me}dpaq)]^+$, which makes this complex more acidic than $[Mn^{II}(OH_2)(dpaq)]^+$ (pK_a = 29.3). Together the $E_{1/2}$ and pK_a values combine to yield a O–H BDFE of 80.2 kcal/mol for $[Mn^{II}(OH_2)(^{6Me}dpaq)]^+$, which is larger than that of $[Mn^{III}(OH)(dpaq)]^+$ (79.1 kcal/mol). It is important to note that the $E_{1/2}$ and pK_a terms for $[Mn^{II}(OH_2)(^{6Me}dpaq)]^+$ shift in directions that oppose one another when considering the net BDFE, but the shift in $E_{1/2}$ is larger and therefore dominant. Specifically, while $[Mn^{II}(OH_2)(^{6Me}dpaq)]^+$ is less basic than $[Mn^{III}(OH)(dpaq)]^+$ by 0.7 pK_a units (0.96 kcal/mol contribution to BDFE), the Mn^{III} center in $[Mn^{III}(OH)(^{6Me}dpaq)]^+$ has a more positive $E_{1/2}$ than $[Mn^{III}(OH)(dpaq)]^+$ by 0.10 V (2.08 kcal/mol contribution to BDFE). The slightly higher O-H BDFE of $[Mn^{II}(OH_2)(^{6Me}dpaq)]^+$ than $[Mn^{II}(OH_2)(dpaq)]^+$ is as expected given the slight rate enhancement for TEMPOH oxidation observed for $[Mn^{III}(OH)(^{6Me}dpaq)]^+$ (Table 4.2).

The rate of TEMPOH oxidation by $[Mn^{III}(OH)(^{6Me}dpaq)]^+$ can be plotted against the O–H BDFE of the $[Mn^{II}(OH_2)(^{6Me}dpaq)]^+$ product (Figure 4.9). As shown in this plot, the $[Mn^{III}(OH)(^{6Me}dpaq)]^+$ complex nicely follows the linear correlation previously observed for Mn^{III}-hydroxo complexes.[20] The individual contributions of the pK_a and $E_{1/2}$ to the Mn^{II}-aqua O – H BDFEs for these complexes are presented in Figure 4.10, and the correlations of these parameters to the reaction rates of the Mn^{III}-hydroxo complexes with TEMPOH are shown in

Figure 4.11. Among this series, the more significant change to BDFE originates from the $E_{1/2}$ contributions, with only a slight contribution originating from the pK_a (Table 4.2 and Figure 4.11). The pK_a change across the series is 1.7 pK_a units (2.33 kcal/mol), whereas the calculated $E_{1/2}$ changes by 0.22 V (5.07 kcal/mol). Thus, the $E_{1/2}$ contributes about twice as much as the pK_a to the net BDFE across the series.

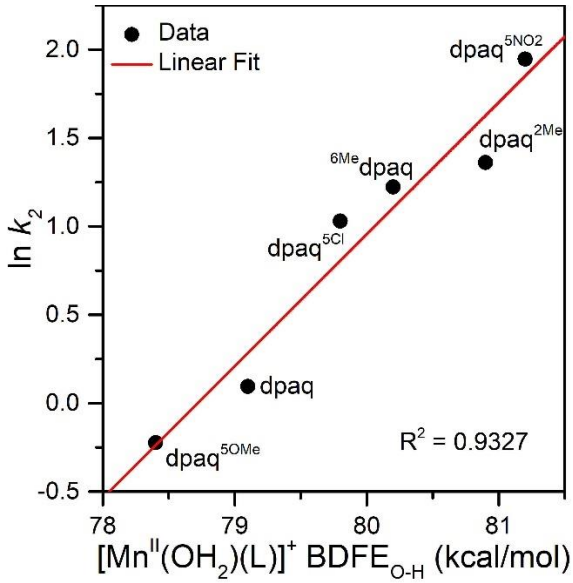

Figure 4.9. A plot of ln k_2 vs Mn^{II}-aqua O – H BDFE (kcal/mol).

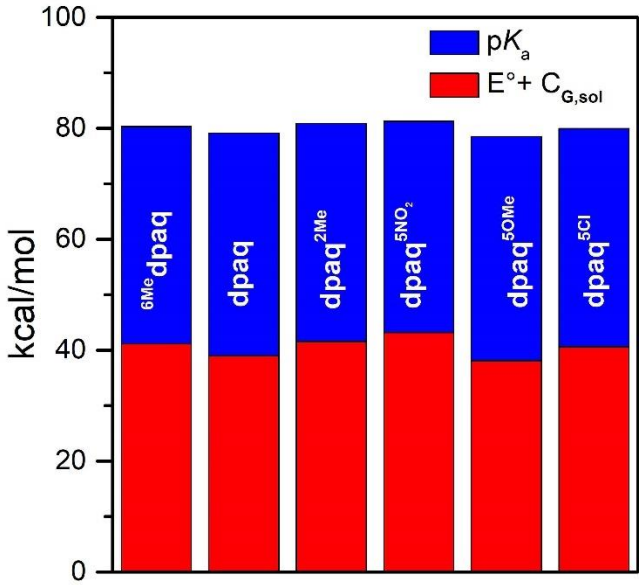

Figure 4.10. Thermodynamic contributions to the O–H BDFE of Mn^{II}-aqua complexes from the Mn^{III}-OH/Mn^{II}-OH reduction potentials and Mn^{II}-aqua pK_a values.

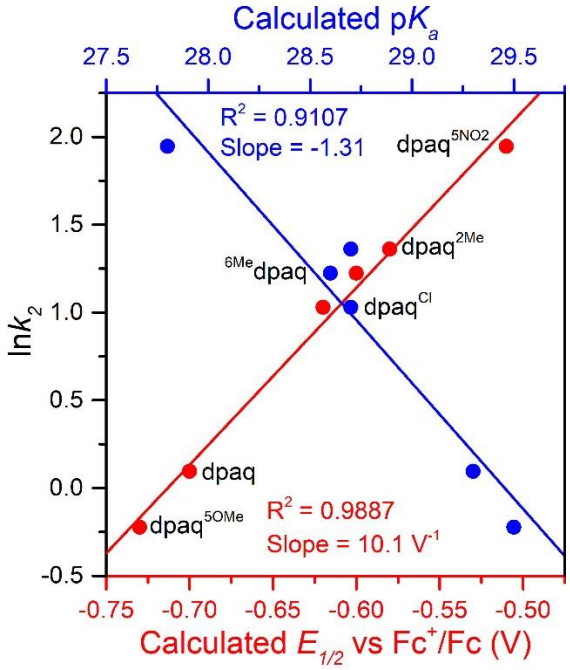

Figure 4.11. A plot of ln k_2 vs calculate $E_{1/2}$ vs Fc^+/Fc (V) and pK_a.

From Figure 4.11, we observe a strong, linear correlation between the $E_{1/2}$ of the $Mn^{III/II}$ couple and the ln(k_2) for TEMPOH oxidation, with more positive potentials translating to faster reaction rates. In contrast, the plot of ln(k_2) for TEMPOH oxidation versus the Mn^{II}-aqua pK_a value shows an inverse correlation, where the more basic complexes show slower reaction rates. Thus, the pK_a and $E_{1/2}$ contributions to the O–H BDFE are counterbalancing each other to affect the rate of reaction. However, from the slope of the $E_{1/2}$ and pK_a plots (slope = 10.1 V^{-1} and -1.31/pK_a unit, respectively, see Figure 4.11), the $E_{1/2}$ term has a superior effect on the reaction rate relative to pK_a. Thus, increasing pK_a only leads to slight damping of the reactivity of these complexes.

Ligand Substitution Reactions of $[Mn^{III}(OO^tBu)(^{6Me}dpaq)]^+$ with protic solvents.

While the reaction of TEMPOH with $[Mn^{III}(OH)(^{6Me}dpaq)]^+$ mimics one of the elementary reactions proposed in the catalytic cycle of MnLOX, one of the proposed mechanisms for this enzyme postulates a ligand substitution reaction, where a Mn^{III}-alkylperoxo adduct reacts with water to give the alkylhydroperoxo product and a Mn^{III}-hydroxo adduct.[55] Since both $[Mn^{III}(OH)(^{6Me}dpaq)]^+$ and its Mn^{III}-alkylperoxo analogue $[Mn^{III}(OO^tBu)(^{6Me}dpaq)]^+$ are both well characterized and stable at room-temperature, we took advantage of these complexes to explore if we could mimic this proposed ligand substitution reaction. The addition of 100 equiv. H_2O to $[Mn^{III}(OO^tBu)(^{6Me}dpaq)]^+$ in an anerobic solution of MeCN results in a loss of intensity of the electronic absorption band of the Mn^{III}-alkylperoxo adduct at 650 nm and growth in absorbance at ~500 nm (Figure 4.12). This conversion showed isosbestic behavior (with an isosbestic point at ~574 nm), suggesting a simple conversion involving no accumulating intermediates. The final spectrum is identical to that of $[Mn^{III}(OH)(^{6Me}dpaq)]^+$, suggesting the occurrence of a ligand substitution reaction. Mass spectral analysis of the solution following the reaction of

$[Mn^{III}(OO^tBu)(^{6Me}dpaq)]^+$ with H_2O revealed a peak at *m/z* = 482.14, further confirming the formation of $[Mn^{III}(OH)(^{6Me}dpaq)]^+$ (calculated *m/z* = 482.14, Figure 4.13). At longer time periods, we observed precipitation of a brown solid, which may be evidence of some demetallation of the $[Mn^{III}(OH)(^{6Me}dpaq)]^+$ due to the presence of water.

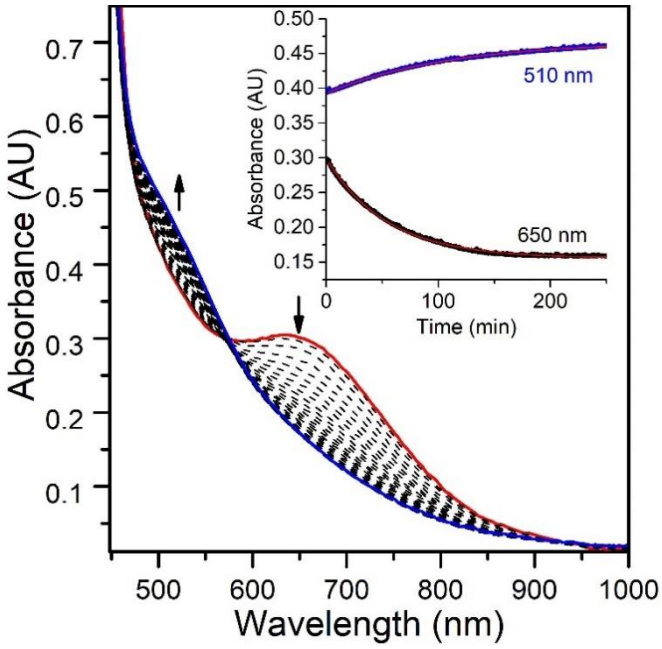

Figure 4.12. Electronic absorption spectra monitoring the reaction of anaerobic sample of 2 mM solution of $[Mn^{III}(OO^tBu)(^{6Me}dpaq)]^+$ in MeCN with 100 equiv. of H_2O at 298 K. (Inset) time course for the spectral changes.

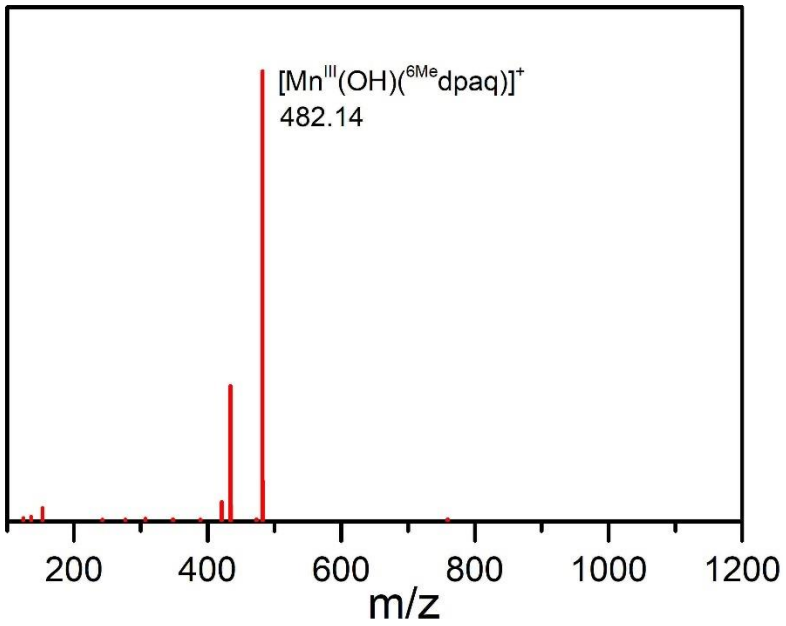

Figure 4.13. ESI-MS data for a 2 x 10^{-3} mM solution of anaerobic reaction of $[Mn^{III}(OO^tBu)(^{6Me}dpaq)]^+$ with H_2O at 298 K.

4.4 Conclusions

In this study, we were able to explain the observed difference in the electronic spectrum of the $[Mn^{III}(OH)(^{6Me}dpaq)]^+$ relative to those of $[Mn^{III}(OH)(dpaq)]^+$ and its derivatives using TD-DFT calculations. The spectral change result from the elongation of the Mn-$N_{pyridine}$ bonds caused by the 6-Me-pyridyl groups in $[Mn^{III}(OH)(^{6Me}dpaq)]^+$, which leads to the stabilization of the Mn dx^2-y^2 orbital. This stabilization results in the blue shift of the dx^2-$y^2 \rightarrow dz^2$ electronic transition relative to that observed in the $[Mn^{III}(OH)(dpaq)]^+$ complex and its derivatives. The blue shift caused the dx^2-$y^2 \rightarrow dz^2$ transition to be enveloped into a single band from *ca.* 800 nm – 489 nm, together with a more intense $d_{xz} \rightarrow dz^2$ at 469 nm. The oxidative capability of the $[Mn^{III}(OH)(^{6Me}dpaq)]^+$ complex was assessed by exploring the rate of TEMPOH oxidation. The reactivity of $[Mn^{III}(OH)(^{6Me}dpaq)]^+$ with TEMPOH is 3-fold faster than that of $[Mn^{III}(OH)(dpaq)]^+$. This rate enhancement has its basis in the more positive $Mn^{III/II}$ reduction potential of $[Mn^{III}(OH)(^{6Me}dpaq)]^+$

than $[Mn^{III}(OH)(dpaq)]^+$. The TEMPOH oxidation rate for $[Mn^{III}(OH)(^{6Me}dpaq)]^+$ is thus congruent with a previously established linear free energy relationship established for Mn^{III}-hydroxo complexes. The related $[Mn^{III}(OO^tBu)(^{6Me}dpaq)]^+$ species reacts with water to form the Mn^{III}-hydroxo adduct $[Mn^{III}(OH)(^{6Me}dpaq)]^+$. This reaction mimics an elementary step proposed in some mechanisms for the MnLOX enzyme.

4.5 Acknowledgement

This work was supported by the U.S. National Science Foundation (CHE-1900384 to T.A.J). Support for the NMR instrumentation was provided by NIH Shared Instrumentation Grant # S10OD016360. The U.S. NSF is also acknowledged for funds used for the purchase of X-ray instruments (CHE-0079282) and the EPR spectrometer (CHE-0946883).

4.6 References

1. J. J. Warren, T. A. Tronic and J. M. Mayer, *Chemical Reviews*, 2010, **110**, 6961-7001.
2. M. K. Coggins, L. M. Brines and J. A. Kovacs, *Inorganic Chemistry*, 2013, **52**, 12383-12393.
3. J. M. Mayer, *Accounts of Chemical Research*, 2011, **44**, 36-46.
4. Y. Chen, A. Wennman, S. Karkehabadi, Å. Engström and E. H. Oliw, *Journal of Lipid Research*, 2016, **57**, 1574-1588.
5. W. Zhu and N. G. J. Richards, *Essays in Biochemistry*, 2017, **61**, 259-270.
6. C. Krebs, D. Galonić Fujimori, C. T. Walsh and J. M. Bollinger, *Accounts of Chemical Research*, 2007, **40**, 484-492.
7. C. Arunkumar, Y.-M. Lee, J. Y. Lee, S. Fukuzumi and W. Nam, *Chemistry – A European Journal*, 2009, **15**, 11482-11489.
8. D. E. Lansky and D. P. Goldberg, *Inorganic Chemistry*, 2006, **45**, 5119-5125.
9. V. Dantignana, J. Serrano-Plana, A. Draksharapu, C. Magallón, S. Banerjee, R. Fan, I. Gamba, Y. Guo, L. Que, M. Costas and A. Company, *Journal of the American Chemical Society*, 2019, **141**, 15078-15091.
10. W. Rasheed, A. Draksharapu, S. Banerjee, V. G. Young Jr., R. Fan, Y. Guo, M. Ozerov, J. Nehrkorn, J. Krzystek, J. Telser and L. Que Jr., *Angewandte Chemie International Edition*, 2018, **57**, 9387-9391.
11. P. Pirovano and A. R. McDonald, *European Journal of Inorganic Chemistry*, 2018, **2018**, 547-560.

12. D. B. Rice, A. A. Massie and T. A. Jackson, *Accounts of Chemical Research*, 2017, **50**, 2706-2717.
13. C. R. Goldsmith, A. P. Cole and T. D. P. Stack, *Journal of the American Chemical Society*, 2005, **127**, 9904-9912.
14. A.-F. Miller, F. Padmakumar, D. Sorkin, A. Karapetian and C. K. Vance, *J. Inorg. Biochem.*, 2003, **93**, 71-83.
15. A.-F. Miller, *Curr. Opin. Chem. Biol.*, 2004, **8**, 162-168.
16. C. Su, M. Sahlin and E. H. Oliw, *Journal of Biological Chemistry*, 2000, **275**, 18830-18835.
17. A. Wennman, S. Karkehabadi and E. H. Oliw, *Archives of Biochemistry and Biophysics*, 2014, **555–556**, 9-15.
18. D. B. Rice, G. B. Wijeratne, A. D. Burr, J. D. Parham, V. W. Day and T. A. Jackson, *Inorganic Chemistry*, 2016, **55**, 8110-8120.
19. G. B. Wijeratne, B. Corzine, V. W. Day and T. A. Jackson, *Inorganic Chemistry*, 2014, **53**, 7622-7634.
20. D. B. Rice, A. Munasinghe, E. N. Grotemeyer, A. D. Burr, V. W. Day and T. A. Jackson, *Inorganic Chemistry*, 2019, **58**, 622-636.
21. D. Chen, Y. Wang and J. Klankermayer, *Angewandte Chemie International Edition*, 2010, **49**, 9475-9478.
22. J. J. Warren and J. M. Mayer, *Biochemistry*, 2015, **54**, 1863-1878.
23. M. K. Coggins, V. Martin-Diaconescu, S. DeBeer and J. A. Kovacs, *Journal of the American Chemical Society*, 2013, **135**, 4260-4272.
24. M. K. Coggins, S. Toledo, E. Shaffer, W. Kaminsky, J. Shearer and J. A. Kovacs, *Inorganic Chemistry*, 2012, **51**, 6633-6644.
25. D. B. Rice, G. B. Wijeratne, A. D. Burr, J. D. Parham, V. W. Day and T. A. Jackson, *Inorganic Chemistry*, 2016, **55**, 8110-8120.
26. F. Neese, F. Wennmohs, U. Becker and C. Riplinger, *The Journal of Chemical Physics*, 2020, **152**, 224108.
27. C. Lee, W. Yang and R. G. Parr, *Physical Review B*, 1988, **37**, 785-789.
28. A. D. Becke, *The Journal of Chemical Physics*, 1993, **98**, 5648-5652.
29. F. Weigend and R. Ahlrichs, *Physical Chemistry Chemical Physics*, 2005, **7**, 3297-3305.
30. F. Weigend, *Physical Chemistry Chemical Physics*, 2006, **8**, 1057-1065.
31. S. Grimme, S. Ehrlich and L. Goerigk, *Journal of Computational Chemistry*, 2011, **32**, 1456-1465.
32. S. Grimme, J. Antony, S. Ehrlich and H. Krieg, *The Journal of Chemical Physics*, 2010, **132**, 154104.
33. S. Grimme, *Journal of Computational Chemistry*, 2006, **27**, 1787-1799.
34. S. Grimme, *Journal of Computational Chemistry*, 2004, **25**, 1463-1473.
35. A. V. Marenich, C. J. Cramer and D. G. Truhlar, *The Journal of Physical Chemistry B*, 2009, **113**, 6378-6396.
36. R. Izsák and F. Neese, *The Journal of Chemical Physics*, 2011, **135**, 144105.
37. T. Petrenko, S. Kossmann and F. Neese, *The Journal of Chemical Physics*, 2011, **134**, 054116.
38. D. B. Rice, S. D. Jones, J. T. Douglas and T. A. Jackson, *Inorganic Chemistry*, 2018, **57**, 7825-7837.

39. C. R. Goldsmith, A. P. Cole and T. D. P. Stack, *Journal of the American Chemical Society*, 2005, **127**, 9904-9912.
40. S. El Ghachtouli, B. Lassalle-Kaiser, P. Dorlet, R. Guillot, E. Anxolabéhère-Mallart, C. Costentin and A. Aukauloo, *Energy & Environmental Science*, 2011, **4**, 2041-2044.
41. Z. Shirin, B. S. Hammes, V. G. Young and A. S. Borovik, *Journal of the American Chemical Society*, 2000, **122**, 1836-1837.
42. B. Cheng, P. H. Fries, J.-C. Marchon and W. R. Scheidt, *Inorganic Chemistry*, 1996, **35**, 1024-1032.
43. A. A. Eroy-Reveles, Y. Leung, C. M. Beavers, M. M. Olmstead and P. K. Mascharak, *Journal of the American Chemical Society*, 2008, **130**, 4447-4458.
44. D. M. Eichhorn and W. H. Armstrong, *Journal of the Chemical Society, Chemical Communications*, 1992, DOI: 10.1039/C39920000085, 85-87.
45. T. J. Hubin, J. M. McCormick, N. W. Alcock and D. H. Busch, *Inorganic Chemistry*, 2001, **40**, 435-444.
46. Z. Shirin, A. S. Borovik and V. G. Young Jr, *Chemical Communications*, 1997, DOI: 10.1039/A703395H, 1967-1968.
47. J. D. Parham, G. B. Wijeratne, D. B. Rice and T. A. Jackson, *Inorganic Chemistry*, 2018, **57**, 2489-2502.
48. T. A. Jackson, A. Karapetian, A.-F. Miller and T. C. Brunold, *Biochemistry*, 2005, **44**, 1504-1520.
49. T. A. Jackson, A. Karapetian, A.-F. Miller and T. C. Brunold, *J. Am. Chem. Soc.*, 2004, **126**, 12477-12491.
50. R. A. Geiger, S. Chattopadhyay, V. W. Day and T. A. Jackson, *Journal of the American Chemical Society*, 2010, **132**, 2821-2831.
51. H. E. Colmer, A. W. Howcroft and T. A. Jackson, *Inorganic Chemistry*, 2016, **55**, 2055-2069.
52. H. E. Colmer, R. A. Geiger, D. F. Leto, G. B. Wijeratne, V. W. Day and T. A. Jackson, *Dalton Transactions*, 2014, **43**, 17949-17963.
53. F. G. Bordwell, J. Cheng, G. Z. Ji, A. V. Satish and X. Zhang, *Journal of the American Chemical Society*, 1991, **113**, 9790-9795.
54. B. H. Solis and S. Hammes-Schiffer, *Inorganic Chemistry*, 2014, **53**, 6427-6443.
55. A. Company, J. Lloret-Fillol and M. Costas, 2013.

Chapter 5

Summary and Outlook

5.1 Summary

This work contributed to the knowledge in the field of Mn^{III}-hydroxo and Mn^{III}-alkylperoxo complexes. Summary from this work include the following:

- Using a pair of Mn^{III}-hydroxo complexes (with and without hydrogen bonding), we mimicked a hydrogen-bonding interaction observed in the active site of the MnLOX and MnSOD enzymes. The Mn^{III}-hydroxo complex showed an enhancement in rate by 15- and 100-fold relative to the complex without hydrogen bonding in a CPET reaction. A detailed analysis of the thermodynamic contributions to CPET reactions of two Mn^{III}-hydroxo complexes revealed that the complex with a hydrogen-bonding interaction is significantly more basic. Thus, we were able to show that the hydrogen-bonding interaction observed in the active-site of biological enzymes like MnSOD and MnLOX likely serves a functional role of increasing the basicity of the hydroxo ligand. This increase in basicity will activate the Mn^{III}-hydroxo unit towards CPET reactions with biological substrates.
- The synthesis of two new, room-temperature stable Mn^{III}-alkylperoxo complexes, $[Mn^{III}(OO^{t}Bu)(^{6Me}dpaq)]^{+}$ and $[Mn^{III}(OOCm)(^{6Me}dpaq)]^{+}$, was achieved based on the inspiration from previously developed structure-reactivity correlations. These new complexes have structural perturbation at the 6-position of the pyridine rings that resulted in an elongation of the equatorial Mn^{III}-$N_{pyridine}$ bonds. These complexes are the most stable Mn^{III}-alkylperoxo complexes known to date. Because of this stability, we were able to structurally characterize one of these complexes by X-ray crystallography, thereby obtaining structural information to assess correlations with other Mn^{III}-alkylperoxo complexes.

- The new Mn^{III}-alkylperoxo complexes display direct reactivity with phosphines, making them the only known Mn^{III}-alkylperoxo complexes to react with substrates. The Mn^{III}-alkylperoxo complexes also react with 9,10-DHA indirectly, by decomposing to give high valent Mn-oxo species that oxidize the C-H bond of 9,10-DHA. These results exemplify the effect of structural perturbation and local coordination environment on the stability and reactivity of Mn^{III}-alkylperoxo complexes.
- The Mn^{III}-alkyperoxo complexes are sensitive to protic solvents, undergoing hydrolysis in the presence of water, TFE and MeOH. In the case of water, hydrolysis leads to the formation of the Mn^{III}-hydroxo compound, and this reaction mimics the reactivity of the Mn^{III}-alkylperoxo intermediate in the proposed alternative mechanism of MnLOX.
- The Mn^{II} complex of the H^{6Me}dpaq ligand showed a significantly suppressed reactivity with dioxygen. This could be due to the elongated equatorial Mn-$N_{pyridine}$ bonds resulting from the steric perturbation from the 6-methyl substituents. This elongation leads to an increase in the Lewis acidity of the Mn-center, thus increasing the $Mn^{III/II}$ reduction potential. The increased $Mn^{III/II}$ reduction potential presumably leads to suppression of the reactivity of the Mn^{II} complex with dioxygen.
- The structural perturbation from the 6-methyl substituents also enhanced the CPET capability of the $[Mn^{III}(OH)(^{6Me}dpaq)]^{+}$ complex by three-fold relative to the $[Mn^{III}(OH)(dpaq)]^{+}$ complex. These results exemplify how structural perturbation can modulate thermodynamic parameters, which will eventually affect the rate of a CPET reaction.

5.2 Outlook

The effort to develop metal complexes that model biological enzymes is continually thriving, with new and interesting discoveries that provide knowledge and principles that can be employed to develop synthetic biocatalysts. It is a privilege to make some contributions and be a part of this great effort. However, there is still more work to be done.

Starting with the Mn^{III}-hydroxo chemistry, we have been able to provide insights into the functional role of the hydrogen bonding interaction observed in the active sites of MnLOX and MnSOD, but it has been difficult to obtain structural information for the model complex containing the hydrogen bond acceptor. Although we provided experimental and computational evidence to establish the structure of the complex with hydrogen bonding interaction, it will also be ideal to obtain the actual crystal structure of this complex. This structural information will help gain an insight into the degree of hydrogen bonding interaction present in the hydrogen-bonding complex. The crystal structure of this complex and its proposed derivatives (Figure 6.1) can be useful to create structure-activity correlations (*i.e.*, hydrogen-bonding distance between acceptor and donor atoms vs. reactivity). While the solid-state structures may be difficult to obtain, and the solid-state structures may not be an exact representation of the structure in the solution, the electron density on the nitrogen donor atom can be modulated by functionalizing the para position to hydrogen bond acceptor (nitrogen atom) with electron-donating and electron-withdrawing groups. This will regulate the degree of hydrogen-bonding interaction in the Mn^{III}-hydroxo complex. Being able to control the degree of hydrogen-bonding interaction will allow us to understand the correlation between the degree of the hydrogen-bonding interaction and the reactivity of the Mn^{III}-hydroxo complexes. Additionally, these studies will help to establish that the observed enhancement in the

reactivity of the complex with hydrogen-bonding interaction relative to the complex without hydrogen bonding originates from this hydrogen-bonding effect.

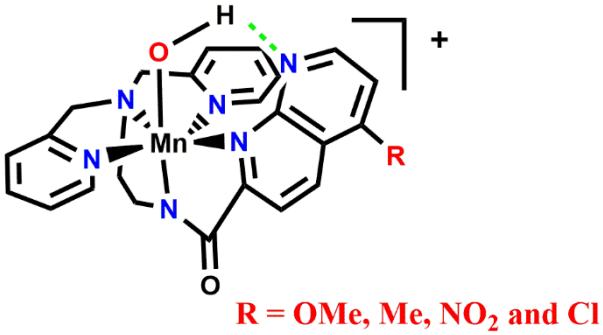

Figure 6.1. Functionalization of the 1,8-naphthyridine group to modulate the degree/strength of hydrogen-bonding interaction.

Another important progress will be the protonation of the Mn^{III}-hydroxo complexes (with and without hydrogen bonding) to obtain their Mn^{III}-aqua complexes. This approach seems promising as observed from exploratory experiments. For example, the reaction of the $[Mn^{III}(OH)(PaPy_2N)]^+$ with 1.0 equiv. $HClO_4$ gave a new species observed by electronic absorption spectroscopy and proposed to be $[Mn^{III}(OH_2)(PaPy_2N)]^{2+}$ (Figure 6.2). This new species can also be deprotonated with 1.0 equiv. of Et_3N to reform $[Mn^{III}(OH)(PaPy_2N)]^+$ (Figure 6.3). Similar results have been observed with the $[Mn^{III}(OH)(PaPy_2Q)]^+$. More detailed studies to confirm the formation of the Mn^{III}-aqua complexes should be pursued. The attainment of this feat will be useful in measuring the experimental pK_a of the Mn^{III}-aqua complexes, which when combined with electrochemical measurements, can be used to calculate the bond dissociation free energy (BDFE) of the Mn^{II}-aqua complexes. The obtainment of experimentally determined BDFE will be useful for correlating reactivity with thermodynamic properties.

Additionally, more work needs to be done on the investigation of the reaction of the $[Mn^{III}(OH)(PaPy_2Q)]^+$ and $[Mn^{III}(OH)(PaPy_2N)]^+$ with 4-nitro-2,6-*di*-*tert*-butylphenol (4-NO_2-

2,6-DTBP) substrate. We observed faster reaction rates than expected with this substrate. Perhaps, there is a change of mechanism in the reaction of this substrate with the Mn^{III}-hydroxo complexes.

The Mn^{III}-alkylperoxo complexes are very interesting and our group is very excited to further explore their chemistry. While we have shown the influence of the local coordination environment on the stability and the reactivity of the complexes, we can tentatively propose that the combined effect of steric perturbations along the equatorial Mn-$N_{pyridine}$ bonds, coupled with the N_5- coordination sphere of the dpaq ligand contributes to the dramatic enhancement in stability and reactivity of these complexes. Although the bond length of the equatorial Mn-$N_{pyridine}$ bonds *cis* to the alkylperoxo O-O bonds have been correlated to stability; it is currently unclear how this leads to a dramatic improvement in the stability of dpaq complexes compared to the thiolate-ligated complexes. Future work will include the synthesis of the ^{6Me}dpaq derivatives of the Mn^{III}-alkylperoxo complexes by functionalization at the 5-position of the quinoline group – $[Mn^{III}(OOR)(^{6Me}dpaq^{5R})]^+$ (R = NO_2 and OMe and R = ^{t}Bu or cumyl) (Figure 6.4) to investigate the effect of modulating the donation strength through the amide nitrogen *trans* to the alkylperoxo ligand on the complex stability and reactivity, and we are eagerly looking forward to the exciting results from the studies. I am particularly looking forward to the structure and reactivity of the $H^{6Me}dpaq^{5NO2}$ complex. It will be interesting to see the effect of weakening the Mn-N_{amide} bond, resulting from the electron-withdrawing property of the $5NO_2$ group on the complex stability and reactivity with substrates. My assumption is that the Mn^{III}-center in $[Mn^{III}(OOR)(^{6Me}dpaq^{5NO2})]^+$ complex will have a relatively higher Lewis acidity and a consequentially higher $Mn^{III/II}$ reduction potential compared to the other $H^{6Me}dpaq^{5R}$ complexes. Thus, $[Mn^{III}(OOR)(^{6Me}dpaq^{5NO2})]^+$ is expected to be potentially more reactive towards substrates. A library of these Mn^{III}-alkylperoxo complexes will allow us to correlate structure with activity and thus gain more insights into the

factors that control the reactivity, enhance stability and determine the thermal decomposition pathway of the Mn^{III}-alkylperoxo complexes.

Additionally, more work should be done to investigate the reaction mechanism of the Mn^{III}-alkylperoxo complexes with *para*-substituted 2,6-*di*-*tert*-buytlphenolic substrates. We observed the reaction of these substrates with Mn^{III}-alkylperoxo complexes, but the plots to obtain the second-order rate constants are always with intercepts. Also, the characterizations of the resulting organic products from the reactions showed mixtures of oxidized organic compounds. Thus, this reaction should be investigated for an understanding of the reaction mechanism

Finally, work should also be done to obtain the second-order rate constant (k_2) for the reaction of the Mn^{III}-alkylperoxo complexes with protic solvents to give the hydrolyzed products (Mn^{III}-OH in the case of water). Currently, we are only informed of these reactions, but we have no kinetic information about the reaction. Thus, it will be necessary to pursue the obtainment of the k_2 for these reactions and the information from these studies can provide some insight into the step involving the conversion of Mn^{III}-alkylperoxo to Mn^{III}-OH in the alternative pathway for the activity of MnLOX enzyme.

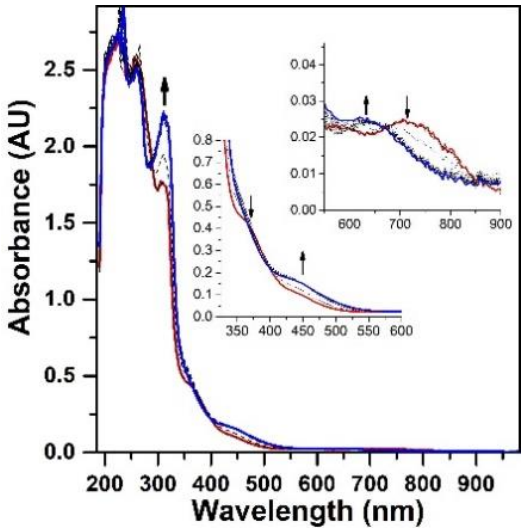

Figure 6.2. Reaction of $[Mn^{III}(OH)(PaPy_2N)]^+$ (red trace) with 1.0 equiv. of $HClO_4$ in MeCN at 25 °C. The black dashed lines represent intermediates, and the blue trace is the final reaction mixture. Insets show zoomed-in regions.

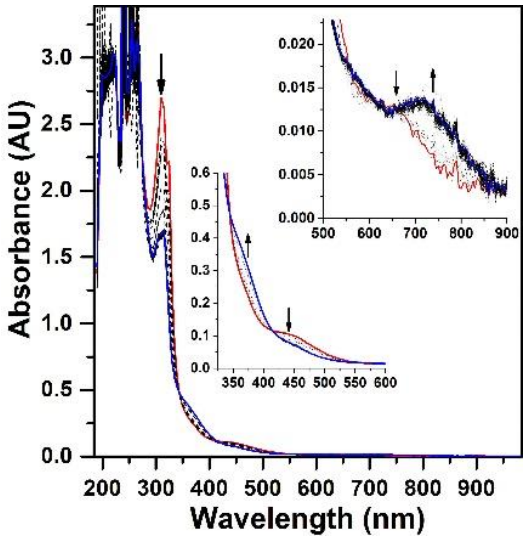

Figure 6.3. Reaction of putative $[Mn^{III}(OH_2)(PaPy_2N)]^{2+}$ (red trace) with 1.0 equiv. of Et_3N in MeCN at 25 °C. The black dashed lines represent intermediates, and the blue trace is the final reaction mixture. Insets show zoomed-in regions.

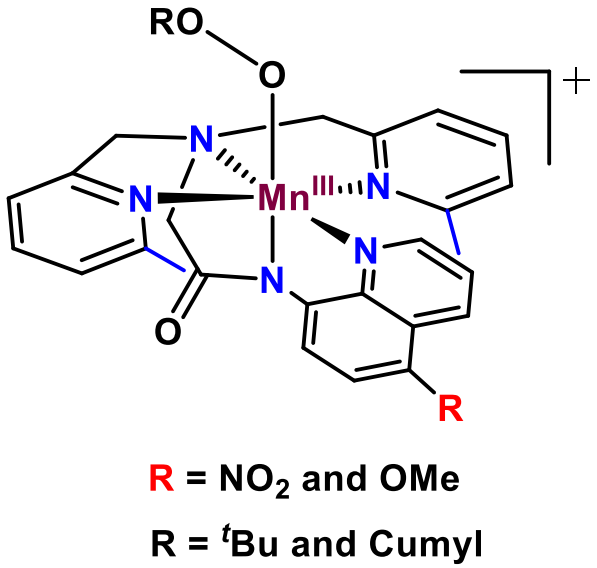

Figure 6.4. $[Mn^{III}(OOR)(^{6Me}dpaq^{5R})]^{+}$ showing functionalization at the 5-position of the quinoline ring to modulate donation to the Mn^{III}-center through the N_{amide} atom.

Appendix 1

Table A1.1. Crystal data and structure refinement for Mn^{II} complexes.

Parameter	$[Mn^{II}(PaPy_2Q)](OTf)$	$[Mn^{II}(PaPy_2N)](OTf)\cdot CH_3CN$	$[Mn^{II}(PaPy_2N)](PF_6)\cdot CH_3CN$
Formula	$C_{25}H_{22}F_3MnN_5O_4S$	$C_{26}H_{24}F_3MnN_7O_4S$	$C_{25}H_{22.5}F_6MnN_{6.75}OP$
Identification code	q76k	v04f	q68k
Formula weight	600.47	642.52	633.41
Crystal system	Monoclinic	Monoclinic	Triclinic
Space group	$P2_1/c$	$P2_1/c$	P-1
Crystal size (mm^3)	0.035 x 0.035 x 0.010	0.260 x 0.135 x 0.060	0.126 x 0.113 x 0.043
a/Å	10.9171(3)	12.1535(5)	7.6747(2)
b/ Å	21.5758(6)	29.7838(13)	12.1236(4)
c/ Å	11.9690(3)	7.8581(3)	30.3033(9)
α/°	90.00	90.00	78.610(2)
β/°	112.0894(15)	97.228(2)	88.801(2)
γ/°	90.00	90.00	80.682(2)
V/ $Å^3$	2612.30(12)	2821.8(2)	2727.39(14)
Z	4	4	4
Dcalcd/g cm^{-3}	1.527	1.512	1.543
F(000)	1228	1316	1287
Absorption coefficient /mm^{-1}	5.422	5.081	5.163
T/K	200(2)	200(2)	200(2)
λ/ Å	1.54178	1.54178	1.54178
θ range/°	4.098-70.233	2.967-68.165	1.487-70.367
Reflections collected	18292	15551	36334
Completeness to θ = 66.000° (%)	98.7	98.7	96.2
Index ranges	-11≤h≤12,-25≤k≤22,-13≤l≤14	-14≤h≤14, -32≤k≤35, -7≤l≤9	-8≤h≤9, -14≤k≤14, -36≤l≤35
Data/Restraint/parameters	4782 / 0 / 356	5004 / 0 / 464	9581 / 0 / 750
R1(F), $wR_2(F^2)$ (> $2\sigma(F^2)$)	0.0475, 0.1282	0.0679, 0.1688	0.0747, 0.1963
R1(F), $wR_2(F^2)$ (all data)	0.0611, 0.1356	0.0764, 0.1738	0.0841, 0.2038
Absorption correction	Multi-scan	Multi-scan	Multi-scan
GOF on F^2	1.048	1.089	1.088
Largest peak/hole/ $eÅ^{-3}$	0.918/-0.439	0.668/-0.740	1.366/-0.512
Max and min transmission	0.7533/0.5717	0.7533/0.4727	0.7533 /0.4654
CCDC #	2089847	2046920	2089919

Table A1.2. Crystal data and structure refinement for Mn^{III}-methoxy complexes.

Parameter	$[Mn^{III}(OMe)(PaPy_2Q)](OTf)$	$[Mn^{III}(OMe)(PaPy_2N)](OTf)$
Formula	$C_{26}H_{25}F_3MnN_5O_{5.45}S$	$C_{25}H_{24}F_3MnN_6O_{5.30}S$
Identification code	q87k	q14l
Formula weight	638.71	637.30
Crystal system	Triclinic	Triclinic
Space group	P-1	P-1
Crystal size (mm^3)	0.274 x 0.070 x 0.028	0.040 x 0.040 x 0.035
a/Å	7.7533(3)	7.71890(10)
b/ Å	13.6242(4)	13.5521(3)
c/ Å	14.9049(5)	14.8199(3)
α/°	114.9368(15)	115.0816(11)
β/°	96.128(2)	96.1141(13)
γ/°	93.4281(19)	93.3409(12)
V/ $Å^3$	1409.88(8)	1386.86(5)
Z	2	2
Dcalcd/g cm^{-3}	1.505	1.526
F(000)	655	653
Absorption coefficient /mm^{-1}	5.098	5.188
T/K	200(2)	200(2)
λ/ Å	1.54178	1.54178
θ range/°	3.305-70.139	3.625-70.422
Reflections collected	20814	18726
Completeness to θ = 66.000° (%)	96.3	96.2
Index ranges	-8≤h≤9,-16≤k≤16,-17≤l≤17	-8≤h≤9, -16≤k≤15, -17≤l≤16
Data/Restraint/parameters	4991 / 6 / 384	4889 / 44 / 454
R1(F), $wR_2(F^2)$ (> $2\sigma(F^2)$)	0.0735, 0.2023	0.0580, 0.1617
R1(F), $wR_2(F^2)$ (all data)	0.0789, 0.2097	0.0659, 0.1692
Absorption correction	Multi-scan	Multi-scan
GOF on F^2	1.043	1.050
Largest peak/hole/ $eÅ^{-3}$	1.109/-1.232	0.842/-0.522
Max and min transmission	0.7533/0.4261	0.7533/0.5326
CCDC #	2047833	2089852

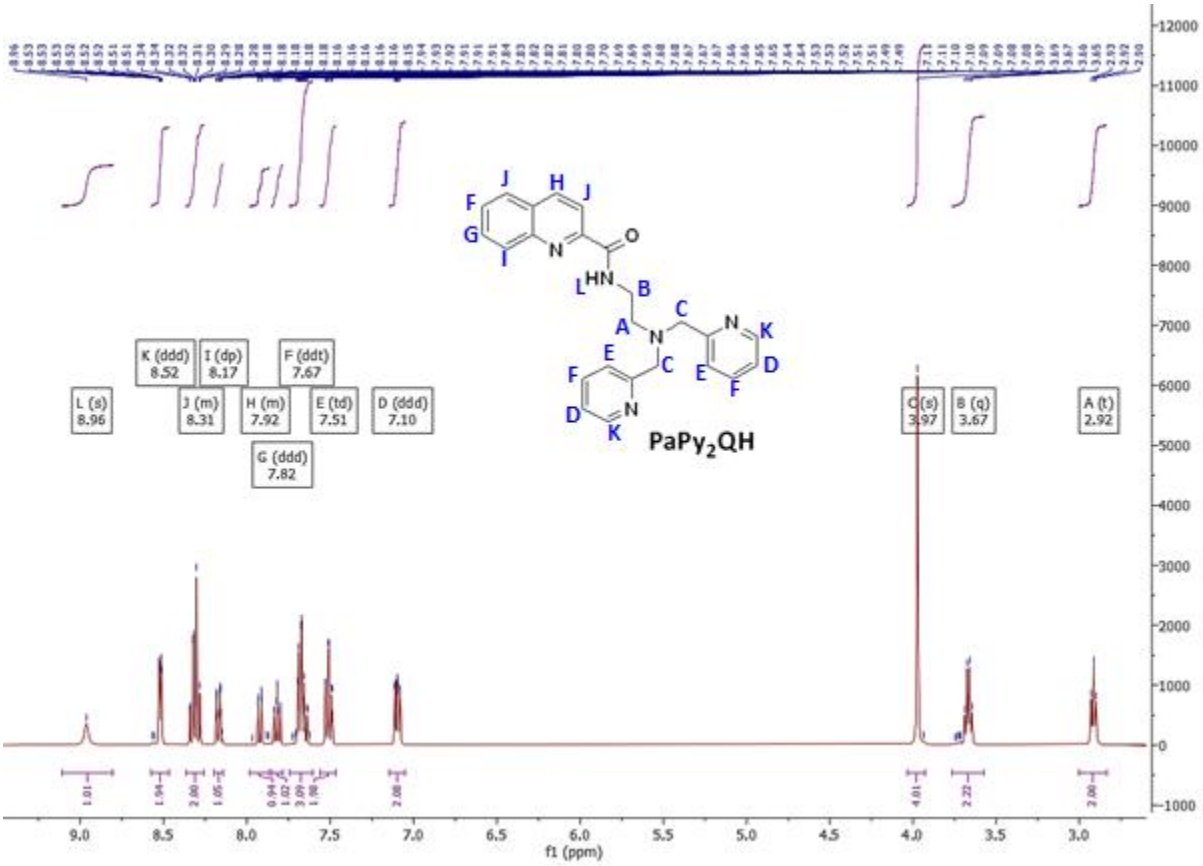

Figure A1.1. ^{1}H NMR spectrum of $PaPy_2QH$ ligand in $CDCl_3$. Letters mark the peak assignments. The assignment of peaks were performed with the aid of an online ^{1}H NMR simulator from nmrdb.org. [1-3]

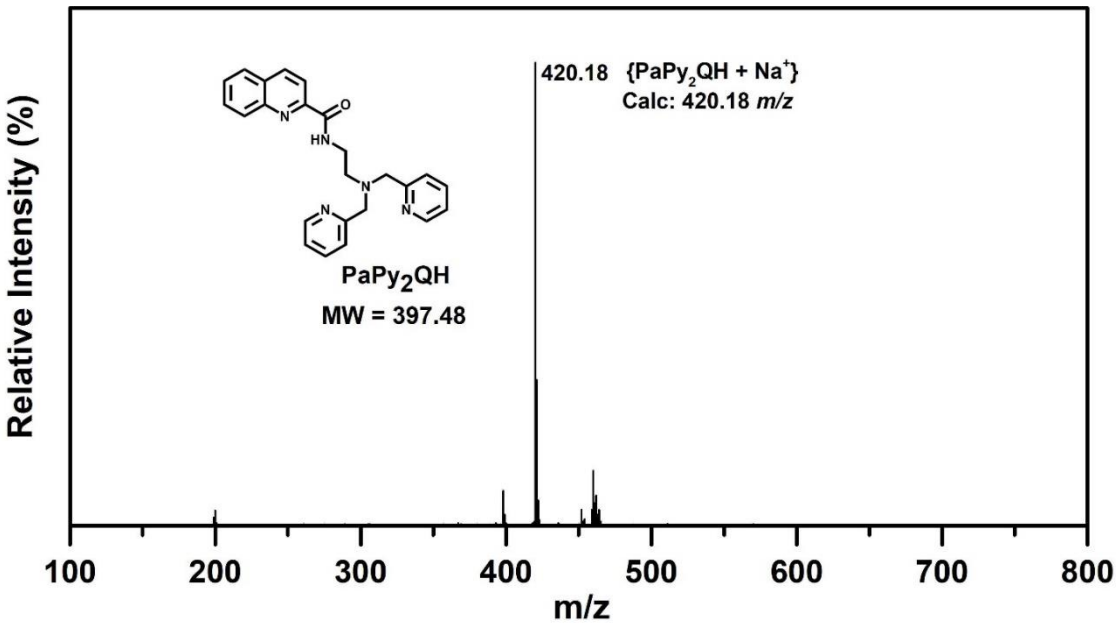

Figure A1.2. ESI-MS data for $PaPy_2QH$ ligand in CH_3CN at 298 K.

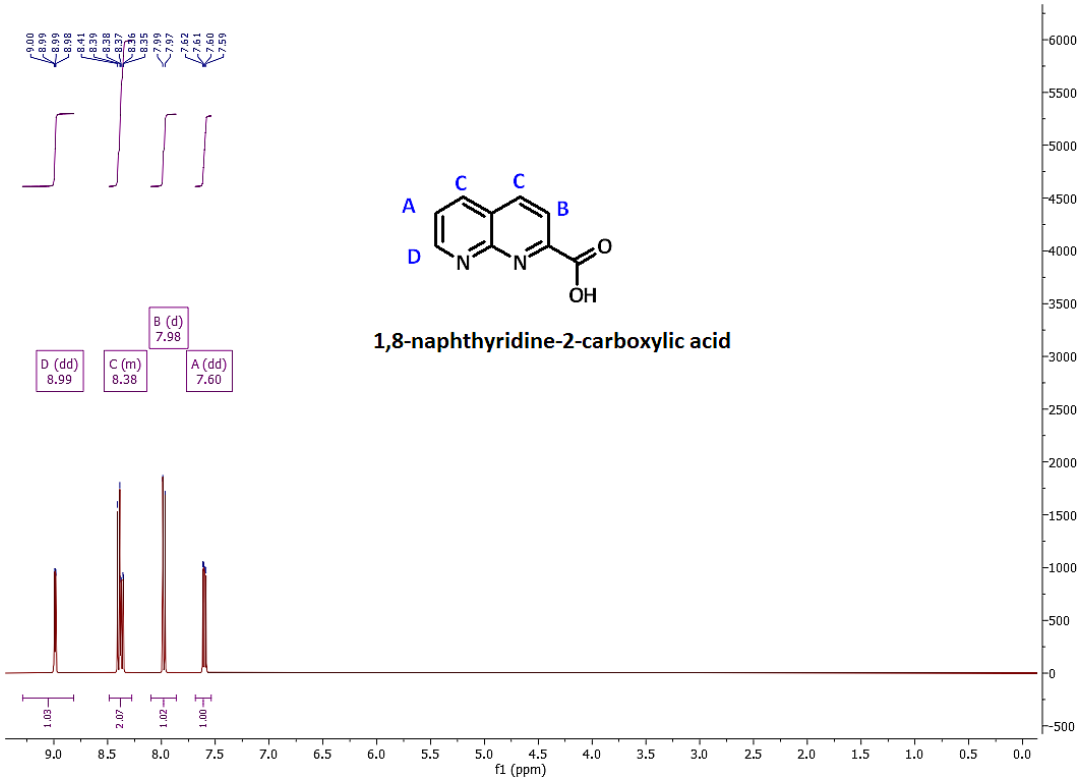

Figure A1.3. ^1H NMR spectrum of 1,8-naphthyridine-2-carboxylic acid in D_2O. Letters mark the peak assignments. The assignment of peaks were performed with the aid of an online ^1H NMR simulator from nmrdb.org.[1-3]

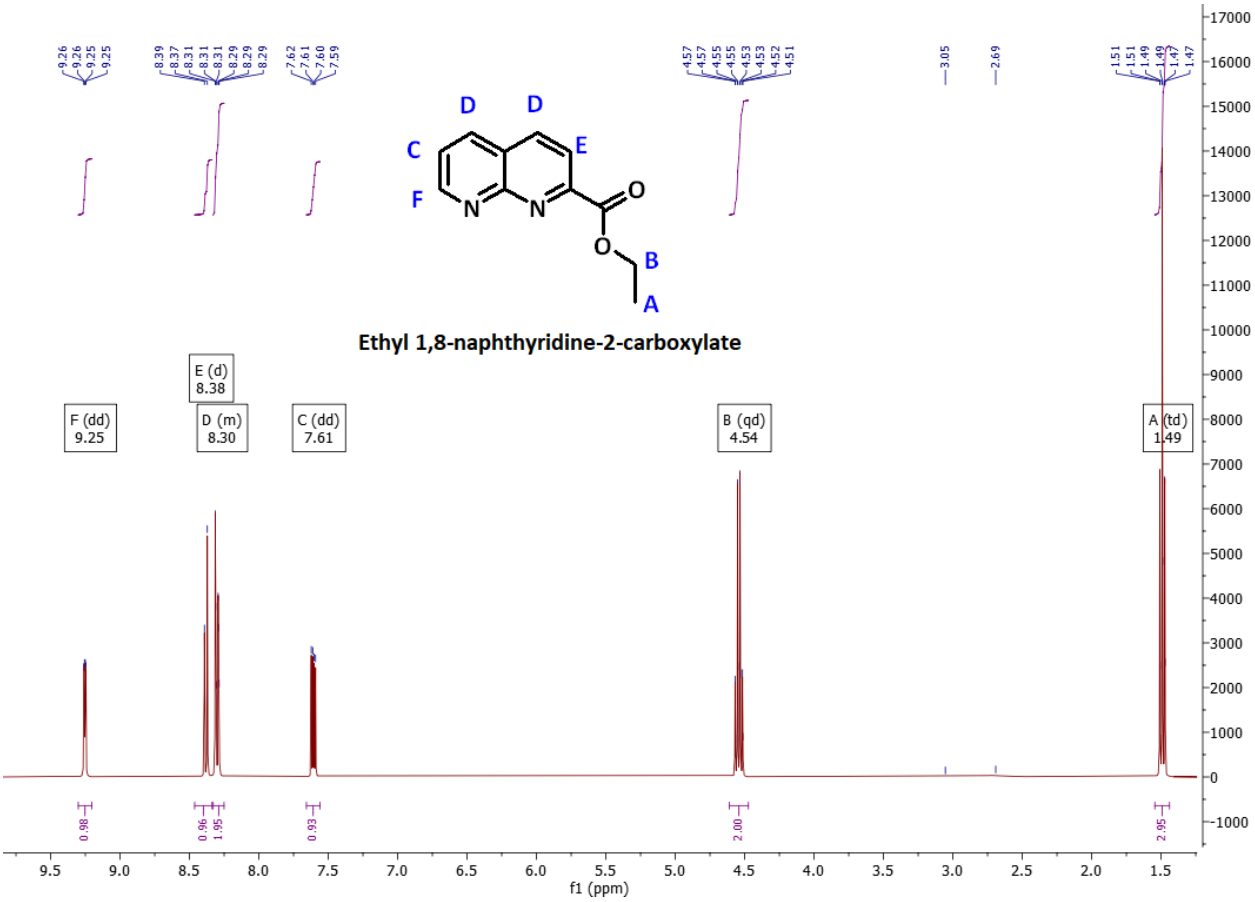

Figure A1.4. ^{1}H NMR spectrum of ethyl-1,8-naphthyridine-2-carboxylate in $CDCl_3$. Letters mark the peak assignments. The assignment of peaks were performed using the knowledge from the ^{1}H NMR data from the precursor's synthesis and with the aid of an online ^{1}H NMR simulator from nmrdb.org.[1-3]

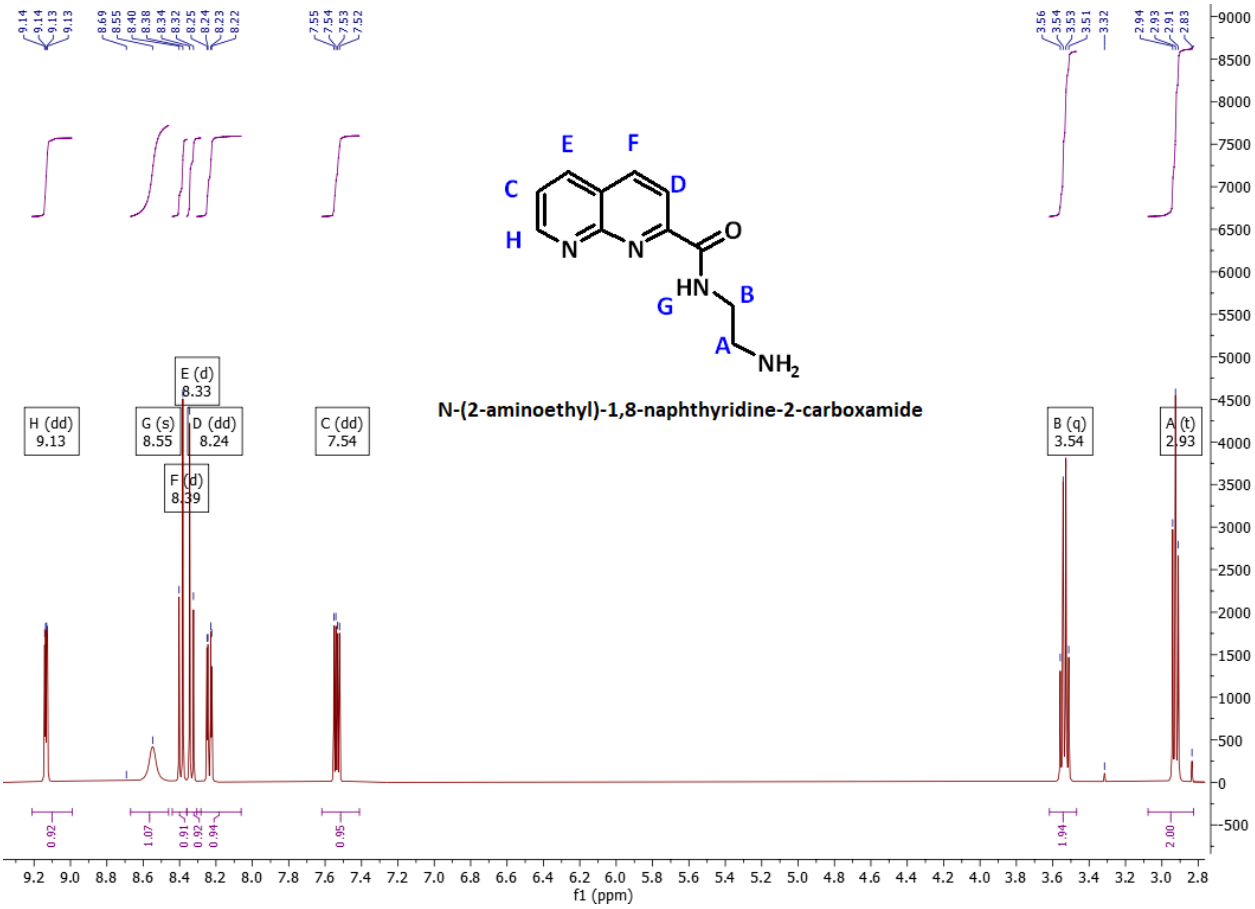

Figure A1.5. ^{1}H NMR spectrum of N-(2-aminoethyl)-1,8-naphthyridine-2-carboxamide in $CDCl_3$. Letters mark the peak assignments. The assignment of peaks were performed using the knowledge from the ^{1}H NMR data from the precursors' synthesis and with the aid of an online ^{1}H NMR simulator from nmrdb.org.[1-3]

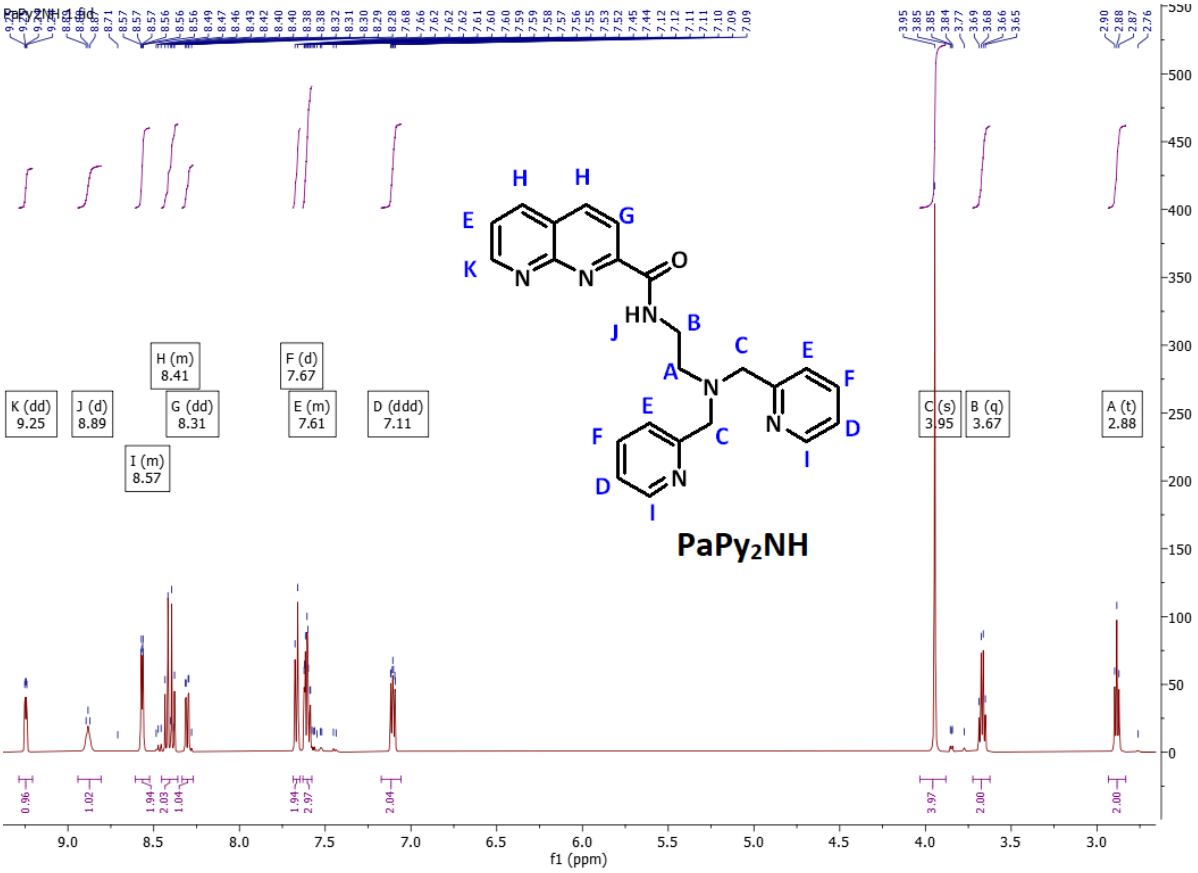

Figure A1.6. ^{1}H NMR spectrum of N-(2-(bis(pyridin-2-ylmethyl)amino)ethyl)-1,8-naphthyridine-2-carboxamide (**PaPy$_2$NH**) in $CDCl_3$. Letters mark the peak assignments. The assignment of peaks were performed using the knowledge from the ^{1}H NMR data from the precursors synthesis, ^{1}H-^{13}C HSQC of the PaPy$_2$NH ligand, and with the aid of an online ^{1}H NMR simulator from nmrdb.org.[1-3]

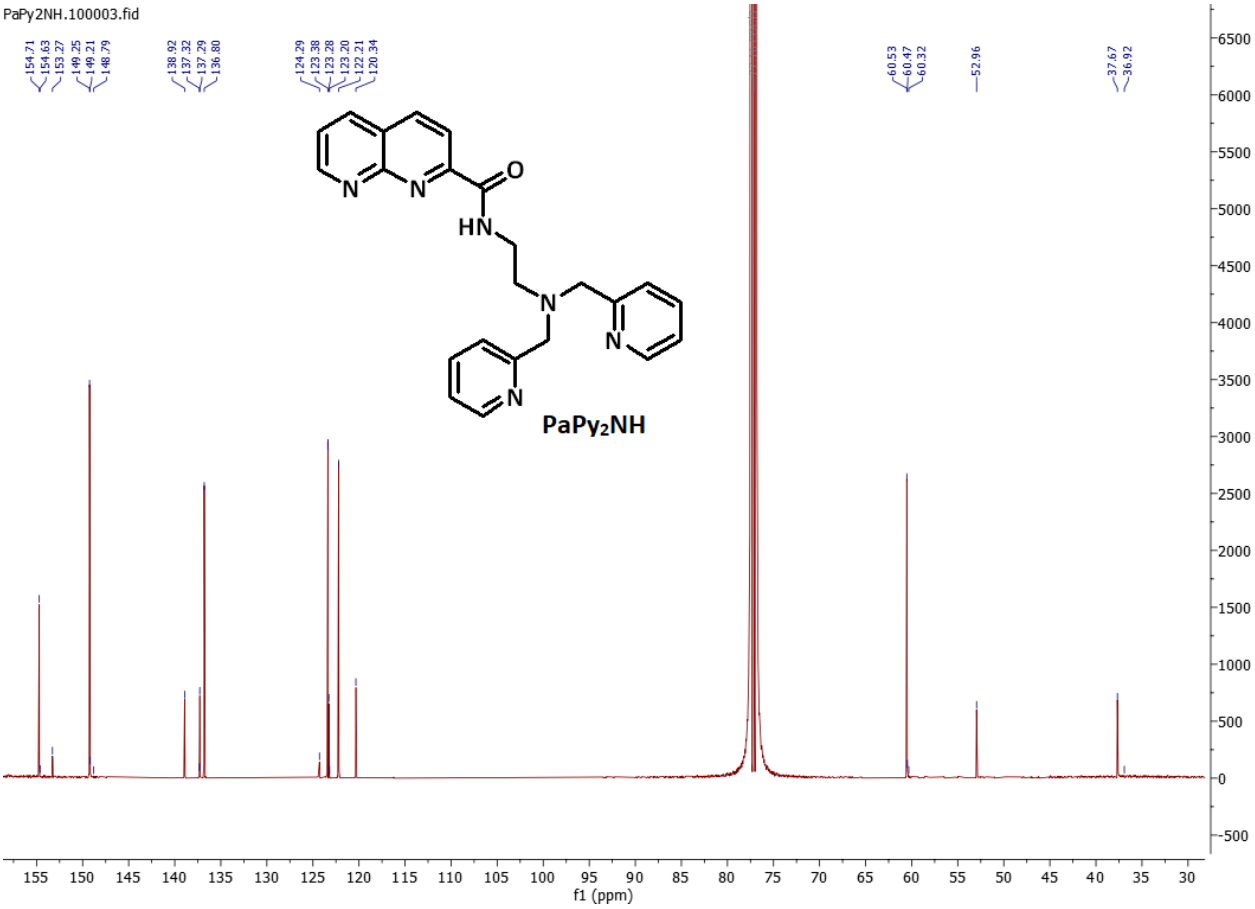

Figure A1.7. ^{13}C NMR spectrum of $PaPy_2NH$ in $CDCl_3$.

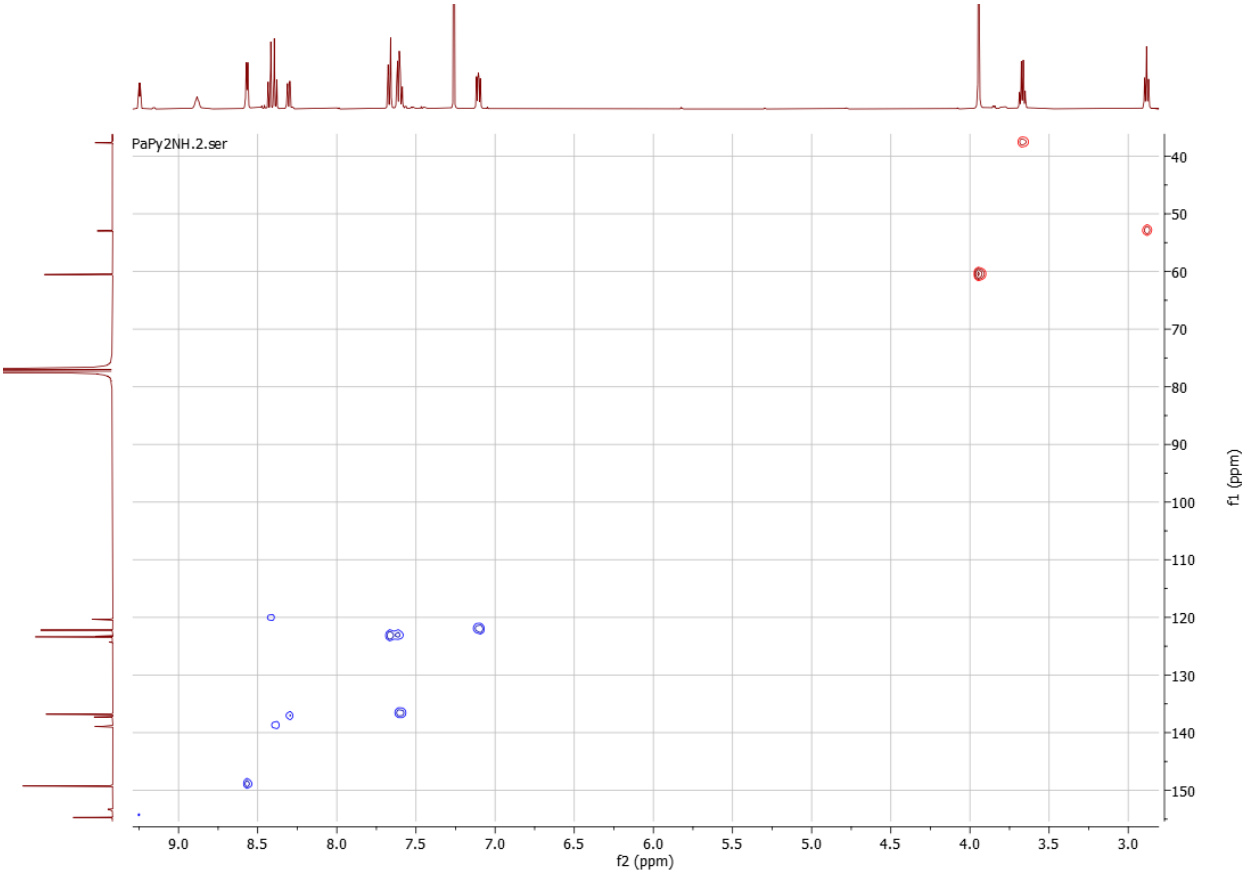

FigureA1.8. $^{1}H - {}^{13}C$ HSQC data for $PaPy_2NH$ ligand in $CDCl_3$.

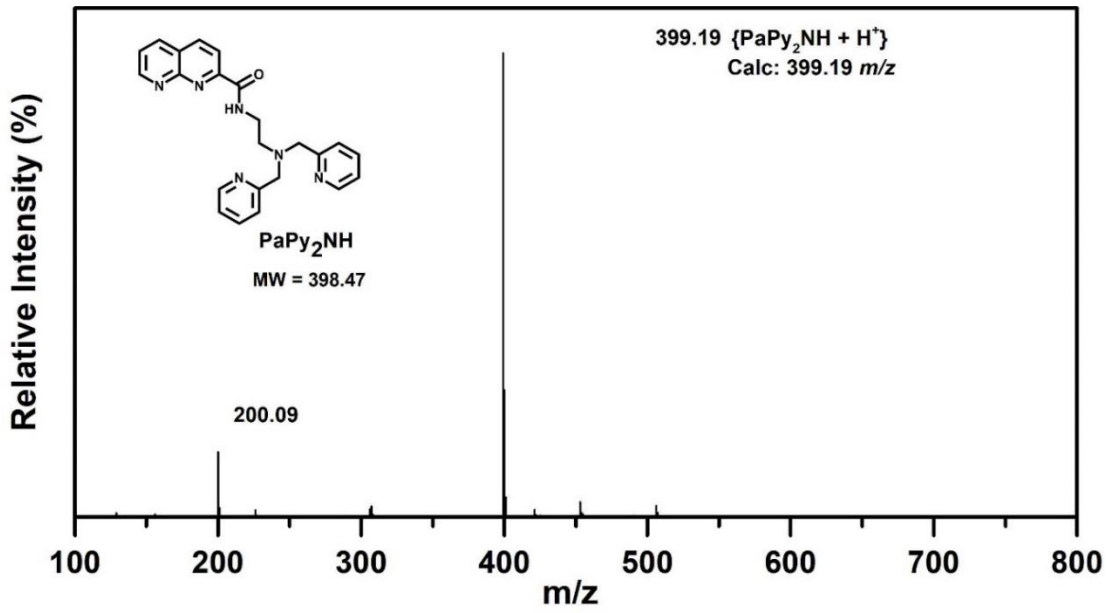

Figure A1.9. ESI-MS data for $PaPy_2NH$ ligand in CH_3CN at 298 K.

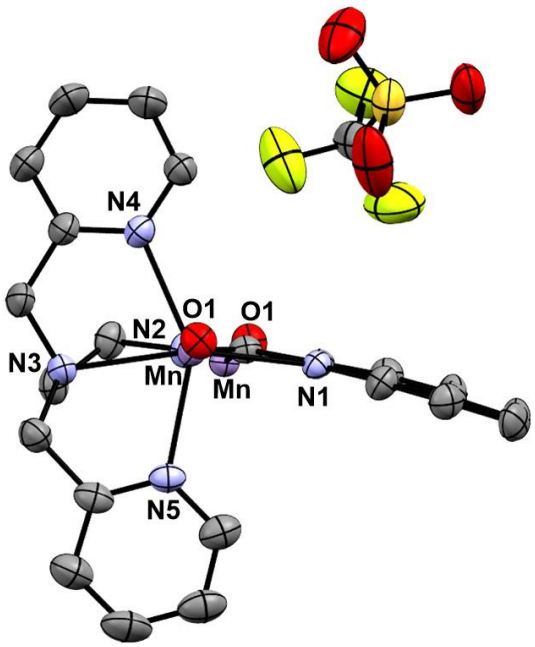

Figure A1.10. X-ray crystal structure of $[Mn^{II}(PaPy_2Q)](OTf)$ showing the triflate counterion occupying the pocket between the quinolinyl and N4-pyridyl group. Structure shown at 50% probability thermal ellipsoid.

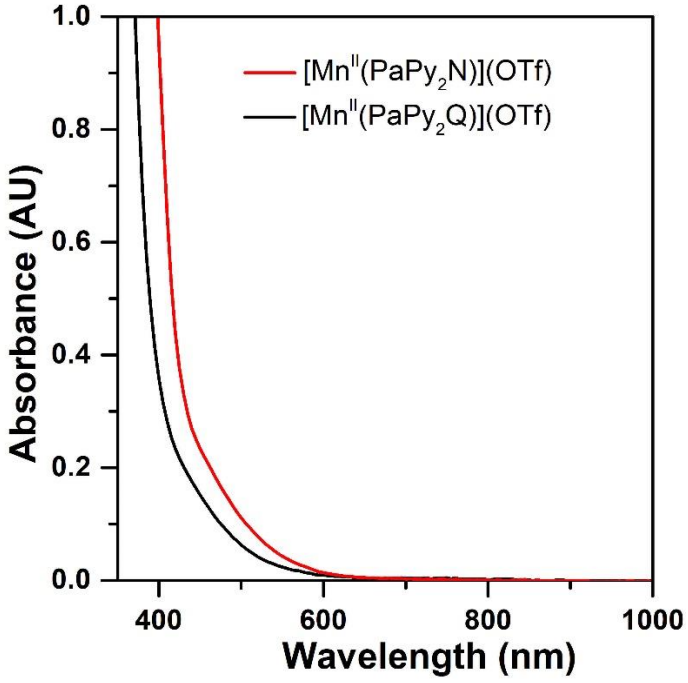

Figure A1.11. Electronic absorption spectra of 1.25 mM solutions of $[Mn^{II}(PaPy_2Q)](OTf)$ (black trace) and $[Mn^{II}(PaPy_2N)](OTf)$ (red trace) in CH_3CN at 25°C.

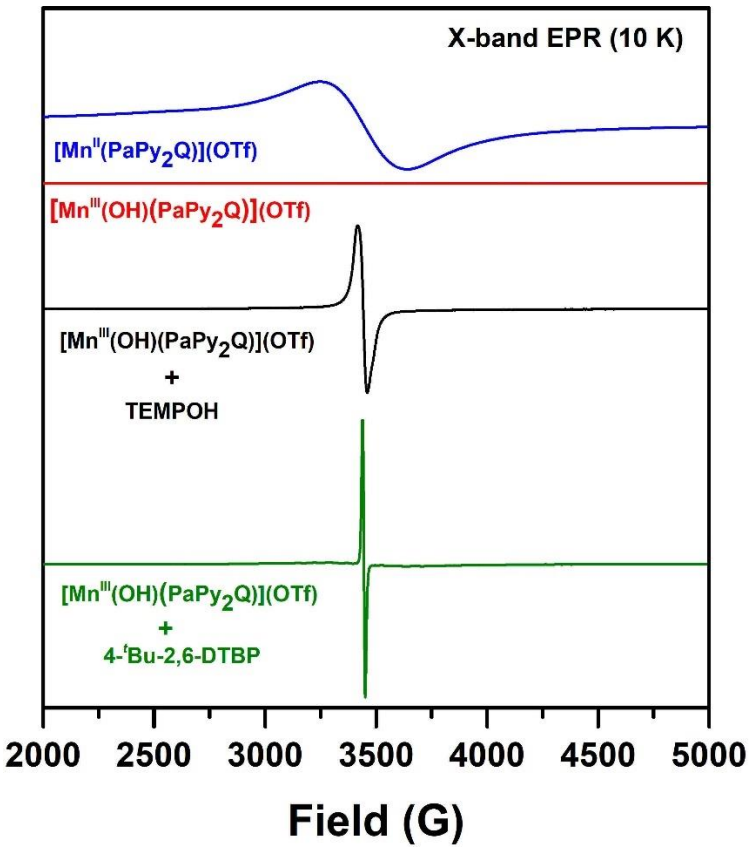

Figure A1.12. Perpendicular-mode X-band EPR spectra of 3 mM solution of $[Mn^{II}(PaPy_2Q)](OTf)$ (blue trace) and 5 mM solution of $[Mn^{III}(OH)(PaPy_2Q)](OTf)$ (red trace) in CH_3CN. Perpendicular-mode X-band EPR spectra of CH_3CN solutions obtained from the reaction of 1.25 mM solution of $[Mn^{III}(OH)(PaPy_2Q)](OTf)$ with 20 equiv. TEMPOH at -35 °C (black trace) and 20 equiv. 4-^{t}Bu-2,6- DTBP at 50 °C (green trace) in CH_3CN. Experimental conditions: temperature = 10 K, microwave frequency = 9.64 GHz, modulation amplitude = 0.4 G, and modulation frequency = 100 kHz.

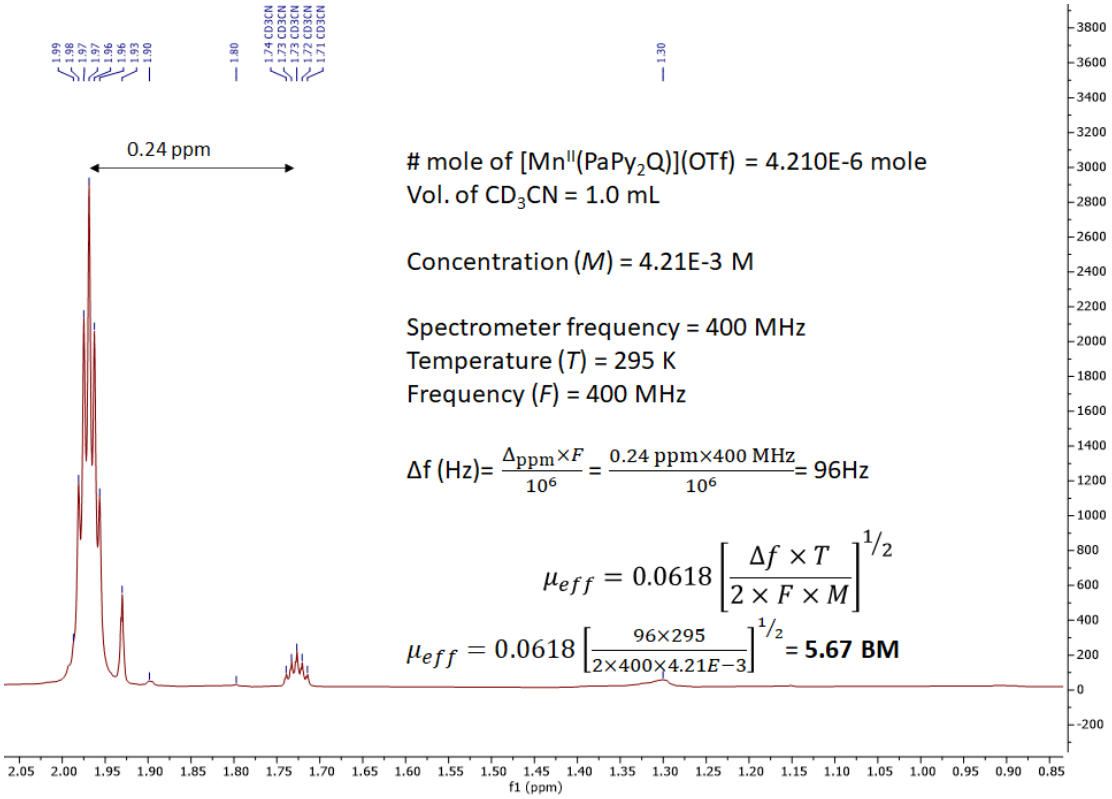

Figure A1.13. Evans NMR data for [Mn^{II}($PaPy_2Q$)](OTf) in CD_3CN and calculations to determine its effective magnetic moment.

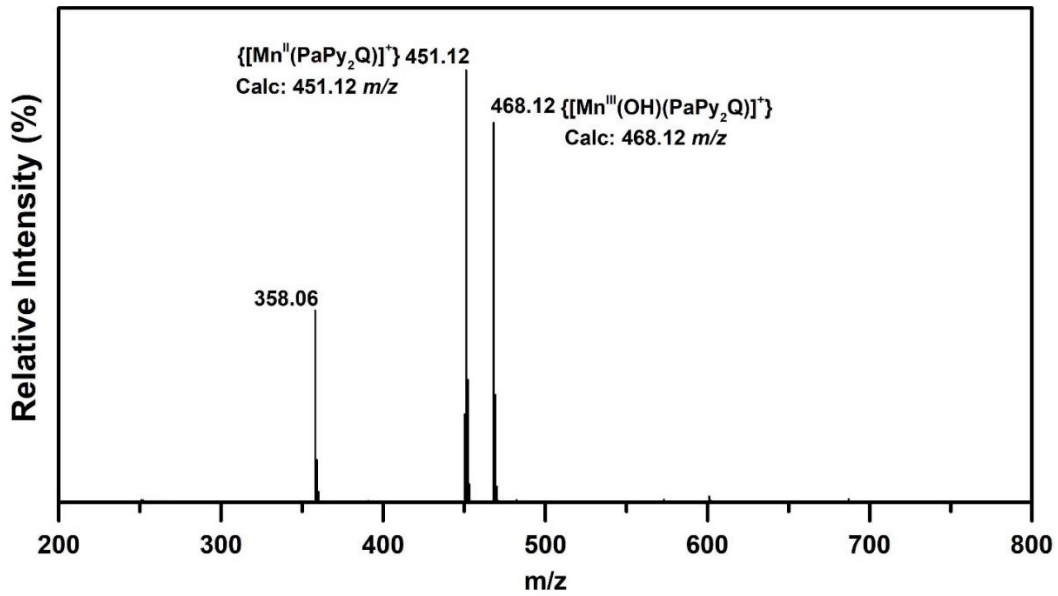

Figure A1.14. ESI-MS data for [Mn^{II}($PaPy_2Q$)](OTf) in CH_3CN at 298 K.

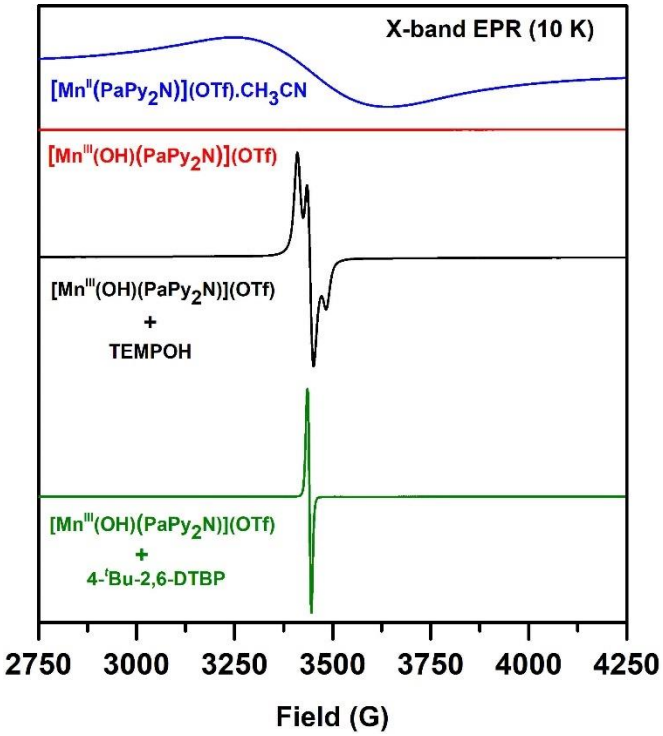

Figure A1.15. Perpendicular-mode X-band EPR spectra of 3 mM solution of $[Mn^{II}(PaPy_2N)](OTf)$ (blue trace) and 5 mM solution of $[Mn^{III}(OH)(PaPy_2N)](OTf)$ (red trace) in CH_3CN. Perpendicular-mode X-band EPR spectra of CH_3CN solutions obtained from the reaction of 1.25 mM solution of $[Mn^{III}(OH)(PaPy_2N)](OTf)$ with 20 equiv. TEMPOH at -35 °C (black trace) and 20 equiv. 4-^{t}Bu-2,6- DTBP at 50 °C (green trace) in CH_3CN. Experimental conditions: temperature = 10 K, microwave frequency = 9.64 GHz, modulation amplitude = 0.4 G, and modulation frequency = 100 kHz.

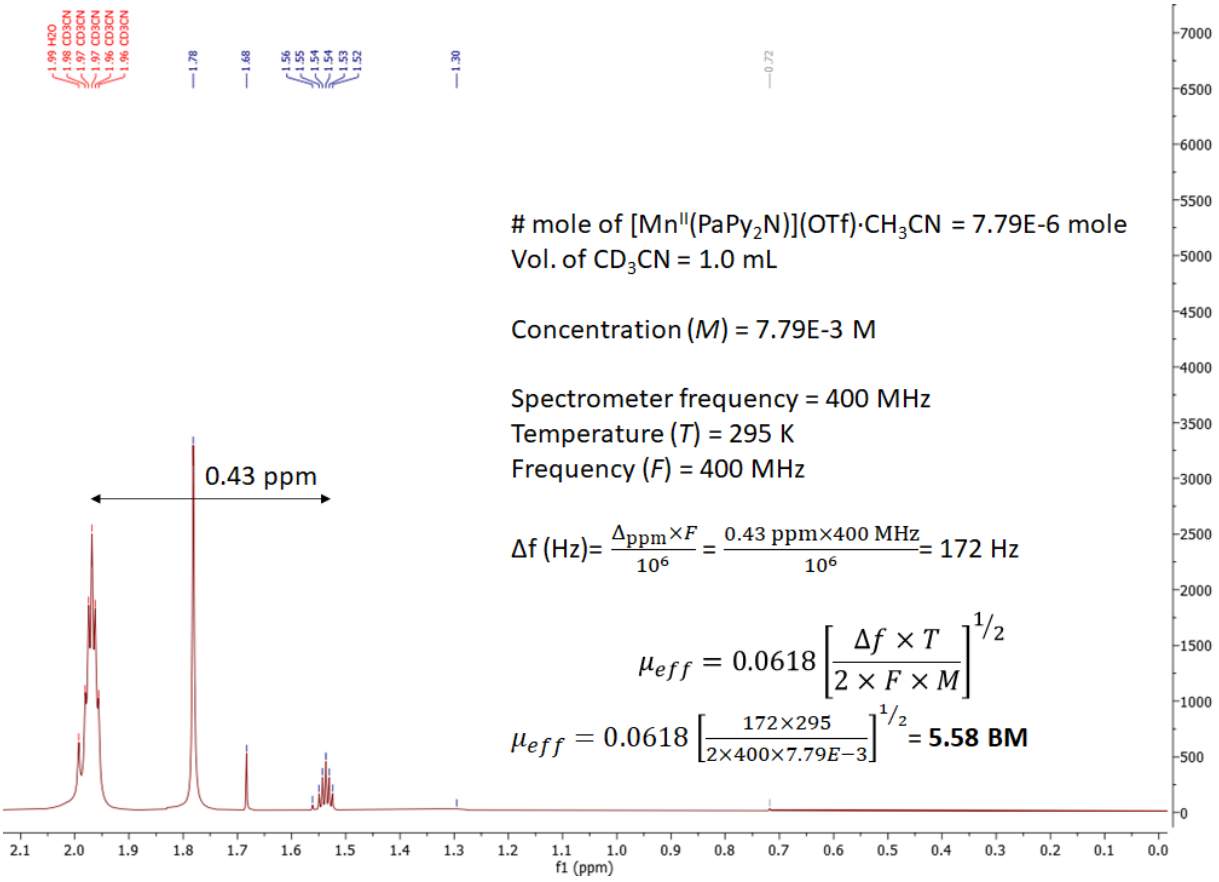

Figure A1.16. Evans NMR data for $[Mn^{II}(PaPy_2N)](OTf)\cdot CH_3CN$ in CD_3CN and calculations to determine its effective magnetic moment.

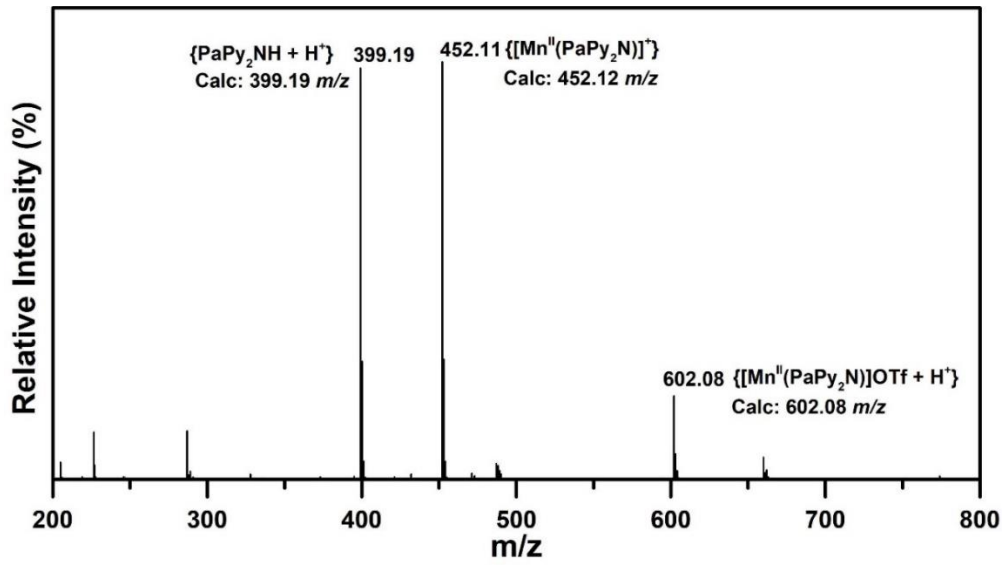

Figure A1.17. ESI-MS data for $[Mn^{II}(PaPy_2N)](OTf)\cdot CH_3CN$ in CH_3CN at 298 K.

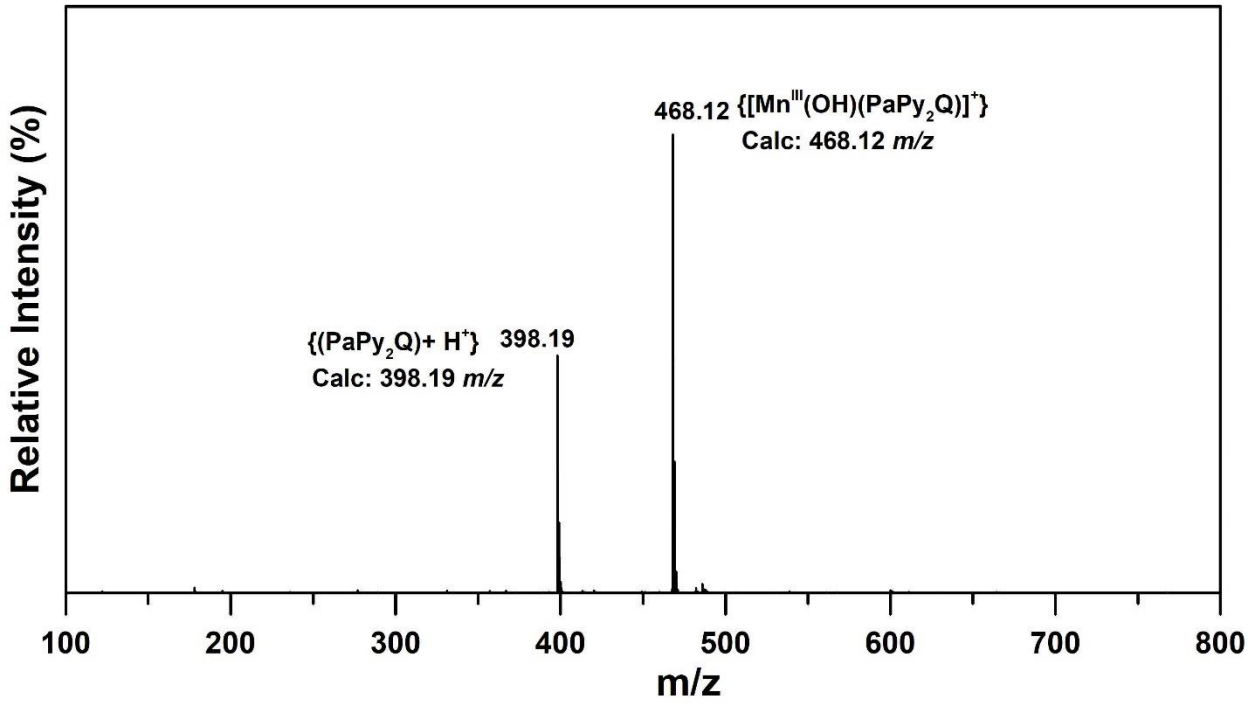

Figure A1.18. ESI-MS data for $[Mn^{III}(OH)(PaPy_2Q)](OTf)$ in CH_3CN at 298 K.

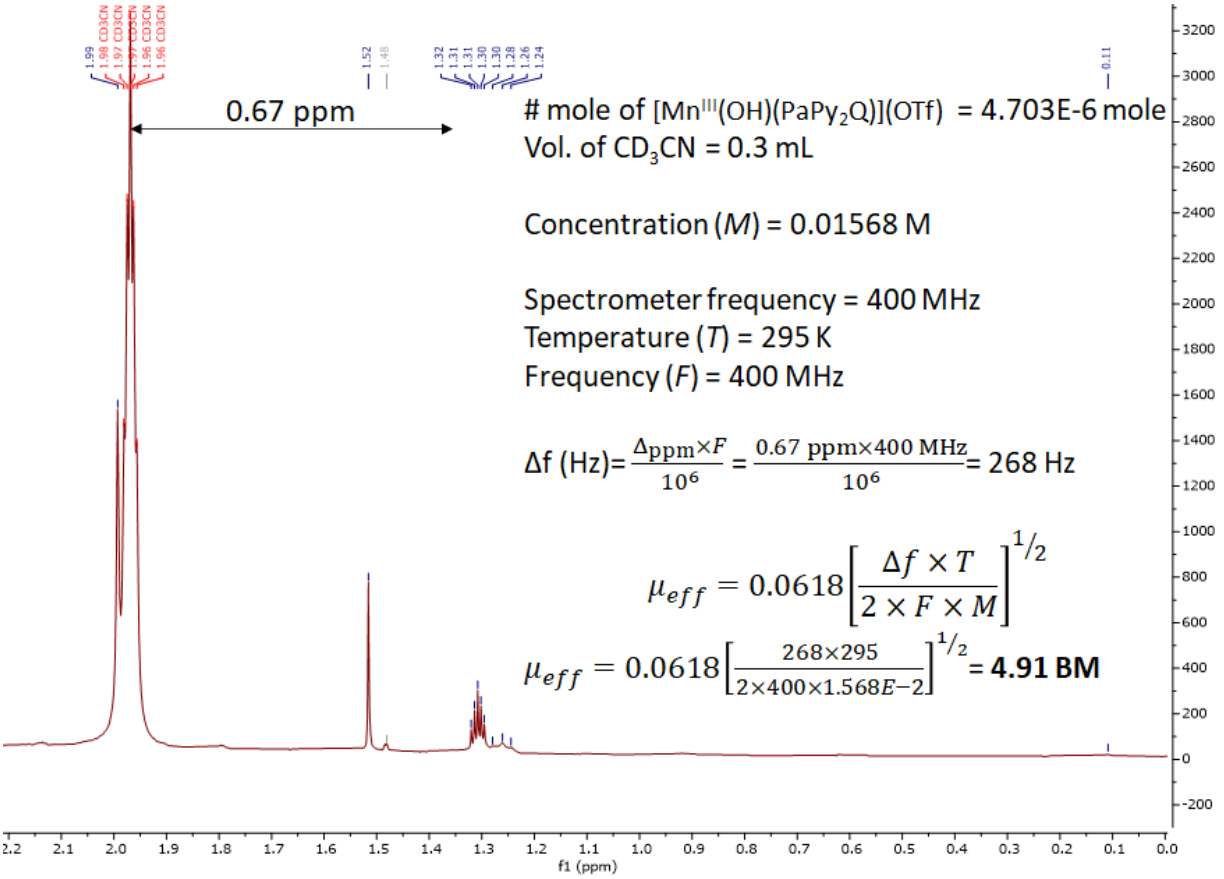

Figure A1.19. Evans NMR data for [Mn^{III}(OH)(PaPy$_2$Q)](OTf) in CD$_3$CN and calculations to determine its effective magnetic moment.

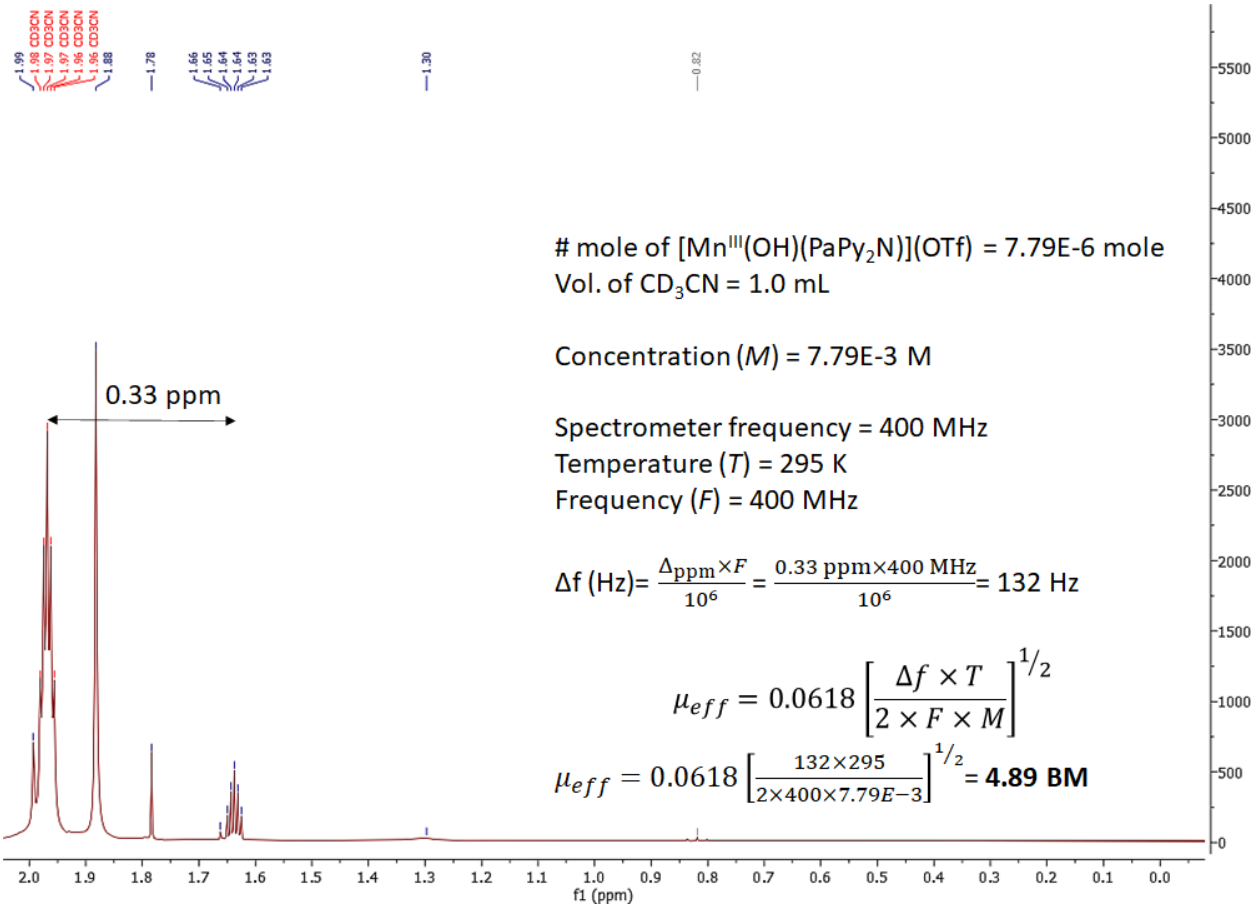

Figure A1.20. Evans NMR data for [Mn^{III}(OH)($PaPy_2N$)](OTf) in CD_3CN and calculations to determine its effective magnetic moment.

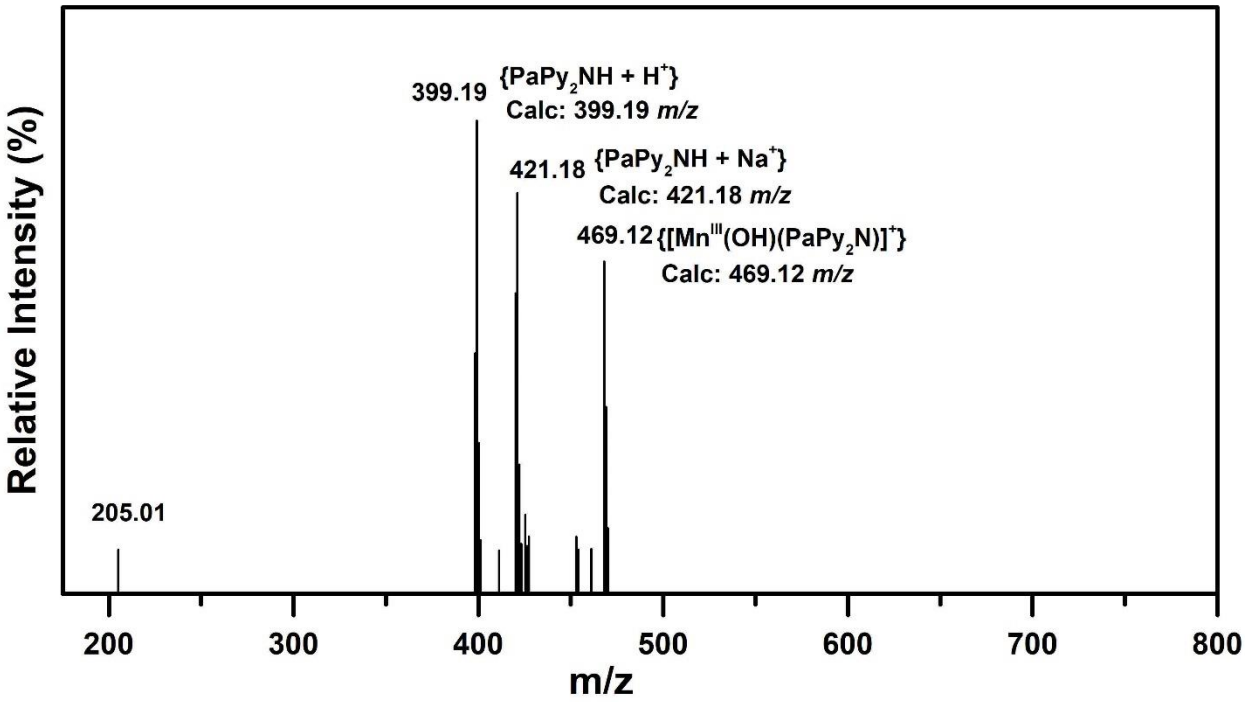

Figure A1.21. ESI-MS data for $[Mn^{III}(OH)(PaPy_2N)](OTf)$ in CH_3CN at 298 K.

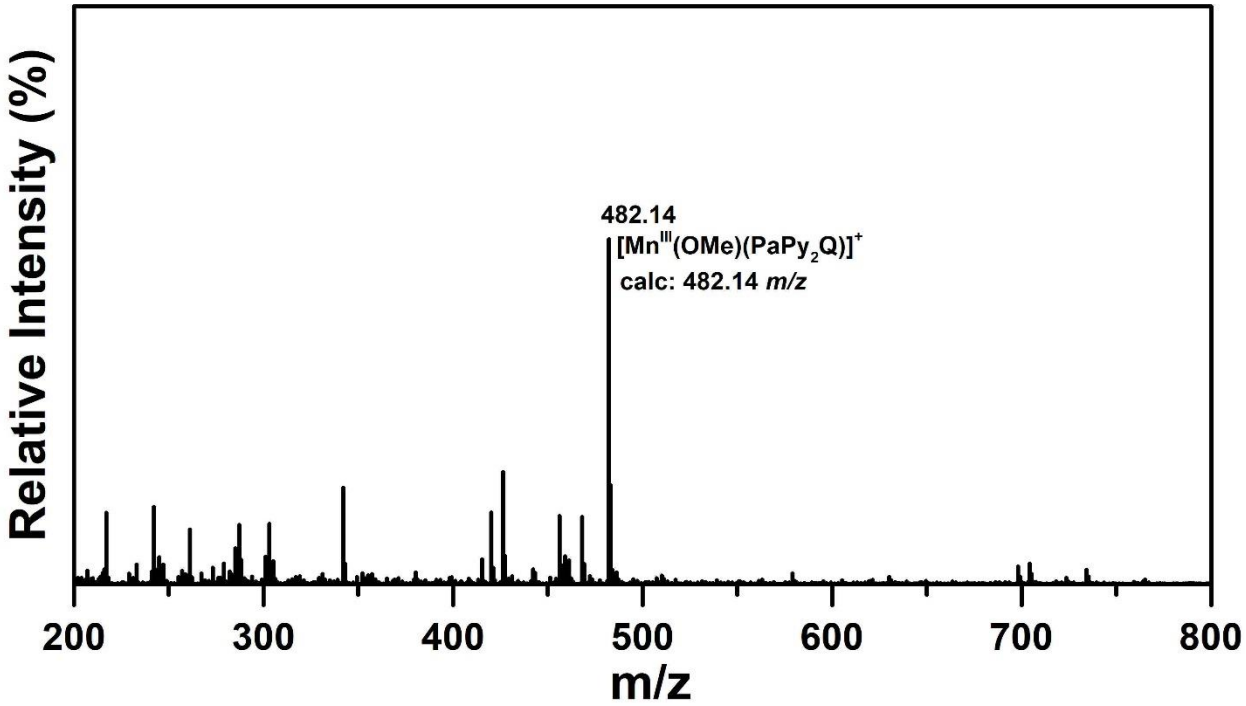

Figure A1.22. ESI-MS data for $[Mn^{III}(OMe)(PaPy_2Q)](OTf)$ in CH_3OH at 298 K.

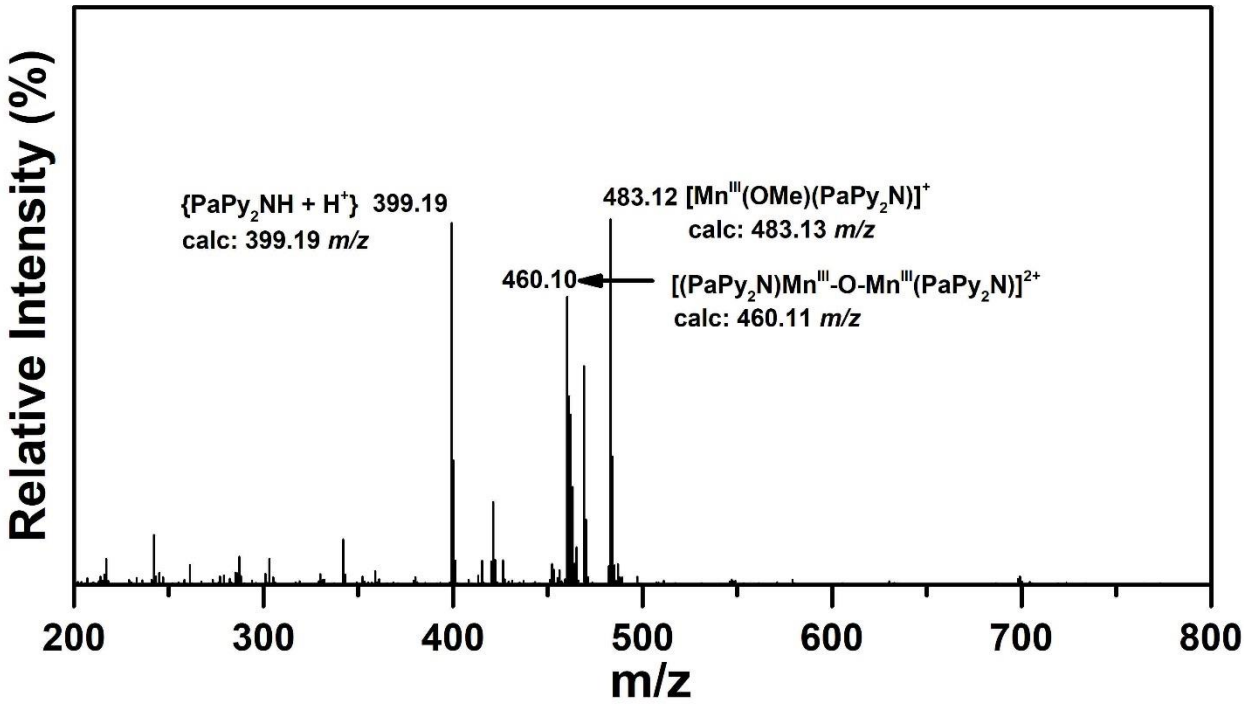

Figure A1.23. ESI-MS data for $[Mn^{III}(OMe)(PaPy_2N)](OTf)$ in CH_3OH at 298 K.

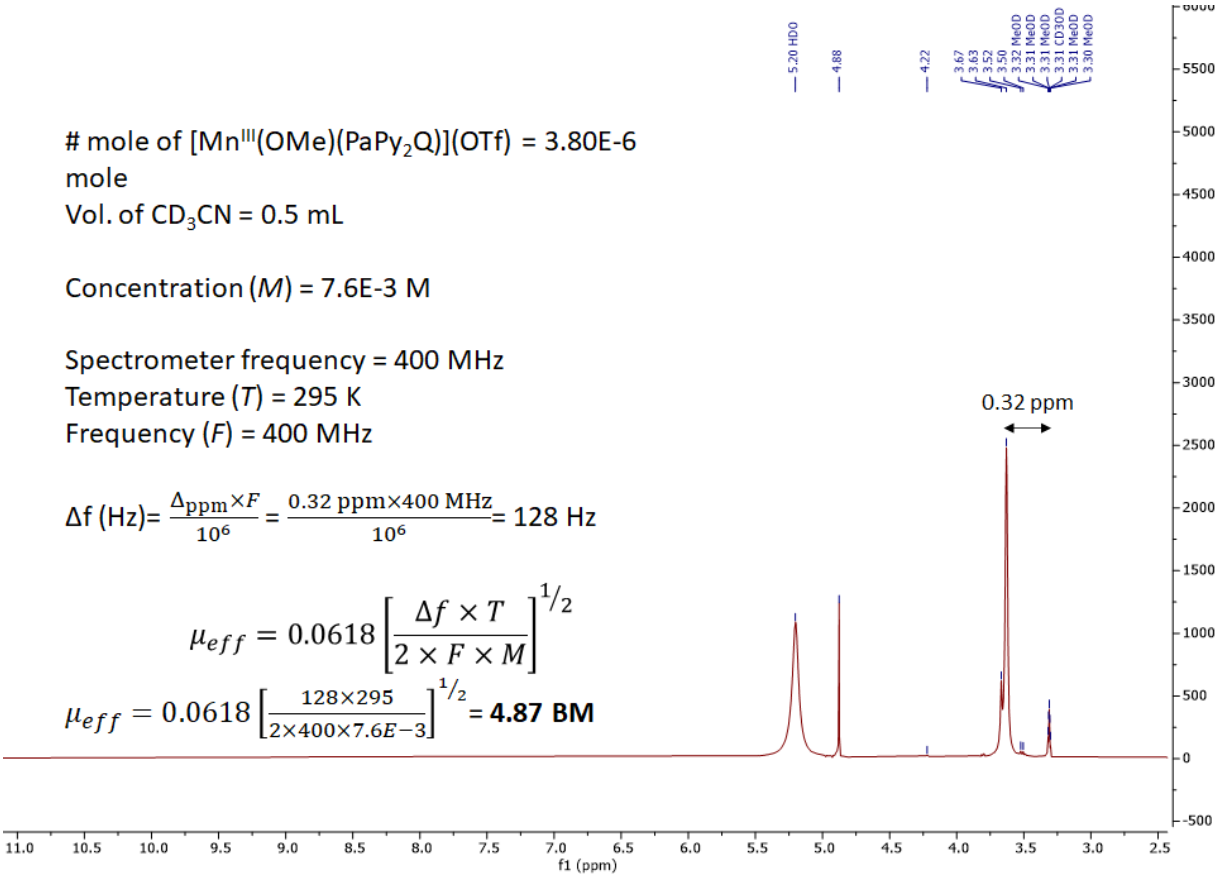

Figure A1.24. Evans NMR data for [Mn^{III}(OMe)($PaPy_2Q$)](OTf) in CD_3OD and calculations to determine its effective magnetic moment.

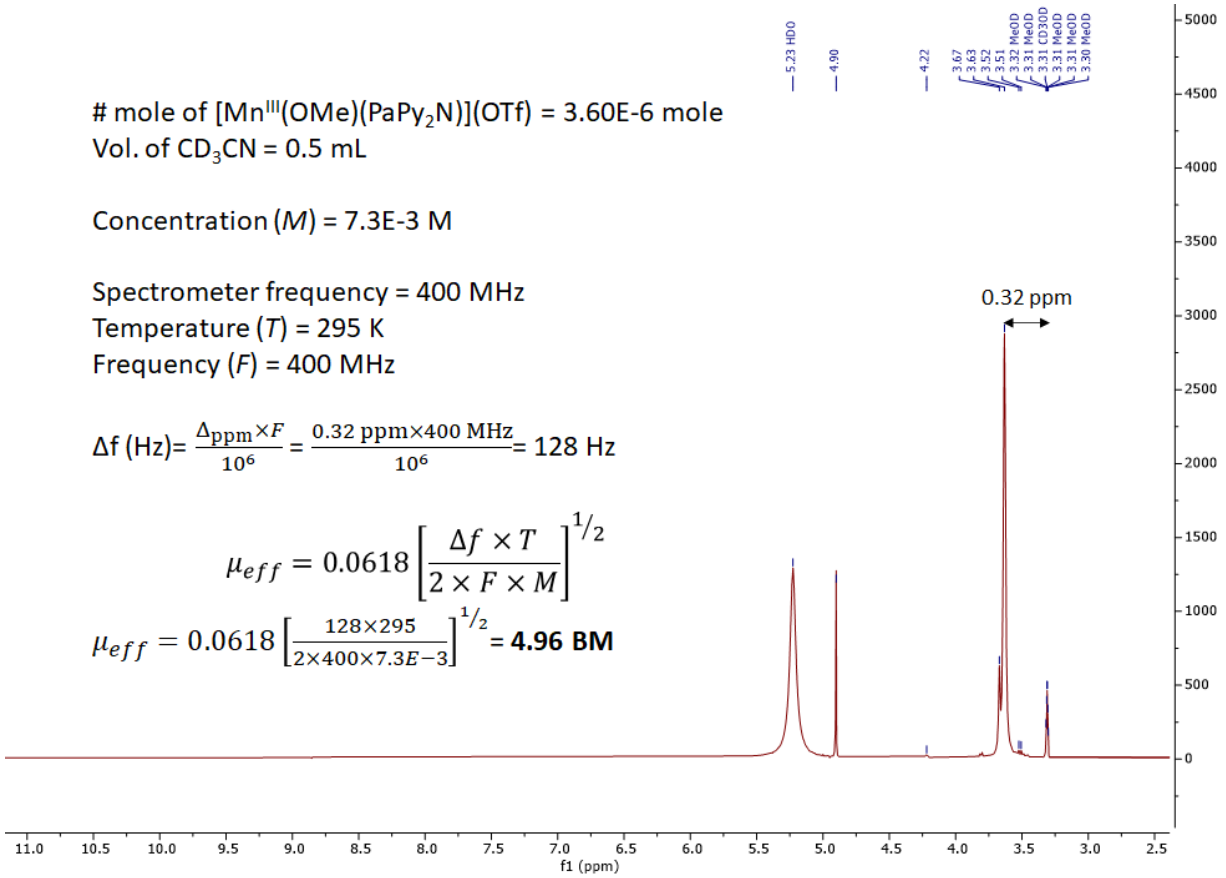

Figure A1.25. Evans NMR data for [Mn^{III}(OMe)($PaPy_2N$)](OTf) in CD_3OD and calculations to determine its effective magnetic moment.

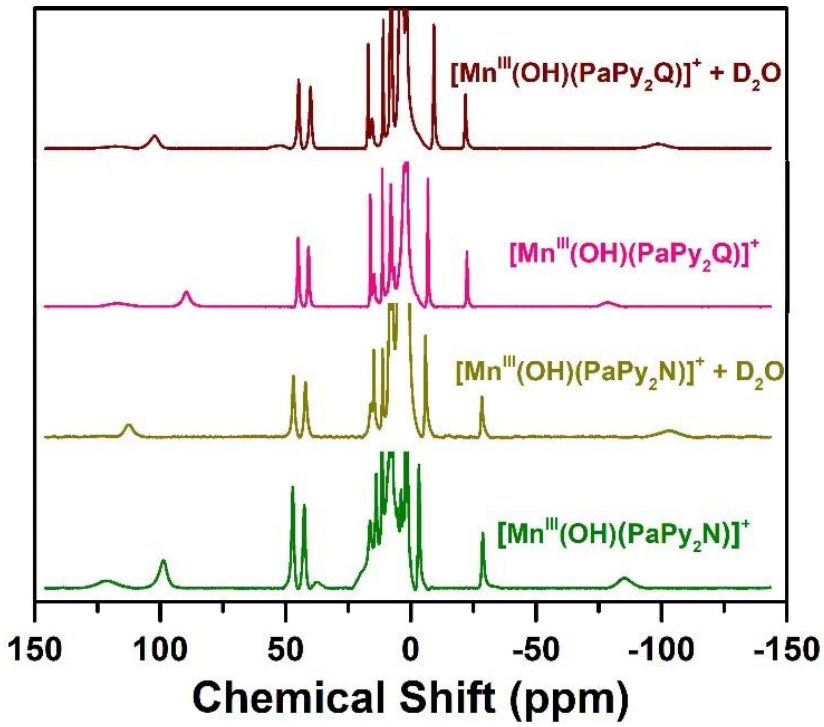

Figure A1.26. ^{1}H NMR spectra for 15 mM solutions of $[Mn^{III}(OH)(PaPy_2N)]^+$ (green) and $[Mn^{III}(OH)(PaPy_2Q)]^+$ (pink) in 500 µL of CD_3CN. ^{1}H NMR spectra for $[Mn^{III}(OH)(PaPy_2N)]^+$ (dark yellow) and $[Mn^{III}(OH)(PaPy_2Q)]^+$ (wine) in CD_3CN with 25 µL added D_2O. All experiments were performed at 298 K.

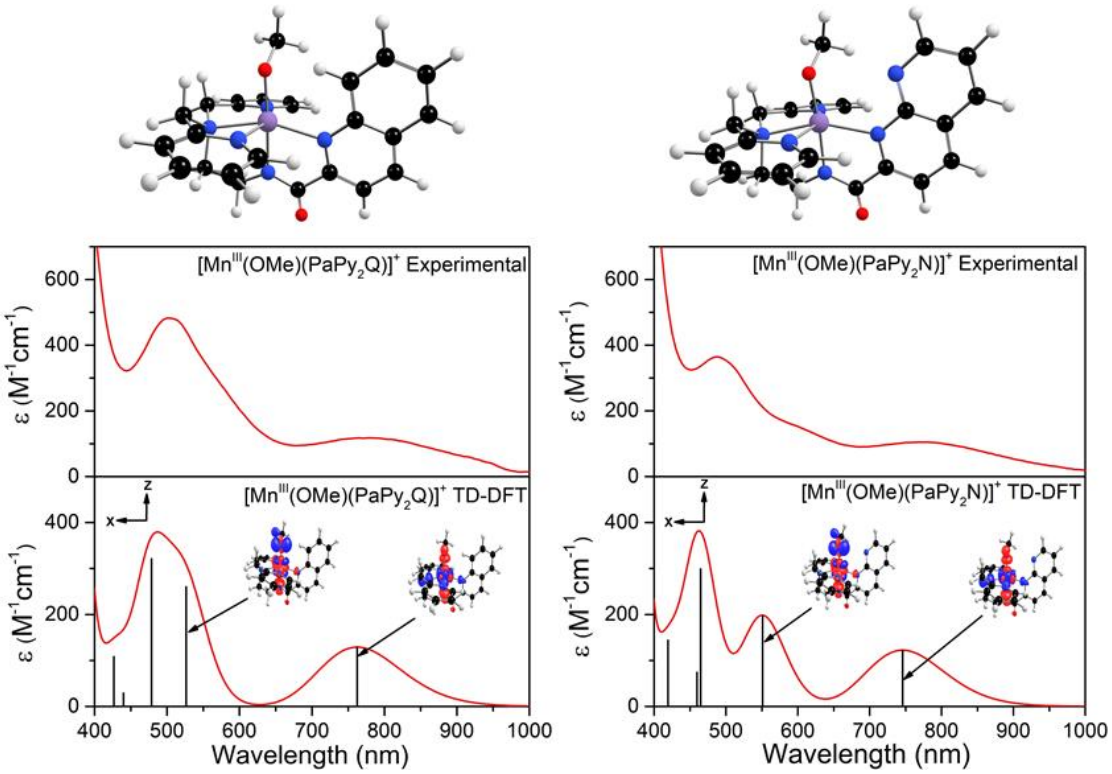

Figure A1.27. TD-DFT computed absorption spectra for $[Mn^{III}(OMe)(PaPy_2Q)]^+$ (left), $[Mn^{III}(OMe)(PaPy_2N)]^+$ (right). The sticks indicate the electronic transitions, with selected EDDMs shown in the inset. Red and blue colors in the EDDMs denotes gain and loss of electron density, respectively. The structures at the top indicate those obtained from DFT calculations.

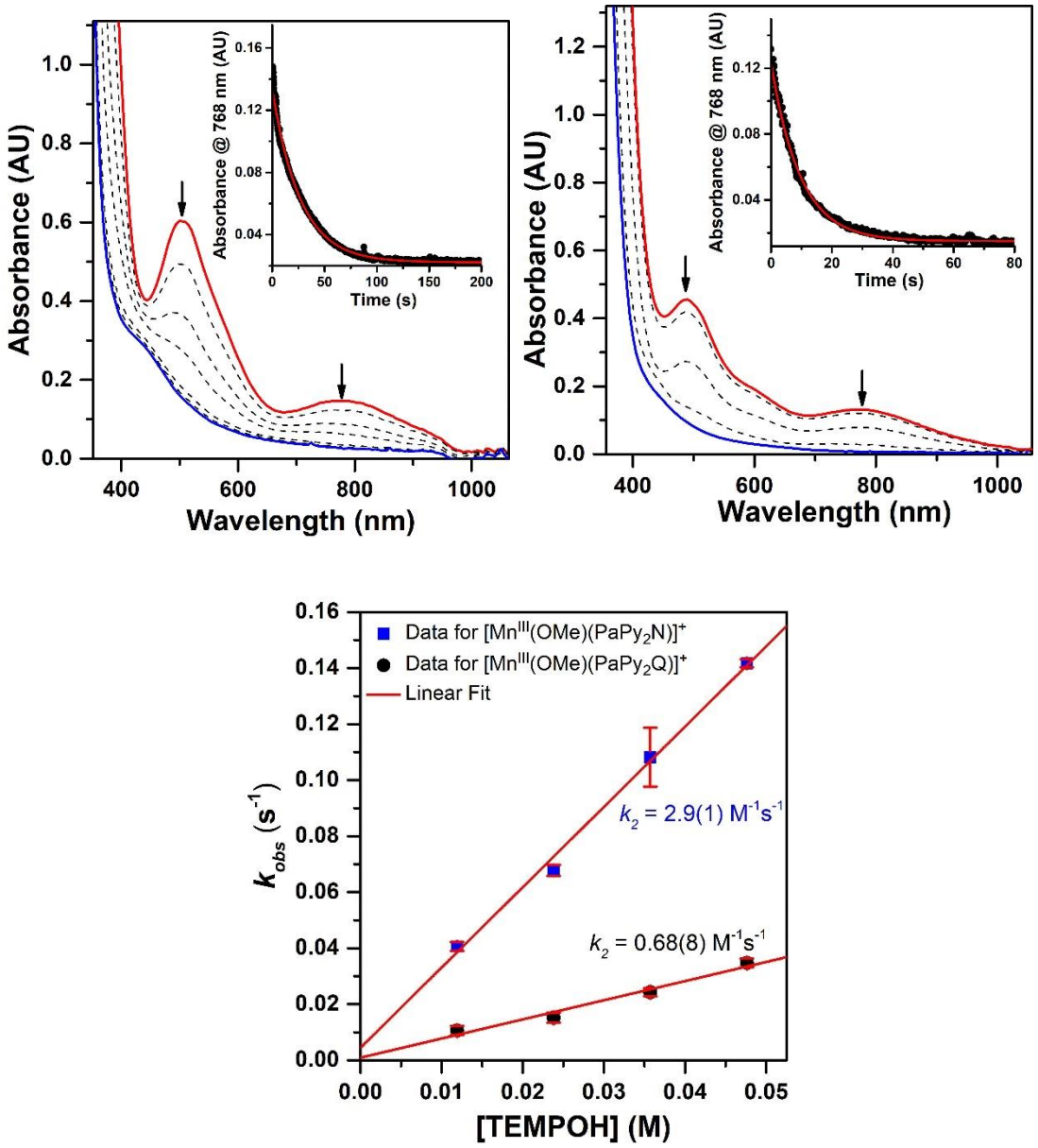

Figure A1.28. Reactions of 1.25 mM $[Mn^{III}(OMe)(PaPy_2Q)]^+$ (top right) and $[Mn^{III}(OMe)(PaPy_2N)]^+$ (top left) with 10 equiv. TEMPOH in CH_3CN at -35 °C. The inset shows the decay of the electronic absorption signal over time (black dots) and a fit (red trace) to a first-order decay. Bottom: Plot of first-order rate constants versus TEMPOH concentration. The error bars represent +/- one standard deviation.

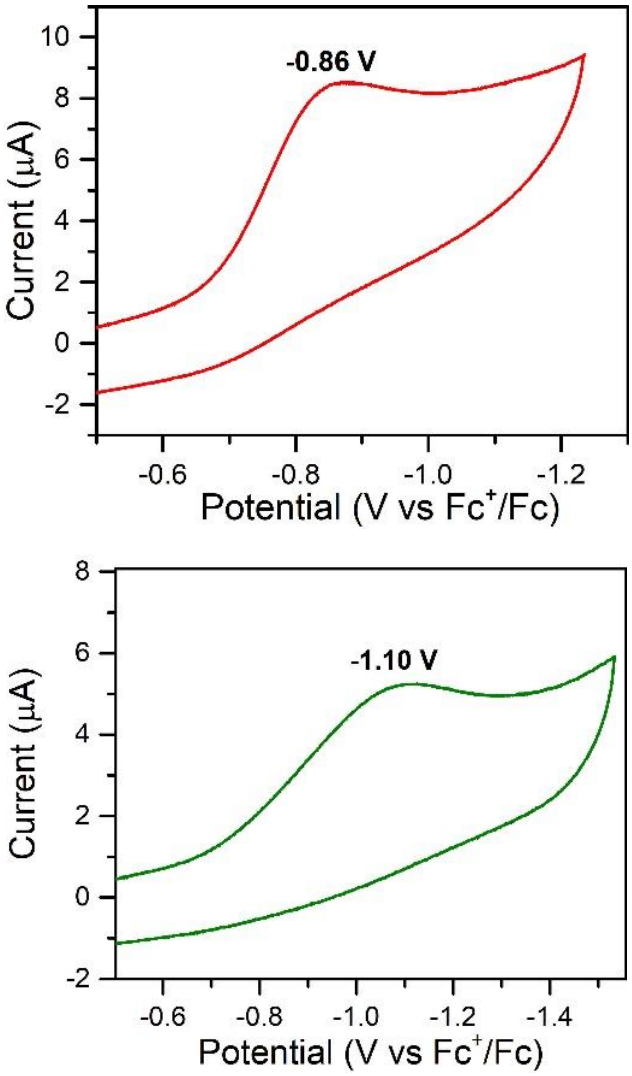

Figure A1.29. Cyclic voltammetry traces of $[Mn^{III}(OH)(PaPy_2Q)]^+$ (top) and $[Mn^{III}(OH)(PaPy_2N)]^+$ (bottom) showing the Mn^{III}/Mn^{II} wave with a scan rate of 100 mV s^{-1}. The working electrode was a glassy carbon electrode with a Pt wire as the counter electrode. Ag/AgCl quasi-reference electrode was used, and Fc^+/Fc potential was measured as an external reference. 2 mM solutions of $[Mn^{III}(OH)(PaPy_2Q)]^+$ and $[Mn^{III}(OH)(PaPy_2N)]^+$ prepared from 0.1 M Bu_4NPF_6 electrolyte solution in CH_3CN were used for measurements at 298 K.

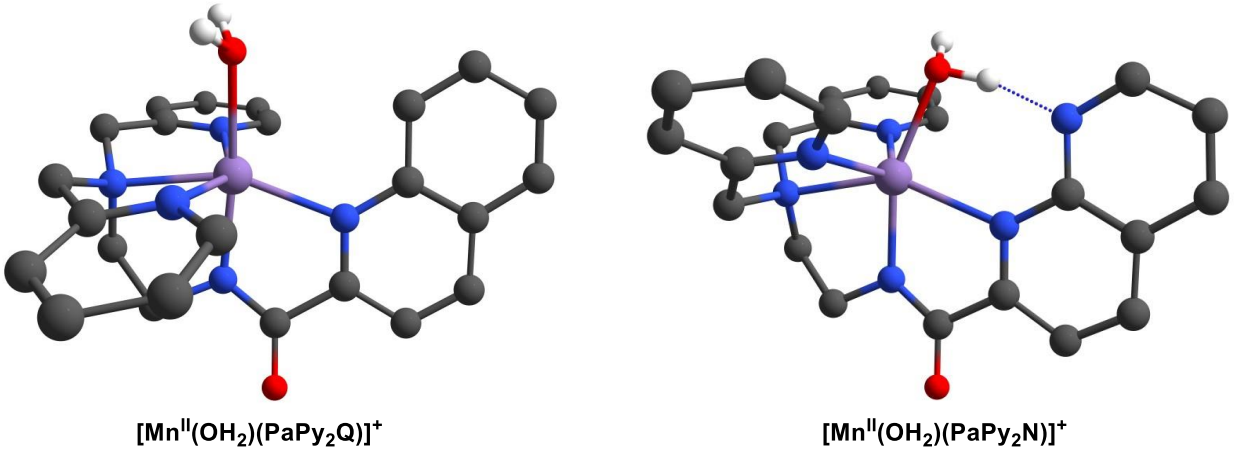

Figure A1.30. DFT optimized structures of $[Mn^{III}(OH_2)(PaPy_2Q)]^+$ complex (left) and $[Mn^{III}(OH_2)(PaPy_2N)]^+$ complex (right).

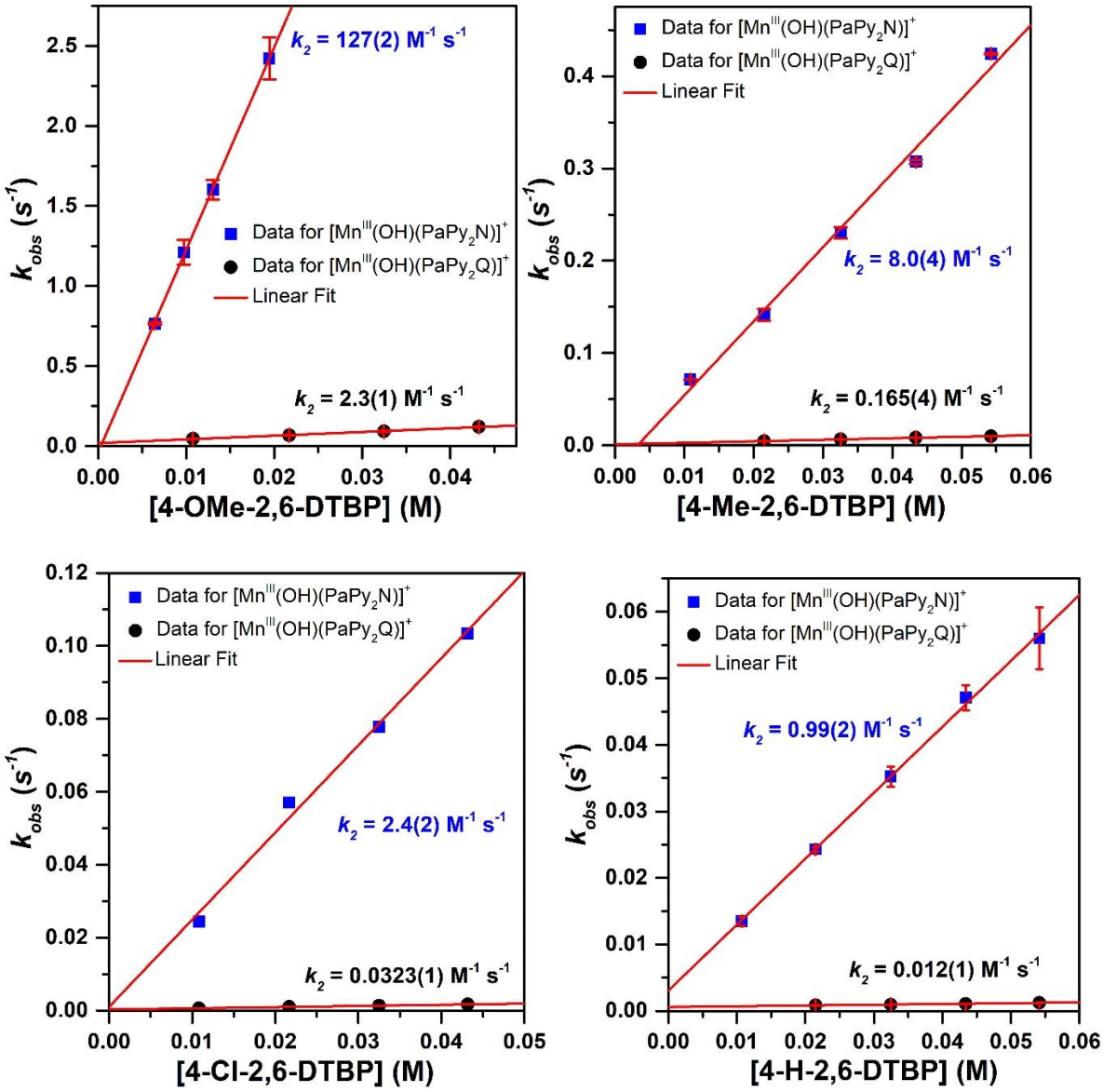

Figure A1.31. Plot of first-order rate constants versus 4-X-2,6-DTBP concentration for reactions with $[Mn^{III}(OH)(PaPy_2Q)]^+$ (black dots) and $[Mn^{III}(OH)(PaPy_2N)]^+$ (blue squares). The red lines represent linear fits. The error bars represent +/- one standard deviation.

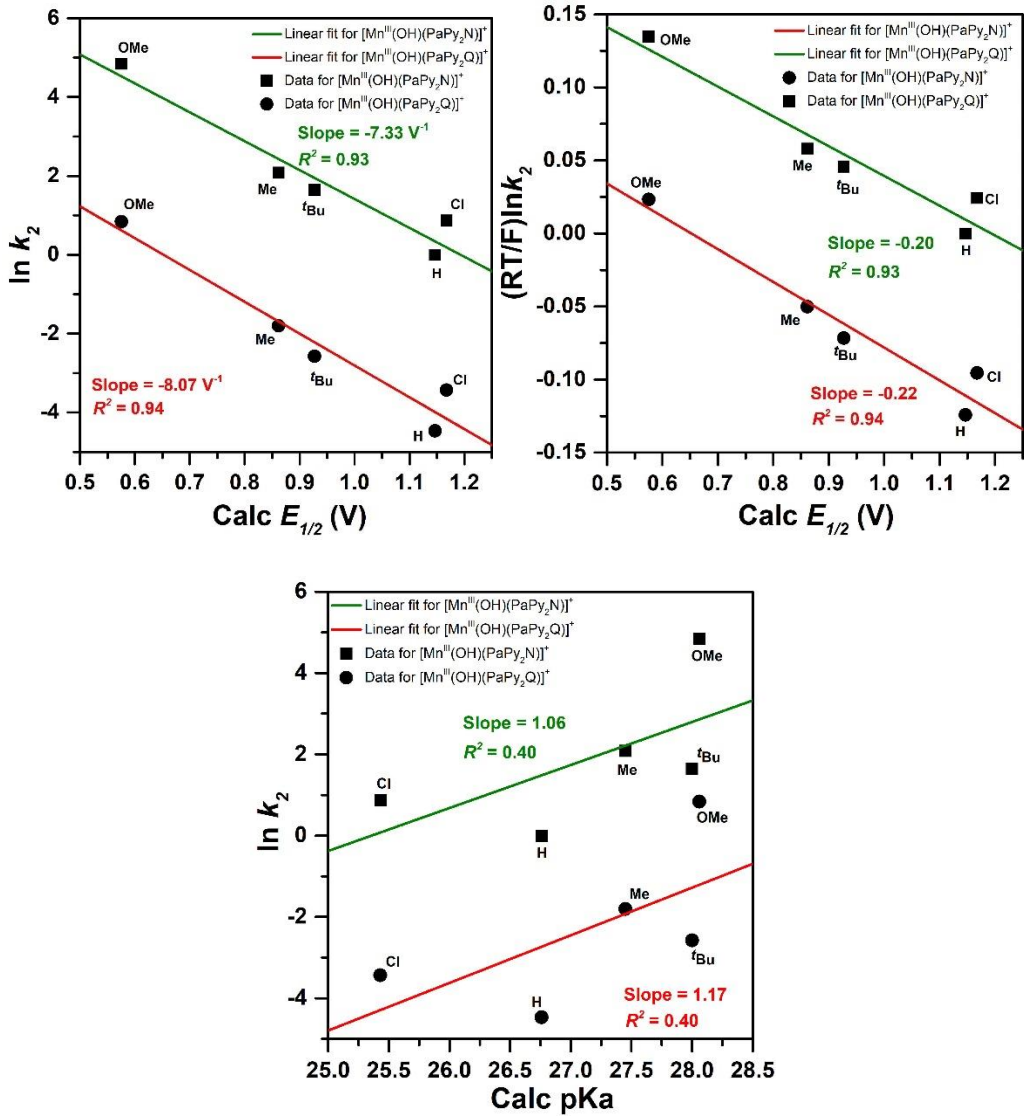

Figure A1.32. Plot of lnk_2 vs calculated $E_{1/2}$ (vs. Fc/Fc^+) (top left), (RT/F)lnk_2 vs calculated $E_{1/2}$ (vs. Fc^+/Fc) (top right) of 4-X-2,6-di-*tert*-butylphenols, and plot of lnk_2 vs calculated pK_a of 4-X-2,6-di-*tert*-butylphenols (bottom).

Table A1.3. DFT-Calculated ΔG values (in kcal/mol) for the addition of a proton or electron used in calculating the E_{red} and p*K*a values.

Ligand	$\Delta G(Mn^{III}(OH_2)$-$Mn^{III}(OH))$	$\Delta G(Mn^{II}(OH_2)$ - $Mn^{III}(OH_2))$	$\Delta G(Mn^{II}(OH)$ - $Mn^{III}(OH))$	$\Delta G(Mn^{II}(OH_2)$ - $Mn^{II}(OH))$
dpaq	-266.7	-109.4	-79.9	-296.2
$PaPy_2Q$	-266.1	-109.1	-78.6	-296.7
trans-$PaPy_2N$	-275.6	-105.4	-72.5	-308.4

Table A1.4. DFT-calculated thermodynamic parameters used to determine Mn^{II}-OH_2 BDFEs for the $[Mn^{III}(OH_2)(PaPy_2Q)]^+$, and *trans*-$[Mn^{III}(OH_2)(PaPy_2N)]^+$ complexes.

Ligand	p*K*a(Mn^{III}–OH_2)	*E*($Mn^{III/II}$–OH_2)	p*K*a(Mn^{II}–OH_2)	*E*($Mn^{III/II}$–OH)	BDFE
dpaq	6.8	0.65	29.3	-0.69	79.1
$PaPy_2Q$	6.4	0.64	29.6	-0.75	78.3
trans-$PaPy_2N$	13.3	0.47	38.2	-1.01	84.0

Table A1.5. DFT-Calculated ΔG (in kcal/mol) for the p*K*a and $E_{1/2}$ parameters of phenol substrates.

Phenols	Δ*G*(PhOH-PhO^-)	Δ*G*(PhOH-$PhO^{\cdot+}$)
4-MeO-2,6-DTBP	-299.2	-124.9
4-Me-2,6- DTBP	-298.4	-131.5
4-^{t}Bu-2,6- DTBP	-299.1	-133.1
4-H-2,6- DTBP	-297.4	-138.0
4-Cl-2,6- DTBP	-295.6	-138.5

Table A1.6. DFT-calculated p*K*a and $E_{1/2}$ values for phenol substrates in CH_3CN and experimental $E_{1/2}$ values.

Phenols	p*K*a(PhOH)	*E*($PhOH^{\cdot+/0}$)	Exp $E_{1/2}$ [b]
4-MeO-2,6-DTBP	28.1	0.58	0.59
4-Me-2,6- DTBP	27.4	0.86	0.81
4-^{t}Bu-2,6- DTBP	28.0 [a]	0.93 [b]	0.93
4-H-2,6- DTBP	26.8	1.15	1.07
4-Cl-2,6- DTBP	25.4	1.17	-

[a] From ref.[4]. [b] From ref.[5].

Table A1.7. BDEs (kcal mol^{-1}) of phenol substrates in CH_3CN and DMSO.

Phenols	Calc BDE (CH_3CN)	Calc BDE (DMSO)	Exp BDE (DMSO)[a]
4-MeO-2,6-^{t}Bu-PhOH	77.3	77.5	79.6
4-Me-2,6-^{t}Bu-PhOH	81.6	81.0	80.1
4-^{t}Bu-2,6-^{t}Bu-PhOH	82.3	82.2	82.3
4-H-2,6-^{t}Bu-PhOH	83.9	83.8	82.7
4-Cl-2,6-^{t}Bu-PhOH	83.5	83.5	-

[a] From ref.[6].

References

1. D. Banfi and L. Patiny, *CHIMIA International Journal for Chemistry*, 2008, **62**, 280-281.
2. A. M. Castillo, L. Patiny and J. Wist, *Journal of Magnetic Resonance*, 2011, **209**, 123-130.
3. J. Aires-de-Sousa, M. C. Hemmer and J. Gasteiger, *Analytical Chemistry*, 2002, **74**, 80-90.
4. J. J. Warren, T. A. Tronic and J. M. Mayer, *Chemical Reviews*, 2010, **110**, 6961-7001.
5. J. Y. Lee, R. L. Peterson, K. Ohkubo, I. Garcia-Bosch, R. A. Himes, J. Woertink, C. D. Moore, E. I. Solomon, S. Fukuzumi and K. D. Karlin, *Journal of the American Chemical Society*, 2014, **136**, 9925-9937.
6. F. G. Bordwell and X.-M. Zhang, *Journal of Physical Organic Chemistry*, 1995, **8**, 529-535.

Appendix 2

Table A2.1. Crystal and refinement data for $[Mn^{II}(H_2O)(^{6Me}dpaq)](OTf)$, $[Mn^{III}(OH)(^{6Me}dpaq)](OTf)$, and $[Mn^{III}(OOCm)(^{6Me}dpaq)]$ (OTf).

Parameter	$[Mn^{II}(H_2O)(^{6Me}dpaq)]$ (OTf)	$[Mn^{III}(OH)(^{6Me}dpaq)]$ (OTf)	$[Mn^{III}(OOCm)(^{6Me}dpaq)]$ (OTf)
Formula	$C_{26}H_{26}F_3MnN_5O_5S$	$C_{26}H_{25}F_3MnN_5O_5S$	$C_{37}H_{38}F_3MnN_6O_6S$
Identification code	q66k	v60d	q05l
Formula weight	632.52	631.51	806.73
Crystal system	Orthothombic	Orthorhombic	Triclinic
Space group	$Pna2_1$	$Pna2_1$	P-1
Crystal size (mm^3)	0.109 x 0.082 x 0.025	0.100 x 0.050 x 0.030	0.140 x 0.020 x 0.010
a/Å	22.4917(5)	22.7367(9)	8.8894(4)
b/ Å	10.2847(2)	10.2260(4)	12.1129(5)
c/ Å	12.0025(3)	11.5888(4)	18.7531(9)
α/°	90.00	90.00	81.779(3)
β/°	90.00	90.00	82.588(3)
γ/°	90.00	90.00	72.703(3)
V/ $Å^3$	2776.42(11)	2694.46(18)	396.68(8)
Z	4	4	2
Dcalcd/g cm^{-3}	1.513	1.557	1.410
F(000)	1300	1296	836
μ(MoKα)/mm^{-1}	5.158	5.315	3.924
T/K	200(2)	200(2)	200(2)
λ/ Å	1.54178	1.54178	1.54178
θ range/°	3.931-70.211	3.888-68.257	2.390-70.328
Reflections collected	16163	9990	30272
Completeness to θ=66.000° (%)	96.7	99.5	96.0
Index ranges	-26≤h≤23, -12≤k≤11, -11≤l≤13	-26≤h≤24, -12≤k≤8, -13≤l≤13	-10≤h≤10, -14≤k≤14, -22≤l≤22
Data/Restraint/parameters	4144 / 1 / 381	4121 / 1 / 378	6685 / 2 / 492
R(F), w $R_2(F^2)$ (> $2\sigma(F^2)$)	0.040, 0.0987	0.0603, 0.1696	0.0766, 0.2200
R(F), w $R_2(F^2)$ (all data)	0.0452, 0.1006	0.0659, 0.1767	0.0873, 0.2282
Absorption correction	Multi-scan	Multi-scan	Multi-scan
GOF on F^2	1.007	1.162	1.081
Largest peak/hole/ $eÅ^{-3}$	0.864/-0.420	0.398/-0.752	1.001/-0.456
Max and min transmission	0.7533/0.4398	1.000/0.699	0.7533/0.5237
CCDC #	2048663	2049911	2048664

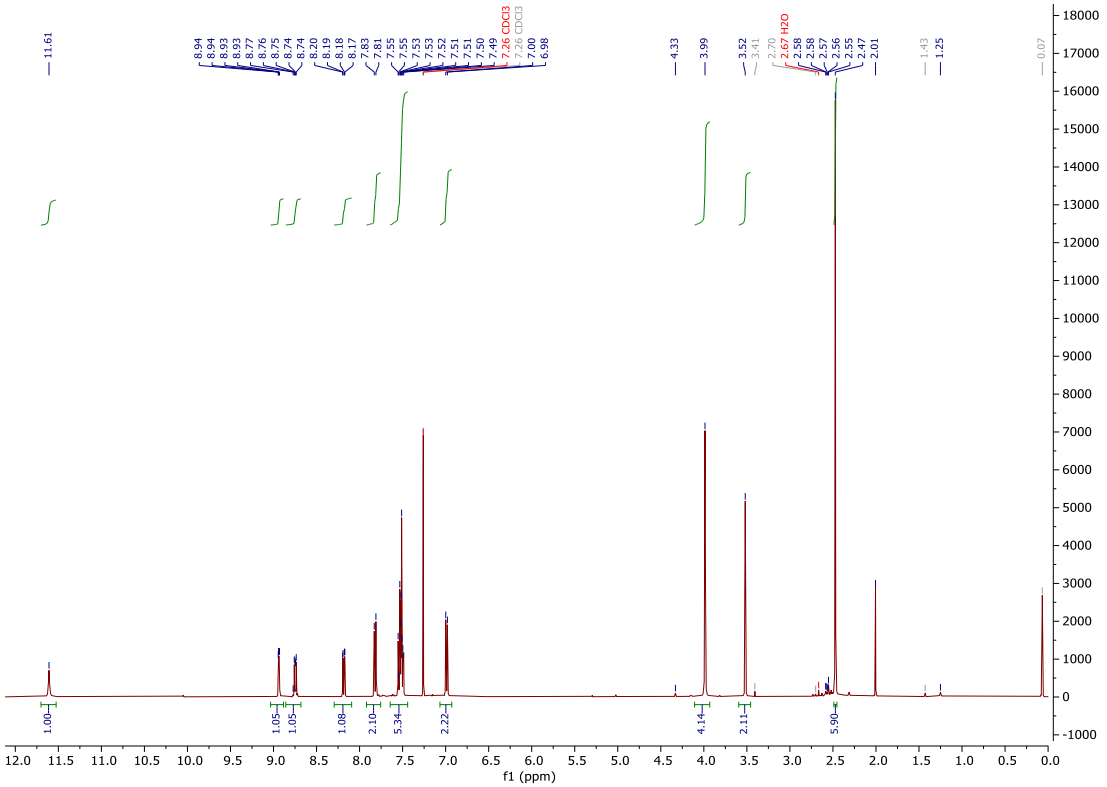

Figure A2.1. ^{1}H NMR spectrum of H^{6Me}dpaq dissolved in $CDCl_3$ at 298 K.

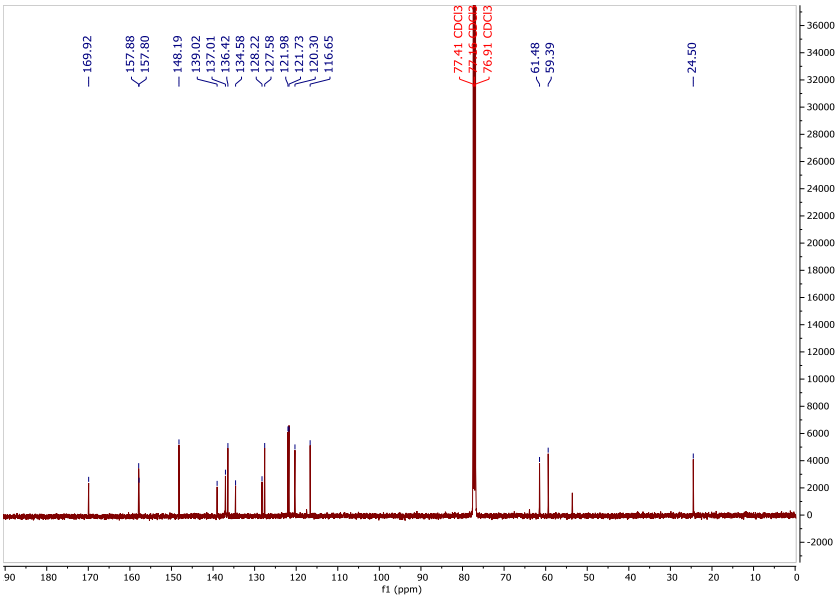

Figure A2.2. ^{13}C NMR spectrum of H^{6Me}dpaq dissolved in $CDCl_3$ at 298 K.

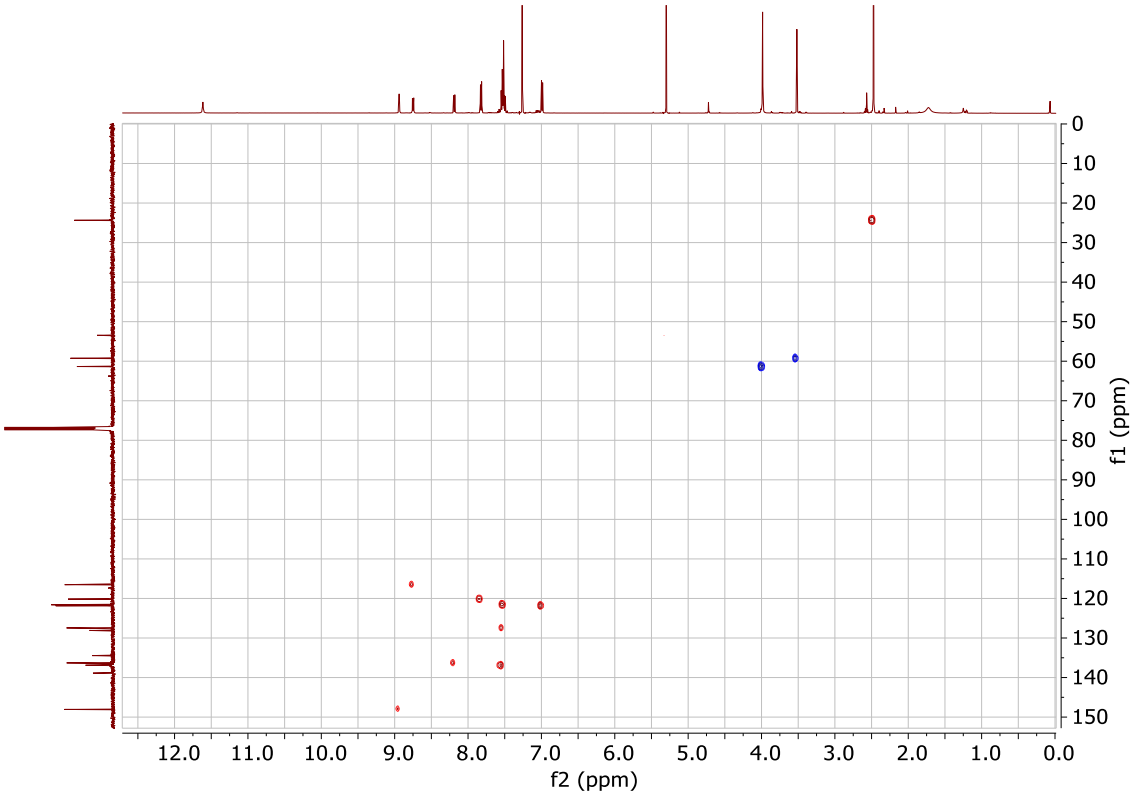

Figure A2.3. HSQC NMR data for H^{6Me}dpaq dissolved in $CDCl_3$ at 298 K.

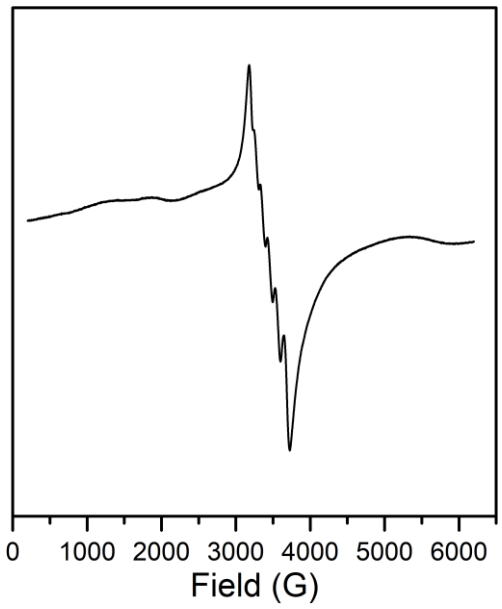

Figure A2.4. EPR spectrum obtained for a 2 mM solution of $[Mn^{II}(H_2O)(^{6Me}dpaq)]OTf$ in CH_3CN showing a six-line signal consistent with the assignment of a mononuclear Mn^{II} species (g = 2.00 , A = 93.9 G).

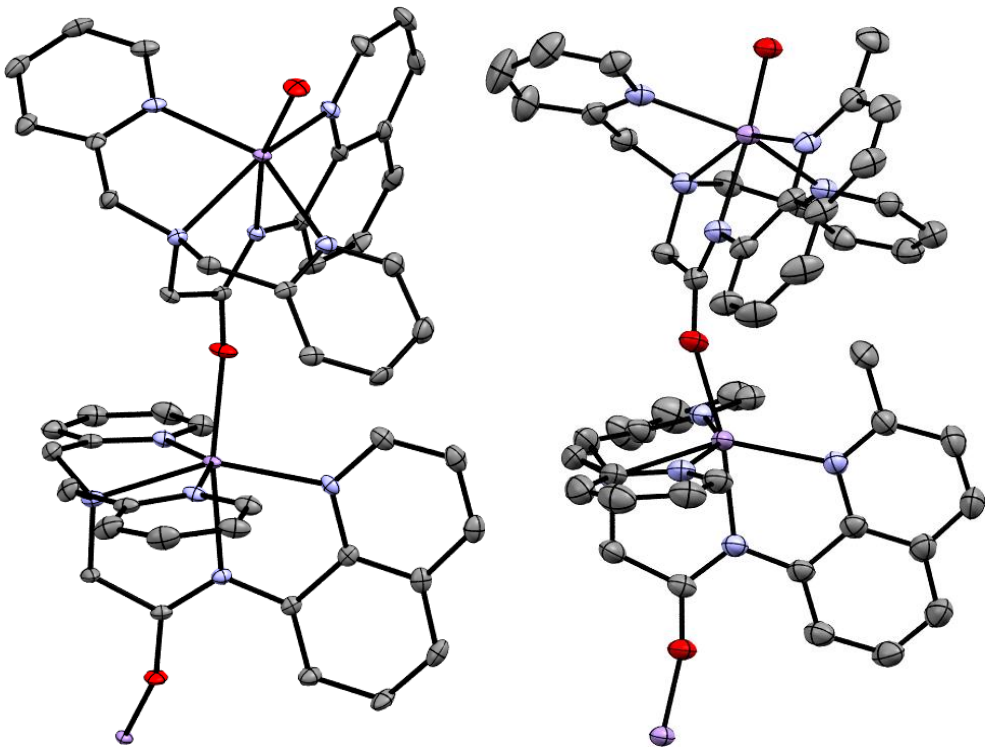

Figure A2.5. Left: Polymeric structures of $[Mn^{II}(dpaq)](OTf)$[1] and $[Mn^{II}(dpaq^{2Me})](OTf)$[2] obtained by X-ray diffraction experiments described in ref. 7 and 4, respectively.[2]

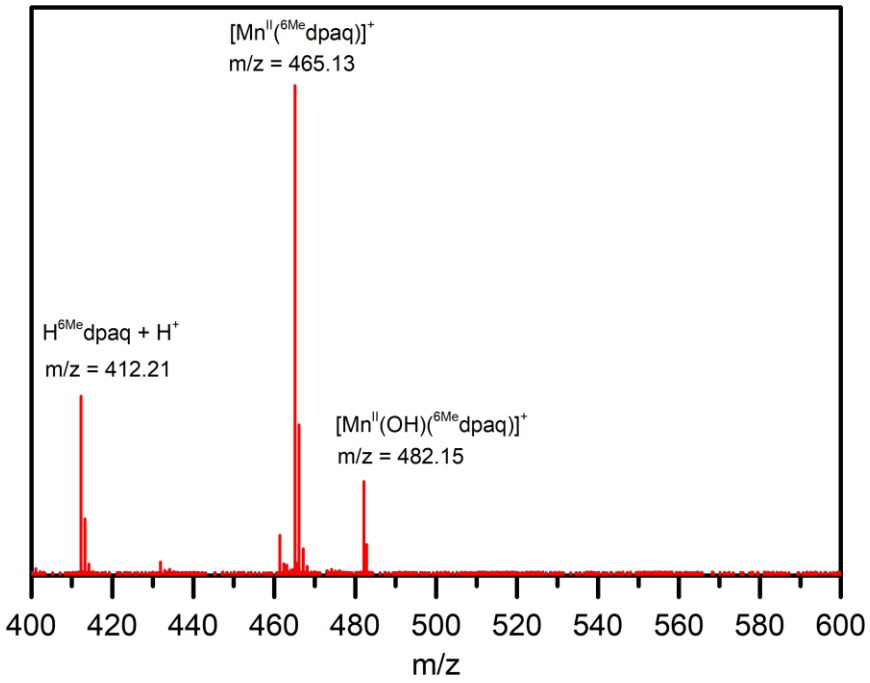

Figure A2.6. ESI-MS spectrum of $[Mn^{II}(^{6Me}dpaq)]^+$ in CH_3CN.

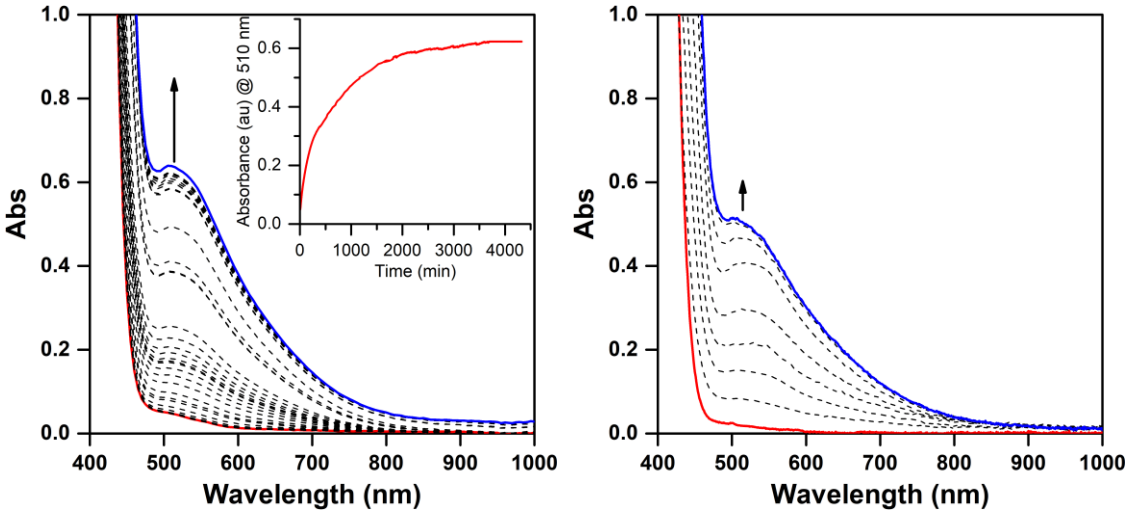

Figure A2.7. Electronic absorption spectra monitoring the reaction of a 2.5 mM solution of $[Mn^{II}(H_2O)(^{6Me}dpaq)]OTf$ (red trace) with dioxygen (left) and 2.0 mM solution of $[Mn^{II}(H_2O)(^{6Me}dpaq)]OTf$ (red trace) with 0.5 equiv. PhIO in CH_3CN at 298 K (right). The dashed traces show the reaction progress, and the blue trace is the final spectrum.

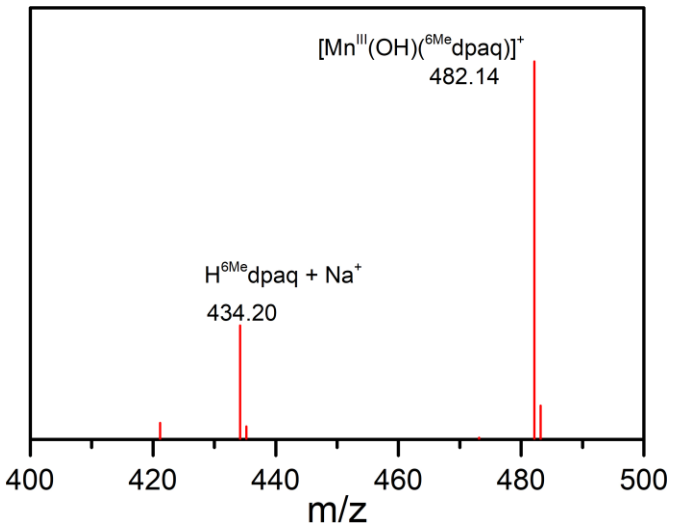

Figure A2.8. ESI-MS of 0.002 mM $[Mn^{III}(OH)(^{6Me}dpaq)]^{+}$ in CH_3CN.

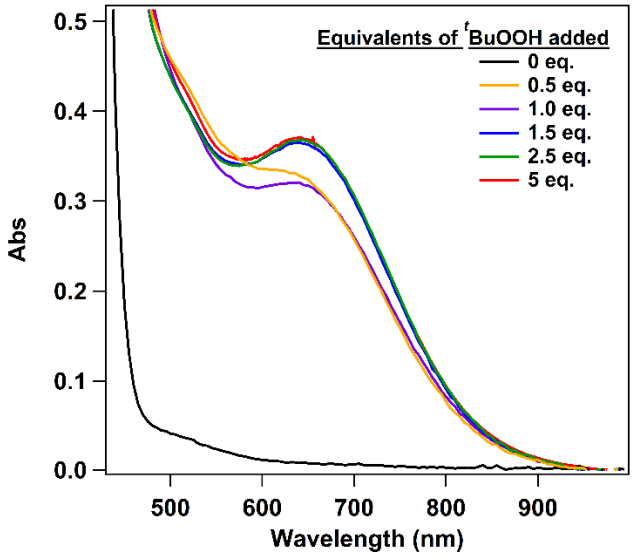

Figure A2.9. Electronic absorption spectra obtained upon the addition of aliquots of ^{t}BuOOH to a 2 mM solution of $[Mn^{II}(H_2O)(^{6Me}dpaq)]OTf$ in CH_3CN at 298 K. Full formation of $[Mn^{III}(OO^{t}Bu)(^{6Me}dpaq)]^{+}$ (λ_{max} = 650 nm) is achieved upon the addition of 1.5 equiv. of ^{t}BuOOH.

Table A2.2. Manganese-ligand bond lengths (Å) from the crystal structures of $[Mn^{II}(OH_2)(^{6Me}dpaq)](OTf)$, $[Mn^{II}(dpaq)](OTf)$, $[Mn^{II}(dpaq^{2Me})](OTf)$, $[Mn^{III}(OH)(^{6Me}dpaq)](OTf)$, $[Mn^{III}(OH)(dpaq^{2Me})](OTf)$, $[Mn^{III}(OH)(dpaq^{2Me})](OTf)$, and $[Mn^{III}(OH)(dpaq^{Cl})](OTf)$.

	$[Mn^{II}(OH_2)(L)](OTf)$	$[Mn^{II}(L)](OTf)$		$[Mn^{III}(OH)(L)](OTf)$		
	L = ^{6Me}dpaq	L = dpaq	L= dpaq^{2Me}	L = ^{6Me}dpaq	L = dpaq	L = dpaq^{2Me}	L = dpaq^{5Cl}
Mn–O1	2.108(3)	2.079(2)	2.116(2)	1.806(6)	1.806(13)	1.819(3)	1.8067(18)
Mn–N1	2.233(3)	2.214(3)	2.268(3)	2.041(7)	2.072(14)	2.186(3)	2.066(2)
Mn– N2	2.152(4)	2.191(3)	2.172(3)	1.962(6)	1.975(14)	1.979(3)	1.9758(18)
Mn–N3	2.280(3)	2.314(3)	2.317(3)	2.130(6)	2.173(14)	2.303(3)	2.1668(19)
Mn–N4	2.354(4)	2.244(3)	2.275(3)	2.322(6)	2.260(14)	2.148(3)	2.245(2)
Mn–N5	2.417(3)	2.286(3)	2.286(3)	2.381(7)	2.216(15)	2.158(3)	2.218(2)

[a] Data for $[Mn^{II}(dpaq)](OTf)$ and $[Mn^{III}(OH)(dpaq)](OTf)$ are described in reference[1]. Data for $[Mn^{II}(dpaq^{2Me})](OTf)$ and $[Mn^{III}(OH)(dpaq^{2Me})](OTf)$ are described in reference[2]. Data for $[Mn^{III}(OH)(dpaq^{5Cl})](OTf)$ are described in reference[3].

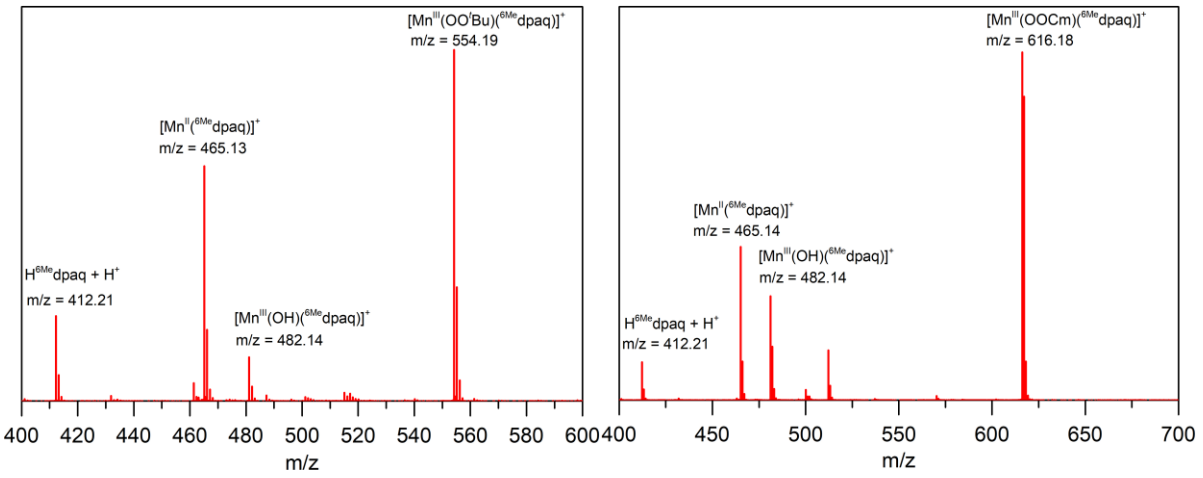

Figure A2.10. ESI-MS of 0.002 mM $[Mn^{III}(OO^tBu)(^{6Me}dpaq)]^+$ (left) and $[Mn^{III}(OOCm)(^{6Me}dpaq)]^+$ (right) in CH_3CN.

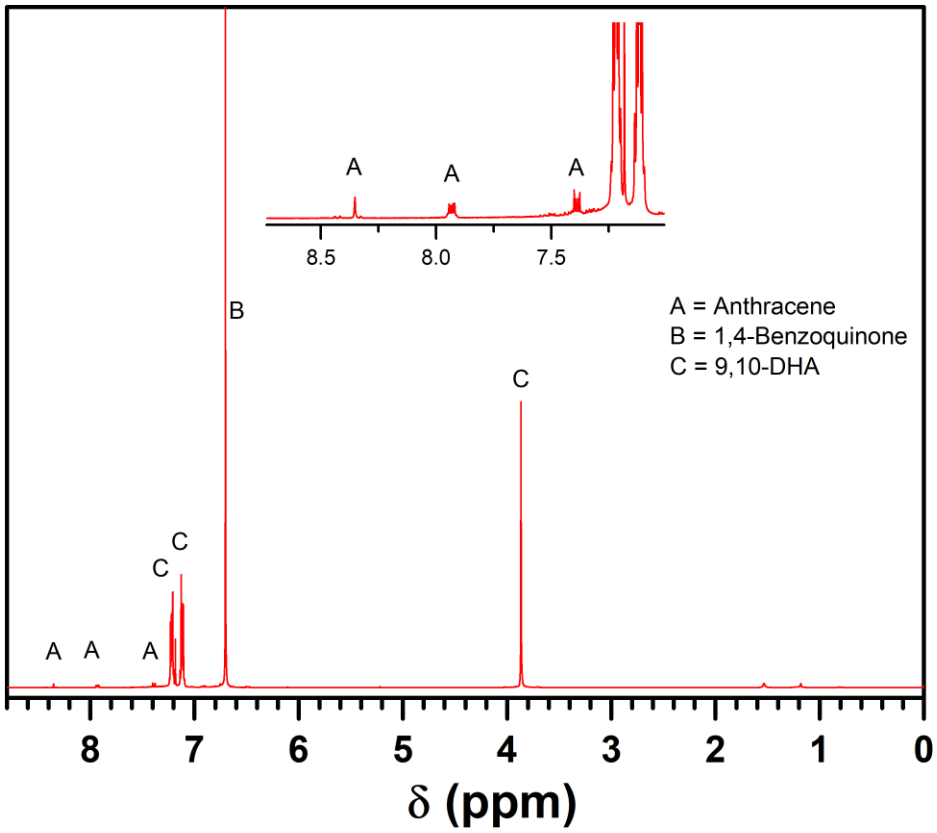

Figure A2.11. ^{1}H-NMR spectrum of the organic product resulting from the reaction of 100 equiv. DHA with 1.75 mM $[Mn^{III}(OO^{t}Bu)(^{6Me}dpaq)]^{+}$ in $CDCl_3$ at 298 K under anaerobic conditions. Quantification of products was obtained using 1,4-benzoquinone (10 molar equiv. relative to starting Mn^{II} complex) as an internal standard.

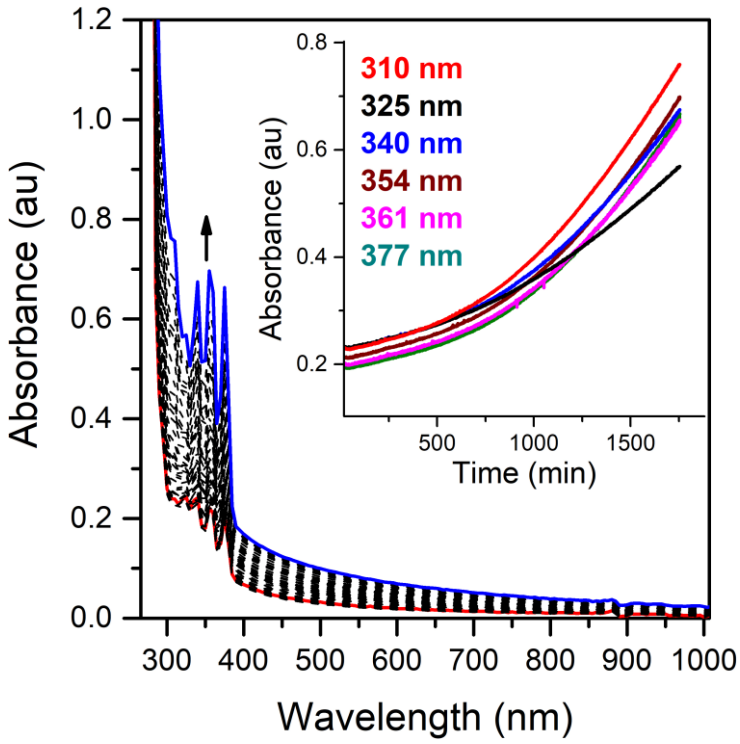

Figure A2.12. Control experiments: DHA without $[Mn^{III}(OO^tBu)(^{6Me}dpaq)]^+$ at 323 K irradiated with UV light at 323 K under anaerobic condition for 33 hrs to investigate the contribution of Uv-radiation to the higher than expected conversion of DHA to anthracene.

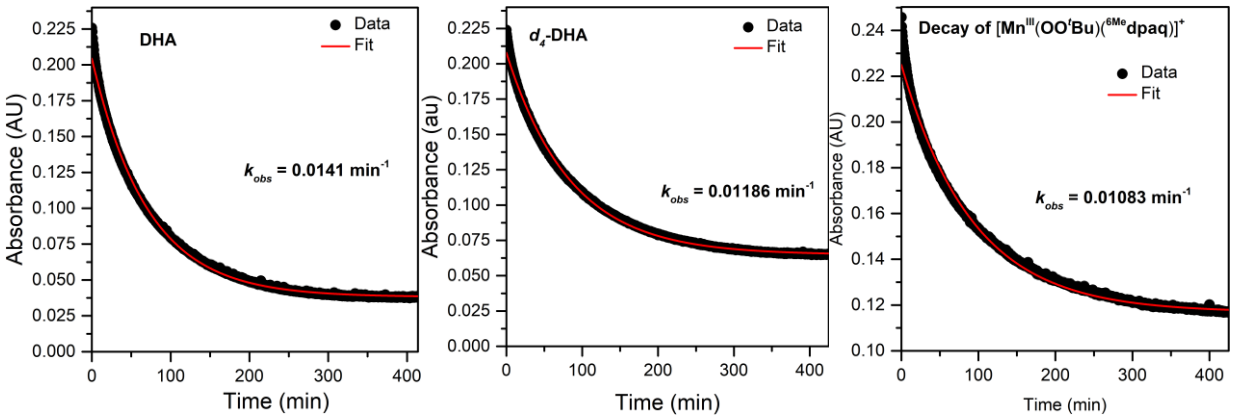

Figure A2.13. Time trace for the reaction of 1.0 mM $[Mn^{III}(OO^tBu)(^{6Me}dpaq)]^+$ with 100 equiv. DHA (left) d_4-DHA (middle) at 323 K and the decay of $[Mn^{III}(OO^tBu)(^{6Me}dpaq)]^+$ in CH_3CN at 323 K.

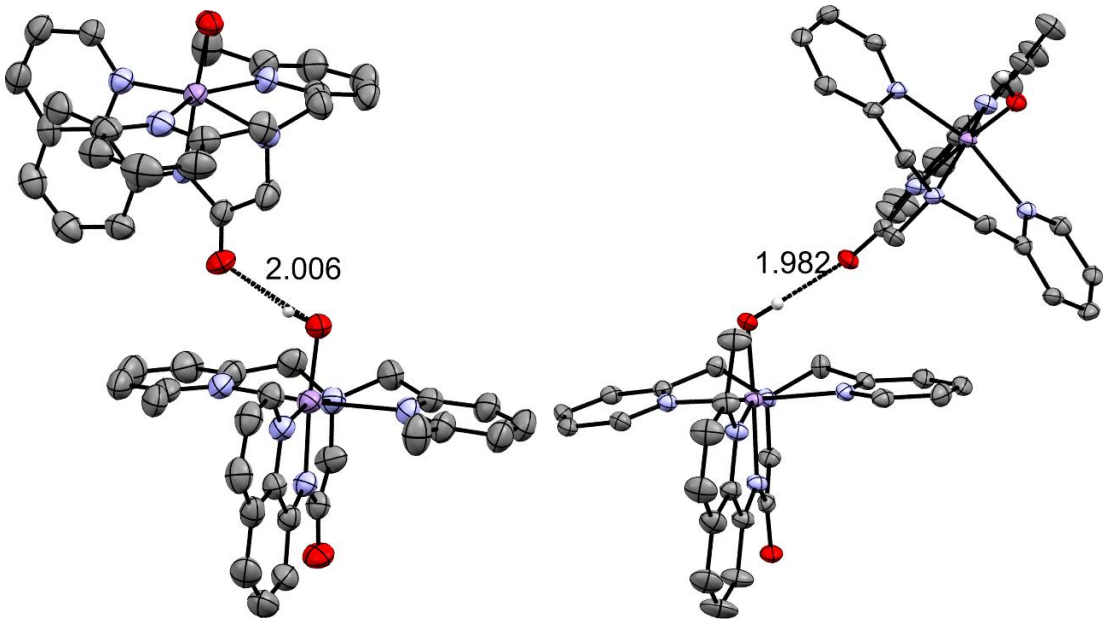

Figure A2.14. ORTEP diagrams showing the hydrogen bonding interaction between two $[Mn^{III}(OH)(^{6Me}dpaq)]^+$ (left) and $[Mn^{III}(OH)(^{2Me}dpaq)]^+$ (right) molecules in the unit cell. Data for $[Mn^{III}(OH)(^{2Me}dpaq)]^+$ are described in reference [2].

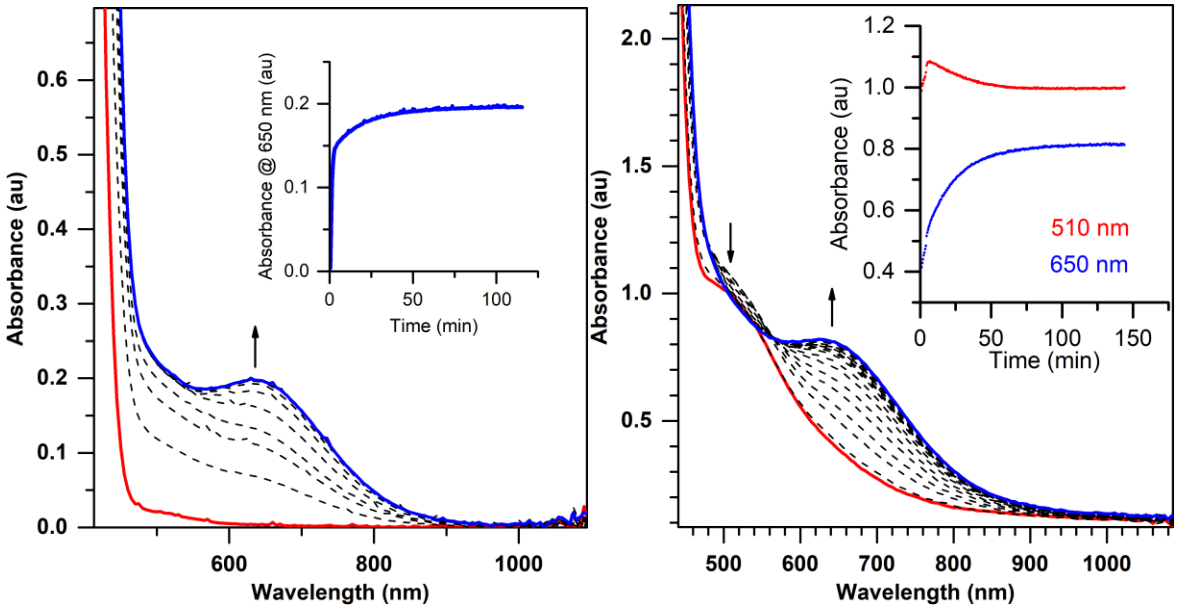

Figure A2.15. Left: Electronic absorption spectra showing the formation of the green $[Mn^{III}(OOCm)(^{6Me}dpaq)]^+$ species (blue trace) from the oxidation of 1.0 mM $[Mn^{II}(H_2O)(^{6Me}dpaq)]OTf$ (red trace) with 1.5 equiv. CmOOH. Right: Electronic absorption spectra showing the formation of $[Mn^{III}(OOCm)(^{6Me}dpaq)]^+$ from the reaction of 3.0 mM $[Mn^{III}(OH)(^{6Me}dpaq)]^+$ (red trace) with 1.0 equiv. CmOOH (blue trace is the final spectrum). Time courses for each reaction are shown in the insets.

Table A2.3. Electronic Absorption Band Maxima (nm), Selected Bond Lengths (Å) and Angles (°), and O–O Stretching Frequencies ($\nu_{O\text{-}O}$, cm^{-1}) for Mn^{III}-alkylperoxo Complexes.

complex	λ		Mn-O	O-O	Mn-O-O	Mn-N[a]	$\nu_{O\text{-}O}$	Ref.
$[Mn^{III}(OO^tBu)(^{6Me}dpaq)]^+$	500	650					877	[b]
$[Mn^{III}(OOCm)(^{6Me}dpaq)]^+$	500	650	1.849(3)	1.466(4)	110.4(2)	2.339	861	[b]
$[Mn^{III}(OO^tBu)(dpaq)]^+$	475	710					872	11
$[Mn^{III}(OO^tBu)(dpaq^{2Me})]^+$	475	690					NR	11
$[Mn^{III}(OO^tBu)(S^{Me2}N_4(6\text{-Me-DPPN}))]^+$	420	585	1.843(3)	1.431(5)	124.2(3)	2.511	893	10
$[Mn^{III}(OO^tBu)(S^{Me2}N_4(QuinoPN))]^+$	415	590	1.840(4)	1.438(5)	121.1(3)	2.484	895	10
$[Mn^{III}(OO^tBu)(S^{Me2}N_4(QuinoEN))]^+$	385	590	1.861(5)	1.457(7)	109.2(4)	2.436	888	9, 10
$[Mn^{III}(OO^tBu)(S^{Me2}N_4(6\text{-Me-DPEN}))]^+$	355	600	1.853(6)	1.468(7)	112.4(4)	2.413	875	10

[a] Mn–N bond length for the elongated bonds associated with the 6-Me-pyridyl or quinolinyl donors. [b] From this work.

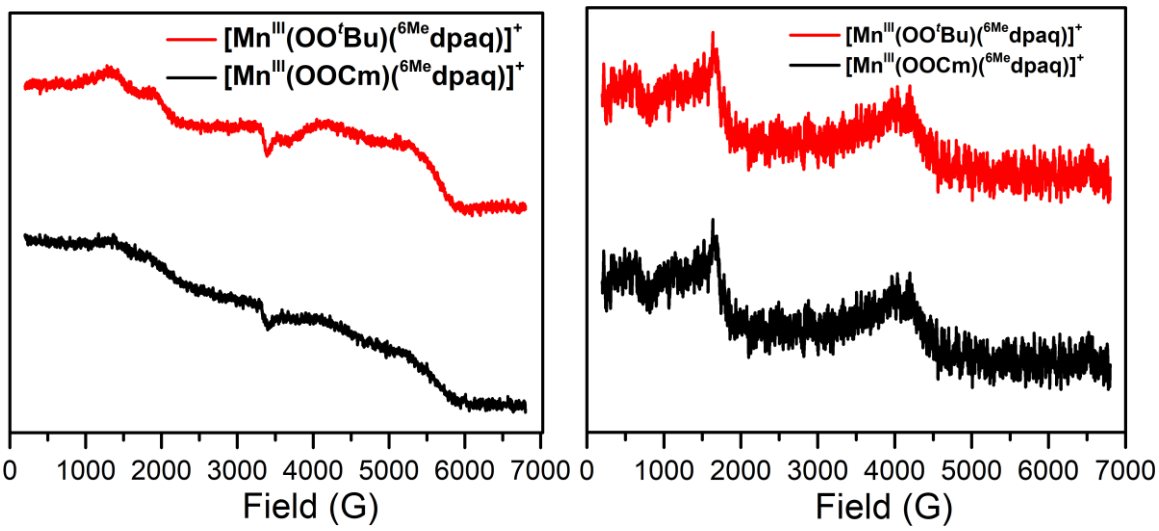

Figure A2.16 X-band EPR spectra of frozen 5m M acetonitrile solutions of $[Mn^{III}(OO^tBu)(^{6Me}dpaq)]^+$ and $[Mn^{III}(OOCm)(^{6Me}dpaq)]^+$ at 10 K in perpendicular-mode (left) and parallel-mode (right).

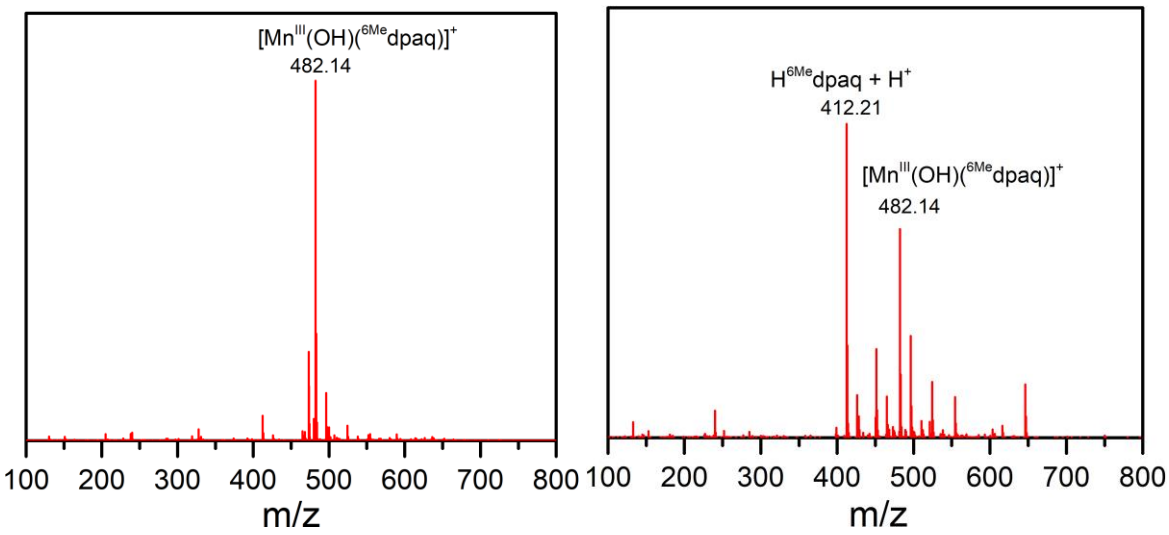

Figure A2.17. ESI-MS data for $[Mn^{III}(OO^tBu)(^{6Me}dpaq)]^+$ decay product (left) and $[Mn^{III}(OOCm)(^{6Me}dpaq)]^+$ decay product (right) in CH_3CN.

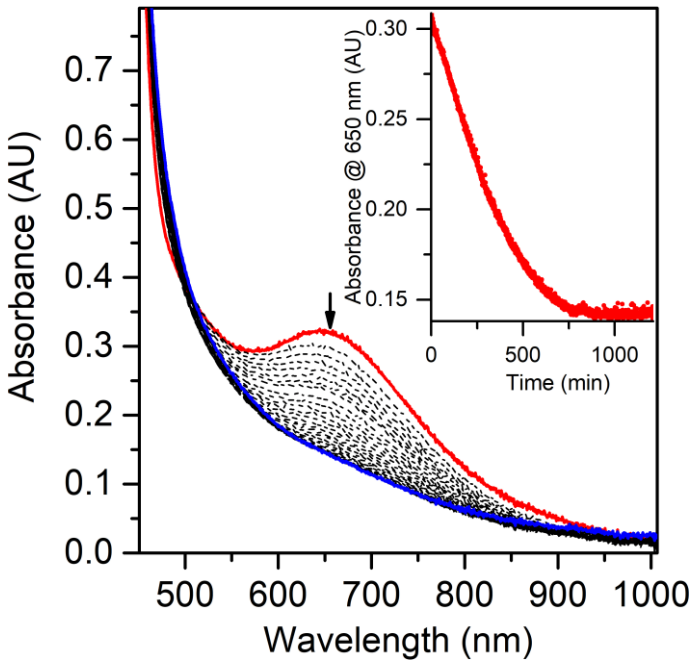

Figure A2.18. Electronic absorption spectra showing the decay of anerobic CH_3CN solutions of 1.5 mM crude $[Mn^{III}(OOCm)(^{6Me}dpaq)]^+$ at 323K.

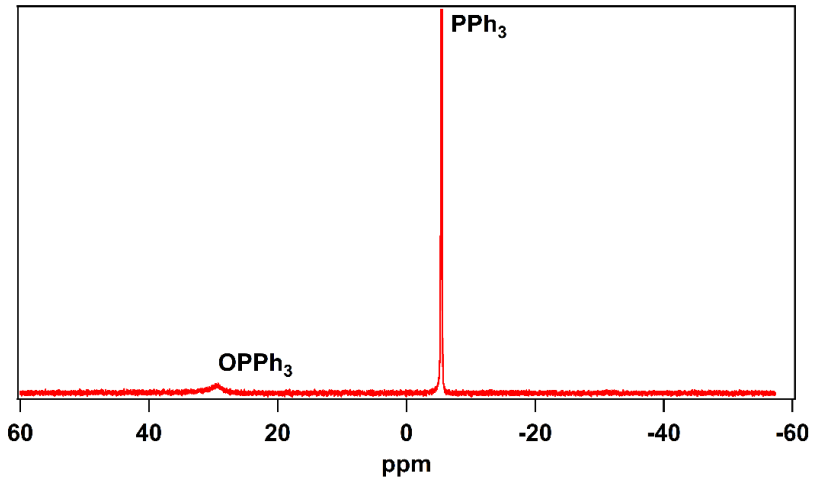

Figure A2.19. ^{31}P NMR analysis of the products of the reaction of PPh_3 with $[Mn^{III}(OO^tBu)(^{6Me}dpaq)]^+$ in CH_3CN at 298 K.

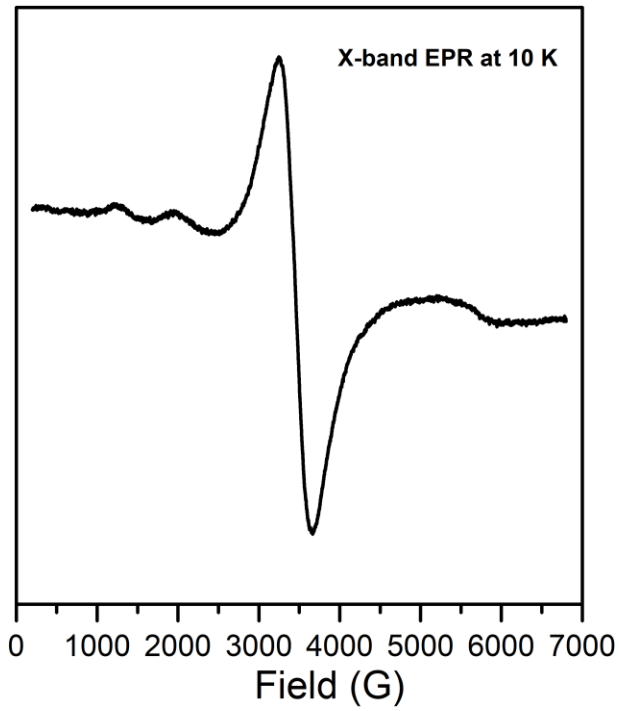

Figure A2.20. 10 K, perpendicular-mode X-band EPR spectrum of the frozen CH_3CN solution following the reaction of 2 mM $[Mn^{III}(OO^tBu)(^{6Me}dpaq)]^+$ with 100 equiv. PPh_3 at 298 K.

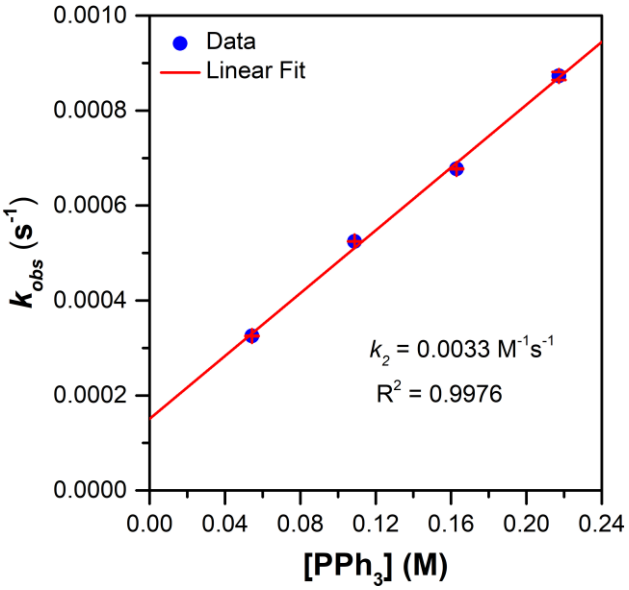

Figure A2.21. Pseudo-first-order rate constants, k_{obs} (s^{-1}), versus PPh_3 concentration for a 1.0 mM CH_3CN solution of $[Mn^{III}(OOCm)(^{6Me}dpaq)]^+$ at 298 K.

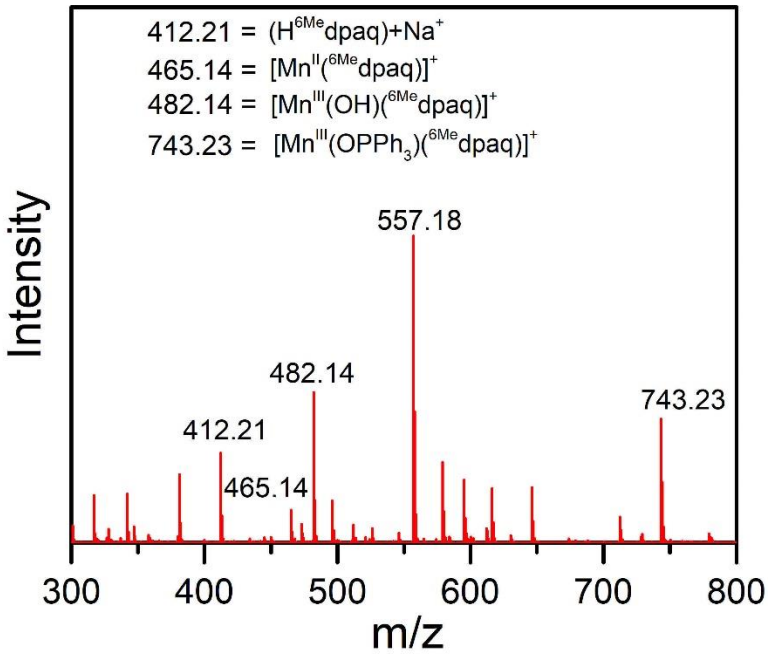

Figure A2.22. ESI-MS data for the reaction of 22 mM of $[Mn^{III}(OOCm)(^{6Me}dpaq)]^+$ with 5 equiv. of PPh_3 in CH_3CN at 298K.

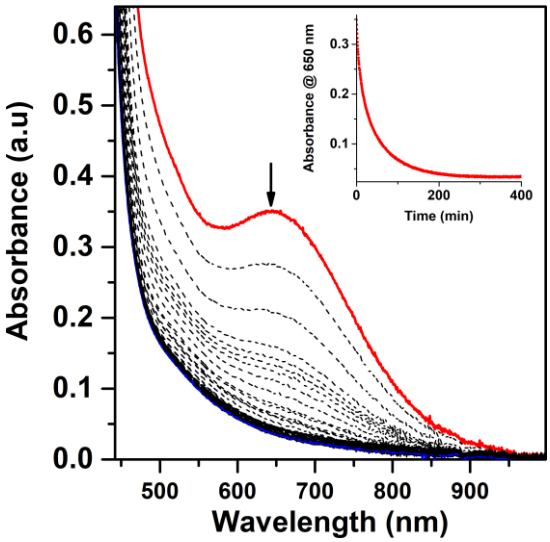

Figure A2.23. Electronic absorption spectra monitoring the reaction of a 1.75 mM anaerobic solution of $[Mn^{III}(OO^{t}Bu)(^{6Me}dpaq)]^{+}$ (red trace) in CH_3CN with 100 equiv. of DHA at 323 K. The dashed traces show the reaction progress over time and the blue trace is the final product solution. Inset: time course for spectral changes at 650 nm.

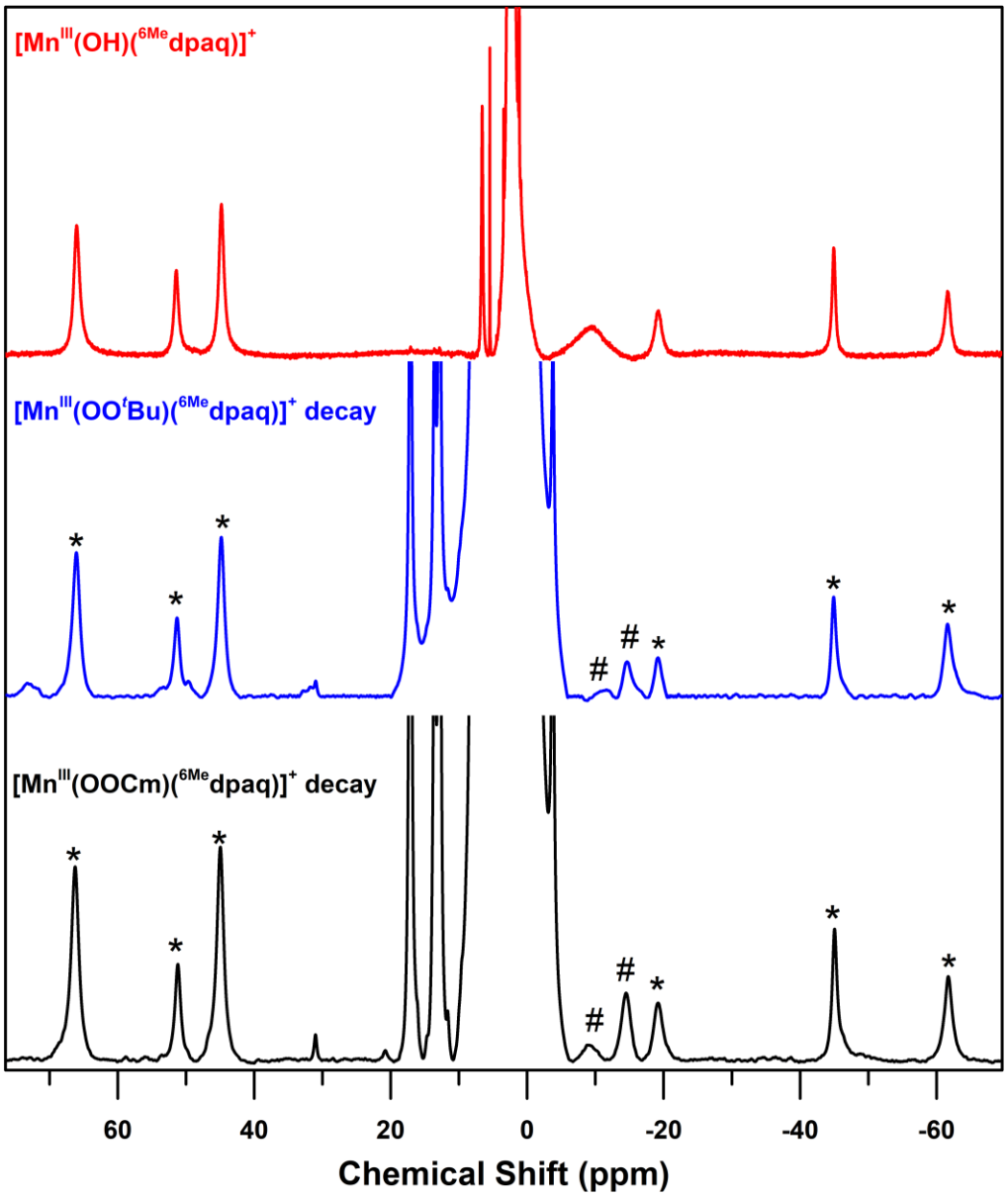

Figure A2.24. ^{1}H NMR spectra of 20 mM solutions of $[Mn^{III}(OH)(^{6Me}dpaq)]^{+}$ (red) and the decay products from 12 mM solution $[Mn^{III}(OO^{t}Bu)(^{6Me}dpaq)]^{+}$ (blue), and 12 mM solution of $[Mn^{III}(OOCm)(^{6Me}dpaq)]^{+}$ (black). All samples were prepared in CD_3CN at 298 K. The asterisk marks peaks found in $[Mn^{III}(OH)(^{6Me}dpaq)]^{+}$. The hashtag marks peaks that could result from the resolution of the broad peak found at -9.6 ppm in $[Mn^{III}(OH)(^{6Me}dpaq)]^{+}$.

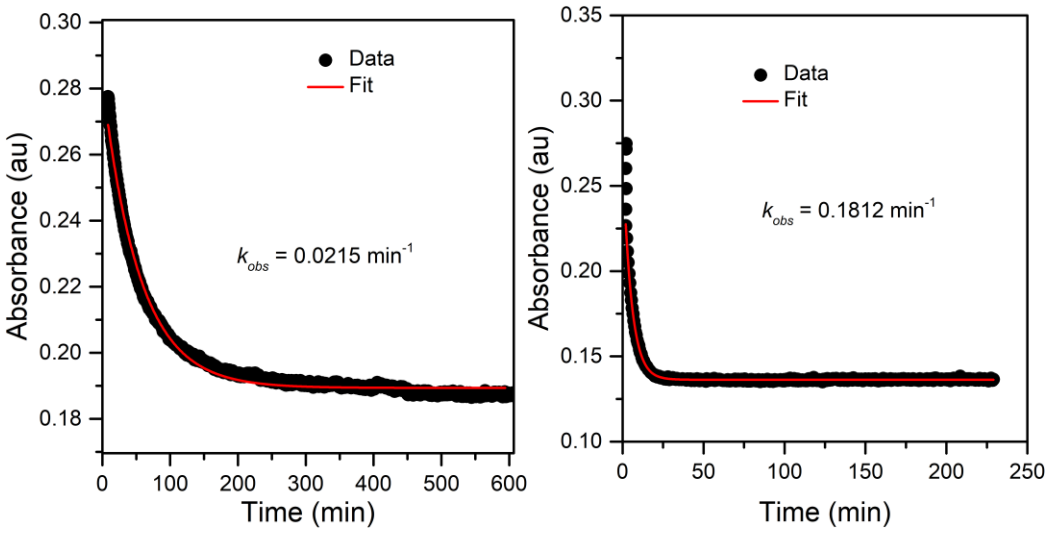

Figure A2.25. Time traces for the thermal decay of 1.2 mM solutions of [Mn^{III}(OOCm)(^{6Me}dpaq)]$^{+}$ at 323 K in CH_3CN (left) and CD_3CN (right).

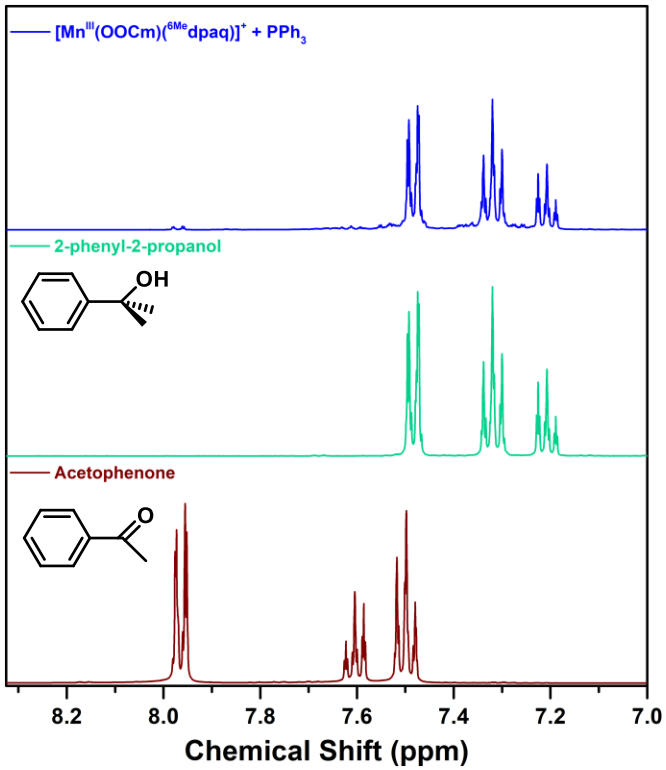

Figure A2.26. ^{1}H NMR of the organic products from the reaction of 22 mM [Mn^{III}(OOCm)(^{6Me}dpaq)]$^{+}$with 5 equiv. of PPh3 at 298 K (blue, top), 2-phenyl-2-propanol (cyan, middle) and acetophenone (brown, bottom) in CD_3CN at 298 K.

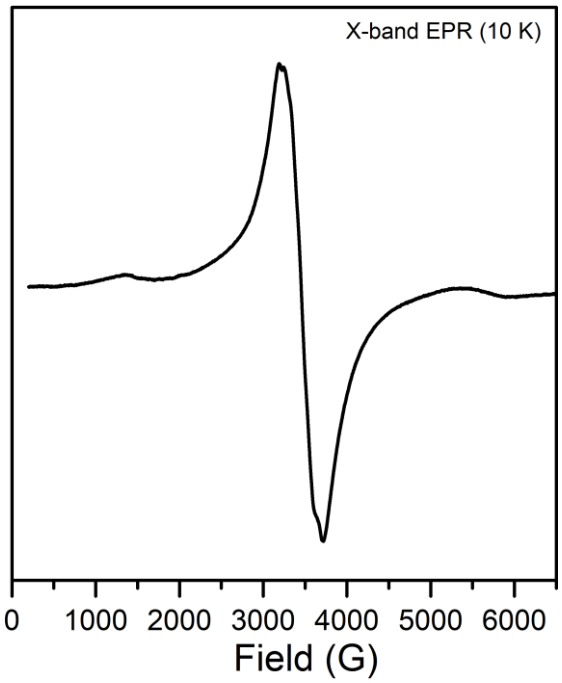

Figure A2.27. 10 K, perpendicular-mode X-band EPR spectrum of the frozen CH_3CN solution following the reaction of 2 mM $[Mn^{III}(OO^tBu)(^{6Me}dpaq)]^+$ with 100 equiv. DHA at 298 K.

References

1. G. B. Wijeratne, B. Corzine, V. W. Day and T. A. Jackson, *Inorganic Chemistry*, 2014, **53**, 7622-7634.
2. D. B. Rice, G. B. Wijeratne, A. D. Burr, J. D. Parham, V. W. Day and T. A. Jackson, *Inorganic Chemistry*, 2016, **55**, 8110-8120.
3. D. B. Rice, A. Munasinghe, E. N. Grotemeyer, A. D. Burr, V. W. Day and T. A. Jackson, *Inorganic Chemistry*, 2019, **58**, 622-636.

Appendix 3

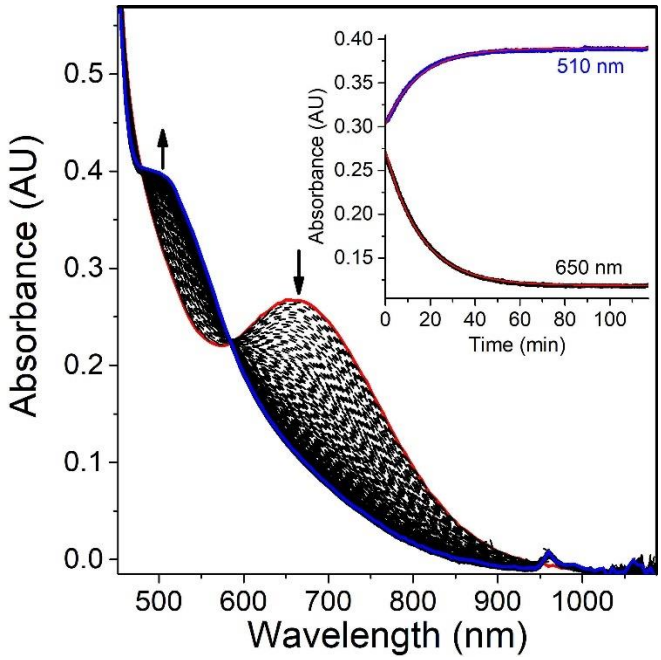

Figure A3.1. Electronic absorption spectra monitoring the reaction of anaerobic sample of 1.75 mM solution of $[Mn^{III}(OO^{t}Bu)(^{6Me}dpaq)]^{+}$ in TFE (red trace) at 323 K to form the $[Mn^{III}(OCH_2CF_3)(^{6Me}dpaq)]^{+}$(blue tace). (Inset) time course for the spectral changes.

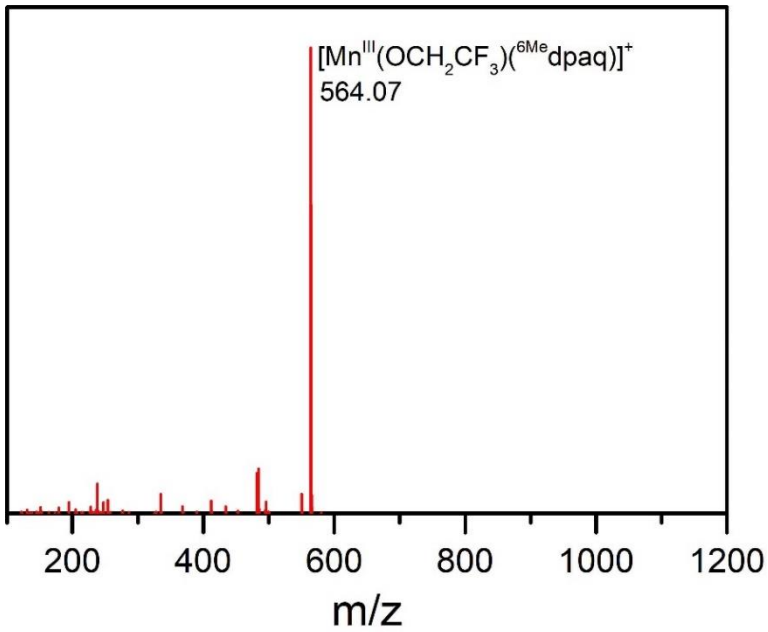

Figure A3.2. ESI-MS data for a 2 x 10^{-3} mM solution of anaerobic reaction of $[Mn^{III}(OO^{t}Bu)(^{6Me}dpaq)]^{+}$ with TFE.

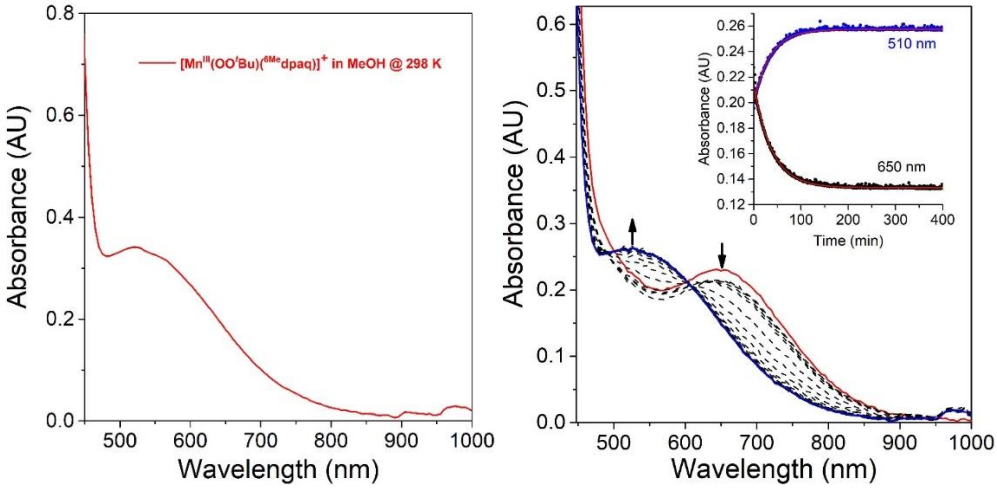

Figure A3.3. Electronic absorption spectra of final reaction mixture from the dissolution of $[Mn^{III}(OO^{t}Bu)(^{6Me}dpaq)]^{+}$ in MeOH anaerobically. Reaction of 1.0 mM solution $[Mn^{III}(OO^{t}Bu)(^{6Me}dpaq)]^{+}$ in MeCN with 100 µL of MeOH anaerobically at 25 °C.

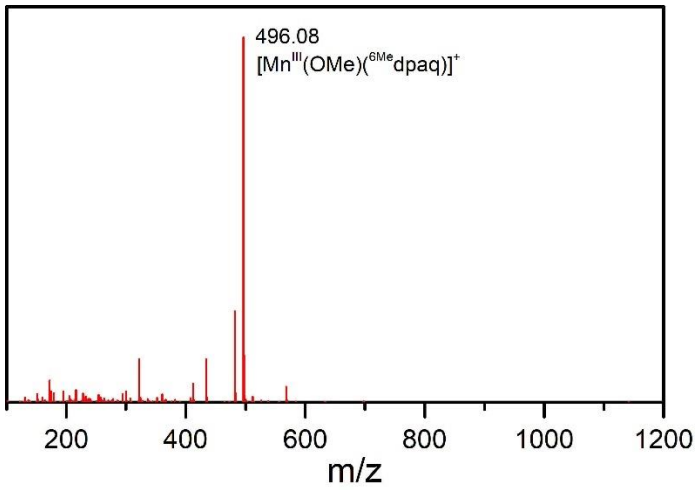

Figure A3.4. ESI-MS data for a 2 x 10^{-3} mM solution of anaerobic reaction of $[Mn^{III}(OO^{t}Bu)(^{6Me}dpaq)]^{+}$ with MeOH.

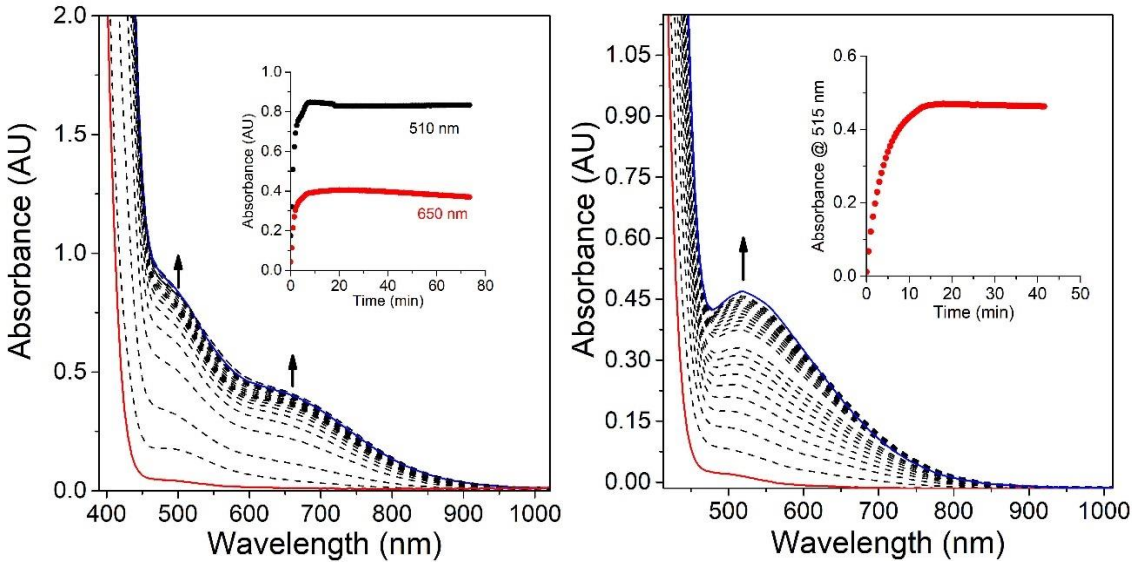

Figure A3.5. Electronic absorption spectra monitoring the reaction of 2.5 mM solution of $[Mn^{II}(OH_2)(^{6Me}dpaq)]^+$ in TFE (red trace) with 1.5 equiv. of ^{t}BuOOH at 25 °C (left) and 2.0 mM solution of $[Mn^{II}(OH_2)(^{6Me}dpaq)]^+$ in MeOH (red trace) with 1.5 equiv. of ^{t}BuOOH at 25 °C (right). Final reaction mixture are the blue traces. (Inset) time course for the spectral changes.

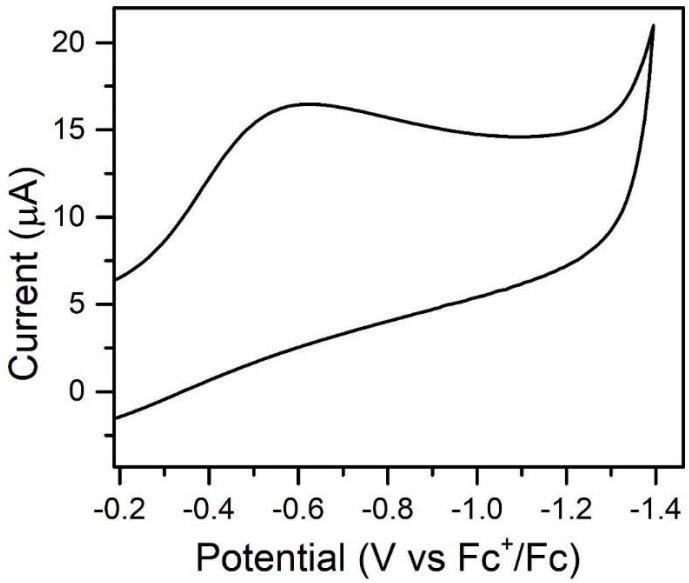

Figure A3.6. Cyclic voltammetry traces of $[Mn^{III}(OH)(^{6Me}dpaq)]^+$ showing the Mn^{III}/Mn^{II} wave with a scan rate of 100 mV s^{-1}. The working electrode was a glassy carbon electrode with a Pt wire as the counter electrode. Ag/AgCl quasi-reference electrode was used, and Fc^+/Fc potential was measured as an external reference. 2 mM solutions of $[Mn^{III}(OH)(^{6Me}dpaq)]^+$ prepared from 0.1 M Bu_4NPF_6 electrolyte solution in CH_3CN were used for measurements at 298 K.

Table A3.1. TD-DFT calculated energies, percent contributions from dominant one-electron excitations, and oscillator strengths for the major electronic transitions in $[Mn^{III}(OH)(dpaq)]^+$ and $[Mn^{III}(OH)(^{6Me}dpaq)]^+$.

Ligand	State	Energy (cm^{-1})	f_{osc}	Transition	%	Donor MO (%)	Acceptor MO (%)	Comment
dpaq	1	13000 (770 nm)	0.00124	117a→119a	91.0	Mn $3d_{x^2-y^2}$ (39.1) N p_x (19.9) N p_y (14.8)	Mn $3d_{z^2}$ (51.5) O p_z (10.3) N p_x (6.2) N p_z (7.6)	*d-d & LMCT*
	2	19800 (505 nm)	0.00113	118a→119a	81.5	Mn $3d_{yz}$ (2.3) O p_y (9.6) N p_y (23.4) C p_y (54.7)	Mn $3d_{z^2}$ (51.5) O p_z (10.3) N p_x (6.2) N p_z (7.6)	LMCT
	4	20600 (486 nm)	0.00238	114a→119a	38.9	Mn $3d_{xz}$ (11.7) O p_x (43.4) C p_y (23.6) N p_x (5.2)	Mn $3d_{z^2}$ (51.5) O p_z (10.3) N p_x (6.2) N p_z (7.6)	LMCT & *d-d*
				116a→119a	29.3	Mn $3d_{xz}$ (6.8) O p_x (53.3) O p_2 (56.9)	Mn $3d_{z^2}$ (51.5) O p_z (10.3) N p_x (6.2) N p_z (7.6)	LMCT & *d-d*
^{6Me}dpaq	1	15900 (630 nm)	0.00051	125a→127a	86.1	Mn $3d_{x^2-y^2}$ (33.4) N p_x (16.4) N p_y (19.1)	Mn $3d_{z^2}$ (45.8) O p_z (8.8) N p_x (6.2) N p_z (7.0)	*d-d* & LMCT
	3	20000 (498 nm)	0.00052	126a→127a	58.5	Mn $3d_{yz}$ (2.4) N p_y (22.9) O p_y (9.4) C p_y (48.8)	Mn $3d_{z^2}$ (45.8) O p_z (8.8) N p_x (6.2) N p_z (7.0)	LMCT
				126a→128a	15.7	Mn $3d_{yz}$ (2.4) N p_y (22.9) O p_y (9.4) C p_y (48.8)	N p_y (15.3) C p_y (67.2)	ILCT
	4	21300 (469 nm)	0.00345	120a→127a	10.1	Mn $3d_{xz}$ (3.0) O p_x (12.2) C p_y (64.9)	Mn $3d_{z^2}$ (45.8) O p_z (8.8) N p_x (6.2) N p_z (7.0)	LMCT & *d-d*
				121a→127a	43.1	Mn $3d_{xz}$ (12.4) O p_x (52.3) C p_y (13.9)	Mn $3d_{z^2}$ (45.8) O p_z (8.8) N p_x (6.2) N p_z (7.0)	LMCT & *d-d*
				124a→127a	27.0	Mn $3d_{xz}$ (5.3) O p_x (53.1) C p_x (6.3) C p_z (8.5)	Mn $3d_{z^2}$ (45.8) O p_z (8.8) N p_x (6.2) N p_z (7.0)	LMCT & *d-d*

Table A3.2. Calculated energies (eV) and contributions (%) of Mn 3*d*, O 2*p* and N 2*p*-based MOs of $[Mn^{III}(OH)(dpaq)]^+$ and $[Mn^{III}(OH)(^{6Me}dpaq)]^+$.

	MO	Spin	Occ.	Energy (eV)	% Contribution		
					Mn 3*d*	N 2*p*	OH
dpaq	114	α	1	-7.3415	13.2	6.90	41
	115	α	1	-7.3322	4.5	2.20	11.8
	116	α	1	-6.9145	8.3	9.9	11.0
	117	α	1	-6.0988	40.4	36.9	0.6
	118	α	1	-5.9111	2.5	23.5	0.1
	119	α	0	-2.3101	57.3	16.7	11.6
^{6Me}dpaq	121	α	1	-7.4285	14.3	3.3	42.7
	122	α	1	-7.2994	1.2	1.4	0.6
	123	α	1	-7.1537	0.0	0.0	0.0
	124	α	1	-6.9890	5.6	6.3	10.4
	125	α	1	-6.4543	37.0	14.7	2.0
	126	α	1	-5.9682	2.9	23.5	0.2
	127	α	0	-2.3528	54.3	12.0	9.6
	128	α	0	-2.2140	2.8	16.6	0.4

Thermodynamic Parameters Calculations

The pK_a value, reduction potential, and BDFE of $[Mn^{III}(OH)(^{6Me}dpaq)](OTf)$ were determined following an approach we previously employed for Mn^{III}-hydroxo complexes.[1] This procedure is based on principles employed in the work of Solis and Hammes-Schiffer.[2] This technique relies on the use of a reference complex (similar to the complex of study), for which experimental pK_a and reduction potential values are known. We utilized the $[Mn^{III}(OH_2)(dpaq)]^{2+}$ complex as our reference, with pK_a = 6.8 and $E_{1/2}$ = 0.65 (versus Fc^+/Fc).[3] The calculated p*K*a and $E_{1/2}$ parameters were determined using the optimized structures of the $[Mn^{III}(OH)(^{6Me}dpaq)]^+$, $[Mn^{II}(OH_2)(^{6Me}dpaq)]^+$, $[Mn^{II}(OH)(^{6Me}dpaq)]$, and $[Mn^{III}(OH_2)(^{6Me}dpaq)]^{2+}$complexes. Single-point energy and analytical frequency calculations for these optimized structures provided the data for the determination of $\Delta\Delta G$ for the proton- and electron-transfer reactions between the reference compound and the compound of interest (Table A3.3). These $\Delta\Delta G$ values were then converted to

pK_a and $E_{1/2}$ values relative to the reference complex (Table A3.4). From these values, the BDFEs for the $[Mn^{II}(OH_2)(^{6Me}dpaq)]^+$ complexes was calculated using the Bordwell equation.[4]

Table A3.3. DFT-Calculated Δ*G* values (in kcal/mol) for the addition of a proton or electron used in calculating the E_{red} and p*K*a values.

Ligand	$\Delta G(Mn^{III}(OH_2)$-$Mn^{III}(OH))$	$\Delta G(Mn^{II}(OH_2)$ - $Mn^{III}(OH_2))$	$\Delta G(Mn^{II}(OH)$ - $Mn^{III}(OH))$	$\Delta G(Mn^{II}(OH_2)$ - $Mn^{II}(OH))$
dpaq	-266.7	-109.4	-79.9	-296.2
6Medpaq	-266.4	-110.7	81.9	-295.2

Table A3.4. DFT-calculated thermodynamic parameters used to determine Mn^{II}-OH_2 BDFEs for the $[Mn^{II}(OH_2)(^{6Me}dpaq)]^+$ complex.

Ligand	p*K*a(Mn^{III}–OH_2)	*E*($Mn^{III/II}$–OH_2)	p*K*a(Mn^{II}–OH_2)	*E*($Mn^{III/II}$–OH)	BDFE
dpaq	6.8	0.65	29.3	-0.69	79.1
6Medpaq	6.6	0.71	28.6	-0.60	80.2

References

1. D. B. Rice, A. Munasinghe, E. N. Grotemeyer, A. D. Burr, V. W. Day and T. A. Jackson, *Inorganic Chemistry*, 2019, **58**, 622-636.
2. B. H. Solis and S. Hammes-Schiffer, *Inorganic Chemistry*, 2014, **53**, 6427-6443.
3. M. Sankaralingam, Y.-M. Lee, D. G. Karmalkar, W. Nam and S. Fukuzumi, *Journal of the American Chemical Society*, 2018, **140**, 12695-12699.
4. F. G. Bordwell, J. Cheng, G. Z. Ji, A. V. Satish and X. Zhang, *Journal of the American Chemical Society*, 1991, **113**, 9790-9795.

Coordinates for Calculations in Chapter 2 and Appendix 1

Table A1.8. Coordinates for the DFT optimized structure of $[Mn^{III}(OH)(dpaq)]^{+}$

	x	y	z
Mn	-0.14219165609036	-0.07253586590930	0.03607249738240
O	0.33122965488788	-1.20168526217487	-3.87229617381038
O	-0.19849237073471	-0.09656943160246	1.86376611350255
H	-1.07143935588853	-0.33399235757235	2.21202830594289
N	-0.74660079068655	1.90600332187026	-0.25519170390517
N	-0.07367099098497	0.00971768662552	-1.94109656174860
N	0.49902570255718	-2.16819791227168	-0.33473525618378
N	-2.06154811810668	-1.15962145752629	-0.14399246017459
N	2.06355247844104	0.04148873600204	0.09299462741103
C	-1.06408701816670	2.78969263609687	0.67596457829911
H	-0.99261608291609	2.45143625024986	1.71116599527579
C	-1.47216841924601	4.09853048131705	0.35111831754528
H	-1.72597014373794	4.79406615163105	1.15206916882673
C	-1.54174055117505	4.47116536795690	-0.97690634644377
H	-1.85452554376855	5.47952343220576	-1.25832033430262
C	-1.20424776960893	3.54132208662100	-1.99516424640734
C	-1.24311008470694	3.83163626758326	-3.38520008618476
H	-1.54824720293904	4.82628500693898	-3.71687814518010
C	-0.89252791977610	2.84886212218416	-4.28885452579482
H	-0.91842240184035	3.06452695568419	-5.36003668391427
C	-0.49475060841919	1.55279287888408	-3.87643593790228
H	-0.22682607705947	0.80480287910606	-4.61709996040394
C	-0.44281153255795	1.22597258917500	-2.52318705495967
C	-0.80329100964632	2.24044649886853	-1.57993259489325
C	0.28020121629306	-1.09407405226742	-2.64585501388067
C	0.67223727140655	-2.30805582891548	-1.80363972798089
H	1.72591941888893	-2.52389155739413	-2.03312696054286
H	0.09713229013950	-3.16913969218246	-2.17349812585978

C	-0.57227892626038	-3.03411677520719	0.19304539760490
H	-0.48654094066340	-3.03999654152999	1.28967193297595
H	-0.46008249410669	-4.07280213364442	-0.15482043089258
C	-1.93488472520184	-2.49544924835089	-0.16775823889411
C	-3.02093342803376	-3.31935302926983	-0.46054247491006
H	-2.89041743724205	-4.40249836019944	-0.48746865872848
C	-4.26246282396130	-2.73280048625363	-0.71566194050750
H	-5.12830177209073	-3.35675660327192	-0.94754215356754
C	-4.37963123313547	-1.34161386380974	-0.67891486582871
H	-5.32960808468429	-0.84273767826421	-0.87656874705749
C	-3.24359145365833	-0.58854096352645	-0.39343982478705
H	-3.27680640627013	0.50260522246721	-0.36586519396218
C	1.76744457573486	-2.33913153612788	0.40041595537648
H	1.52620994391939	-2.40327132821974	1.47153941338759
H	2.27763772245356	-3.27232813666299	0.11417501220687
C	2.67220707288147	-1.14965947041526	0.18954981062438
C	4.06165480899833	-1.25829745796042	0.13539694588957
H	4.53374719135460	-2.23991464637611	0.20317335641537
C	4.82298941239088	-0.09668055245048	-0.00828209839859
H	5.91276250232629	-0.15502194972326	-0.05488246915240
C	4.17398668232074	1.13664155004439	-0.10080299045284
H	4.73052016322734	2.06759088355517	-0.21903931884633
C	2.78253550324586	1.15798320779004	-0.05030498303693
H	2.22523276189734	2.09380696622294	-0.13046213917051

Table A1.9. Coordinates for the DFT optimized structure of *trans*-$[Mn^{III}(OH)(PaPy_2N)]^+$

	x	**y**	**z**
Mn	0.39949841945765	6.06543090474191	6.10283305186313
O	-3.66364809601144	6.43796290542018	5.84241723148554
O	2.04795946181531	5.74695682612619	6.81029077642681

H	1.91658521911178	5.06594922728338	7.50248364208399
N	-0.87944238572019	4.95562716019559	7.46239232342622
N	-1.39480720854487	6.49380033943891	5.41172194826287
N	0.99361571859196	7.20248064207324	4.24133810585422
N	0.43447796611805	8.11220335934841	6.79436209031023
N	0.71007957434259	4.51703404006104	4.58447064195283
C	-0.50598138773406	4.12458929374992	8.47379706068590
N	0.82110746732277	3.96400201994405	8.68305850074355
C	1.21407572194740	3.15727957681448	9.64738937082262
H	2.29434658227217	3.05331910483333	9.78705445691163
C	0.32361918587335	2.44124375825472	10.48510385373100
H	0.72198684712852	1.78982986066314	11.26444977387726
C	-1.03117933942337	2.58879808631257	10.29113224320417
H	-1.75861457589985	2.05832484965172	10.90961256440318
C	-1.48898859599279	3.45061885666985	9.26070988037600
C	-2.85663255225602	3.67609439971142	8.96665422520740
H	-3.62286053043328	3.16960413985797	9.55792849322168
C	-3.19690626404529	4.52879890047792	7.93880936755301
H	-4.23252528939125	4.73890653187351	7.67301754210641
C	-2.16942363192401	5.15061310506019	7.20124475941915
C	-2.49114213498250	6.10321030128738	6.06573059533856
C	-1.48341076079974	7.50173374639583	4.36843103269241
H	-1.53901516169687	8.50979700779756	4.81646846383165
H	-2.39750696248745	7.37209751114218	3.76871917081402
C	-0.26512695641408	7.36807549333511	3.46235883159224
H	-0.38994689997060	6.46660468395290	2.85019355730618
H	-0.17949225708782	8.22871295844646	2.77942989449629
C	1.58590983560979	8.47248551794190	4.68233197791507
H	1.56183010014875	9.23164413244749	3.88382113588498

H	2.64421983112743	8.28782154752027	4.92073717730817
C	0.92942169795742	9.01153279698180	5.93263151392042
C	0.89278964615019	10.37796009971025	6.21900982270882
H	1.29127525525127	11.09311947396914	5.49735170358212
C	0.34141553631973	10.80180202260600	7.42778407442609
H	0.30089562463977	11.86573342151322	7.67173560178496
C	-0.16389247849800	9.84915789043447	8.31718055278129
H	-0.60645868084657	10.13665014236279	9.27195200362872
C	-0.10071383019924	8.50789967086714	7.95446328778205
H	-0.49189215521162	7.72474905003155	8.60693756502222
C	1.95198906583172	6.32963646413449	3.54665308271879
H	2.90437574368422	6.36653519912220	4.09630598021164
H	2.14770470419060	6.66885537998265	2.51598324824918
C	1.46039837748669	4.90066396736638	3.54001694805770
C	1.78169238386966	4.00853973136700	2.51607199709679
H	2.38322732348609	4.34765720747980	1.67079790582610
C	1.31829094868216	2.69445585850742	2.59212224641839
H	1.55827490012733	1.97907943453623	1.80247071278118
C	0.53581317979536	2.31246085964842	3.68432018016102
H	0.14406452082963	1.29878215807697	3.78071717959358
C	0.25266011219642	3.26399589907609	4.66002253195484
H	-0.36204081579487	3.01778648339527	5.52717912018571

Table A1.10. Coordinates for the DFT optimized structure of $[Mn^{III}(OH)(PaPy_2Q)]^+$

	x	**y**	**z**
Mn	0.41205321683494	6.05743002075925	6.06638022953848
O	-3.62807384628258	6.53464695329451	5.90508333956709
O	2.13399398483123	5.75658395270687	6.65162021083690
H	2.45978065742164	6.45621697780065	7.23708736231620

N	-0.87645327132917	4.92935616597811	7.46505913114188
N	-1.37783866424592	6.49613565929047	5.40951083482831
N	0.97152933573933	7.19735831299552	4.19632591219330
N	0.48032858853614	8.06457352851926	6.79413104915657
N	0.73988778994741	4.50599616278276	4.59103813510971
C	-0.52802116923313	4.05574028126980	8.46038132862151
C	0.83761437618357	3.75924380803411	8.70432167078687
H	1.59318381372646	4.25035598474198	8.08903902600720
C	1.18035967775682	2.86849653831262	9.70134123081082
H	2.23398615381285	2.64284833018968	9.88300246806112
C	0.18657193915984	2.24013553790557	10.49435647847323
H	0.48361816417361	1.53951439165665	11.27820232289391
C	-1.14753941567283	2.51054066480619	10.27520795985358
H	-1.92409966037992	2.03173350932050	10.87636511362774
C	-1.53832053743275	3.41945417415796	9.25532856117208
C	-2.89545263920580	3.72316534510903	8.98239120125067
H	-3.68045577187544	3.25051312286513	9.57752418343753
C	-3.20693898384634	4.60309021762867	7.97030921814488
H	-4.23410532805623	4.86707400512581	7.72015049988021
C	-2.15936874728870	5.18295441609057	7.22627562589068
C	-2.46791642171819	6.14783525843288	6.10363966977201
C	-1.48629376404036	7.50725939871172	4.36871267549424
H	-1.52310599364783	8.51626259649961	4.81680059725978
H	-2.41829688439754	7.38276520080669	3.79673549358255
C	-0.29452981743685	7.36121922372801	3.43487423364522
H	-0.43438426944459	6.45355165392228	2.83485730680407
H	-0.21862542823471	8.21520408344978	2.74241098469531
C	1.55990779035810	8.46604405133702	4.64615241077823
H	1.50871973879709	9.23864647408346	3.86234099803694

H	2.62497404754636	8.28951594805169	4.85832974979133
C	0.92476334801345	8.98048372765628	5.91888041812680
C	0.85322866334857	10.34317964800580	6.21280950668872
H	1.20941741692964	11.07239938169278	5.48337722753814
C	0.32061380811295	10.74662728007278	7.43709043639330
H	0.25327489484586	11.80828165646578	7.68469325450882
C	-0.13287839204398	9.77790214262633	8.33690342328225
H	-0.56010309321442	10.04984851531910	9.30301253183968
C	-0.03864170035345	8.44030520641069	7.97007989715758
H	-0.38919364829629	7.64288980321454	8.62812513220917
C	1.92305956899119	6.32649424354881	3.49117297719835
H	2.88795671024612	6.38339723454479	4.01547551304263
H	2.08522370369626	6.65110463747580	2.45030435758763
C	1.45292160129722	4.88962771086335	3.51987206618446
C	1.76288224245669	3.98605641209003	2.50280715258079
H	2.33313151854583	4.32222367262805	1.63504796595402
C	1.33022022710556	2.66391690872676	2.61485734692215
H	1.56239004976214	1.94051180577785	1.83021136936065
C	0.59034005389195	2.28267658951526	3.73673110449352
H	0.22643585983564	1.26190354331928	3.86240770292571
C	0.31427866216356	3.24399108252048	4.70431598154167
H	-0.26472015639101	3.00095584716011	5.59661042100322

Table A1.11. Coordinates for the DFT optimized structure of $[Mn^{III}(OH_2)(dpaq)]^{2+}$

	x	**y**	**z**
Mn	0.00359682636831	0.03169564455405	-0.05413822792886
N	2.01378671781676	-0.01216824606624	-0.33034272440799
N	0.00326390754511	0.05306919915105	-1.97001938816066
N	-0.51292410652266	-2.14915334158977	0.05372721362052
N	-2.12569977724857	0.08271757381175	-0.27026592470785

N	-0.41398687748138	2.22758762964648	0.11499604670438
C	-2.21773906552642	3.78155540393570	-0.06293973089373
H	-3.29302885687186	3.96663119464049	-0.06000002736328
O	-1.32833861927580	0.10602754051657	-3.85057558340438
O	-0.01916626921470	0.00633444039478	1.98002588058148
H	0.18696601872839	0.78867091263130	2.52690068547934
H	0.15265798624032	-0.79765694113086	2.50708547841543
C	1.26599198110166	0.02622921075183	-2.58848898187796
C	2.34440912619394	-0.00899489484752	-1.66186647878459
C	-1.73205803602677	2.49064100972883	0.12727123443701
C	-1.84187051884747	-2.35121181563653	0.05179278535693
C	-1.19239059481445	0.08991240849541	-2.63569716342322
C	-2.41850550562201	0.11214067594499	-1.73584211720748
H	-2.99615686768522	1.01360059421766	-1.98131795528949
H	-3.04885836963853	-0.74561343553894	-2.00671732469090
C	2.96217625925154	-0.04203343721083	0.59743322077953
H	2.64360126485497	-0.04223186230736	1.64038011971032
C	4.69343878881414	-0.07025760909994	-1.07478381810005
H	5.74729707724053	-0.09276667778124	-1.36145434792615
C	3.69925706717982	-0.03834010663642	-2.08581555795345
C	0.06445790205558	4.53442164268298	-0.25966933379828
H	0.81017973302175	5.31620671541446	-0.41068399043877
C	3.96740492025160	-0.03370485833663	-3.48105179928223
H	5.00320969889976	-0.05649198343877	-3.82514627246700
C	-2.62034838389027	1.30945336284603	0.41612414177699
H	-2.60229640209279	1.11425114730799	1.49771965745462
H	-3.66291772787984	1.51019005526790	0.13323799609905
C	0.46799294860275	3.21402905741641	-0.07713898492678
H	1.52393848594409	2.93592486235134	-0.08646646894961

C	-2.38585584748528	-3.61072401286434	-0.18497284518647
H	-3.46854898743485	-3.74550210561715	-0.19265462145728
C	1.56335832803019	0.03025797519257	-3.94570014155265
H	0.76172573587060	0.05713067955502	-4.67823608998002
C	-1.51856313135489	-4.68331303546635	-0.40996062957587
H	-1.91830641739052	-5.68178066673899	-0.59959149976488
C	4.32625975577543	-0.07165083929877	0.25809900779742
H	5.07013713705636	-0.09564406981862	1.05498110109033
C	0.32327500902856	-3.16839272452124	-0.16903641028250
H	1.39099706783864	-2.93945350674582	-0.16531147488013
C	2.91519772714899	-0.00005416204145	-4.37350934353909
H	3.11528466750373	0.00400334701049	-5.44743058346705
C	-0.14007475473348	-4.46170547462174	-0.39845063931315
H	0.56937526454545	-5.27163229384923	-0.57380818428601
C	-2.67612708707600	-1.14089890271055	0.37785333325396
H	-3.72628155106035	-1.28526948214790	0.08896141903586
H	-2.65037718105818	-0.98098660865711	1.46507325998295
C	-1.30231165282244	4.81979736521955	-0.25583779645267
H	-1.65590181385425	5.84175944603467	-0.40838911985564

Table A1.12. Coordinates for the DFT optimized structure of *trans*-$[Mn^{III}(OH_2)(PaPy_2N)]^{2+}$

	x	**y**	**z**
Mn	0.29102241687487	6.11053641830512	6.06477742203396
O	-3.69794825326999	6.44305160229246	5.77978999996512
O	2.00753652846776	5.61312664194430	6.94520555407638
H	1.68722670315815	4.92309441098183	7.67925753874012
N	-0.92173180716064	4.99230293604457	7.40848375050568
N	-1.43031048274608	6.54555607253294	5.40187831559171
N	0.95646453146100	7.20103852062424	4.22481662227769
N	0.49096054831040	8.12614783788805	6.79250134932609

N	0.70187370996375	4.51255942880838	4.61409786140471
C	-0.51459094150349	4.15357136734831	8.39496558379683
N	0.82085266793419	4.01795520954627	8.57858610918875
C	1.26230587522173	3.20068857527081	9.51593229847707
H	2.34653411227658	3.12728407188779	9.62774103990855
C	0.40109699935295	2.44827973454965	10.34718360378178
H	0.82854541620403	1.78910065917461	11.10348753702418
C	-0.96132683753837	2.56789830731755	10.18233057123942
H	-1.66154706697301	2.00570163830664	10.80357995646335
C	-1.46372230027479	3.44058784305448	9.18159528177965
C	-2.84007586749530	3.64230575910677	8.91227540385055
H	-3.58545879649259	3.10600490379608	9.50308500914530
C	-3.21950957720489	4.50821841173775	7.90545919153774
H	-4.26530398521177	4.69417175647849	7.66185045707866
C	-2.21967749711651	5.16396989117420	7.16781265581587
C	-2.54262939349201	6.12040949050034	6.04317653970009
C	-1.50270180902683	7.55308978573979	4.34786590742976
H	-1.52326305383876	8.56223579949033	4.79246913329451
H	-2.43038939805677	7.43142321963984	3.77069637645418
C	-0.30176019930549	7.36496936448338	3.43529683827308
H	-0.44600037979399	6.44570266260152	2.85532061080272
H	-0.19779768301142	8.20255364797837	2.72921218485680
C	1.55755116177789	8.48402354949150	4.63548248502293
H	1.48820234643482	9.23248922659755	3.83171928743881
H	2.62823739338884	8.31430336032462	4.82466702614036
C	0.95095226107141	9.02552383530273	5.90809213386134
C	0.92700575043092	10.39014909410591	6.19603858792270
H	1.29694373329305	11.10470187305680	5.45922067818682
C	0.42439258755619	10.81312348337949	7.42634248422431

H	0.39408187374614	11.87706531756411	7.67090136289185
C	-0.04662353326116	9.86267802103996	8.33693500643457
H	-0.45097178548665	10.15183850232309	9.30772082561319
C	-0.00148061458009	8.52212218496521	7.97545962955290
H	-0.36972700446721	7.74100233316333	8.64314577558701
C	1.91503725123334	6.31968237210170	3.53084182466916
H	2.87955414862266	6.38095415241954	4.05729258084350
H	2.08625932624249	6.64794293050492	2.49366877720080
C	1.44127046098008	4.88567680772684	3.55666003371034
C	1.77702962951271	3.97564398515864	2.55498736262341
H	2.37029797975211	4.30507823945553	1.70042069109267
C	1.33962176519212	2.65510451290101	2.66632385544673
H	1.59109157301956	1.92548917425595	1.89368898821393
C	0.56938022474831	2.28344041059621	3.77076312966442
H	0.19954503685753	1.26470393604423	3.89424221241668
C	0.26962372953948	3.25107648361181	4.72368215929974
H	-0.33657218340633	3.01172293157189	5.59803413927126
H	2.47861970808909	6.33459031373242	7.40219525885014

Table A1.13. Coordinates for the DFT optimized structure of $[Mn^{III}(OH_2)(PaPy_2Q)]^{2+}$

	x	**y**	**z**
Mn	0.28978902983860	6.05004110320411	6.02241306305484
O	-3.66135045249112	6.55936669133842	5.86658282008626
O	2.21518068090563	5.80898998014648	6.63454716377619
H	2.70435544599657	6.48009453397625	7.14490101789105
N	-0.92653730606573	4.94280240977203	7.42500326264343
N	-1.42087188890337	6.50759118388695	5.38536735564747
N	0.93028780608586	7.16538616786168	4.20976332050751

N	0.48641597444783	8.03308705375725	6.82130143164189
N	0.76010333600695	4.46553857014171	4.60532081294884
C	-0.56689940404736	4.07317225945309	8.42293540161737
C	0.79397483098104	3.76328925450547	8.66418570015645
H	1.56776460622751	4.22751263327912	8.05984076717287
C	1.13828740421189	2.87749168196142	9.66461189980463
H	2.19198532687770	2.64779038833669	9.83749291360778
C	0.14659434956581	2.26311472057581	10.46908119996114
H	0.44364839743287	1.56584913423388	11.25540379703641
C	-1.18529337748851	2.54506045111571	10.25649591398431
H	-1.96311495825501	2.07895285620462	10.86529265087981
C	-1.57560752155034	3.45048410740874	9.23354523966807
C	-2.93305303868399	3.75905248870149	8.97875491408524
H	-3.71162662651388	3.29405587890876	9.58747662371326
C	-3.25566759716613	4.63567140544987	7.96584019092905
H	-4.28479339324081	4.90450890788692	7.72937180075235
C	-2.21624866875101	5.20035080259604	7.20903351095874
C	-2.52306928288717	6.15813387596210	6.09190821852031
C	-1.50571666029506	7.53910794391472	4.35384330362332
H	-1.51361910277964	8.54016116520835	4.81644828308114
H	-2.44575782969335	7.43092180669822	3.79468575656274
C	-0.32453485036405	7.35339934378687	3.42398132846826
H	-0.48158286779520	6.44107194546502	2.83613251255522
H	-0.21380740664206	8.19824516406609	2.72780501542183
C	1.53458707915969	8.43642688927428	4.65941897504872
H	1.46959590469531	9.20438198961355	3.87446085726357
H	2.60383611924558	8.25682146691102	4.84573186937545
C	0.92709739308032	8.95071988190094	5.94422971138752
C	0.88347981834783	10.31055064776925	6.24967925402992

H	1.23692962553169	11.04059344992069	5.52008778738598
C	0.38103596975154	10.70972343287645	7.48849762932371
H	0.33463862160199	11.76999392721923	7.74602980572842
C	-0.07011608786386	9.74121284943052	8.38971759350876
H	-0.47387465011780	10.01210819471576	9.36596136223939
C	-0.00630873608213	8.40576554435188	8.01146163885258
H	-0.35899236762455	7.60962256104185	8.66967889065827
C	1.88333486078709	6.30581147086124	3.47979548758881
H	2.86577939058985	6.38470614562868	3.96787329878441
H	2.01178899296077	6.64384589201490	2.44019973433868
C	1.43662091040331	4.86242471584130	3.51273648751703
C	1.74092716348546	3.96606003035176	2.49017767662828
H	2.28287801110471	4.31281464249904	1.60894780211232
C	1.33932707903657	2.63509094670665	2.61627505336523
H	1.56739934942345	1.91558814863845	1.82710856666795
C	0.63683644088610	2.23854335166744	3.75684420091856
H	0.29953970382827	1.21015245825345	3.89229229628178
C	0.36275874435720	3.19248006360708	4.73050547599675
H	-0.18977382737812	2.93636365477578	5.63558327058280
H	2.85466053582516	5.17028773431768	6.26537508364973

Table A1.14. Coordinates for the DFT optimized structure of [Mn^{II}(OH)(dpaq)]

	x	**y**	**z**
Mn	-0.06184013783564	-0.10005685093054	-0.31440124123193
O	0.01034038279805	-0.13715694856685	-2.30384496110999
H	0.00758904659900	0.74769680153444	-2.68861179705784
O	0.94619329651927	0.58932717142174	3.85403725256904
N	-2.25865182341704	0.04127559283403	0.10459441046680
N	-0.26393613096456	0.16695237173168	1.90258739018641
N	2.16375560842986	-0.04486495666073	0.47604781204049

N	0.52380518987930	2.23161635865984	-0.09974058673883
N	0.62412194814581	-2.29165664918173	-0.05408741378106
C	-3.18538145600149	-0.04302174268681	-0.83063512763348
C	-4.55711387252393	0.15244727960966	-0.56073414448172
C	-4.93905908374469	0.45105990996881	0.73038046750780
C	-3.96161779844187	0.55389557574135	1.75659388977540
C	-4.28403228215768	0.86762242169676	3.10382635642480
C	-3.26683715928022	0.95333476776796	4.03385764846814
C	-1.91396191645737	0.73532199099347	3.68570143192127
C	-1.53534313396595	0.41712683160483	2.37461590051218
C	-2.59691217595096	0.33098872527218	1.39148260285181
C	0.84113033958549	0.27172785667865	2.65284895081496
C	1.68722803773548	-4.81418288923085	0.40189543104429
C	0.30547946765923	-4.63657212106009	0.30647879975860
C	2.14498339057965	-0.13763239370618	1.94563585479118
C	2.72198189731639	1.22784700395936	0.00129266761449
C	1.79593767611421	2.38427782719339	0.30118295074199
C	2.22666474963426	3.54748757007970	0.94236355321024
C	1.30832497929225	4.57880652894980	1.16015436045746
C	-0.01021338739038	4.41131649578260	0.73501787845090
C	-0.35529579016068	3.21090293867113	0.11040455579200
C	2.79428597490559	-1.20757565556475	-0.16013516261637
C	1.95436614540839	-2.45040357096093	0.03273761018148
C	2.52393805508997	-3.70409412950297	0.26821918020647
C	-0.17983297917215	-3.34868202795705	0.08128495816632
H	-2.83052639743499	-0.26838678599258	-1.84014984651058
H	-5.28725532338849	0.06800158026254	-1.36778288313082
H	-5.99103255199845	0.61252121343810	0.98061208984999
H	-5.32739388888862	1.03683012970849	3.38061130187443

H	-3.50427456386267	1.19687528315595	5.07356386450139
H	-1.13698840092979	0.81332350669511	4.44168201267693
H	2.10997335831105	-5.80447748006546	0.58729049245970
H	-0.38646187488674	-5.47408301294852	0.41197904219405
H	2.31606724754356	-1.18592220475006	2.23481174578532
H	2.96990645044587	0.44454295113482	2.38886028428731
H	2.83348323578831	1.15542789003576	-1.09114470877043
H	3.72164107383206	1.42111731434525	0.42991308288329
H	3.26446316302394	3.63970012147337	1.26855278139949
H	1.61981212642801	5.49811852164960	1.66166781307279
H	-0.76217835006362	5.18780035588738	0.88768000490201
H	-1.37870491002913	3.02766697809428	-0.22891091484346
H	2.85990448829195	-1.00149285830104	-1.23994431975355
H	3.82139704630974	-1.38478143929649	0.20600015622951
H	3.60816022839590	-3.80312459027525	0.34972284459497
H	-1.25367421511547	-3.15483555839316	0.00959167699437

Table A1.15. Coordinates for the DFT optimized structure of *trans*-[Mn^{II}(OH)($PaPy_2N$)]

	x	**y**	**z**
Mn	0.36510426236386	6.00185087179449	6.13901060271678
O	-3.65862631945285	6.52847208253222	5.87101133278526
O	2.03074877870271	5.65694927320508	6.81965744399549
H	1.86671626997963	4.99375213180622	7.53129237946610
N	-0.84619986766186	4.97361979173102	7.47425194543411
N	-1.39441729575236	6.47928264838551	5.42250341476758
N	1.02491973094310	7.14536663946891	4.32475920649517
N	0.41772614555302	8.12387493222232	6.84808340487774
N	0.68731213845006	4.45037994115882	4.51851597911672
C	-0.46620606830373	4.13775849228234	8.48001200928520
N	0.85186843763733	3.93995559881428	8.67300110168945

C	1.26150701710551	3.11080171826634	9.65147798729929
H	2.34501369783647	2.99493237048737	9.75593377603979
C	0.38916919609256	2.43074850162266	10.49165799568827
H	0.77506860155282	1.76792434948765	11.26913113643774
C	-0.99069426344541	2.61970177642968	10.31468008327197
H	-1.71418144512329	2.10480719617724	10.95259510542468
C	-1.45616324456160	3.48082533226507	9.30458176011722
C	-2.83683987617419	3.74478900846491	9.04237774093024
H	-3.60061656360427	3.26129580542460	9.65598614982915
C	-3.18169467278154	4.61088358878781	8.00794485586868
H	-4.22334423275145	4.84051206007550	7.77625183280994
C	-2.19065814079627	5.20658309841504	7.23483308109422
C	-2.49901830211087	6.13365126458112	6.11427252663956
C	-1.45040667650030	7.50424315459266	4.40035942241080
H	-1.50230568896155	8.51208809764251	4.85317338183702
H	-2.35051272768171	7.39934041373368	3.77308789049851
C	-0.21364465809129	7.36339818817366	3.51979444587109
H	-0.34494342683351	6.47870436453949	2.88508634115970
H	-0.08453643337711	8.23544619586437	2.85782837247611
C	1.64783477618588	8.39825846896125	4.78251117803583
H	1.71972197043218	9.13517951259313	3.96591677674343
H	2.67415038369416	8.16167448377470	5.10109926855820
C	0.92935485493997	8.99484140741589	5.96996943947993
C	0.84439554321891	10.37298479968806	6.18129795684396
H	1.25937293527965	11.06387720006700	5.44517347578718
C	0.21792579631268	10.83929769521998	7.33798638500075
H	0.13518843894075	11.91234634886762	7.52550819945553
C	-0.30901815928622	9.91657139253256	8.24597786910561
H	-0.81055660462232	10.23882792321960	9.15998689331897

C	-0.18937247263472	8.55981218254504	7.95409309956888
H	-0.59502500561453	7.79451240621401	8.62019210951520
C	1.98319406390742	6.28469850997417	3.60992266765480
H	2.91958605397370	6.27482565279680	4.18745846302573
H	2.21312088425682	6.67744531740404	2.60534467193275
C	1.46814626323407	4.86707465084073	3.51370565577551
C	1.80128668648301	4.02046820593420	2.45398768613887
H	2.42903282685532	4.38659206885672	1.63927175074691
C	1.31411885103501	2.71222372345528	2.45824300571845
H	1.56108862079160	2.02965919805502	1.64188703538622
C	0.49979440907029	2.29304822350833	3.51330796824685
H	0.09163652153573	1.28166352460886	3.55176283900551
C	0.20812054520186	3.20547617795274	4.52552325639977
H	-0.43129155544313	2.93540703708167	5.36892064222156

Table A1.16. Coordinates for the DFT optimized structure of [Mn^{II}(OH)($PaPy_2Q$)]

	x	**y**	**z**
Mn	0.65239774344183	5.93512377378912	6.24664852663612
O	-3.56601674354863	6.68502070465683	6.19583025059718
O	2.44779943027155	5.58006214785517	7.04618969884431
H	2.73953060497831	6.29241924532845	7.62844163143776
N	-0.89027336149581	4.83591057581479	7.64370057874039
N	-1.33438071234802	6.49795620678119	5.58886503529661
N	1.04211822452678	7.19084719592912	4.23323471939772
N	0.71371835677763	8.26535623455164	6.85302289388607
N	0.96081714122711	4.41757610452180	4.53839942335376
C	-0.61368701003653	3.90939977571089	8.60732931972971
C	0.74078005179736	3.57025988333055	8.87532692770948
H	1.52225480400050	4.09541851517859	8.31098146827523

C	1.03113720362251	2.62311924469946	9.83721516610835
H	2.07247740911710	2.36198382763150	10.04391494524338
C	-0.00364034389132	1.98235411086136	10.56755197841343
H	0.25188908445352	1.23528607277154	11.32328290231303
C	-1.32481823396110	2.30193030471677	10.32900100956416
H	-2.12848762111901	1.81691486904889	10.88922466173464
C	-1.66226699659259	3.27164740104942	9.34624885880720
C	-2.99826696083997	3.65187186340916	9.05223149981483
H	-3.82138561022494	3.18570656447941	9.60038117179351
C	-3.23812404374788	4.60040131510187	8.08474705062267
H	-4.24541749561125	4.92891506713847	7.82979387219168
C	-2.14462022545548	5.17211650005746	7.38480896383956
C	-2.40583498723226	6.21547341235739	6.30356510877202
C	-1.43377640254586	7.50896174342801	4.56258743173966
H	-1.43459327431280	8.52213361613359	5.00623494712094
H	-2.37918112959169	7.43206261381661	3.99558604799216
C	-0.27418392829207	7.34770231987809	3.57676377456913
H	-0.45674666612952	6.43338472957425	2.99623273536785
H	-0.25042281824580	8.19096458012494	2.86142984856827
C	1.65793455452601	8.46202385396468	4.62543558395608
H	1.67734309479785	9.18519540599901	3.78960235631885
H	2.70314474336817	8.25197408464228	4.89971912430548
C	0.98864329227143	9.08722952839863	5.82974784026733
C	0.69629191616468	10.45333620328016	5.89061788514372
H	0.92306818270437	11.09779741759196	5.03907744522390
C	0.10179389851410	10.96791534056057	7.04437507085223
H	-0.14133698626560	12.03086902359681	7.11405025869219
C	-0.18777810135407	10.10078873612474	8.10061832312302
H	-0.65902744892537	10.45715986207401	9.01847533147217

C	0.13721234070382	8.75219693420554	7.95355979918782
H	-0.07929778560950	8.03183664196134	8.74801032612724
C	1.95066941390126	6.35421284607910	3.44351685266278
H	2.94065535244867	6.38845659373639	3.92469345123947
H	2.07582777246914	6.72658675178009	2.41015595063500
C	1.49798757451206	4.91016420522809	3.41187503688841
C	1.65758857729965	4.11289714556649	2.27492533079307
H	2.08401310303103	4.54085624709265	1.36557839647826
C	1.26008106558202	2.77537017143118	2.32234509105519
H	1.37690812790210	2.13379269551619	1.44571452003354
C	0.70417665615671	2.27513310237162	3.50188129475220
H	0.37377013806230	1.23808698761687	3.58329942170641
C	0.57046468793243	3.14169303489614	4.58577502644307
H	0.13236434081509	2.80237766655898	5.52825083416154

Table A1.17. Coordinates for the DFT optimized structure of $[Mn^{II}(OH_2)(dpaq)]^+$

	x	**y**	**z**
Mn	-0.01870712377586	-0.06779311127309	-0.05381023578198
O	-0.08435601225045	-0.05539162110846	-2.32653669693055
H	0.22882164711714	0.75292828233864	-2.76956733615101
H	0.31217511458491	-0.79583426116426	-2.81487144314608
O	0.97605144851502	0.51080310974552	4.03079630628412
N	-2.19379038493572	0.08864782142177	0.22741608871708
N	-0.22806094385100	0.15646003325818	2.06702318450057
N	2.19890845129446	-0.05079714130942	0.63128953615758
N	0.53796335170307	2.11632731670337	-0.15967705839275
N	0.61816923634166	-2.19402949731091	-0.18512459023384
C	-3.11351545928105	0.02898769729715	-0.71998791059427
C	-4.48737712095129	0.20985035199827	-0.45908471552147

C	-4.88575566261765	0.46387126375680	0.83642944412010
C	-3.92168055892850	0.53596016940774	1.87668804312927
C	-4.26434943631761	0.80013525117566	3.22949696542454
C	-3.26375482378817	0.85835303377963	4.17833608738394
C	-1.90475558009311	0.65874554396840	3.84181747489916
C	-1.51144774212826	0.38949365130263	2.52744633893361
C	-2.55189757873714	0.33298276402244	1.52406237145468
C	0.87822650549974	0.22783572650867	2.82540711995638
C	1.52437177991425	-4.78391385634734	0.21359113454388
C	0.16849435860291	-4.53761408709118	-0.01074382454448
C	2.17382373881213	-0.18351386588644	2.10477486464079
C	2.76891139080576	1.23310613756562	0.18915290574629
C	1.77690149333400	2.36744920457707	0.30091829371259
C	2.12508961580222	3.62066607428118	0.80405326119548
C	1.16616319943288	4.63708057494254	0.81476126281034
C	-0.11238260923780	4.36853366951771	0.32387285332824
C	-0.38275576001617	3.08565934363678	-0.14904961754560
C	2.83320179092775	-1.20951566373552	-0.02000658639121
C	1.92822391826741	-2.41956486816530	0.02416665156234
C	2.41619430821133	-3.70941191838360	0.23470383140035
C	-0.24081486817487	-3.22015799755193	-0.20099716975290
H	-2.75889041089042	-0.16532561068994	-1.73513836570066
H	-5.20602897584789	0.14857955157006	-1.27785813289185
H	-5.94117358964167	0.61202422760201	1.07912503798622
H	-5.31275518297125	0.95313665049554	3.49540669413539
H	-3.51787445989066	1.06253521706549	5.22213874935344
H	-1.13893631754007	0.71106999490928	4.61152602935133
H	1.88481329427599	-5.80192979586441	0.37794799705978
H	-0.56387996727018	-5.34616924757831	-0.03086739319479

H	2.32211954144885	-1.24383120359968	2.36059472715067
H	3.01122242486503	0.36972222766533	2.55849292077848
H	3.03723459825684	1.13347418437053	-0.87359403507218
H	3.69336060217226	1.47852751246547	0.73746969049259
H	3.13344473367494	3.79298181101586	1.18434218385637
H	1.41518301246985	5.62522755706638	1.20803960518462
H	-0.89306155896640	5.13089783386452	0.31345172602098
H	-1.37340108547007	2.82216657925409	-0.52666034001021
H	3.00711796645508	-0.95166994925711	-1.07618953394373
H	3.81563055969704	-1.45057118799127	0.41903854158850
H	3.48120560634929	-3.86409849508229	0.41632644909443
H	-1.29247447525852	-2.97405798915988	-0.36679038615455

Table A1.18. Coordinates for the DFT optimized structure of *trans*-$[Mn^{II}(OH_2)(PaPy_2N)]^+$

	x	**y**	**z**
Mn	0.08694164964558	5.94903214478161	5.95471296619030
O	-4.15103298344493	5.92767072566000	5.70677179070251
O	1.82809063586357	5.24245802241053	7.19247820299777
H	1.37706306244350	4.73582554538889	7.94480941966193
N	-1.31215835347078	4.85502155663282	7.57625717246138
N	-1.89191924600892	6.09662517327133	5.24411456802396
N	0.28809510182140	7.32652899275485	4.03724459792493
N	0.71966854738184	7.95956680586422	6.72005660013229
N	1.15902797461625	4.74067885185687	4.37921733789759
C	-0.99190396274532	4.19418509925560	8.72080363033293
N	0.32503630084614	4.10772992479637	9.03946077458794
C	0.68905910496495	3.48700050932876	10.14388465598281
H	1.76245557029641	3.44941846224546	10.35066595468291
C	-0.22740324053470	2.88886042667526	11.03824316143711
H	0.14044665526695	2.39124387914640	11.93659946729358

C	-1.57141199645218	2.95207017142333	10.74263280686638
H	-2.32057421298671	2.50298207767914	11.39886726620756
C	-1.99092534577559	3.61529207674127	9.56159923426246
C	-3.34590280945689	3.74114629562305	9.16541416244918
H	-4.13136876196828	3.30537110546307	9.78731299373179
C	-3.64183183750828	4.41421694065407	8.00403665434967
H	-4.66383532742351	4.54735557895882	7.65186998477792
C	-2.58961424165110	4.96306339463937	7.22911913803985
C	-2.94340580646273	5.72342815663785	5.95722780467694
C	-2.14955532113626	6.86999814624787	4.04250536939949
H	-2.51950085667597	7.87909476609605	4.30608034929873
H	-2.94439895093874	6.41429869239979	3.42698891819471
C	-0.87687081216629	6.96025073922307	3.20563294013131
H	-0.67183098072181	5.97366486031839	2.76944478320355
H	-1.00662164555733	7.67069091478851	2.36935766216859
C	0.27029963059212	8.73151541326170	4.45078566330949
H	-0.77774870269776	9.06093309682235	4.50218846673068
H	0.76701398035938	9.38520989126518	3.71349106049642
C	0.86327872566281	8.94901505476443	5.82341882080525
C	1.46679203266777	10.16150499028201	6.16935791623415
H	1.58828336285479	10.94034689767937	5.41425611598604
C	1.90164477050020	10.35459802952498	7.48003952249253
H	2.37468077012988	11.29487627016659	7.77239076769094
C	1.72605708208666	9.32665192887060	8.41019184277775
H	2.04729303237259	9.43282540762341	9.44755486901292
C	1.13817571847068	8.14155754154854	7.98032457521203
H	1.00066498436758	7.30297609571490	8.66508620383579
C	1.56358197348365	6.94093159823773	3.42705228907296
H	2.37729495742386	7.35329464412043	4.04642517214361

H	1.68485725061453	7.36609573011841	2.41469981933175
C	1.71506621754105	5.43758082965679	3.37470206893276
C	2.41060717466927	4.79801259270794	2.34635384491434
H	2.84405533388701	5.38700902844053	1.53611959900837
C	2.53170027578550	3.40811812107712	2.37135276942163
H	3.07014308776597	2.88727964372770	1.57631071811454
C	1.94502577313540	2.69379023387169	3.41886946269475
H	2.00615545646896	1.60570608978485	3.47406335991041
C	1.26485976792511	3.40618326663026	4.40240960742232
H	0.78631667380539	2.89304242633703	5.24033395662346
H	2.44807976006734	4.62982914080281	6.76806613975703

Table A1.19. Coordinates for the DFT optimized structure of $[Mn^{II}(OH_2)(PaPy_2Q)]^+$

	x	**y**	**z**
Mn	0.41769477387614	5.92243721043423	6.07538814744143
O	-3.68408236304395	6.78454239340848	6.14120786737266
O	2.57566285096043	5.67748382184866	6.85395176443538
H	3.02593749600359	6.48406725118556	7.15971779776865
N	-0.98408138320828	4.93134588492240	7.54528832826505
N	-1.50224470315658	6.48429262271382	5.42047763174532
N	0.90454001387883	7.17449546463412	4.14650674662092
N	0.68135012820742	8.02052691441250	6.84658312322380
N	1.03957509713218	4.41348595929377	4.56633373209098
C	-0.68439524474907	4.04093870822078	8.53873151142557
C	0.66700301787460	3.67379766763637	8.77029326526444
H	1.45146316452146	4.12403643308834	8.16080255036677
C	0.97930245010686	2.76603742654896	9.76207190478710
H	2.02219133457865	2.48777519207569	9.93169186658163
C	-0.03749669757442	2.19050494612146	10.56585915122642

H	0.23159825839636	1.47406228613206	11.34553863924786
C	-1.35823899729396	2.53428284437960	10.36470541364190
H	-2.15040970583925	2.09835289133713	10.97838982477606
C	-1.71336880240224	3.46425014092157	9.35071675363170
C	-3.05239044277508	3.85713693811508	9.09589279157600
H	-3.85903973776009	3.43503270939988	9.70055329059984
C	-3.31719759599176	4.76088011943061	8.09271420916253
H	-4.32839112484577	5.09595436071590	7.86396404944256
C	-2.24851639513757	5.27626286155103	7.32163339235502
C	-2.54416002608892	6.27563454279878	6.20663860093216
C	-1.57587655204184	7.48007771649365	4.37579788940573
H	-1.56912725144597	8.50129125253264	4.80202733101249
H	-2.50818981664998	7.40243748782656	3.78924095095299
C	-0.39206667250894	7.27799323375111	3.43210887815683
H	-0.54366626982695	6.32863761851443	2.90058602621286
H	-0.34592407665028	8.08166054236072	2.67599204375213
C	1.43801529821435	8.47576241059862	4.57255103047783
H	1.28326396430715	9.25087077721298	3.80294689643271
H	2.52567913928573	8.36904869070481	4.70304986624061
C	0.87603460440159	8.95000266928465	5.89544630661415
C	0.62843393545597	10.30251968446537	6.14269923384104
H	0.78443672880404	11.03584797878353	5.34946104906635
C	0.17888964276309	10.69197731103839	7.40480215818376
H	-0.02369332219981	11.74409303072867	7.61762430478746
C	-0.01553842220748	9.71699248022341	8.38651766618846
H	-0.36884016393614	9.97479963933148	9.38615401180107
C	0.24484241782936	8.38990457863605	8.05756433052042
H	0.09422496159477	7.58950656420179	8.78625668665120
C	1.87543962605772	6.37732299257897	3.38444453403062

H	2.86372737857996	6.50697338957713	3.85213958434447
H	1.96747699875979	6.71727867709325	2.33863074967743
C	1.53574444313128	4.90287880365844	3.41513395522645
C	1.76490077152319	4.07248759358999	2.31680648662520
H	2.15549861715223	4.49588127654107	1.38982560783928
C	1.48446467709362	2.70916032205733	2.42401642558368
H	1.65749128273542	2.04275473675725	1.57601855986426
C	0.97340448413285	2.21356360277494	3.62547207706102
H	0.73476143055497	1.15658296194447	3.75338563444982
C	0.76175576796993	3.10803779908003	4.67093643142621
H	0.35381270086567	2.77028944324516	5.62659059049495
H	3.23496731058512	5.17853314308626	6.34123134909678

Table A1.20. Coordinates for the DFT optimized structure of 4-H-2,6-DTBP in CH_3CN

	x	y	z
C	-1.77916225669049	1.92661198190107	-0.02124592152722
C	-1.93784568975178	0.55842272539990	0.19586275154852
C	-0.46499760886532	2.41225821108902	-0.15701431340580
C	0.66383979216317	1.56933484759659	-0.09424992240254
C	0.43008575295567	0.21172959303543	0.11342774583961
C	-0.85060065635311	-0.29549848502213	0.26353317896936
H	-2.92747547199291	0.14378338733432	0.30919775653302
H	1.26308583438084	-0.47269473829637	0.16287645416884
O	-0.23179757893115	3.73495395275017	-0.36211975908005
H	-1.05003178071107	4.23403204201192	-0.37624165697799
C	-2.99349656373699	2.85865182352208	-0.13256055895597
C	-2.99487818793010	3.91891307474656	0.98449538106334
H	-3.11810601966421	3.43343731080743	1.95372906711824
H	-3.83483017307687	4.59987471510193	0.83941427754296

H	-2.09358098838792	4.52824558140373	1.05389768344665
C	-4.30539970146201	2.08600934536143	0.02168239139713
H	-4.37500893789157	1.59438939779160	0.99235335640233
H	-4.42525048660212	1.33364032264019	-0.75883436399418
H	-5.13828368044068	2.78553620788825	-0.05715719272255
C	-3.04681846754355	3.51214111865849	-1.52712671208766
H	-2.19526918870326	4.14403524106323	-1.77811376500807
H	-3.93972953369267	4.13426153174127	-1.60535661040617
H	-3.10390937309061	2.74025696694978	-2.29599910811684
C	2.09445032073496	2.10616377237501	-0.23011624622679
C	2.40234924120101	3.08270316508635	0.91372870024594
H	1.74822715762472	3.95126412674713	0.89239703674849
H	3.43490375127041	3.42982149751391	0.83300954014308
H	2.29030131766605	2.58877665645629	1.88106133978835
C	3.13127602661856	0.98134332935962	-0.15314500038966
H	3.10109583569562	0.45715628337849	0.80323595301825
H	4.12677457442900	1.41432941705954	-0.26197930379132
H	3.00152566461957	0.24982537562319	-0.95228812378719
C	2.29899869454306	2.80275348266122	-1.58206717916105
H	1.66079613784992	3.67511571038298	-1.69378611463696
H	2.09363646685673	2.11396278258192	-2.40422600393161
H	3.33848283280135	3.12613318236179	-1.67037934495688
H	-0.99851705589225	-1.35411493706348	0.42912458759238

Table A1.21. Coordinates for the DFT optimized structure of 4-OMe-2,6-DTBP in CH_3CN

	x	y	z
C	-1.76618605680037	2.01107743701154	-0.13352928518110
C	-1.94249715470669	0.65395416866979	0.11071788652564

C	-0.44831507430274	2.49098531456599	-0.27463013234853
C	0.66094011528717	1.63581873798590	-0.18643536041091
C	0.42464510994790	0.28073042058521	0.04964807599406
C	-0.85942934387897	-0.21082524618600	0.20419016558721
H	-2.92901702237701	0.23269786225138	0.23064026925215
H	1.25741174856903	-0.39719713636558	0.11349826042110
O	-0.20177027970443	3.81257947269938	-0.50772971642433
C	-2.97629838683657	2.94687173485078	-0.26393959819475
C	-2.96865940224668	4.02763207066233	0.83354145034979
H	-3.10889042618937	3.56250090057306	1.81041336413195
H	-3.79563834363903	4.71998809054886	0.66879715116783
H	-2.05705934566976	4.62142131324996	0.89949130473329
C	-4.29591279470604	2.19066818720703	-0.09616024247604
H	-4.37211436226557	1.71941050555395	0.88404353428171
H	-4.42415010489446	1.42522788628298	-0.86239461663017
H	-5.12093162319798	2.89801965338972	-0.18908147630606
C	-3.02094524633549	3.57325662148042	-1.67093944127267
H	-2.15881265238972	4.18458290653587	-1.93526502687331
H	-3.90365711096172	4.20833834719602	-1.76041778758654
H	-3.09221307114103	2.78722393524616	-2.42410184548807
C	2.10353805471496	2.13773225603688	-0.32400684519564
C	2.41779407876608	3.13823205400994	0.79670126565217
H	1.77791286484753	4.01611122779198	0.74725313123175
H	3.45712180743765	3.46473158886478	0.71856484679657
H	2.28726393452675	2.66988679447503	1.77449678399770
C	3.11966256068328	0.99704223153020	-0.20591994094050
H	3.07400244319565	0.50295697115023	0.76593775758271
H	4.12348452387872	1.40850565385977	-0.31885506598413

H	2.98454289734831	0.24424201304974	-0.98434873149122
C	2.32581355588975	2.78817817319928	-1.69549242584951
H	1.69774124455099	3.66347427511118	-1.83865151587135
H	2.11464641869196	2.07475560131138	-2.49499882543554
H	3.36982528312287	3.09454461737302	-1.78910152490686
O	-1.13797017534932	-1.51655105057468	0.44626868298889
H	-1.01610381932256	4.31658333039624	-0.53265007196944
C	-0.05544629850596	-2.39993574807521	0.62062201901220
H	-0.48519514777925	-3.36917986746726	0.85895508597264
H	0.58911086568102	-2.08328833721623	1.44408975710112
H	0.54142573606110	-2.48850496882109	-0.29015131594382

Table A1.22. Coordinates for the DFT optimized structure of 4-Me-2,6-DTBP in CH_3CN

	x	y	z
C	-1.74242457172023	1.98424630554885	-0.10951985409104
C	-1.90462571436658	0.61576566579204	0.10668641935886
C	-0.43011239532278	2.46797552030396	-0.24342762791563
C	0.69179894970766	1.62120913060851	-0.16366997291863
C	0.45011963604794	0.26464927387882	0.03758029115586
C	-0.82879583900770	-0.25904569044891	0.17734773751296
H	-2.89795129881329	0.20512869316085	0.21530763179474
H	1.28348108331874	-0.42096364931098	0.09075498358962
O	-0.19777182469234	3.78877127748670	-0.47082732678098
C	-2.95658540053371	2.91501178675034	-0.25821301731321
C	-2.90468675608399	4.12872764915211	0.69867455093483
H	-2.53467810251479	3.84686223959353	1.68498314627682
H	-3.91169461890399	4.52920846911148	0.81898674531349
H	-2.30911589452551	4.97358231265657	0.34567308856757

C	-4.25937724048992	2.17812214247391	0.06207049525282
H	-4.27597403655220	1.82057321122799	1.09301681282154
H	-4.42317145167591	1.32960143403281	-0.60180322927830
H	-5.09463095447184	2.86635093445635	-0.06874834636124
C	-3.05232529015048	3.39442038359461	-1.71588409970602
H	-2.16678661310468	3.93571555412002	-2.05161860252583
H	-3.90981478114474	4.05937571336658	-1.83446536005270
H	-3.18539983015523	2.54257350744338	-2.38433465725100
C	2.12585678932472	2.15193294711999	-0.27865582774573
C	2.41072683841269	3.13905777418206	0.86234580682169
H	1.75275626106573	4.00413246846974	0.82350152670268
H	3.44306938981106	3.49005120307818	0.79740808422842
H	2.28374435588040	2.65157006084407	1.83116015981096
C	3.16000786562326	1.02754858779901	-0.16835103204230
H	3.10447876685408	0.50964474470610	0.79033437653251
H	4.15817192569756	1.45958040158889	-0.25414382123329
H	3.05084188134567	0.29057662684891	-0.96552868155670
C	2.35524222137272	2.83341804208250	-1.63418644677351
H	1.71875018527097	3.70422189436636	-1.76676138566843
H	2.16269312427271	2.13496696879360	-2.45137711978353
H	3.39625462884453	3.15529335143535	-1.70896168744127
C	-1.03114711377314	-1.72753663092861	0.42841162705862
H	-1.01810124083875	4.28372512812950	-0.47539159698231
H	-0.21423831164299	-2.31294631884139	0.00648566178159
H	-1.96512927182004	-2.08143769470354	-0.00785791487482
H	-1.06689535054557	-1.94323141997051	1.49872846278091

Table A1.23. Coordinates for the DFT optimized structure of 4-^{t}Bu-2,6-DTBP in CH_3CN

	x	y	z
C	-1.90162170666343	1.76381102660918	-0.10141057924461
C	-2.11633976506827	0.41063741974511	0.18042465064297
C	-0.58224661373609	2.18017524949414	-0.33195114652981
C	0.49990903193626	1.27723168156368	-0.28342647052042
C	0.20403995435610	-0.05189516413620	-0.01219734873346
C	-1.08711264550729	-0.51794064014358	0.22563189996566
H	-3.12436386052852	0.07776471795192	0.36470105127988
H	1.01399189240663	-0.76364493820421	0.02139151851000
O	-0.28980269435062	3.47726361333201	-0.61826647979296
C	-3.07745528421702	2.74855044931658	-0.18205749681147
C	-2.94970671117272	3.87068323490921	0.86471193806993
H	-2.99724100342078	3.44867882826656	1.86972457389886
H	-3.78117124208545	4.56819102897724	0.75224844718994
H	-2.03248880433770	4.45708105723845	0.81282693024825
C	-4.41245173264630	2.05840165103213	0.10938062433571
H	-4.43365159760088	1.62103148670075	1.10819871975438
H	-4.63373861608289	1.27661870105940	-0.61830396537226
H	-5.21124256067801	2.79884555086068	0.05505482286465
C	-3.19435112173359	3.32675196686975	-1.60496281901472
H	-2.33293084190769	3.90369514223827	-1.94127709736225
H	-4.06186310458978	3.98603775659864	-1.66338173137850
H	-3.33332544673137	2.51838208744982	-2.32425338000775
C	1.95276586999215	1.72115290099652	-0.49697021669685
C	2.36055261842047	2.72502844034425	0.59055291415709
H	1.74867500706722	3.62385980073951	0.56247703961818
H	3.40381779096907	3.01665510973279	0.45003147549346
H	2.26953631209281	2.27502409969181	1.58136422469051

C	2.92559423908846	0.54111482199593	-0.40918725852105
H	2.90355391482534	0.05896068659420	0.56947760296215
H	3.93957132459941	0.90889742892772	-0.57212587544652
H	2.72325416488969	-0.21321266679982	-1.17155283063796
C	2.14225981546987	2.34754285635667	-1.88494838785963
H	1.55586918369573	3.25417247248616	-2.00748908119808
H	1.85730744345136	1.64104837363907	-2.66745783149554
H	3.19515285848491	2.59870141285320	-2.03001687675351
C	-1.29940270075544	-1.99886430799636	0.53546644339701
H	-1.08247157523106	4.01568721356225	-0.63478642110733
C	-0.55519810080810	-2.35979210473040	1.82802832462187
H	0.52010848911993	-2.20482561670556	1.72618307615576
H	-0.72000321142902	-3.41051262546397	2.07668049346229
H	-0.90736778241368	-1.75275135196717	2.66429333186995
C	-0.73986744452568	-2.85221109439834	-0.60994012789966
H	0.32567038192423	-2.67615923919642	-0.76026214996529
H	-1.25487285742322	-2.63498097063655	-1.54766621386342
H	-0.87159130324693	-3.91321021340785	-0.38742001748171
C	-2.77588950669188	-2.34677308839950	0.71361147551470
H	-3.22142244900204	-1.80807674861461	1.55190978599540
H	-2.87504898322096	-3.41468408361166	0.91443887972346
H	-3.35349902498319	-2.12343341372145	-0.18533844072729

Table A1.24. Coordinates for the DFT optimized structure of 4-Cl-2,6-DTBP in CH_3CN

	x	y	z
Cl	-0.05540438028219	-3.90969269723378	-0.41883320735085
O	-0.02744857749122	1.90244231268208	0.29498263182382
C	-2.56544767439323	0.67430594520837	0.10020414226973

C	2.55716445813274	0.63366713729945	-0.01639979927973
C	-1.24135823199565	-0.09479928259804	0.00519571941114
C	1.22187435324292	-0.12094944884062	-0.05134514517786
C	0.00164929581013	0.56302727245314	0.08271949260312
C	-3.77127768936022	-0.24993339571369	-0.08213878206537
C	-2.65644338124487	1.74216708265542	-1.00075285953138
C	-2.70286076909211	1.33283299664096	1.48061359139002
C	2.62556406721210	1.69104860193035	-1.13640341606773
C	2.78606262813902	1.26529342015466	1.36932890481217
C	3.73955183534101	-0.30436614441213	-0.26033617896431
C	-1.22791158005047	-1.47930823132272	-0.15399926977817
C	1.17830028647231	-1.50631888909302	-0.20796368909340
C	-0.03282817823652	-2.17125003256527	-0.24614183102809
H	-3.76336479900238	-0.74315843760986	-1.05544814541643
H	-3.82466782461064	-1.01462836572945	0.69417939640627
H	-4.68207932354842	0.34716329931233	-0.01946411861653
H	-2.56776951135161	1.28621414955345	-1.98876872542370
H	-3.62976790786517	2.23433563950846	-0.94538702493775
H	-1.88737086737010	2.50305129188813	-0.90284369411462
H	-1.90326479694616	2.04286087167511	1.67641906551485
H	-3.65414649054957	1.86686459309857	1.53752304514046
H	-2.69662594977188	0.57704343834713	2.26848068871665
H	1.88391552175254	2.48686880069535	-1.08099647481164
H	2.50143929000408	1.21173631791681	-2.10833883543523
H	3.60476188562536	2.17123000087369	-1.11721007889874
H	2.00142153556134	1.94166137924420	1.70876557720609
H	3.71770314940146	1.83352280750548	1.36363193698717
H	2.86920921623982	0.48209133333170	2.12393068267147

H	3.67448695080543	-0.78713199269192	-1.23611734318863
H	3.81228853106545	-1.07501725965423	0.50737224365559
H	4.66116010645127	0.27793360928143	-0.23502509735877
H	-2.15346999939885	-2.03147295511529	-0.20411589812952
H	2.08949577324816	-2.07621922597098	-0.29876680894515
H	0.85675904805610	2.26608405729473	0.36574930500507

Table A1.25. Coordinates for the DFT optimized structure of 4-H-2,6-DTBP radical in CH_3CN

	x	y	z
C	-1.84548552718155	1.88365532390856	-0.07384539593327
C	-1.98770097939028	0.53787996602940	0.15520154374162
C	-0.48469151465997	2.41597086438592	-0.21803699315644
C	0.67209046859694	1.51636462167351	-0.12365782866420
C	0.43264675391707	0.18239977787638	0.09255525794971
C	-0.87218450001419	-0.30540486617671	0.23660906971102
H	-2.96724947570169	0.09936861551933	0.27212887918266
H	1.24996485854592	-0.51971526201573	0.16031176812513
O	-0.31317597341181	3.62759575583974	-0.42209670783559
C	-3.03343445657983	2.82917063865416	-0.19848042618235
C	-2.96911900996301	3.93237776437643	0.86961783835819
H	-2.95496939132710	3.50315389424346	1.87336528679032
H	-3.85756548668743	4.56206937439863	0.78698372119731
H	-2.09113246287684	4.56006635252074	0.74572707413588
C	-4.35789790516938	2.08893482873656	-0.01343689856304
H	-4.43406818483869	1.63097191303533	0.97401168133940
H	-4.49962662989068	1.31334339669546	-0.76769770721551
H	-5.17675556840147	2.80267727188574	-0.11264652615996
C	-3.05089941035016	3.47214798113085	-1.59558723250438

H	-2.17044338764256	4.08624443113000	-1.76529621136016
H	-3.93649518798697	4.10420445786032	-1.69063101477457
H	-3.09985967912918	2.70891646488038	-2.37463371992025
C	2.07654456606923	2.08794778541372	-0.26363916874134
C	2.34017292089483	3.12215130281783	0.84345169787792
H	1.66761707575967	3.97239042930476	0.76522449158908
H	3.36681455485575	3.48508481969965	0.76034005050262
H	2.22204626002593	2.67405539509458	1.83181630692908
C	3.14145208513196	0.99805290323445	-0.13886427745146
H	3.10519933636147	0.50107498363225	0.83173786032634
H	4.12598116389743	1.45601809658111	-0.24275387208170
H	3.04408301098612	0.24274647771810	-0.92016548105998
C	2.25483302775534	2.75096443625476	-1.63881969747265
H	1.59201024538271	3.60327680066058	-1.76113786469066
H	2.06038295367843	2.03807164150834	-2.44259584848200
H	3.28567993702117	3.09671785302306	-1.74035683088542
H	-1.02185448767717	-1.36128649153171	0.41435717537863

Table A1.26. Coordinates for the DFT optimized structure of 4-OMe-2,6-DTBP radical in CH_3CN

	x	y	z
C	-1.81403742651737	1.98396445728879	-0.09022290988638
C	-1.95281515558186	0.64699387565691	0.13961585012947
C	-0.46047300187989	2.52839830375383	-0.25742077573508
C	0.68924205215738	1.62641072910078	-0.17840730809566
C	0.47269507877496	0.29264967799121	0.04691406911328
C	-0.82766808059755	-0.20317942202565	0.21263086395473
H	-2.92078560577865	0.18634839226631	0.27424854149528
H	1.30245832553743	-0.39105095622052	0.10178521576383

O	-0.29330854222444	3.74232446737019	-0.46667246214918
C	-3.01377189988542	2.92164516173110	-0.19067382942006
C	-2.93690116759782	4.02036079612407	0.88035125718276
H	-2.93219156499963	3.58730490573080	1.88267325211273
H	-3.81586099256598	4.66355849780923	0.79830635045260
H	-2.04902546996072	4.63492520603983	0.76020408319716
C	-4.33167094093635	2.17508602644312	0.01493275860654
H	-4.38785279652586	1.71077004551118	1.00080152609269
H	-4.48606104761917	1.40377984133248	-0.74150247207074
H	-5.15516581586313	2.88642404430706	-0.06353226218699
C	-3.05840576678303	3.56892863609157	-1.58434261514017
H	-2.18016161087085	4.18227509066414	-1.76756717624232
H	-3.94529124245101	4.20184489109982	-1.66162856690796
H	-3.12222019456494	2.80773305862226	-2.36442254402567
C	2.09839903546711	2.18135394255860	-0.34114788129272
C	2.38451384071973	3.21284526617525	0.76141528445688
H	1.71441640394859	4.06572170574735	0.69088007814395
H	3.41264776846116	3.56849795216920	0.66707907555262
H	2.27447915045236	2.76385148234631	1.75053593437791
C	3.15618462148210	1.08231456389000	-0.22995129457966
H	3.13527883454510	0.59234615484737	0.74494080493755
H	4.14276330664575	1.52959596366155	-0.35566315382517
H	3.03793131287897	0.32227023524738	-1.00418264851811
C	2.25793816076195	2.83651548666713	-1.72095547237179
H	1.59222974672855	3.68766741598415	-1.83568878952785
H	2.04889477276733	2.11856707163742	-2.51679250927774
H	3.28754833230106	3.17956112366676	-1.84145621246108
O	-1.08663671164163	-1.48429569601750	0.44927101741734

C	-0.00903703626786	-2.39672470167896	0.58183012016986
H	-0.45820310004557	-3.35677958057830	0.81361917414384
H	0.65244921772898	-2.09725912419901	1.39470571179259
H	0.55341520980024	-2.47060498881329	-0.34891008537929

Table A1.27. Coordinates for the DFT optimized structure of 4-Me-2,6-DTBP radical in CH_3CN

	x	y	z
C	-1.80589998455308	1.95197712706256	-0.11167766219169
C	-1.94736160137588	0.60693959209716	0.10531214344602
C	-0.44742095743453	2.49210920988554	-0.23955764140300
C	0.70429632825626	1.58860076464779	-0.14091494573615
C	0.46283137034692	0.25668498311522	0.06519945167952
C	-0.83977618585097	-0.25594515029406	0.19945399674902
H	-2.93002814520372	0.16831115974693	0.20715617516402
H	1.28295263006812	-0.44369641032860	0.13560503317936
O	-0.27493702871251	3.70554976837225	-0.43507776671059
C	-2.99839942998354	2.89288592256288	-0.24236029232022
C	-2.95243463222151	3.98619483372642	0.83649591097236
H	-2.97401160246675	3.54752699445729	1.83614216268304
H	-3.83015672656383	4.62798335686608	0.73397553994703
H	-2.06307432115038	4.60337105619718	0.74424637218710
C	-4.32296306191003	2.14707172849976	-0.08053652578362
H	-4.40860302474307	1.67654380943379	0.90019914089728
H	-4.45512197160013	1.38055691052741	-0.84585519458485
H	-5.14255135902495	2.86018412106007	-0.17918249204828
C	-3.00184201395598	3.54812969949176	-1.63365508282456
H	-2.12221423220805	4.16785309409653	-1.78620597432694
H	-3.88975012512674	4.17593537660188	-1.73541182363536
H	-3.03613535690824	2.79101668354498	-2.41953979100972

C	2.11360513219634	2.15317088670080	-0.26752737399401
C	2.37361852015563	3.17692602614410	0.84955578805544
H	1.70263032928432	4.02870287401523	0.77392947714748
H	3.40170186124051	3.53818741896543	0.77700171454060
H	2.24772889457569	2.72012433084674	1.83307353989034
C	3.17381949486077	1.05819359492810	-0.14394429486700
H	3.13049956372673	0.55483292479261	0.82310692465973
H	4.16079271885228	1.51279198755804	-0.23933084513603
H	3.07816251902319	0.30789110237538	-0.93035190246608
C	2.30360936439925	2.82460769701671	-1.63642633782830
H	1.64324441381163	3.67904045048669	-1.75726066060753
H	2.11232697854536	2.11703319617313	-2.44579081817071
H	3.33616525663457	3.16781015658469	-1.72941211519720
C	-1.04056385403937	-1.70543465715668	0.48570904344980
H	-0.22315739949216	-2.30476861495673	0.08771779990690
H	-1.98388322268517	-2.06620303509738	0.07804671392192
H	-1.06800913876697	-1.86627097074775	1.56764261236487

Table A1.28. Coordinates for the DFT optimized structure of 4-^{t}Bu-2,6-DTBP radical in CH_3CN

	x	y	z
C	-1.95089325389280	1.73057057244277	-0.08417643838599
C	-2.14994510838403	0.39803968599887	0.18526266492196
C	-0.57888419250040	2.20233613350941	-0.29159536128248
C	0.52272449129621	1.23428946745218	-0.26069084639864
C	0.22251484918521	-0.07219361304787	-0.00445600191017
C	-1.09336675606444	-0.52353515858388	0.23741060678628
H	-3.15150821738550	0.04041412529902	0.35828619899873
H	1.01733895836606	-0.80113781828090	0.02447008522011

O	-0.35190316151764	3.40647363026194	-0.48930048729827
C	-3.10712516420405	2.71786186038609	-0.18694530473841
C	-2.98385804649874	3.81754648206896	0.87898331791040
H	-3.01596829231173	3.39006659559684	1.88310598607060
H	-3.82568212087195	4.50660347190174	0.78223845036414
H	-2.06230700380863	4.38238315664824	0.76730300958681
C	-4.45803810643439	2.03137597046110	0.01923335669371
H	-4.54219518726194	1.58204481329010	1.01009931294129
H	-4.64209736925840	1.25928654398180	-0.72981487637535
H	-5.24856755700452	2.77725684108814	-0.07247466626436
C	-3.12196431541693	3.35690912437115	-1.58576659148431
H	-2.22660601907146	3.94562657264171	-1.76634013348688
H	-3.99153097009563	4.01138277377745	-1.67541234820480
H	-3.19776496513227	2.59145730950983	-2.36060679852949
C	1.95252923187423	1.70362178434337	-0.49915913933034
C	2.36935900539723	2.70362815576568	0.59029809772685
H	1.74834656594179	3.59577381808124	0.56912074260312
H	3.40802028145075	3.00071614230780	0.43004326363196
H	2.29847428892913	2.25153298301912	1.58157013782755
C	2.94223675931333	0.53813553638157	-0.46322851143134
H	2.95750404618441	0.04184756167344	0.50858629668650
H	3.94523539854544	0.92110516735249	-0.65509681890161
H	2.72074133600333	-0.20616492542355	-1.23017211706627
C	2.07692083308342	2.36834044601667	-1.87808290781602
H	1.46264786511867	3.26218030222418	-1.94557167367408
H	1.78102975836306	1.67820521436148	-2.67091587469096
H	3.11799409454335	2.64904794802937	-2.05053847347458
C	-1.30472566807071	-1.99101652113862	0.55647029310691

C	-0.53397223208248	-2.32787055996259	1.84182991376189
H	0.53956263882218	-2.18332805617884	1.71754728757846
H	-0.70431692021901	-3.37235982951241	2.10830435118201
H	-0.86859695569886	-1.70388610338485	2.67247400912207
C	-0.75633040119633	-2.84276566510768	-0.59662604421135
H	0.30760373290520	-2.67142172708068	-0.75813315134335
H	-1.28255049325954	-2.62461948190048	-1.52744677930292
H	-0.89168280862410	-3.90095761639819	-0.36722204235773
C	-2.77641430530803	-2.34086844059657	0.76169603222128
H	-3.21102191558165	-1.79044602848163	1.59778132285903
H	-2.86516876325271	-3.40509193875998	0.98173131881162
H	-3.36807786491413	-2.13661670640502	-0.13222266865360

Table A1.29. Coordinates for the DFT optimized structure of 4-Cl-2,6-DTBP radical in CH_3CN

	x	y	z
C	-1.84355061776932	1.88322220696433	-0.08943684512623
C	-1.99496770497242	0.53490216080887	0.11482752464402
C	-0.48523493737418	2.41716496803722	-0.23442032237744
C	0.66969610495793	1.51902813324879	-0.13237692194061
C	0.43849693209109	0.18089445377135	0.06146006258076
C	-0.87220490576705	-0.30349614098125	0.17979270584903
H	-2.97296204317295	0.09162483847353	0.22429489923777
H	1.25380645660793	-0.52315549378811	0.12817460265789
O	-0.31477889019083	3.62456118604056	-0.45013653689148
C	-3.02329820287998	2.84314180118489	-0.19357155523449
C	-2.92650979983542	3.94940699551808	0.87064926081855
H	-2.88999934029282	3.52640270067257	1.87616952118614
H	-3.81431712543576	4.58189586384818	0.80495137900732

H	-2.05135914345271	4.57555018929662	0.72297361146783
C	-4.35248318792589	2.12021166172774	0.01503326214474
H	-4.41311242424563	1.65854079461633	1.00181027915656
H	-4.52168986545252	1.35231878332769	-0.74130752586580
H	-5.16245884530841	2.84655353627489	-0.06250811348100
C	-3.05552018146371	3.48981472640528	-1.58969770055085
H	-2.17318829822050	4.09755478846084	-1.77149609462757
H	-3.93611006084598	4.13138022942074	-1.66581075058965
H	-3.12537347818920	2.73163355293579	-2.37164141333253
C	2.07059724631965	2.10514665433211	-0.25821173976456
C	2.30817099606133	3.17039696441676	0.82673922201717
H	1.64051661677117	4.01962649553995	0.71094241830618
H	3.33660939775117	3.53004376785438	0.75286379822422
H	2.17052280766875	2.75243797619549	1.82541687465552
C	3.14582272235301	1.03265929955536	-0.09141949723530
H	3.09228084396720	0.55284255533167	0.88702982082887
H	4.12584011654103	1.50316825598633	-0.17963711167696
H	3.07814265666261	0.26413726577823	-0.86270503864776
C	2.25938119726048	2.74166530553251	-1.64560965026377
H	1.58507037031316	3.58023710681034	-1.79756977859626
H	2.09217797830306	2.00960296703517	-2.43786769635910
H	3.28548357561781	3.10434572670163	-1.73583421360241
Cl	-1.11058696645209	-1.99580227733492	0.41714926338118

Table A1.30. Coordinates for the DFT optimized structure of $[4\text{-H-2,6-DTBP}]^{\cdot+}$ in CH_3CN

	x	y	z
C	-1.82835738417383	1.89076147483542	-0.08943122565092
C	-1.97494876217707	0.54568459257325	0.09016841661476

C	-0.47592538007368	2.37142948509278	-0.23465107293972
C	0.69512190155131	1.52552742609205	-0.14058485744109
C	0.45522042681323	0.18911088683253	0.02667933383490
C	-0.85315593483124	-0.30280185616932	0.13695047734687
H	-2.95164107527786	0.10388799102691	0.20100742712237
H	1.27042792534779	-0.51316639234382	0.08753043196490
O	-0.25795248804900	3.63001022250221	-0.46913968512724
H	-1.07280237036018	4.15152684824996	-0.52253996685126
C	-2.99946198006117	2.86202452417664	-0.13522110599389
C	-2.86573267155205	3.93520539576887	0.96521369836636
H	-2.66653178101237	3.47250509940204	1.93180605667972
H	-3.80703686839407	4.47972809625935	1.03444211243345
H	-2.09645962775969	4.69180483460031	0.80118839347725
C	-4.30814892015745	2.11971987859211	0.12844831235496
H	-4.30980584065321	1.64484460928184	1.10999668605328
H	-4.50052013525949	1.36009902842012	-0.62948318668254
H	-5.12884972250030	2.83518911608754	0.09929537805085
C	-3.11862503916174	3.50588144591791	-1.52955378339410
H	-2.27663701609482	4.12840455222916	-1.83752637574514
H	-3.99894661071561	4.14846439585654	-1.54367688610988
H	-3.24137299340330	2.73836462858987	-2.29348473574634
C	2.09745585454351	2.10631152428382	-0.20833106005490
C	2.30485315073574	3.10657358316544	0.94141756457524
H	1.66184478730211	3.97924749828508	0.86095245521534
H	3.33942504961232	3.45194880350542	0.92189783580984
H	2.12740714418706	2.63158630794988	1.90723094314937
C	3.14663496307615	1.00529520718988	-0.05263300981062
H	3.05355116949875	0.48447837490933	0.90111524637833

H	4.13528879105116	1.46230617674676	-0.08670727593386
H	3.09274775231699	0.27279016915953	-0.85887456571775
C	2.34593203819944	2.79111993980113	-1.56129854150646
H	1.74545121318385	3.68622891915672	-1.69661973964145
H	2.14539781708135	2.10683872386800	-2.38698468389725
H	3.39575403346891	3.08215271261129	-1.61491651414436
H	-1.00476141630150	-1.36352422450682	0.27533750296098

Table A1.31. Coordinates for the DFT optimized structure of $[4\text{-OMe-2,6-DTBP}]^{\cdot+}$ in CH_3CN

	x	y	z
C	-1.80519951136468	1.97861620979919	-0.17604508768340
C	-1.96959972240797	0.64739892515978	0.04765289971441
C	-0.45758476447039	2.44661816208321	-0.33653911589970
C	0.69641021868783	1.59729443219685	-0.19531087393558
C	0.46701681502139	0.27030527281844	0.01928955266791
C	-0.84915009577455	-0.21989320614765	0.13111099793551
H	-2.94353541983851	0.20073531386293	0.17268725524259
H	1.28787520828230	-0.41856168462019	0.11338750242455
O	-0.22209695172556	3.69972313093791	-0.63061471381373
C	-2.98038742265029	2.94911541706216	-0.25405832966972
C	-2.83864264001966	4.06492937462606	0.80034341461473
H	-2.66430075187763	3.63841860730193	1.78835088394232
H	-3.76809121872729	4.63320931277265	0.83302123452638
H	-2.04749134273569	4.79241471782403	0.61598115115203
C	-4.29130896997271	2.22397445759256	0.04920777920955
H	-4.28735567679106	1.78675716924106	1.04824777759661
H	-4.49641170403941	1.43754243882813	-0.67767971032348
H	-5.10836338702344	2.94292977759851	0.00076303340224

C	-3.10726431617004	3.53435067970591	-1.67240217420333
H	-2.26289486189977	4.13741131177747	-2.00994078521167
H	-3.98487918762646	4.18005705329453	-1.70981476723185
H	-3.23875350753582	2.73476396789258	-2.40145578588417
C	2.11252806633761	2.15010277831558	-0.27870280261377
C	2.32294134867035	3.22449455925222	0.80015573273121
H	1.69149170410561	4.09648907155824	0.65417009279151
H	3.36282151417096	3.55273706603593	0.77180464800059
H	2.12652446587957	2.81637601308003	1.79282045144453
C	3.14454484673660	1.04863632817156	-0.02942893784126
H	3.02854096036248	0.59682827674463	0.95696683692033
H	4.13985368236491	1.48913321532650	-0.07766674327332
H	3.09679317097258	0.26237271749664	-0.78420306712857
C	2.38006605479050	2.72199527760047	-1.67875308880949
H	1.76066254597808	3.58605377982815	-1.90361820471231
H	2.20879080614093	1.96153864612862	-2.44247278792040
H	3.42515040219879	3.02855732451738	-1.73943768603080
O	-1.12353993195120	-1.47704180822792	0.33453817805609
H	-1.02699849026869	4.22911731922877	-0.71221422668774
C	-0.07620012759170	-2.44226668921845	0.46775707121330
H	-0.57483513165269	-3.38463731905822	0.66205851266730
H	0.56723371567859	-2.18114806659226	1.30515488984839
H	0.49530960773617	-2.50296933179605	-0.45604100722780

Table A1.32. Coordinates for the DFT optimized structure of $[4\text{-Me-2,6-DTBP}]^{\cdot+}$ in CH_3CN

	x	y	z
C	-1.82593475195402	1.95670674139711	-0.16865175414630
C	-1.96760942352317	0.61774646297351	0.05471164380674

C	-0.47151613939056	2.44176700726844	-0.30123336290929
C	0.68786480460381	1.59723185400764	-0.17109501695024
C	0.45403787851775	0.27152519698825	0.04169007840257
C	-0.85666060271208	-0.24631416227137	0.15878869984186
H	-2.94832820835123	0.18039908096887	0.15894837472443
H	1.27391055851029	-0.42344523309729	0.13459534536977
O	-0.33678951705221	3.71193728528015	-0.55584764468132
C	-3.01954441605635	2.89471266716046	-0.28028761443040
C	-2.93811626925977	4.00162554262743	0.78266089475959
H	-2.84696918483609	3.57389864564866	1.78225108765086
H	-3.85930611315455	4.58507774307906	0.74863198551760
H	-2.10720226487927	4.68146511542504	0.61762637491295
C	-4.32733684787670	2.13612019928531	-0.05050978691062
H	-4.36772340533619	1.68266900220498	0.94073901137528
H	-4.48495333637166	1.35741413649965	-0.79792240822215
H	-5.15499341531921	2.84093960484159	-0.12746298824259
C	-3.08190295001653	3.51198482120272	-1.68650784932980
H	-2.22822716999264	4.14870971373538	-1.90279448815627
H	-3.98379639785604	4.12150484190775	-1.76208396060384
H	-3.13817298786874	2.73358742763655	-2.44884063876279
C	2.09012754300497	2.18250505760048	-0.26743606305562
C	2.31293942172448	3.22298837910458	0.84677604855375
H	1.67712358544183	4.10753314887969	0.79881957468988
H	3.34313084001804	3.57491360020503	0.79733910346467
H	2.15390676954987	2.76815118321340	1.82461396449037
C	3.14275280380858	1.09275050105066	-0.06685825054224
H	3.04909924653666	0.61771697120331	0.91001268058449
H	4.13083350923405	1.54730860907488	-0.12630604218762

H	3.08154978282405	0.32554526206958	-0.83893021211520
C	2.33792145447338	2.78350813261837	-1.66386582328136
H	1.72777674910890	3.64932295280958	-1.92431915865878
H	2.16945765940795	2.03057569143155	-2.43403496799577
H	3.37605579581004	3.10912120803176	-1.72555889996135
C	-1.05772434258093	-1.68255604955530	0.44648227019996
H	0.58579256796734	3.99345936558165	-0.64381800788477
H	-0.24101649752951	-2.28722819128568	0.05764357114034
H	-2.01145375194366	-2.03964696565438	0.06282513835688
H	-1.07244297668088	-1.81480255114926	1.53493909118633

Table A1.33. Coordinates for the DFT optimized structure of [4-^{t}Bu-2,6-DTBP]$^{\cdot+}$ in CH_3CN

	x	y	z
C	-1.95767129712402	1.71441515892268	-0.16996965918590
C	-2.16143436295156	0.39269246104428	0.10931001739701
C	-0.60397696427700	2.11617580482147	-0.44745102283381
C	0.52293372754212	1.22498194095786	-0.32278292404253
C	0.22661585280194	-0.07473055663757	-0.04793917757128
C	-1.09799569336554	-0.53387938196226	0.15838555121356
H	-3.15891337678315	0.03950373262204	0.30483650687444
H	1.02588468187634	-0.79245144924183	0.03056221951443
O	-0.34444911144786	3.32970256915342	-0.83663840442762
C	-3.08001736068979	2.74333196728468	-0.15678067847274
C	-2.78117971188049	3.82542474351559	0.89859153384019
H	-2.62921844956992	3.37096102549214	1.87791337734403
H	-3.63619257921733	4.49835361276469	0.96109561794508
H	-1.90922390586977	4.44523784663272	0.68946915887042
C	-4.40261554940893	2.08522198027123	0.23765313901765

H	-4.34248087062263	1.61487686138526	1.21959237484486
H	-4.71385072346361	1.33670833793246	-0.49190867660336
H	-5.17558836289389	2.85110199695573	0.28231171370424
C	-3.29413539114179	3.37161101036073	-1.54814958943787
H	-2.50181909711150	4.03275697981589	-1.90568399069364
H	-4.19460081143426	3.98468867824379	-1.51403596704144
H	-3.43531821592893	2.59822202840206	-2.30279679194924
C	1.95474103682924	1.71877783874924	-0.47446346307099
C	2.23629902861911	2.83416735591419	0.54579206492267
H	1.62932521669847	3.72015900618080	0.37894650908844
H	3.28417053941716	3.12690867223036	0.46661462380351
H	2.06190189286933	2.48120869972846	1.56334268597081
C	2.95007973471555	0.58948333215405	-0.20230665625050
H	2.84032402279695	0.18129938414304	0.80370422240610
H	3.95981260727084	0.98969732243750	-0.28923140843826
H	2.85649537794068	-0.22279272368835	-0.92434457723916
C	2.20682763399569	2.22239656146197	-1.90358660646798
H	1.63255469185975	3.11449539880302	-2.13980012372241
H	1.96688786654142	1.44841869600814	-2.63416912734475
H	3.26523764831151	2.46504319156220	-2.00744159078342
C	-1.31198947378380	-1.99053841323404	0.47342415316381
H	-1.13366186359246	3.88679512408931	-0.90883888946249
C	-0.57188831133851	-2.31156076915894	1.78434790512058
H	0.50575546074700	-2.18159761402053	1.68824030330865
H	-0.76366123323644	-3.35290408286389	2.04632321891580
H	-0.92629567430173	-1.68149216997561	2.60102880318313
C	-0.71214077707672	-2.83591389906676	-0.66173222058606
H	0.35478599411464	-2.65733016769028	-0.78795193890804

H	-1.21194626857691	-2.63188757568012	-1.60913646676930
H	-0.84655600503032	-3.89134174466852	-0.42234040546771
C	-2.78500674351677	-2.35355651907960	0.63486893407822
H	-3.24465597693029	-1.82568765880822	1.47159845047614
H	-2.86491409197947	-3.42197211063374	0.83400597521029
H	-3.35534476040226	-2.14047248363083	-0.27031870344355

Table A1.34. Coordinates for the DFT optimized structure of $[4\text{-Cl-2,6-DTBP}]^{\cdot+}$ in CH_3CN

	x	y	z
Cl	-0.04127289440144	-3.88395504239192	-0.24364803074470
O	-0.02023254960882	1.78664503326993	0.44003445986248
C	-2.56398540915483	0.66892401222814	0.09353445125287
C	2.55818606048798	0.63881581614783	-0.03390438499340
C	-1.27395284401561	-0.13762124635205	0.05845964274027
C	1.26385251260717	-0.16188348407851	-0.00543722190191
C	0.00750516701851	0.51801802495879	0.16622888754814
C	-3.76928877030482	-0.22692366858733	-0.18537875530563
C	-2.54656899053926	1.76226676398007	-0.98970325506325
C	-2.76228331707708	1.30564535246901	1.47900278796056
C	2.50366707147344	1.71631429112652	-1.13780044156284
C	2.84213657210533	1.26060619453424	1.34702990489206
C	3.74058050714332	-0.26595552595920	-0.36867218101549
C	-1.25128498593022	-1.49950151429536	-0.07011129712485
C	1.21582248580393	-1.52087339424013	-0.12986491771845
C	-0.02640128372319	-2.18961129039259	-0.13236805163570
H	-3.69763774038288	-0.70665684418815	-1.16245452751636
H	-3.89235527159439	-0.99697929632689	0.57669907788373

H	-4.66727724401047	0.39050895816809	-0.18068681636063
H	-2.34337570383402	1.33620436607718	-1.97309628678145
H	-3.53154982742330	2.22965337913456	-1.02263599371769
H	-1.81822039161954	2.54318600458657	-0.79152402475364
H	-1.97435830198545	2.00853514971204	1.73616410002430
H	-3.70801681492065	1.85029931237116	1.47696184144944
H	-2.81478798131244	0.54026104194901	2.25407924046641
H	1.78652760845369	2.52262950091689	-0.98390053347827
H	2.27340229197703	1.26188054918445	-2.10138524899830
H	3.48312819730932	2.18848492709783	-1.20799059460340
H	2.08645513447760	1.95003496230355	1.72667583389688
H	3.77383229982687	1.82381666253473	1.29009930060858
H	2.95491842237495	0.47815941672301	2.09673940227133
H	3.61271480355481	-0.74310028185177	-1.34072776129447
H	3.88663270786222	-1.03696490148846	0.38751936274189
H	4.64430397297285	0.34113333738649	-0.40715244523508
H	-2.16532934627199	-2.06906367756910	-0.12724808496904
H	2.11618851959292	-2.10613696037506	-0.22874891643809
H	0.85762533306848	2.19240407123640	0.50751147761372

Table A1.35. Coordinates for the DFT optimized structure of $[4\text{-H-}2,6\text{-DTBP}]^-$ in CH_3CN

	x	y	z
C	-1.81202735555574	1.89470318366915	-0.06100917924390
C	-1.96329114162606	0.53416462136936	0.17489887192155
C	-0.47923917432477	2.44682871107765	-0.20533557963511
C	0.64445187222850	1.53494975261169	-0.11407959551152
C	0.40964619592350	0.18537399618357	0.11436518397834
C	-0.87530333846186	-0.33206976111476	0.26740735515086

H	-2.95652646847691	0.11876747452763	0.28830891592963
H	1.24638495311453	-0.49868726544172	0.17845700216855
O	-0.30300859042230	3.68827007898672	-0.40943880449925
C	-3.02494684190084	2.82563453268358	-0.19601034136023
C	-2.99624514434745	3.92491161064448	0.87674303089303
H	-3.09268668386914	3.49248742602635	1.87587903189477
H	-3.83366599595941	4.61348886645816	0.73180633316421
H	-2.06626023514544	4.48627514660087	0.82307863518241
C	-4.35214542362431	2.08123420465698	-0.03899565138022
H	-4.44508916687722	1.61375215625591	0.94315573719445
H	-4.47954837311801	1.30877329215701	-0.79998754372505
H	-5.17482557837670	2.79168437067376	-0.14601514354600
C	-3.03414750435862	3.48226014525511	-1.58596301141239
H	-2.12547850158518	4.05934256812543	-1.74080933246743
H	-3.89821177088872	4.14545824318694	-1.68563799410813
H	-3.10494222451022	2.72314042177183	-2.36883159179344
C	2.06832630986272	2.08494509051455	-0.26745390513289
C	2.35991811119100	3.11907132627152	0.83113841406601
H	1.64437009980150	3.93695729408235	0.78184893481575
H	3.36949936681897	3.52290937965111	0.71247231998011
H	2.29849249894715	2.65926803500311	1.82052689637758
C	3.13461877679814	0.99298109379170	-0.15625567717478
H	3.11366651358820	0.49632526223056	0.81571641445239
H	4.12180848040049	1.44457315780670	-0.27719003280848
H	3.02335125157637	0.23321932851242	-0.93221544287174
C	2.24337143315944	2.74841780106480	-1.64171228006138
H	1.52027487455831	3.55051151352767	-1.77062434076543
H	2.10514446835492	2.01718296322763	-2.44210379752474

H	3.25210443935649	3.16065035925155	-1.73699815306789
H	-1.02493013225131	-1.38809638130146	0.44992432092035

Table A1.36. Coordinates for the DFT optimized structure of [4-OMe-2,6-DTBP]$^-$ in CH_3CN

	x	y	z
C	-1.79451076606426	1.99180298054060	-0.12291055809449
C	-1.96391753799319	0.62969265031468	0.09296476615629
C	-0.46001259101044	2.54211242622545	-0.24075548153767
C	0.64145285258517	1.61991043674423	-0.15369597421541
C	0.40431299802470	0.26048924870169	0.05639922649063
C	-0.88129831327062	-0.23995453514485	0.18858145935916
H	-2.95277052429666	0.20040486659000	0.19156196698490
H	1.24086580281486	-0.41767172567804	0.11703837791484
O	-0.27309159212033	3.79451773326875	-0.41771994521866
C	-3.00481452333771	2.92691369047585	-0.25286371723437
C	-2.98064597480914	4.00296803931964	0.84328804147377
H	-3.09667790053781	3.55026137153989	1.83135883485255
H	-3.80878712581416	4.70320651215012	0.70097134265827
H	-2.04293814982148	4.55334425347615	0.81357094036413
C	-4.33819564873191	2.18752035715545	-0.12820381300214
H	-4.44872064794328	1.70267711814584	0.84365766764541
H	-4.46003732848605	1.43061006082331	-0.90557701463429
H	-5.15461768036367	2.90552699531934	-0.23352827078334
C	-2.99140659060377	3.61135920932166	-1.62907620697909
H	-2.07122845256148	4.17571766221202	-1.76190548509975
H	-3.84405042224715	4.29011483285596	-1.72177479353255
H	-3.06792691411655	2.86941612967167	-2.42774819320603
C	2.07799531731279	2.14121446545616	-0.27835762003817

C	2.37123469261914	3.14018031323529	0.85085644362485
H	1.66708868397786	3.96881590158520	0.81149239584982
H	3.38896403752328	3.53037148357164	0.75969593616090
H	2.28566608868115	2.65372068324494	1.82576990838613
C	3.12312712102936	1.02706792448526	-0.18323080174672
H	3.09056202061436	0.51493651584702	0.78051763873211
H	4.11927149429461	1.46079711413990	-0.29359483599193
H	3.00014141299376	0.28220739935315	-0.97202180402959
C	2.27790194565981	2.83315023189377	-1.63379679780558
H	1.56291168004822	3.64448092579511	-1.75075473955580
H	2.14053073428094	2.12031026158112	-2.45096610258121
H	3.29228858759524	3.23544506016169	-1.70827923975323
O	-1.16694350413931	-1.56726002190556	0.40602881794841
C	-0.08317942797043	-2.42106701048303	0.64391548679763
H	-0.49873579533523	-3.39775883177153	0.88156695131753
H	0.52342288255699	-2.07769991776103	1.48772626151063
H	0.56204905896243	-2.51588281245857	-0.23481106918791

Table A1.37. Coordinates for the DFT optimized structure of [4-Me-2,6-DTBP]$^-$ in CH_3CN

	x	y	z
C	-1.77142221791058	1.96691779492739	-0.09974337380370
C	-1.92237662277401	0.60115283206482	0.11755734852039
C	-0.44231314957196	2.52507344260757	-0.22590164735930
C	0.67522835938338	1.61118138053799	-0.12892819627317
C	0.43584832919004	0.25831441885584	0.08238187427611
C	-0.84426982813556	-0.27921421324795	0.21574202550099
H	-2.91861879303989	0.18447217550645	0.21284970056231
H	1.27452916916267	-0.42515348968788	0.14918616783950

O	-0.26438343287243	3.77067025679085	-0.42522606894667
C	-2.98669381034986	2.89476572361123	-0.23999444721012
C	-2.96520837714666	3.99182411521098	0.83556009553974
H	-3.07102821998547	3.55747655131110	1.83296678477732
H	-3.80000735707820	4.68250863095089	0.68520477573495
H	-2.03316099473222	4.55055303363573	0.79035256276979
C	-4.31512340721921	2.15062727238545	-0.09269245851462
H	-4.41269476276319	1.67835987168649	0.88676701961157
H	-4.44070912008839	1.38219415573773	-0.85797821889249
H	-5.13645998486404	2.86279764685399	-0.19959757689927
C	-2.98655407330369	3.55508051519305	-1.62820288228532
H	-2.07372148844524	4.12778559182829	-1.77574593222462
H	-3.84686648671334	4.22278565820623	-1.73090352257548
H	-3.05680756087594	2.79813668816067	-2.41326177437648
C	2.10304981937406	2.15488578620264	-0.26747614034151
C	2.38602559713109	3.18867985541756	0.83358835043360
H	1.67008063438620	4.00584055311408	0.77829916367440
H	3.39669597422202	3.59239528296747	0.72369872826473
H	2.31636026269371	2.72819112008758	1.82217810190632
C	3.16627243098512	1.06113854266955	-0.14435838920267
H	3.13245295743217	0.56394132089845	0.82700489205572
H	4.15548785558026	1.51153639753946	-0.25273011145559
H	3.06398011283277	0.30161309778314	-0.92176757004585
C	2.29169739156402	2.81619752170240	-1.64077424009867
H	1.56926092511169	3.61793431031496	-1.77660840481354
H	2.15972864279396	2.08324571667622	-2.44076195658114
H	3.30149232470048	3.22765317257341	-1.72832463372708
C	-1.04585255558119	-1.74372256329970	0.50157883763536

H	-0.23849059465977	-2.34353092143366	0.07803379747859
H	-1.98551309210809	-2.10761560471283	0.08250095207285
H	-1.07022685632474	-1.95427464162766	1.57507836697304

Table A1.38. Coordinates for the DFT optimized structure of [4-^{t}Bu-2,6-DTBP]$^-$ in CH_3CN

	x	y	z
C	-1.91504004103474	1.74665567621225	-0.09041016323576
C	-2.12254086807466	0.39403345813141	0.17618308742791
C	-0.57398347423033	2.23707426823077	-0.30363257805576
C	0.49623544834760	1.26212589377083	-0.26753739039903
C	0.20109202079014	-0.06664294458363	-0.00591870804520
C	-1.09222581234567	-0.54369637016158	0.23064463673492
H	-3.13461123623093	0.05635460540863	0.34733137631709
H	1.01474452651342	-0.77935469560575	0.02253763565081
O	-0.33834356546813	3.47044392974818	-0.51915060680436
C	-3.09332384802372	2.72686341939270	-0.17790053441449
C	-2.96946322941464	3.82414101059290	0.88996310835122
H	-3.04893934835954	3.39641493050909	1.89262983117487
H	-3.77530433989952	4.55531175728311	0.77678985769439
H	-2.01390404020525	4.33602209950972	0.79874647312513
C	-4.44695666290256	2.04525492675271	0.03358058484674
H	-4.52701250983869	1.58759080672646	1.02164230717883
H	-4.63968612077382	1.27627817323372	-0.71735799791282
H	-5.23915637182432	2.79282582041791	-0.04786755817825
C	-3.12790801706631	3.38009709024415	-1.56893535710164
H	-2.19856393980999	3.91114489080970	-1.76158241707438
H	-3.96221736568957	4.08414482852926	-1.63785834398491

H	-3.26578037419693	2.62295564955106	-2.34489324948403
C	1.94156518206120	1.71541144512788	-0.50889610983662
C	2.36539549787854	2.72953407460778	0.56400787749068
H	1.70096066257484	3.59100651306748	0.55177091936005
H	3.38980207321517	3.06746004304603	0.38276126961677
H	2.33389115121601	2.27585064163336	1.55778679734095
C	2.93862134110065	0.55527753242297	-0.46009785614015
H	2.95418909108385	0.06661576528233	0.51618361523785
H	3.94297590296208	0.93758327593969	-0.65438885499231
H	2.72158887254553	-0.19995050304598	-1.21820277030631
C	2.07465988741038	2.36558689685024	-1.89352561014384
H	1.40108514120461	3.21545733693295	-1.97699371704248
H	1.83517672486682	1.64678837925070	-2.68127939529470
H	3.10138828944383	2.70654441980223	-2.05380470342355
C	-1.30265678018137	-2.02102455300643	0.55674765470143
C	-0.57820780589128	-2.36705927169224	1.86530472167317
H	0.49651882598164	-2.19805653202860	1.77698415576144
H	-0.73370605045026	-3.41608186701186	2.12985637686909
H	-0.94832836318309	-1.74952594422046	2.68662055465232
C	-0.72896625900326	-2.89605748235354	-0.56571013780918
H	0.33517759078119	-2.70825222140327	-0.71328774962124
H	-1.23893417558815	-2.69834062779221	-1.51101142563638
H	-0.84964471859913	-3.95594926801505	-0.32889393006137
C	-2.78108549087526	-2.36981467542923	0.72095475091385
H	-3.23697163214180	-1.81755860674180	1.54499461116814
H	-2.88654857349271	-3.43508784608338	0.93447402323365
H	-3.34733721518183	-2.15461614984323	-0.18750906152254

Table A1.39. Coordinates for the DFT optimized structure of $[4\text{-Cl-2,6-DTBP}]^-$ in CH_3CN

	x	y	z
C	-1.80955188103716	1.90232644902305	-0.06847428206538
C	-1.96901888167602	0.53903138053077	0.15121730056598
C	-0.47869070916556	2.45522796770260	-0.21261704088048
C	0.64392159227381	1.54487857560669	-0.11861034308790
C	0.41673495103658	0.19076018716620	0.09357439502076
C	-0.87184516321222	-0.30968853907821	0.22891031865866
H	-2.95731539895536	0.11400008634977	0.26049590667308
H	1.24692967101861	-0.49914948956233	0.15625946426333
O	-0.30330846940527	3.69430598396266	-0.41956499275244
C	-3.01789355163779	2.84121783087846	-0.19415034724706
C	-2.97150281918559	3.94565313838907	0.87362123950536
H	-3.06033378608809	3.52129186070210	1.87663698991748
H	-3.80736722146568	4.63643913545679	0.73091069248478
H	-2.04110808852026	4.50452842851638	0.80721709636064
C	-4.34762319247880	2.10703902353947	-0.02243787720745
H	-4.43159407439070	1.64040007376323	0.96095095852425
H	-4.49071718936904	1.33727403295214	-0.78320330529498
H	-5.16513331463999	2.82478084550503	-0.11874027223008
C	-3.03262134674666	3.49633272949040	-1.58542596667540
H	-2.12319702352446	4.07012533253622	-1.74746584154251
H	-3.89356054099287	4.16458996177079	-1.67709465505999
H	-3.11380220466506	2.73873424922757	-2.36840083695031
C	2.06568715139348	2.10301830533045	-0.26494868278276
C	2.34351778472386	3.15288551555002	0.82317446865744
H	1.62813145007564	3.96935486039412	0.75759673771154
H	3.35291093838334	3.55689867692560	0.70459664992785

H	2.27708895056876	2.70792868033285	1.81873802547322
C	3.13743095940880	1.02019683117385	-0.13316185899305
H	3.10700125713318	0.53165365686387	0.84266907793130
H	4.12215151680016	1.47916568449402	-0.24466372366708
H	3.04230282485624	0.25479333632995	-0.90556283073118
C	2.24391528882677	2.75458035168540	-1.64515961944386
H	1.51856625884159	3.55258146203944	-1.78623845803663
H	2.11507676987454	2.01610466651785	-2.44014620779634
H	3.25076984472146	3.17193082543938	-1.73698190765627
Cl	-1.11304235278027	-2.03153209750574	0.49549972842549

Table A1.40. Coordinates for the DFT optimized structure of 4-H-2,6-DTBP in DMSO

	x	y	z
C	-1.77828420774110	1.92728216592047	-0.02244326740026
C	-1.93733164092840	0.55929250505423	0.19482369688748
C	-0.46400285901368	2.41260703930053	-0.15876846805310
C	0.66452149946037	1.56963804466266	-0.09535509257314
C	0.43037355775408	0.21219743113558	0.11235826770573
C	-0.85026962290579	-0.29463628761524	0.26229058282617
H	-2.92670276548961	0.14423187931869	0.30878732713763
H	1.26291350152247	-0.47280138733068	0.16214322226752
O	-0.23331838498718	3.73573456689450	-0.36444382298027
H	-1.05586509312874	4.22668420123789	-0.37881754704766
C	-2.99285263546385	2.85947105333603	-0.13267836164817
C	-2.99473336937028	3.91976163334626	0.98393625847665
H	-3.11162368775761	3.43477909980606	1.95420901219280
H	-3.83835941633271	4.59684624168820	0.84213051071631
H	-2.09697700670683	4.53485581838326	1.05039689499838

C	-4.30370705976959	2.08585221653663	0.02289499274297
H	-4.37182382938264	1.59318669485218	0.99312101225426
H	-4.42474778666122	1.33414411701864	-0.75809676217790
H	-5.13763587237290	2.78436826983473	-0.05370055037987
C	-3.04917533897226	3.51378460722958	-1.52649837112495
H	-2.20381330989462	4.15455401014503	-1.77668344320283
H	-3.94702160907786	4.12862474290908	-1.60567973209385
H	-3.09839660308140	2.74299895877678	-2.29701003356055
C	2.09526014528487	2.10547326971142	-0.23003643578765
C	2.40220141844241	3.08193804455105	0.91360969009879
H	1.74894440464522	3.95106799412117	0.89125497897404
H	3.43500585354757	3.42880522833095	0.83482402591494
H	2.28843292325022	2.58899792343139	1.88127461405364
C	3.13113153596735	0.98033826723323	-0.15164757827747
H	3.09999866607409	0.45606659984378	0.80468627503774
H	4.12724113601203	1.41232023311183	-0.25919230685163
H	3.00262220058413	0.24863351662412	-0.95085638217582
C	2.30114164830196	2.80154239807114	-1.58156426129986
H	1.66414105371450	3.67470472513104	-1.69378860703824
H	2.09500519374011	2.11347075675187	-2.40415629293736
H	3.34091643244784	3.12397361320451	-1.67021965359728
H	-0.99836907171090	-1.35323019255879	0.42791560792284

Table A1.41. Coordinates for the DFT optimized structure of 4-OMe-2,6-DTBP in DMSO

	x	y	z
C	-1.76545656478550	2.01136295715968	-0.13485111348065
C	-1.94231214054522	0.65450350881748	0.10941288586312
C	-0.44751669370138	2.49103969725685	-0.27632685748217

C	0.66118251003842	1.63561433111534	-0.18766990466299
C	0.42429431198173	0.28068299789541	0.04862730139110
C	-0.85978336817621	-0.21092774411882	0.20314416537124
H	-2.92895179036805	0.23382979717462	0.22954296508108
H	1.25709641980008	-0.39716201105097	0.11251361777650
O	-0.20351528952709	3.81305474426337	-0.50982559693932
C	-2.97559711068903	2.94748412245281	-0.26415150209471
C	-2.96863822457507	4.02801902440939	0.83326058527415
H	-3.10560774332411	3.56301362531960	1.81066481428227
H	-3.79766436404839	4.71834905942308	0.67037170269917
H	-2.05931558912516	4.62566670335353	0.89890732113620
C	-4.29452720396736	2.19075887062122	-0.09559874793902
H	-4.36992339549751	1.71852558472287	0.88420406553835
H	-4.42385903335556	1.42603351743901	-0.86239829356136
H	-5.12033582278270	2.89742324504762	-0.18677248867299
C	-3.02257960103182	3.57473906666890	-1.67045306355227
H	-2.16492371472581	4.19269905768956	-1.93456712398475
H	-3.90896334802257	4.20458187711384	-1.76060217237868
H	-3.08803792521268	2.78957086283303	-2.42505345448040
C	2.10398424059446	2.13639833155907	-0.32416528601650
C	2.41747145077062	3.13605383851942	0.79690185216955
H	1.77816668655674	4.01429451265958	0.74715011350663
H	3.45693626230412	3.46267808504860	0.72071755542532
H	2.28556329044174	2.66799303454742	1.77468715846498
C	3.11932284268500	0.99544754956412	-0.20579879694169
H	3.07356639134800	0.50094610412113	0.76587832849140
H	4.12364594001549	1.40599987635156	-0.31802945852558
H	2.98491542402626	0.24269555888976	-0.98443594200066

C	2.32732709604547	2.78727987296293	-1.69471745744077
H	1.70010173689397	3.66316506127303	-1.83790095548895
H	2.11576852390792	2.07496823039480	-2.49514855354767
H	3.37152283634228	3.09313661255786	-1.78834995807946
O	-1.13808647175182	-1.51587954058694	0.44550292290967
H	-1.02200760653571	4.30922813091065	-0.53350783965271
C	-0.05451117895491	-2.39674536181069	0.62129867782912
H	-0.48178611742950	-3.36688884780512	0.86073367399079
H	0.58952248659671	-2.07884574261905	1.44482258580368
H	0.54318184778412	-2.48630820214563	-0.28894772608102

Table A1.42. Coordinates for the DFT optimized structure of 4-Me-2,6-DTBP in DMSO

	x	y	z
C	-1.74323032092861	1.98448949989910	-0.09883381993706
C	-1.90579830439853	0.61545800741584	0.11109156431041
C	-0.43099011869167	2.47060903923760	-0.22526472689476
C	0.69051255929509	1.62265379824348	-0.15502168306656
C	0.44867296080632	0.26498002665125	0.03880612389024
C	-0.82980224026651	-0.25925176922626	0.17858697123183
H	-2.89914593957716	0.20398246050142	0.21603428339692
H	1.28175857638116	-0.42138592254815	0.08633688384012
O	-0.20209767506122	3.79410283860783	-0.43916640207394
C	-2.95694563445486	2.91343355472379	-0.26047442012497
C	-2.90431846991649	4.14781992338158	0.67255056208495
H	-2.45405089397811	3.91194768263761	1.63730519338998
H	-3.91879586205562	4.50228812953590	0.85562830196113
H	-2.38378025374270	5.01377557226702	0.25394963171466
C	-4.26045961868886	2.18210560369182	0.06758776732102

H	-4.28021357507504	1.84148336888641	1.10436180689456
H	-4.42393523516048	1.32339659807814	-0.58294731373782
H	-5.09511304569332	2.86839690790319	-0.07674988527641
C	-3.04332580456091	3.36885180354370	-1.72584788103983
H	-2.14936741447004	3.89700547653646	-2.06067924262146
H	-3.89422368346907	4.03945601234043	-1.86029978853483
H	-3.17928095074523	2.50779431280295	-2.38187763921693
C	2.12445014531756	2.15168413230866	-0.27397962468253
C	2.41927484926959	3.12548200927083	0.87504856831552
H	1.76247691109038	3.99193614855081	0.84959368107197
H	3.45159030140651	3.47602881921867	0.80682671349882
H	2.29835802535856	2.62855612103978	1.83987150049012
C	3.15701376395827	1.02442724349296	-0.18533472846889
H	3.11103909075282	0.49694046404684	0.76862551589413
H	4.15540005104194	1.45476299374957	-0.27735101478825
H	3.03824416434432	0.29546751763054	-0.98853653824601
C	2.34500668452876	2.84889846060709	-1.62238731203336
H	1.71180065717245	3.72442454864447	-1.73798227015207
H	2.14175830409733	2.16249392880983	-2.44718610848903
H	3.38677089762883	3.16703142821709	-1.70278518490233
C	-1.03176634637187	-1.72837518396633	0.42377519649956
H	-1.02278309152586	4.28731755379842	-0.40646060494341
H	-0.21395174449702	-2.31212571321117	0.00124710260397
H	-1.96465939691068	-2.08154264630730	-0.01549912037038
H	-1.06953232220998	-1.94837075101218	1.49316794119094

Table A1.43. Coordinates for the DFT optimized structure of 4-*t*Bu-2,6-DTBP in DMSO

	x	y	z
C	-1.90096232221658	1.76368098473237	-0.10370976877086

C	-2.11610676712618	0.41074939483864	0.17833367187728
C	-0.58148191263662	2.17975710907453	-0.33442383404352
C	0.50037300901950	1.27688561606818	-0.28498351537714
C	0.20426147966482	-0.05208749870049	-0.01337402690982
C	-1.08691369137758	-0.51770818319011	0.22407806220151
H	-3.12406475124475	0.07788489299901	0.36294499677678
H	1.01410898014114	-0.76392341863385	0.02105541220154
O	-0.29169867969936	3.47742193108091	-0.62133110918493
C	-3.07667693791121	2.74900627618993	-0.18222464886105
C	-2.94876600895786	3.86892766815335	0.86654068040984
H	-2.98925543713658	3.44498956897541	1.87102934156446
H	-3.78349784490926	4.56343287387856	0.75990520496610
H	-2.03499491199975	4.46073699165014	0.81241877282734
C	-4.41082760674562	2.05770484217234	0.10895485443255
H	-4.43132067165362	1.61807454038668	1.10679058159378
H	-4.63282399183310	1.27749277900040	-0.62023770404741
H	-5.21051448881638	2.79735130665062	0.05727459953692
C	-3.19629667411435	3.33112244932351	-1.60310536200565
H	-2.34070997339933	3.91790072583400	-1.93787725473145
H	-4.06906714299933	3.98352576099376	-1.66033618907583
H	-3.32772468589930	2.52495658945268	-2.32627386174304
C	1.95328446239324	1.72002209430793	-0.49750495110084
C	2.35978183842282	2.72486923698070	0.58900955830253
H	1.74857551409749	3.62402843075989	0.55894427081101
H	3.40334636312460	3.01635127864524	0.45029973790005
H	2.26700814452407	2.27684968237743	1.58058298490055
C	2.92559944257292	0.54018826977147	-0.40729217501443
H	2.90282351417036	0.05892711710831	0.57183253300749

H	3.94007666366957	0.90708697909742	-0.56932504920297
H	2.72463416001512	-0.21515166598100	-1.16904278025060
C	2.14360742620901	2.34459681501286	-1.88569901203117
H	1.55704857635826	3.25087572370623	-2.01002855116263
H	1.85920556349130	1.63748923891520	-2.66788234556660
H	3.19638696023816	2.59617745286521	-2.03105316575532
C	-1.29921335074364	-1.99813283514659	0.53507726888559
H	-1.08883708570981	4.00830390796638	-0.63445914010369
C	-0.55618311367855	-2.35729908845028	1.82840751380994
H	0.51940731777917	-2.20337850086272	1.72751449451134
H	-0.72146580887212	-3.40743191937130	2.07932176471267
H	-0.90816246857122	-1.74877304203185	2.66371526921739
C	-0.73863468901680	-2.85227650932491	-0.60874702108947
H	0.32711738104146	-2.67688527308780	-0.75861461737273
H	-1.25239987706920	-2.63615810450791	-1.54744637193721
H	-0.87037254276949	-3.91324978670681	-0.38598957023267
C	-2.77549794620004	-2.34591339134736	0.71231320592698
H	-3.22207437115392	-1.80706461251160	1.54999072217610
H	-2.87534718112964	-3.41365947567716	0.91385326151594
H	-3.35286386134175	-2.12356522343761	-0.18706673849469

Table A1.44. Coordinates for the DFT optimized structure of 4-Cl-2,6-DTBP in DMSO

	x	y	z
Cl	-0.05465389080448	-3.90920590181093	-0.41316182395396
O	-0.02624291862854	1.90211859745655	0.30385165316288
C	-2.56615681364193	0.67366288591710	0.09966878263158
C	2.55651700722993	0.63454642849064	-0.01581466340673
C	-1.24182736702059	-0.09487578952463	0.00837827553565

C	1.22118786495613	-0.12061454513674	-0.04526901628283
C	0.00071102210516	0.56287654146986	0.08907948280598
C	-3.77083728478067	-0.25004215704806	-0.09021451143817
C	-2.65221092550878	1.74387141461740	-0.99884211975358
C	-2.70905999416210	1.32873319909762	1.48064039041600
C	2.61996864715209	1.68982599864234	-1.13767220072651
C	2.79403201708803	1.26966392619047	1.36654502413030
C	3.73699606377383	-0.30447811883100	-0.26349961997495
C	-1.22791683577264	-1.47925164455334	-0.15132449713166
C	1.17819326337495	-1.50585947040526	-0.20173172469222
C	-0.03270416262739	-2.17092513141488	-0.24098286564386
H	-3.75871159022705	-0.74131736062151	-1.06450470685871
H	-3.82854569156551	-1.01646694705428	0.68409750122494
H	-4.68227943478992	0.34645898993065	-0.03077679216819
H	-2.55573940399919	1.29125346156186	-1.98769036315704
H	-3.62677030074803	2.23422686230238	-0.94928398148714
H	-1.88570854838894	2.50636163599800	-0.89411794334232
H	-1.91048360414022	2.03851254858464	1.68143008289701
H	-3.66046532342614	1.86279260364085	1.53578111638962
H	-2.70561064935025	0.57150004276184	2.26716879037894
H	1.88713335835869	2.49330053605069	-1.07338834923348
H	2.47907510395283	1.21195581128264	-2.10801720339193
H	3.60329868332063	2.16184243774941	-1.13168870474860
H	2.01837595168513	1.95643335277212	1.70661159439952
H	3.73068829642828	1.82952013354856	1.35593182660069
H	2.87208313207430	0.48978638757019	2.12511174574367
H	3.66771604645660	-0.78870702606651	-1.23827982215949
H	3.81300218064558	-1.07415965563743	0.50487972934496

H	4.65941213165711	0.27667862817318	-0.24323704348063
H	-2.15325436539837	-2.03148108012674	-0.20383128019821
H	2.08936768775209	-2.07579479890522	-0.29228048878980
H	0.86072064696937	2.25645720332756	0.37873372635828

Table A1.45. Coordinates for the DFT optimized structure of 4-H-2,6-DTBP radical in DMSO

	x	y	z
C	-1.84511417213346	1.88471250117635	-0.07437264955877
C	-1.98716416456922	0.53895309079904	0.15462429513950
C	-0.48442845164214	2.41768810849309	-0.21922558209463
C	0.67209540255361	1.51748787089902	-0.12443059900400
C	0.43254635871429	0.18352672558111	0.09146255127463
C	-0.87195859917624	-0.30422934395976	0.23541844392248
H	-2.96647019587623	0.09997910491378	0.27188324170061
H	1.24949061076385	-0.51904293080926	0.15922035304466
O	-0.31300780984028	3.62887881647082	-0.42513362264049
C	-3.03378925460181	2.82910599066575	-0.19860109111187
C	-2.96883553905200	3.93323442511475	0.86786595538807
H	-2.95450842254509	3.50565462797453	1.87234931064310
H	-3.85693408734694	4.56348476594673	0.78520615679924
H	-2.09073910006104	4.56053546659837	0.74301876236407
C	-4.35730786477878	2.08827200555893	-0.01098868525773
H	-4.43167160368393	1.62990691996168	0.97641821485268
H	-4.50086589747147	1.31284506319938	-0.76514021679082
H	-5.17712141175123	2.80126629401027	-0.10805466911962
C	-3.05353357860003	3.47036053137721	-1.59599891065212
H	-2.17535192017519	4.08752130104103	-1.76618909544172
H	-3.94140029497247	4.09906131665704	-1.69251005326396

H	-3.09929764784403	2.70660749612875	-2.37478520915927
C	2.07692041902855	2.08792940289647	-0.26348564697483
C	2.34040224111845	3.12080717623387	0.84438893451384
H	1.66981642701800	3.97244960934555	0.76481301692389
H	3.36796362880363	3.48195078284963	0.76436903278082
H	2.21908454169640	2.67343440595263	1.83273539862506
C	3.14069839034916	0.99718618009738	-0.13892547454974
H	3.10366891602322	0.49893048248645	0.83101715827836
H	4.12608129613345	1.45379370234792	-0.24110132106007
H	3.04400595055329	0.24267135830005	-0.92112495642766
C	2.25667493254621	2.75200263229238	-1.63745515470728
H	1.59702579682417	3.60696012668739	-1.75804967538720
H	2.05893768820199	2.04170789489710	-2.44278580345729
H	3.28863655461351	3.09424041170720	-1.74000337238693
H	-1.02163913882017	-1.36021431389273	0.41263096279496

Table A1.46. Coordinates for the DFT optimized structure of 4-OMe-2,6-DTBP radical in DMSO

	x	y	z
C	-1.81406372876476	1.98452829714883	-0.09195873959640
C	-1.95308080901897	0.64755949556049	0.13736546006352
C	-0.46059937093073	2.52954642897024	-0.25919615283149
C	0.68859471087611	1.62682029856600	-0.18014970581311
C	0.47181352309247	0.29311533629500	0.04507869072233
C	-0.82841711098206	-0.20292775571218	0.21073552017640
H	-2.92136163152913	0.18753015922755	0.27190184999489
H	1.30160579210785	-0.39054738216964	0.09983362240457
O	-0.29337363473046	3.74326751272329	-0.46824475241240
C	-3.01416150442814	2.92155209408888	-0.19097555410409

C	-2.93670049524270	4.01925464445502	0.88049545951762
H	-2.92966614815884	3.58578517088560	1.88266287447561
H	-3.81625259787825	4.66203749531571	0.80103347689749
H	-2.04972046930321	4.63484158428222	0.75926452317003
C	-4.33139313690219	2.17454859196941	0.01501242852206
H	-4.38748574955224	1.70954709107266	1.00058551829740
H	-4.48661825075437	1.40372770850795	-0.74176059421177
H	-5.15552056556586	2.88532862959348	-0.06239434891864
C	-3.05996189490915	3.56956583942692	-1.58378198927081
H	-2.18257409954002	4.18409941266071	-1.76693211203938
H	-3.94754033152966	4.20157940829421	-1.66110076174775
H	-3.12291248621030	2.80918532073024	-2.36479588944008
C	2.09825693020615	2.18043072770737	-0.34161005377954
C	2.38425552209689	3.21037920463948	0.76183363705421
H	1.71571327078776	4.06441213621865	0.69096793619777
H	3.41307448463800	3.56485610156572	0.67008163287664
H	2.27192728958107	2.76140931233987	1.75076787928463
C	3.15488761188720	1.08063268078593	-0.23069134360864
H	3.13368889200613	0.58973313291767	0.74374092808603
H	4.14223676183885	1.52668114381928	-0.35523424571291
H	3.03719052365500	0.32111717297994	-1.00556042951553
C	2.25920192338129	2.83663116412054	-1.72027350187476
H	1.59502620804948	3.68899554214928	-1.83441568282826
H	2.04902473689562	2.12030843034718	-2.51733532111715
H	3.28926172726924	3.17838141438763	-1.84110052188933
O	-1.08696069991148	-1.48389508396797	0.44812313473775
C	-0.00731741056706	-2.39319723779878	0.58412655955391
H	-0.45360985816276	-3.35430779503721	0.81737895146449

H	0.65245201190149	-2.09105548167939	1.39753840505416
H	0.55702006430177	-2.46851794738786	-0.34541678783950

Table A1.47. Coordinates for the DFT optimized structure of 4-Me-2,6-DTBP radical in DMSO

	x	y	z
C	-1.80545763310076	1.95284227877863	-0.11176790574754
C	-1.94692661194812	0.60786844874008	0.10543247731220
C	-0.44719017808275	2.49362603142928	-0.24011246378253
C	0.70412679829128	1.58953565395557	-0.14152883701476
C	0.46270187248813	0.25758661835147	0.06457158051705
C	-0.83958690255877	-0.25495910600581	0.19896307142794
H	-2.92947347395505	0.16905680187494	0.20776649437815
H	1.28269122492016	-0.44292858417908	0.13506128795968
O	-0.27476665569917	3.70678990907257	-0.43655162386660
C	-2.99853098842084	2.89258868537880	-0.24244663614398
C	-2.95244659389288	3.98690580445979	0.83464752648573
H	-2.97123264977249	3.55002726933258	1.83516391917711
H	-3.83125684565574	4.62751102651696	0.73347399103758
H	-2.06435744610405	4.60547842156357	0.73994097599299
C	-4.32246089677648	2.14650933535009	-0.07899929806878
H	-4.40809494319846	1.67723695838233	0.90237055044600
H	-4.45521077358468	1.37892191976742	-0.84314556540075
H	-5.14280381062480	2.85873203522713	-0.17814894856669
C	-3.00307604448795	3.54600908234958	-1.63406547968956
H	-2.12446328194003	4.16697956027250	-1.78738267631499
H	-3.89180916756461	4.17249973406141	-1.73717402385518
H	-3.03607313025222	2.78834487895191	-2.41953452182521
C	2.11371889841053	2.15295476507352	-0.26732698499327
C	2.37407595026423	3.17475899751997	0.85078704382249

H	1.70403771525594	4.02734251941239	0.77609178710823
H	3.40248831275288	3.53553777187554	0.77979448075017
H	2.24731607013537	2.71748707891417	1.83402681659563
C	3.17313253983153	1.05733490652387	-0.14517609956349
H	3.13020955038944	0.55265473809497	0.82123741620413
H	4.16076590426971	1.51076832714161	-0.23982177252571
H	3.07754928842748	0.30786301723018	-0.93241693040261
C	2.30417608189622	2.82606033719364	-1.63478105370598
H	1.64576133756182	3.68224149028936	-1.75355552222961
H	2.11045059001907	2.12085854227907	-2.44569044668476
H	3.33727704528043	3.16744583529204	-1.72888973930015
C	-1.04041453318870	-1.70398993465725	0.48555188641021
H	-0.22243851553967	-2.30373480674632	0.08928042975683
H	-1.98285054490148	-2.06559169781648	0.07644661714592
H	-1.06986755894454	-1.86473465125206	1.56745817715407

Table A1.48. Coordinates for the DFT optimized structure of 4-^{t}Bu-2,6-DTBP radical in DMSO

	x	y	z
C	-1.95089325389280	1.73057057244277	-0.08417643838599
C	-2.14994510838403	0.39803968599887	0.18526266492196
C	-0.57888419250040	2.20233613350941	-0.29159536128248
C	0.52272449129621	1.23428946745218	-0.26069084639864
C	0.22251484918521	-0.07219361304787	-0.00445600191017
C	-1.09336675606444	-0.52353515858388	0.23741060678628
H	-3.15150821738550	0.04041412529902	0.35828619899873
H	1.01733895836606	-0.80113781828090	0.02447008522011
O	-0.35190316151764	3.40647363026194	-0.48930048729827
C	-3.10712516420405	2.71786186038609	-0.18694530473841

C	-2.98385804649874	3.81754648206896	0.87898331791040
H	-3.01596829231173	3.39006659559684	1.88310598607060
H	-3.82568212087195	4.50660347190174	0.78223845036414
H	-2.06230700380863	4.38238315664824	0.76730300958681
C	-4.45803810643439	2.03137597046110	0.01923335669371
H	-4.54219518726194	1.58204481329010	1.01009931294129
H	-4.64209736925840	1.25928654398180	-0.72981487637535
H	-5.24856755700452	2.77725684108814	-0.07247466626436
C	-3.12196431541693	3.35690912437115	-1.58576659148431
H	-2.22660601907146	3.94562657264171	-1.76634013348688
H	-3.99153097009563	4.01138277377745	-1.67541234820480
H	-3.19776496513227	2.59145730950983	-2.36060679852949
C	1.95252923187423	1.70362178434337	-0.49915913933034
C	2.36935900539723	2.70362815576568	0.59029809772685
H	1.74834656594179	3.59577381808124	0.56912074260312
H	3.40802028145075	3.00071614230780	0.43004326363196
H	2.29847428892913	2.25153298301912	1.58157013782755
C	2.94223675931333	0.53813553638157	-0.46322851143134
H	2.95750404618441	0.04184756167344	0.50858629668650
H	3.94523539854544	0.92110516735249	-0.65509681890161
H	2.72074133600333	-0.20616492542355	-1.23017211706627
C	2.07692083308342	2.36834044601667	-1.87808290781602
H	1.46264786511867	3.26218030222418	-1.94557167367408
H	1.78102975836306	1.67820521436148	-2.67091587469096
H	3.11799409454335	2.64904794802937	-2.05053847347458
C	-1.30472566807071	-1.99101652113862	0.55647029310691
C	-0.53397223208248	-2.32787055996259	1.84182991376189
H	0.53956263882218	-2.18332805617884	1.71754728757846

H	-0.70431692021901	-3.37235982951241	2.10830435118201
H	-0.86859695569886	-1.70388610338485	2.67247400912207
C	-0.75633040119633	-2.84276566510768	-0.59662604421135
H	0.30760373290520	-2.67142172708068	-0.75813315134335
H	-1.28255049325954	-2.62461948190048	-1.52744677930292
H	-0.89168280862410	-3.90095761639819	-0.36722204235773
C	-2.77641430530803	-2.34086844059657	0.76169603222128
H	-3.21102191558165	-1.79044602848163	1.59778132285903
H	-2.86516876325271	-3.40509193875998	0.98173131881162
H	-3.36807786491413	-2.13661670640502	-0.13222266865360

Table A1.49. Coordinates for the DFT optimized structure of 4-Cl-2,6-DTBP radical in DMSO

	x	y	z
C	-1.84317928024765	1.88419022905843	-0.09064716342403
C	-1.99461337438490	0.53586641104632	0.11316276669372
C	-0.48504897931907	2.41867112218079	-0.23595930176877
C	0.66958412209281	1.52015168657365	-0.13315184479609
C	0.43841883941271	0.18198667562408	0.06016006277881
C	-0.87206863390906	-0.30247224616369	0.17784581281274
H	-2.97257190663718	0.09247904230160	0.22253900694570
H	1.25369270726785	-0.52208420343030	0.12701230730041
O	-0.31463089156438	3.62585662299701	-0.45241566078037
C	-3.02360935168592	2.84306439559538	-0.19359192919946
C	-2.92607627280484	3.94946520772395	0.86983773686741
H	-2.88709822187360	3.52724060588223	1.87562952696084
H	-3.81443763149906	4.58144383058311	0.80612912154351
H	-2.05197583767214	4.57662853012849	0.72051555719122
C	-4.35179242557356	2.11949326014864	0.01697352691927

H	-4.41124830681179	1.65759865910742	1.00373829138224
H	-4.52244254923071	1.35168010183739	-0.73916390681722
H	-5.16263514210731	2.84508042127212	-0.05907335147954
C	-3.05802824426599	3.48903770205773	-1.58953039451538
H	-2.17714079432309	4.09854879311324	-1.77221220723883
H	-3.93979367535985	4.12900358763607	-1.66603648159362
H	-3.12667896598764	2.73080460341578	-2.37158529782008
C	2.07086776022660	2.10512219937271	-0.25782117177162
C	2.30825736363298	3.17017890944163	0.82676954035401
H	1.64220720180368	4.02044039711041	0.70979839962082
H	3.33726469230428	3.52873145693522	0.75494574464658
H	2.16840407404855	2.75329486999447	1.82563432587518
C	3.14502640342407	1.03215187859473	-0.08992441526932
H	3.09056448723258	0.55201663920753	0.88835154601059
H	4.12566051984451	1.50167715033982	-0.17679513250965
H	3.07843437885907	0.26361748190845	-0.86133019822181
C	2.26112363255994	2.74103018232218	-1.64486538501217
H	1.58914643701365	3.58143593949831	-1.79685769231222
H	2.09171982249402	2.00987767161734	-2.43754570484732
H	3.28808290763681	3.10115311513156	-1.73594718284286
Cl	-1.11047486459638	-1.99480293016387	0.41443114831730

Coordinates for Calculations in Chapter 4 and Appendix 3

Table A3.5. Coordinates for the DFT optimized structure of $[Mn^{III}(OH)(dpaq)]^{+}$

	x	y	z
Mn	-0.14219165609036	-0.07253586590930	0.03607249738240
O	0.33122965488788	-1.20168526217487	-3.87229617381038
O	-0.19849237073471	-0.09656943160246	1.86376611350255
H	-1.07143935588853	-0.33399235757235	2.21202830594289
N	-0.74660079068655	1.90600332187026	-0.25519170390517
N	-0.07367099098497	0.00971768662552	-1.94109656174860
N	0.49902570255718	-2.16819791227168	-0.33473525618378
N	-2.06154811810668	-1.15962145752629	-0.14399246017459
N	2.06355247844104	0.04148873600204	0.09299462741103
C	-1.06408701816670	2.78969263609687	0.67596457829911
H	-0.99261608291609	2.45143625024986	1.71116599527579
C	-1.47216841924601	4.09853048131705	0.35111831754528
H	-1.72597014373794	4.79406615163105	1.15206916882673
C	-1.54174055117505	4.47116536795690	-0.97690634644377
H	-1.85452554376855	5.47952343220576	-1.25832033430262
C	-1.20424776960893	3.54132208662100	-1.99516424640734
C	-1.24311008470694	3.83163626758326	-3.38520008618476
H	-1.54824720293904	4.82628500693898	-3.71687814518010
C	-0.89252791977610	2.84886212218416	-4.28885452579482
H	-0.91842240184035	3.06452695568419	-5.36003668391427
C	-0.49475060841919	1.55279287888408	-3.87643593790228
H	-0.22682607705947	0.80480287910606	-4.61709996040394
C	-0.44281153255795	1.22597258917500	-2.52318705495967
C	-0.80329100964632	2.24044649886853	-1.57993259489325
C	0.28020121629306	-1.09407405226742	-2.64585501388067
C	0.67223727140655	-2.30805582891548	-1.80363972798089
H	1.72591941888893	-2.52389155739413	-2.03312696054286
H	0.09713229013950	-3.16913969218246	-2.17349812585978
C	-0.57227892626038	-3.03411677520719	0.19304539760490
H	-0.48654094066340	-3.03999654152999	1.28967193297595
H	-0.46008249410669	-4.07280213364442	-0.15482043089258
C	-1.93488472520184	-2.49544924835089	-0.16775823889411
C	-3.02093342803376	-3.31935302926983	-0.46054247491006
H	-2.89041743724205	-4.40249836019944	-0.48746865872848
C	-4.26246282396130	-2.73280048625363	-0.71566194050750
H	-5.12830177209073	-3.35675660327192	-0.94754215356754
C	-4.37963123313547	-1.34161386380974	-0.67891486582871
H	-5.32960808468429	-0.84273767826421	-0.87656874705749
C	-3.24359145365833	-0.58854096352645	-0.39343982478705
H	-3.27680640627013	0.50260522246721	-0.36586519396218
C	1.76744457573486	-2.33913153612788	0.40041595537648
H	1.52620994391939	-2.40327132821974	1.47153941338759
H	2.27763772245356	-3.27232813666299	0.11417501220687

C	2.67220707288147	-1.14965947041526	0.18954981062438
C	4.06165480899833	-1.25829745796042	0.13539694588957
H	4.53374719135460	-2.23991464637611	0.20317335641537
C	4.82298941239088	-0.09668055245048	-0.00828209839859
H	5.91276250232629	-0.15502194972326	-0.05488246915240
C	4.17398668232074	1.13664155004439	-0.10080299045284
H	4.73052016322734	2.06759088355517	-0.21903931884633
C	2.78253550324586	1.15798320779004	-0.05030498303693
H	2.22523276189734	2.09380696622294	-0.13046213917051

Table A3.6. Coordinates for the DFT optimized structure of $[Mn^{III}(OH)(^{6Me}dpaq)]^{+}$

	x	y	z
Mn	-0.02567476246197	-0.04459169029074	0.09967676049221
N	-1.97658679169226	0.48071393361650	-0.23448955959005
N	0.04117646579237	-2.37712738434784	-0.05675372548970
N	0.02390988620018	0.11438890384439	-1.86119582667103
O	-0.10295208514034	-0.14014504139624	1.92555675628101
O	1.41441794024280	0.03561908219863	-3.71112011905760
N	2.04742738182688	-0.49135744580290	-0.13896635387216
N	1.01768844183736	2.14142266563744	0.13868260506896
C	-2.92397189871559	0.62440534779709	0.67654105951924
C	-4.23523883992121	1.00259944981477	0.32868030342349
C	-4.54256881495845	1.23061730011237	-0.99893059648529
C	-3.54265780553904	1.08109311560620	-1.99568150066262
C	-3.75567916018994	1.29104295608044	-3.38495310266915
C	-2.70567350462418	1.11424054593534	-4.26402608975788
C	-1.41348520289158	0.72641062064980	-3.82813637663359
C	-1.16500025012785	0.51039398236158	-2.47587853854953
C	-2.24597735654061	0.69481025250400	-1.55915386605533
C	1.19773770827417	-0.09746916013351	-2.50712484192533
C	2.31850662121106	-0.60333084421137	-1.60276354506757
C	2.29740959911618	-1.76817779948695	0.56853766688011
C	1.29062458183852	-2.81275710370378	0.16827099930169
C	1.64033657156648	-4.15813853068180	0.06833557474556
C	0.64614676641376	-5.07782871798268	-0.26454970938781
C	-0.64881528145147	-4.61849225712816	-0.49497738454244
C	-0.92735863261562	-3.24944186837841	-0.39018018355329
C	2.83836881995795	0.59430208467451	0.48442462258636
C	2.34665812787011	1.95355609153614	0.06671528736203
C	3.22529051670481	2.96499987118492	-0.31215629781708
C	2.69886822508009	4.22613460367792	-0.60000751175311
C	1.32586981251519	4.42391617862421	-0.48915695331727
C	0.49766011630384	3.35371336998579	-0.11712982586957
C	-2.30381482939073	-2.71541353373950	-0.64951736217012
C	-0.98605839688791	3.53697463354196	0.00451003070375

H	0.05444595818788	0.71848967417961	2.34749415167464
H	-2.63551178529413	0.43509053334714	1.71151516755635
H	-4.98514563438154	1.11017686656478	1.11331495860291
H	-5.55189999967400	1.52580708163302	-1.29512895194754
H	-4.74617983923081	1.58762921721358	-3.73565238115250
H	-2.86403130662675	1.27315269359910	-5.33350761850459
H	-0.61076427870865	0.59341290280540	-4.54857562759415
H	2.47225325537963	-1.66056252638514	-1.86102423209632
H	3.24873896676434	-0.07833230745454	-1.86023117213415
H	2.19745512028514	-1.57055201437627	1.64537478162750
H	3.32282179934135	-2.12052523816664	0.38017206782263
H	2.67062091819616	-4.47026187399267	0.24631850300523
H	0.88086836635426	-6.14109012147116	-0.35205554717658
H	-1.44878621760418	-5.30973237973225	-0.76443458164830
H	3.90612557057667	0.47262405107894	0.24913414724098
H	2.72045444206872	0.50100814834383	1.57343441457034
H	4.29644098981026	2.76661879715429	-0.37291003826189
H	3.35502433537005	5.04557203081868	-0.90187347443179
H	0.88223444582665	5.40032428720937	-0.69037907683012
H	-2.69053548308173	-2.18316718667333	0.23177823394038
H	-2.99966873299650	-3.52786891719292	-0.89600164349648
H	-2.29412645171946	-2.00735250810862	-1.49104296665313
H	-1.50211199433299	3.13418306550476	-0.88023976541721
H	-1.24250118117270	4.60238579830533	0.07813151763140
H	-1.37688723294067	3.01699831369557	0.88909673820561
O	10.58863310015237	5.15652843088464	10.60319538910858

Table A3.7. Coordinates for the DFT optimized structure of $[Mn^{III}(OH_2)(^{6Me}dpaq)]^{2+}$

	x	y	z
Mn	0.01905221089840	-0.06571896570329	-0.04390103523411
N	-1.90543687505187	0.46032219491222	-0.35119327308200
N	0.02301385132093	-2.35994599040243	0.03469327251355
N	0.09986073694361	0.11886427718180	-1.94819680981538
O	-0.10960119647736	-0.10046076716661	1.97757812265429
O	1.51640923880734	0.07699727380871	-3.76856656012384
N	2.05658733117237	-0.51788097756336	-0.21355266665805
N	0.96097444498162	2.08585692695214	0.19955046501092
C	-2.86362543024227	0.58546003687148	0.55662522476488
C	-4.16315633022645	0.98918021687070	0.20554542164452
C	-4.45423030512674	1.26694923645663	-1.11783039250579
C	-3.44621555950808	1.14099606408393	-2.10756855278146
C	-3.63422553276726	1.40286738279714	-3.49165886358498
C	-2.57423596058772	1.24522503955473	-4.36139907646225
C	-1.29249755194070	0.82532940023660	-3.92177548225852
C	-1.07624337561538	0.55956332152775	-2.57578765869113

C	-2.16055029439843	0.72402693182999	-1.67179639827532
C	1.29357525404584	-0.10399807362547	-2.58097209613010
C	2.35411095615065	-0.69340231757978	-1.66771883835359
C	2.30993622937769	-1.77312751088922	0.54473318054682
C	1.28050182070924	-2.81261967292524	0.20339148616312
C	1.61153009666001	-4.15877287636816	0.09564981031047
C	0.59279324353295	-5.06933024591417	-0.18725650302599
C	-0.70531092204058	-4.59741037372563	-0.36040113812729
C	-0.97011406141887	-3.22648968041608	-0.25075602521090
C	2.84468884378269	0.60004029587419	0.37588482205409
C	2.28531486571709	1.93847760016633	-0.01091148709077
C	3.08852271293045	2.96750220666052	-0.48490919783342
C	2.49544007211825	4.21052787959338	-0.72527541519589
C	1.14013332038155	4.37203721381379	-0.46223299396439
C	0.38392470815800	3.28519338809991	0.00463479553688
C	-2.35443782068590	-2.69224848893504	-0.45362632120742
C	-1.07654591016836	3.44657560084905	0.30183830313007
H	0.20482844249446	0.63691073738748	2.53554873139540
H	-2.60243403657797	0.36643335192787	1.59228888173554
H	-4.91854094471118	1.07892907877016	0.98659218222664
H	-5.45689712226040	1.58452133330122	-1.41243231083487
H	-4.61514493949178	1.72535762660264	-3.84556224269470
H	-2.71341568073531	1.44512656755352	-5.42617834450195
H	-0.48261937208478	0.70932811438638	-4.63667797461669
H	2.39926067600902	-1.76738158210730	-1.89652922096446
H	3.33707510295962	-0.26924619432963	-1.90979877290264
H	2.25559714412567	-1.53493188800410	1.61652787514009
H	3.32701537718253	-2.13529061380452	0.33938375272860
H	2.64563333288398	-4.47940970104758	0.22804001471516
H	0.81220617433540	-6.13505014139410	-0.28099529906683
H	-1.52320705545054	-5.28132293123752	-0.59058872897515
H	3.89898566627230	0.50207351764696	0.08497220905028
H	2.78838432242641	0.50193712759534	1.46885706529982
H	4.15320577894661	2.80059676808245	-0.65304200394901
H	3.09086157744228	5.04466975972934	-1.10239254445936
H	0.65129037692180	5.33560631384962	-0.61338522297117
H	-2.69984178401651	-2.14466287529752	0.43482337602732
H	-3.06078943430370	-3.50915219211310	-0.64763373720013
H	-2.38743246848147	-2.00677525114875	-1.31320453919100
H	-1.68913073878862	3.15997242941179	-0.56699072361551
H	-1.30787251918667	4.49699937387504	0.52454812920924
H	-1.37788101231032	2.83222325574168	1.15945762606172
H	-0.15220681003347	-0.90819134730390	2.52151500363678

Table A3.8. Coordinates for the DFT optimized structure of [Mn^{II}(OH)(^{6Me}dpaq)]

	x	y	z
Mn	-0.14453527641658	-0.21809867116731	0.33083530573059
N	-2.18640315758702	0.45611099652977	-0.34604530582938
N	0.17511498039014	-2.53677386733417	0.12303321329971
N	0.01504047582641	0.16438358190920	-1.85208840772466
O	-0.39111886265709	-0.25673592007281	2.29855478597502
O	1.52343296559108	0.26886092195927	-3.63011068954887
N	2.12251111100167	-0.58581941009260	-0.14729017547205
N	0.99063436038475	2.08349653157401	0.32483430689659
C	-3.22253572090189	0.57888260037317	0.45922351725368
C	-4.45302654919837	1.12609787646094	0.03584451030318
C	-4.57100603060795	1.55218998005115	-1.27092040259701
C	-3.46862462588083	1.43516297249835	-2.15962339074966
C	-3.51463324394159	1.86286195431683	-3.51346536574560
C	-2.38799993566638	1.72028835092733	-4.29899858722373
C	-1.18918341896715	1.16372650746433	-3.79618667042738
C	-1.08481149002035	0.72338402356329	-2.47063894963060
C	-2.26370753162490	0.86549008588611	-1.64073856310881
C	1.19860305312467	-0.00677550326816	-2.45984510795986
C	2.25857600991614	-0.72184321779031	-1.60672798989620
C	2.45465794665088	-1.82232454172702	0.56946021995645
C	1.45530932608231	-2.91370481910806	0.26156759932486
C	1.84785683843290	-4.24798267423000	0.14008473939286
C	0.87192241167201	-5.20937597081777	-0.12401022931784
C	-0.45496908365570	-4.80655148792737	-0.26867935258450
C	-0.77517335748016	-3.44847102819169	-0.14263963580456
C	2.87035114184523	0.56754097145170	0.37422524858223
C	2.25691452533762	1.87157939613578	-0.07551884808670
C	2.95563316297708	2.79342250773102	-0.85126173665054
C	2.31137053233895	3.98087151597972	-1.21576818404282
C	1.00922583756835	4.20177751301298	-0.78119004135263
C	0.36964589152627	3.22324254905356	0.00063257787792
C	-2.17896821085509	-2.94463124974748	-0.30574818305647
C	-1.03512545497397	3.42748010812856	0.49416286755490
H	-0.24962447959370	0.61002450871254	2.69789677520038
H	-3.07386830752992	0.24020901489475	1.48817335115822
H	-5.28269973837482	1.20856384007592	0.74042390876463
H	-5.50526592542264	1.98573756283493	-1.63742841856074
H	-4.43564853654990	2.29794372581576	-3.90852963767037
H	-2.41215193029157	2.04697944374691	-5.34262310935231
H	-0.31902583637451	1.07117363649805	-4.44042807402450
H	2.17622852781139	-1.78726056554148	-1.86939901428450
H	3.25487758953495	-0.39227880995120	-1.94588852759769
H	2.41245392434006	-1.60303365340666	1.64796366601588
H	3.47730534585455	-2.17503795663472	0.34434108493839
H	2.89964758278432	-4.52038918917312	0.24445222291521

H	1.14521226048049	-6.26231024136035	-0.22686208645267
H	-1.24140436855516	-5.53122897340620	-0.48665001044225
H	3.93333040578182	0.52374639822630	0.07647335207905
H	2.82305941419478	0.52404203198143	1.47192693460885
H	3.98009124428446	2.58514410824562	-1.16471916430378
H	2.82582381938736	4.72487114816642	-1.82899420870968
H	0.47988564331657	5.12212985645315	-1.03707198436248
H	-2.50807727125867	-2.41361030346307	0.60073581696996
H	-2.87987050640727	-3.76620328223198	-0.50565731032080
H	-2.23439750753533	-2.22675860431316	-1.13862575561044
H	-1.75921574200334	3.29500927450546	-0.32556803666326
H	-1.16959889621565	4.44924251288694	0.88183633806399
H	-1.27612733188964	2.70664393290545	1.28504881230294

Table A3.9. Coordinates for the DFT optimized structure of $[Mn^{II}(OH_2)(^{6Me}dpaq)]^+$

	x	y	z
Mn	-0.08661871644147	-0.21508642637688	0.04734994738621
N	-2.11212767884189	0.45037198880849	-0.54063779190015
N	0.14962414805521	-2.47770646703602	0.22435505895942
N	0.08888994846283	0.15100749797552	-2.05419806464004
O	-0.39420044915458	-0.15370462696922	2.26618661362503
O	1.65199213094165	0.31967265715080	-3.77523208164309
N	2.15094743621471	-0.61038855656012	-0.30682126431120
N	0.93064107065611	1.95054265430664	0.33362690470620
C	-3.16473721775327	0.55755712307160	0.24997454716490
C	-4.39095010523096	1.10135875045559	-0.18146871433807
C	-4.49436717516686	1.54640352060032	-1.48306011434974
C	-3.38168871580288	1.44521714092376	-2.35900621585943
C	-3.41838581523354	1.88688557487328	-3.70857488624917
C	-2.28902665214431	1.75420952933949	-4.49050774377346
C	-1.09432282676681	1.18980225429836	-3.98592816704111
C	-1.00388633857848	0.73559082604377	-2.66725265464412
C	-2.17993362096779	0.87329752175337	-1.83747306373235
C	1.29162731204479	-0.00895376678268	-2.63462362077018
C	2.29579857657277	-0.78333714942478	-1.76754112566622
C	2.48998987259291	-1.83742745266491	0.42878187635607
C	1.42953430868659	-2.89559621509961	0.24325772994169
C	1.76616972969204	-4.24381562804048	0.13652153960051
C	0.74122404927956	-5.18335226816243	0.02413757605252
C	-0.58066439670238	-4.74393548230782	0.01786808829855
C	-0.85078605775865	-3.37399387012779	0.11593495997706
C	2.90322088943428	0.55550220803138	0.18708236156637
C	2.19898788354105	1.85371665811193	-0.11784324606035
C	2.83400081796512	2.89877237738457	-0.77943887674928
C	2.13329515150347	4.09538689873367	-0.96423241423741

C	0.84443011284914	4.20490085179189	-0.45725628788644
C	0.26284374386583	3.10671956281892	0.19894872151367
C	-2.25416382332997	-2.84828415160039	0.09642524935665
C	-1.12059178944423	3.21351730033233	0.77226387608054
H	0.13088584714660	0.51617244826952	2.73636520423909
H	-3.04485340657330	0.21143540667783	1.27915950263475
H	-5.22810382796676	1.16769978722387	0.51511941327176
H	-5.42600363438968	1.98037240189840	-1.85480673219642
H	-4.33822495904265	2.32393077397079	-4.10337274000113
H	-2.30749488375242	2.09124768659602	-5.53046070842150
H	-0.22088341805881	1.09928330233865	-4.62647121043878
H	2.13869466175621	-1.84583326929581	-2.00745366183261
H	3.31694170696962	-0.52744237060529	-2.09198832970856
H	2.54388139602821	-1.58532464927408	1.49926227429784
H	3.47779101911773	-2.23390389838892	0.13978521020361
H	2.81508668335430	-4.54432403733434	0.14083491872210
H	0.97221856088501	-6.24755219848853	-0.06248329890819
H	-1.40722450624402	-5.45065782333966	-0.06957430608189
H	3.92837261451390	0.57026322208603	-0.21803481320429
H	2.97834785276226	0.46540295599665	1.28053317384160
H	3.85645605922132	2.77812753154451	-1.14056609272432
H	2.59735401074661	4.93406814270978	-1.48837592110530
H	0.27670542351963	5.13168744591380	-0.55948035126595
H	-2.44463159302794	-2.20811626514325	0.97117835973276
H	-2.98505265865250	-3.66724660034206	0.10447258359156
H	-2.42964494714168	-2.24106774073584	-0.80499676717797
H	-1.88066240688170	3.18747082056067	-0.02412635294262
H	-1.24179637492487	4.17249379215143	1.29881588969121
H	-1.32596171602652	2.39876862325393	1.47648505489285
H	-0.29682444237854	-0.97551880989668	2.77927586215692